Quantifying and interpreting the climatic effects of uncertainty in aerosol radiative forcing

Leighton Anunda Regayre

Submitted in accordance with the requirements for the

degree of Doctor of Philosophy

The University of Leeds

School of Earth and Environment

March 2016

Declaration of Authorship

The candidate confirms that the work submitted is his own, except where work which has formed part of jointly-authored publications has been included. The contribution of the candidate and the other authors to this work has been explicitly indicated below. The candidate confirms that appropriate credit has been given within the thesis where reference has been made to work of others.

The majority of the research included in the thesis has been peer reviewed and published. The remaining research has been prepared for submission to suitable journals. This thesis is published using the University of Leeds alternative thesis format so that the research within can be readily identified and accessed. The thesis consists of an introductory chapter, a co-authored article, three first-author articles, a discussion chapter and appendices.

The publication Carslaw et al. 2013, Large contribution of natural aerosols to uncertainty in indirect forcing, Nature, 503, 6771, doi:10.1038/nature12674, jointly authored with Lindsay A. Lee, Carly L. Reddington, Kirsty J. Pringle, Alexandru Rap, Piers M. Forster, Graham W. Mann, Dominick V. Spracklen, Matthew T. Woodhouse, Leighton A. Regayre and Jeff R. Pierce is included as Chapter 2 of this thesis, with supporting information included in Appendix 1. The candidate contributed to this publication by analysing the suitability of the emission inventory used to calculate forcing. Further details of this contribution are included in Appendix 5.

The publication Regayre et al., 2014, Uncertainty in the magnitude of aerosol-cloud radiative forcing over recent decades, Geophysical Research Letters, 41, 9040-9049, doi:10.1002/2014GL062029, jointly authored with Kirsty J. Pringle, Ben B. B. Booth, Lindsay A. Lee, Graham W. Mann, Jo Browse, Matthew T. Woodhouse, Alexandru Rap, Carly L. Reddington, and Ken S. Carslaw, is included as Chapter 3 of this thesis, with supporting information included in Appendix 2. The text was solely written by the candidate with advice from Ken S. Carslaw, Kirsty J. Pringle and Ben B. B. Booth during the manuscript preparation. Remaining co-authors provided comments. The candidate analysed the data and prepared all figures. Ken

S. Carslaw, Kirsty J. Pringle and Ben B. B. Booth contributed to the interpretation of results. The model runs were completed by the candidate with guidance from Kirsty J. Pringle and supercomputing resource provided by N8 and the University of Leeds. Modifications to the statistical emulation code were performed by the candidate with advice from Lindsay A. Lee. The radiative forcing calculations were conducted by the candidate with advice from Alexandru Rap. The emission inventory was prepared by Matthew T. Woodhouse and tested by the candidate. A suitable model configuration was chosen by the candidate with advice from Kirsty J. Pringle, Ken. S. Carslaw, Jo Browse, Carly Reddington and Graham W. Mann.

The publication Regayre et al., 2015, The climatic importance of uncertainties in regional aerosol-cloud radiative forcings over recent decades, Journal of Climate, 28, 65896607, doi:10.1175/JCLI-D-15-0127.1, jointly authored with Kirsty J. Pringle, Lindsay A. Lee, Ben B. B. Booth, Alexandru Rap, Jo Browse, Graham W. Mann, Matthew T. Woodhouse, Carly L. Reddington, and Ken S. Carslaw, is included as Chapter 4 of this thesis. The text was solely written by the candidate with advice from Ben B. B. Booth, Ken S. Carslaw and Kirsty J. Pringle during the manuscript preparation. Remaining co-authors provided comments. The candidate analysed the data and prepared all figures. Ben B. B. Booth, Ken S. Carslaw, Kirsty J. Pringle, Jo Browse and Matthew T. Woodhouse contributed to the interpretation of results. The model runs were completed by the candidate with guidance from Kirsty J. Pringle and supercomputing resource provided by N8 and the University of Leeds. Modifications to the statistical emulation code were performed by the candidate with advice from Lindsay A. Lee. The radiative forcing calculations were conducted by the candidate with advice from Alexandru Rap. The emission inventory was prepared by Matthew T. Woodhouse and tested by the candidate. A suitable model configuration was chosen by the candidate with advice from Kirsty J. Pringle, Ken. S. Carslaw, Jo Browse, Carly Reddington and Graham W. Mann.

The publication Regayre et al., 2016, Observed planetary energy balance does not constrain aerosol radiative forcing, prepared for submission to Nature Geoscience, jointly authored with Jill S. Johnson, Masaru Yoshioka, Kirsty J. Pringle, David M. H. Sexton, Ben B. B. Booth, Graham W. Mann, Lindsay A. Lee, Nicolas

Bellouin, Grenville M. S. Lister, Colin E. Johnson, Ben Johnson, James Mollard and Ken S. Carslaw, is included as Chapter 5 of this thesis, with supporting information included in Appendix 3. Reference format of this chapter has been altered to match the rest of the thesis. Minor changes to content may occur during the review process. The text was written by the candidate and significantly edited by Ken S. Carslaw with advice from Ben B. B. Booth and Kirsty J. Pringle during the manuscript preparation. The candidate tested the model configuration, designed and prepared the ensemble and analysed the results. The candidate analysed the data and prepared all figures. Ken S. Carslaw, Kirsty J. Pringle, Ben B. B. Booth and Jill S. Johnson contributed to the interpretation of results. The model runs were completed by the candidate with guidance from Masaru Yoshioka, Grenville M. S. Lister and Kirsty J. Pringle, using facilities provided and maintained by the UK National Supercomputing service ARCHER under allocation n02-FREEPPE and the Leadership Project allocation n02-CCPPE. A suitable model configuration for use as the template for the ensemble was identified and tested by the candidate with substantial assistance from Ken S. Carslaw, Masaru Yoshioka, Kirsty J. Pringle, Graham W. Mann, Jill S. Johnson, Grenville M. S. Lister, Nicolas Bellouin, James Mollard and Ben Johnson. Atmospheric parameter probability distributions were elicited by David M. H. Sexton, with the screening of parameters conducted by the candidate, David M. H. Sexton and Ken S. Carslaw. The candidate led the elicitation of probability density functions for all aerosol parameters and was assisted by Jill S. Johnson. Ken S. Carslaw, Nicolas Bellouin, Colin E. Johnson, Graham W. Mann, Kirsty J. Pringle, Ben Johnson, James Mollard, Masaru Yoshioka and Lindsay A. Lee participated in the formal elicitation. The candidate designed the experiments by modifying code provided by Jill S. Johnson.

Acknowledgements:

First and foremost I would like to express my sincerest gratitude to my supervisors Kirsty Pringle, Ken Carslaw, Ben Booth and Lindsay Lee, whose unreserved enthusiasm for research and generous commitment of time and resources made conducting this research a valuable and highly rewarding experience. I greatly appreciate the trust my supervisors placed in me to formulate research questions and pursue my own scientific interests. I am especially thankful to have had a supervisory team with such a diverse range of expertise and insight. The professional manner in which Kirsty, Ken, Ben and Lindsay shared their expertise, with myself and each other, allowed me to view each of them as exceptional role models in their own right and afforded me the opportunity to drawn extensively on their shared knowledge, for which I am deeply grateful.

This project benefited greatly from the fact that so many members of the scientific community showed an interest in my work and willingly shared their expert knowledge. I am particularly thankful to David Sexton at the U.K. Hadley Center Met Office, for patiently answering numerous questions about the implementation and behaviour of various physical atmosphere parameters.

I'm grateful to Jill Johnson for her willingness to engage in statistical discussions and challenge my understanding and to Anja Schmidt for being an exceptional role model and inspiring me throughout. Thanks to Steven Turnock, Douglas Hamilton and Joey McNorton for sharing the journey with me and to Richard Rigby for maintaining a cheerful disposition whilst helping with all manner of technical problems. Working with the students and staff in the University of Leeds School of Earth and Environment has been stimulating and entertaining. I appreciate all those who have contributed in recent years to making life in the School dynamic and exciting. UK Hadley Center Met Office staff have always been welcoming, helpful and personable in our collaborations for which I'm thankful.

Finally I would like to express special thanks to my wife Polly for her incredible patience and selfless support throughout.

Abstract

The magnitude of aerosol effective radiative forcing is the dominant source of uncertainty in net anthropogenic forcing over the industrial period. Aerosol effective radiative forcing is also one of the largest sources of uncertainty in recent decadal and near-future anthropogenic forcing. Knowledge about the main sources of aerosol forcing uncertainty can be used to guide the development of models and ultimately reduce forcing uncertainty. The research in this thesis identifies important parametric sources of aerosol radiative forcing uncertainty in global models using perturbed parameter ensembles, statistical emulation and variance-based sensitivity analyses.

Industrial and recent decadal anthropogenic emission periods are used to quantify the sources of aerosol forcing uncertainty over different timescales. Natural aerosol parameters dominate the uncertainty in aerosol forcing over the century-scale industrial period. However, anthropogenic and model process parameters are dominant over recent decades. In each case specific parameters have been identified as priorities for model development that targets aerosol forcing uncertainty reduction.

At the regional scale changes in climatic effects over recent decades may be partly attributable to anthropogenic aerosol forcing. The credible ranges of aerosol radiative forcing, quantified in 11 climatically important regions, support some hypotheses about the role of aerosols in regional climate forcing and call others into question. Reducing uncertainty in the identified parameters would further clarify the role of anthropogenic aerosols in influencing large-scale climate effects.

Physical atmosphere model parameters are found to be far more important than aerosol parameters as sources of top-of-the-atmosphere radiative flux uncertainty. However, aerosols are the dominant source of uncertainty in how the radiative flux changes in response to aerosol emissions (the aerosol radiative forcing). Observations of present-day radiative fluxes provide only a weak constraint of aerosol radiative forcing.

These results provide insight into, and motivation for, model development that focusses on uncertainty reduction rather than quantification.

Contents

List of Figures

List of Tables

Abbreviations

Abbreviations used within the thesis including within published chapters are reproduced here excluding parameter names.

AeroCom Aerosol Comparisons between Observations and Models project

ACCMIP Atmospheric Chemistry and Climate Model Intercomparison Project

ACI Aerosol-Cloud Interaction

ACSIS Atmospheric Observations Model Simulations Project

AMOC Atlantic Meridional Overturning Circulation

ARI Aerosol-Radiation Interaction

ASM Asian Summer Monsoon

AVOC Anthropogenic Volatile Organic Compound

AVOC_SOA Secondary Organic Aerosols produced from Anthropogenic Volatile Organic Compounds

BC Black Carbon

BVOC Biogenic Volatile Organic Compound

CAE Cloud-Albedo Effect

CCN Cloud Condensation Nuclei

CDNC Cloud Drop Number Concentration

CERES Clouds and the Earth's Radiant Energy System

CI Credible Interval

CLARIFY Cloud-Aerosol-Radiation Interactions and Forcing: Year 2016 project

CMIP Coupled Model Intercomparison Project

CMIP5 Coupled Model Intercomparison Project Phase 5

CSSP Climate Science for Service Partnership (China) project

DMS Dimethylsulphide

ECMWF European Center for Medium-range Weather Forecasting

ENSO El Ninõ Southern Oscillation

ERF Effective Radiative Forcing

FAST Fourier Amplitude Sensitivity Test

GASSP Global Aerosol Synthesis and Science Project

GCM Global Climate Model

GHG Greenhouse Gas

GLOMAP Global Model of Aerosol Processes

GP Gaussian Process

HadGEM3 Hadley Center Global Environment Model version 3

IPCC Inter-governmental Panel on Climate Change

ISCCP International Satellite Cloud Climatology Project

ISCCP-D2 International Satellite Cloud Climatology Project D2 reanalysis data

ITCZ Inter-Tropical Convergence Zone

LW Longwave

MASE Marine Stratus/Stratocumulus Experiment

MACCity MACC/CityZEN EU projects emissions dataset

NERC Natural Environment Research Council

OAT One-At-a-Time

OC Organic Carbon

OLR Outgoing Longwave Radiation

P1-P28 Parameter indices (Chapter 2)

PD Present-Day

PI Pre-Industrial

PPE Perturbed Parameter Ensemble

$\mathbf{r_e}$ Cloud drop effective radius

R1-R11 Climatically important region indices (Chapter 4)

RSR Reflected Solar Radiation

S1-S6 Theoretical parameter perturbation forcing scenario indices (Chapter 4)

SAT Surface Air Temperature

SMURPHS Securing Multidisciplinary Understanding and Prediction of Hiatus and Surge Events project

SOA Secondary Organic Aerosols

SST Sea Surface Temperature

SW Shortwave

ToA Top-of-the-Atmosphere

VOC Volatile Organic Compound

Chapter 1

Motivation and background

"An approximate answer to the right problem

is worth a good deal more than an exact answer

to an approximate problem."

John Tukey

1.1 Motivation

The magnitude of aerosol effective radiative forcing (ERF) (Myhre *et al.*, 2013) is the dominant source of uncertainty in surface warming (Rotstayn *et al.*, 2015; Shindell *et al.*, 2015) and total ERF since the pre-industrial (PI) period (Skeie *et al.*, 2011; Stocker *et al.*, 2013b). Substantial uncertainty in the simulation of historical climates reduces the confidence in future climate projections necessary to consolidate agreement on strategies for mitigating the effects of anthropogenic climate change. Although scientific knowledge about aerosol-cloud-radiation interactions has increased considerably in recent years, uncertainty in aerosol ERF has remained the largest source of total ERF uncertainty in consecutive Intergovenmental Panel on Climate Change (IPCC) assessment reports (Schimel *et al.*, 1996; Penner *et al.*, 1996; Forster *et al.*, 2007; Stocker *et al.*, 2013a), with a credible range of aerosol ERF of the same order of magnitude as the forcing known to be caused by anthropogenic CO_2 emissions.

Aerosols affect the Earth's climate by absorbing and scattering solar and terrestrial radiation. Aerosol ERF (Myhre *et al.*, 2013) conflates aerosol-radiation interaction (ARI) forcing; the effect of aerosol absorption and re-emission of energy on atmospheric temperatures, with aerosol-cloud interaction (ACI) forcing; the effect of aerosols on cloud radiative properties and distributions (Twomey, 1977; Boucher *et al.*, 2013). ACI forcing, being the larger component of aerosol ERF, is also the most uncertain, although sources of ARI forcing uncertainty are often neglected (Bond *et al.*, 2013).

There are numerous structural differences in global climate models (GCMs) that lead to a wide range of simulated PI to present-day (PD) aerosol ERF values, including prescribed anthropogenic emissions (Pan *et al.*, 1998; Granier *et al.*, 2011), representations of complex sub-grid processes, such as clouds (Mitchell *et al.*, 1989; Golaz *et al.*, 2013; Neubauer *et al.*, 2014), precipitation (Michibata & Takemura, 2015), aerosols (Storelvmo *et al.*, 2009; Croft *et al.*, 2012), radiation calculations (Steir *et al.*, 2012; Wilcox *et al.*, 2015) and subsequent feedbacks on model dynamics.

Many uncertain aerosol parameters have the potential to influence aerosol ERF, yet sensitivity to these parameters has never before been comprehensively quantified. Perturbed parameter ensembles (PPE) (Lee *et al.*, 2012) provide a suitable method for exploring the uncertainty in aerosol ERF because multiple uncertain parameters are perturbed simultaneously producing an ensemble of credible model variants. Knowledge of the causes of uncertainty in aerosol ERF is currently limited, with PPEs at best quantifying uncertainty in associated quantities such as cloud active aerosol concentrations (Lee *et al.*, 2011, 2012, 2013), precipitation (Qian *et al.*, 2015) and top-of-the-atmosphere (ToA) radiative flux (Shiogama *et al.*, 2012). These studies, although informative, only explore the changes to the current state of the atmosphere. Sensitivity of the atmospheric state and the change-of-state both need to be quantified, because one does not necessarily inform the other (Lee *et al.*, 2016). Aerosol parameters known to significantly influence cloud active aerosol concentrations (Lee *et al.*, 2013) have been neglected in PPEs used to quantify change-of-state sensitivities (eg Harris *et al.* 2013). There is a need to develop existing knowledge about the sources of uncertainty in aerosol ERF, particularly the importance of uncertain aerosol parameters and their interactions with other model processes.

Discussion of total ERF from historical simulations and climate projections typically focus on global annual mean values (Chalmers *et al.*, 2012; Lambert *et al.*, 2012 and Carslaw *et al.*, 2013 for example). Because aerosols have an atmospheric lifetime of order

days and are heterogeneously emitted, their influence on aerosol ERF is highly regional (Shindell *et al.*, 2013). The magnitude and sources of cloud-active aerosol concentration uncertainty vary spatially (Lee *et al.*, 2011, 2012, 2013). Cloud-active aerosol concentration sensitivity to parameter perturbations is also seasonally dependent because emissions of many aerosol species vary throughout the year (Lee *et al.*, 2013). The spatial and seasonal dependence of cloud-active aerosol concentration sensitivity to uncertain parameters suggests that aerosol ERF uncertainty will also vary spatially and temporally.

Over the industrial period anthropogenic emissions have increased globally predominantly in the Northern Hemisphere. However, global anthropogenic sulphate emissions peaked in 1978, (Lamarque *et al.*, 2010) then decreased in Europe and North America as a result of clean air legislation, whilst increasing significantly in Asia (Smith *et al.*, 2011). Current satellite observations reveal a persistence of these regional trends in anthropogenic emissions (Mao *et al.*, 2014) and peak aerosol forcing from Asian anthropogenic emissions relative to the PI period may not be reached for several decades (Li *et al.*, 2014). The magnitude of large-scale climatic responses, such as global mean surface temperature, are sensitive to the spatial position of regional forcings (Chalmers *et al.*, 2012; Shindell *et al.*, 2013), making it important to identify the sources of regional aerosol ERF uncertainty.

Climate uncertainty in the near-future is dominated by parametric uncertainty however on larger timescales the magnitude of greenhouse gas emission uncertainty dominates (Hawkins & Sutton, 2009). In order to improve near-future climate projections a comprehensive analysis of the sensitivity of aerosol ERF in different periods, regions and seasons is required in order to establish a more complete set of priorities for model development that targets the reduction of aerosol ERF uncertainty. The principle aim of this research is to quantify the major parametric sources of uncertainty in aerosol ERF, in recent decades and over the industrial period, on the global mean scale and in climatically important regions. Through a series of PPE experiments and sensitivity analysis of contributions to variance in aerosol ERF or its components at the global and regional scales the key parametric sources of uncertainty will be identified. Furthermore the relative importance of aerosol and atmospheric parameters as sources of aerosol ERF uncertainty will be quantified over different periods. Identifying the the key sources of aerosol ERF uncertainty will inform the model development process so that aerosol ERF uncertainty can be reduced and confidence in climate projections improved.

1.2 Quantifying and analysing uncertainty

Complex physical processes are represented within models using parametrisations, in the form of mathematical equations. Specific values for the parameters in these equations are set by experts, however for some parameters there is limited theory with which to determine an exact value. The resulting parametric uncertainty requires experts to subjectively select combinations of what they deem to be their best estimates for such parameters.

In quantifying the contributions of uncertain parameters to variation in model output, the historical approach in environmental sciences has been to apply a series of one-at-a-time (OAT) tests. In OAT tests a single model parameter value, or structural choice, is perturbed from its default setting and the difference in output between the perturbed and unperturbed cases is used as the measure of sensitivity. OAT tests are a relatively fast method of obtaining insight into the importance of individual model parameter values and structural choices, however they have important limitations. With OAT tests interactions between parameters are impossible to quantify as all sensitivity information is fixed at a single point in parameter space. By perturbing parameters or structures in isolation, OAT tests only investigate a minute part of the multi-dimensional response surface (Saltelli & Annoni, 2010) and as pointed out by Carslaw *et al.* (2013) they do not provide information on model equifinality (Beven & Freer, 2001), where various combinations of parameters or model structures produce equally plausible model output. GCMs that compare favourably with observations may be doing so through a series of compensating errors (Tebaldi & Knutti, 2007; Golaz *et al.*, 2013). The OAT approach produces useful information about model performance, yet is at best a first order indication of the contributions to model output variance.

Because GCMs typically contain multiple structural differences, one method for quantifying uncertainty is to use inter-model comparisons, such as the Coupled Model Intercomparison Project (CMIP) and Atmospheric Chemistry and Climate Model Intercomparison Project (ACCMIP). Inter-model comparisons are typically ensembles of opportunity, with entry criteria relaxed enough to obtain a reasonable ensemble size. The lack of design in this opportunistic sampling approach means that output ranges from inter-model comparisons represent a mixture of uncertainty from structural choices in the members and from parameter values, rather than a systematic quantification of uncertainty from either source (Sexton *et al.*, 2012). In inter-model comparisons, each ensemble member is created using default parameter values, potentially tuned to achieve a desirable representation of

the present-day atmosphere, and is therefore a single realisation of the underlying parametric uncertainty in the host model. The subtle structural similarities between many GCMs causes the added value of new ensemble members to diminish in proportion to the number of models already in the ensemble (Pennell & Reichler, 2010) and suggests that the inter-model diversity is not sufficiently representative of the true uncertainty range.

Another widely used alternative to OAT tests is Bayesian Monte Carlo sampling. The Monte Carlo method repeatedly samples a multi-dimensional parameter space to produce an extremely large sample, a PPE, from which numerical results can be obtained. The application of Monte Carlo sampling to GCM output is limited because the required number of ensemble members, which grows exponentially with the number of parameters to be perturbed, is computationally expensive. Gaussian process emulators (Oakley & O'Hagan, 2004) can be used to circumnavigate much of the computational expense with direct Monte Carlo sampling. A Gaussian Process emulator is a statistical approximation of some aspect of a model. Once an emulator has been constructed using some few hundred simulations, a Monte Carlo sample of tens or hundreds of thousands of data points can be created in a fraction of the time required to produce a single model simulation. The Gaussian Process (GP) emulation technique, described more fully later in this Chapter, is used in all results Chapters 2-5.

The range of credible values sampled from a single-model PPE can be as broad as the range of output from inter-model comparisons (Collins *et al.*, 2010; Klocke *et al.*, 2011). PPEs and inter-model comparisons both inform uncertainty quantification, however PPEs are by design more suited to conducting sensitivity analysis. The GP emulation approach has been used to great effect in the series of sensitivity analyses conducted by Lee *et al.* (2011, 2012, 2013) to quantify parametric contributions to uncertainty in cloud condensation nuclei (CCN) concentrations. The analysis in Lee *et al.* (2011) was restricted to two regions being distinct in the amount of anthropogenic pollution present. The contributions to uncertainty in CCN from the perturbation of eight parameters and their interactions were quantified. Parameter interactions were determined to contribute significantly to variation in CCN concentration in remote marine regions and gain importance with increasing altitude. These findings were confirmed by Lee *et al.* (2012), where the analysis was repeated over the entire globe. Lee *et al.* (2013) created a PPE using the twenty-eight parameters determined by experts to be the most likely sources of CCN concentration variance. Increasing the number of parameters from eight to twenty-eight has the effect of reducing to near-zero the substantial contributions of parameter interactions to CCN

concentration variance detected by Lee *et al.* (2011, 2012).

The breadth of credible aerosol ERF values produced from a single-model PPE is dependent on the number of parameters perturbed, the range of values those parameters take and the probability density functions used in parameter sampling. Distinct PPEs created using GCMs with significant structural differences can produce credible output ranges that do not overlap (Yokohata *et al.*, 2010). This suggests that some of the structural choices in one or both of the models are inherently unreliable. It is essential therefore to ensure model output is thoroughly compared to historical observations. The sensitivity results of Chapters 2-4 are theoretical only however the PPE used in Chapter 5 is compared to ToA radiative flux observations. Furthermore, this PPE has a partner ensemble designed to be compared to a broad range of observational data as part of the Global Aerosol Synthesis and Science Project (GASSP) (GASSP, 2016). Rigorous testing of the GLObal Model of Aerosol Processes (GLOMAP) (Spracklen *et al.*, 2005; Mann *et al.*, 2010, 2012) used in this research is summarised in Appendix 4.

GLOMAP is the aerosol component of the United Kingdom Chemistry and Aerosols (UKCA) model, which is nested inside HadGEM3, the most recent version of UK Met Office's HadGEM suite of models (Collins et al., 2008; HadGEM3, 2016). The HadGEM models and their components are subject to rigorous testing in a variety of conditions before release and have been compared widely to other GCMs (e.g. Taylor *et al.* 2009; Mann *et al.* 2012; Wilcox *et al.* 2013, 2015). Furthermore successive versions of the HadGEM model have contributed to IPCC assessment reports (Schimel *et al.*, 1996; Penner *et al.*, 1996; Forster *et al.*, 2007; Stocker *et al.*, 2013a).

1.3 Methods

1.3.1 Gaussian Process emulation

Gaussian Process emulation (O'Hagan, 2006) is

GCMs typically have computational costs so great that even with the use of world class supercomputers they take days to simulate several months of climate. Choices must be made as to how to approximate a complex computer model within the functional limitations of modern systems. One approach would be to simplify the model (eg Stevens (2015)) and this can often be appropriate where certain model complexities contribute

marginally to the outcomes. However, model complexity often leads to enhanced agreement with observations (Jones *et al.*, 2013). An alternative to model simplification is to use a statistical approach to limit the number of simulations required to produce insight into parameter influences on model output ($y = f(\mathbf{x})$). For deterministic models, where an input vector $\mathbf{x}$, always produces an identical output vector y, the GP emulation technique is one such statistical approach.

GP emulators use multivariate probability theory to produce a probability distribution of some aspect(s) of a complex model conditioned on data from a relatively small set of 'training' simulations. A GP emulator provides information about model output using conditional information about neighbouring values within the parameter space being investigated. A statistical relationship between all values in the parameter space is established using the training data, thus is constructed through Bayesian principles.

1.3.1.1 Bayes' theorem

In order to understand the GP emulator approach, it is important to be familiar with some statistical concepts, in particular the use and application of Bayes' theorem (Bayes, 1958; Berkson, 1930),

$$P(J_n \mid E)P(E) = P(J_n)P(E \mid J_n), \tag{1.1}$$

where, so long as $P(E) \neq 0$,

$$P(J_n \mid E) \propto P(J_n)P(E \mid J_n). \tag{1.2}$$

Here J_n represents a series of n exclusive and exhaustive events and E is some arbitrary event.

Bayes' theorem can also be used to express conditional probabilities of continuous random variables X and Y as

$$p(Y \mid X) \propto p(Y)p(X \mid Y), \tag{1.3}$$

where the constant of proportionality is

$$\frac{1}{p(X)} = \frac{1}{\int p(Y)p(X \mid Y)dY}. \tag{1.4}$$

A similar result is attainable for discrete random variables (Lee, 2004). The richness of equation 1.3 is that it allows for probabilities of outcomes to be revised in the context of new evidence; in this case the data from the training simulations.

1.3.1.2 Expert elicitation of prior distributions

Complex processes are parametrised in models using mathematical equations. Parameters are typically set to values believed by experts to be most likely, however uncertainty exists around many parameter settings. Through the process of expert elicitation (Cooke, 1991; Gosling *et al.*, 2007; Oakley & O'Hagan, 2007; Johnson *et al.*, 2010; Flores *et al.*, 2011), prior probability distributions of uncertain parameters can be generated. Care must be taken to ensure the process is as objective as possible, with detectable sources of bias eliminated from the line of enquiry.

Parametric uncertainty in climate model parameters, derived through expert elicitation, has previously been described using Gaussian (Lee *et al.*, 2011, 2012; Sexton *et al.*, 2012; Harris *et al.*, 2013) and beta (Lee *et al.*, 2013) distributions. In Chapters 2-4 beta distributions are used to describe parameter uncertainty, following (Lee *et al.*, 2013). For PPEs constructed via emulation any shape of distribution chosen by experts is acceptable. However, the joint probability distribution determines the frequency of sampling across the parameter space during the sensitivity analysis described in section 1.3.1.8. Using Gaussian and/or beta distributions to describe parameter uncertainty and sampling from the joint probability density function can overly-centralise the sample for individual parameters compared to expert beliefs. Hence, the expert elicitation conducted for Chapter 5 used trapezoidal distributions to represent parameter uncertainty. The use of trapezoidal distributions avoided having an overly-centralised Monte-Carlo sample of the multi-dimensional parameter space. Furthermore, experts converged on agreement about parameter uncertainty using trapezoidal distributions faster than they did when attempting to use other types of distribution.

The parameter distributions used in Chapter 2 follow those used in Lee *et al.* (2013). This parameter set was updated and extended for Chapters 3-4 by re-eliciting the distributions for some parameters and eliciting distributions for new parameters. The same set of experts contributed to the elicitation as in Lee *et al.* (2013) and the methods, including the literature review and analysis of the model sensitivity to individual parameter perturbations (outlined in Appendix 7), were as similar to Lee *et al.* (2013) as possible. For Chapter 5 the elicitation of physical atmosphere parameters was conducted by Sexton *et al.* (In prep.). The sensitivity of the model output to these parameters was investigated prior to inclusion in the ensemble (Appendix 7). Many of the aerosol parameters perturbed in Chapter 5 are the same as those perturbed in Chapters 2-4. However, in all cases distributions were re-elicited to ensure distributions accurately reflected the current

state of knowledge uncertainty.

1.3.1.3 Mean, covariance and correlation

Once appropriate training data has been gathered and prior distributions about uncertain parameters obtained from experts, as described in section 1.3.1.2, an emulator can be constructed (Conti & O'Hagan, 2010). It is important to note that the emulator does not just provide an output, y, for the model, given some input, $\mathbf{x}$, but provides an entire probability distribution for $y = f(\mathbf{x})$, which is not restricted to being normally distributed (O'Hagan, 2006). Using a Gaussian Process for the prior probability distribution allows the distribution to be completely specified using mean and covariance functions.

It is presumed that uncertainty about the computer model output at a set of data points, $\mathbf{x}_0, \ldots, \mathbf{x}_n$, can be represented as a multivariate normal distribution (Oakley & O'Hagan, 2002), with mean and covariance functions

$$E\{f(\mathbf{x} \mid \beta)\} = h(\mathbf{x})^T \beta \tag{1.5}$$

and

$$cov(f(\mathbf{x}), f(\mathbf{x\prime}) \mid \sigma^2) = \sigma^2 c(\mathbf{x}, \mathbf{x\prime}) \tag{1.6}$$

respectively, where $c(\mathbf{x}, \mathbf{x\prime})$ is the assumed correlation between pairs of parameter combinations and is dependent on the multivariate distance between points, and β and σ^2 are hyperparameters; parameters of the assumed prior distribution, not of the model. These hyperparameters are initially given weak prior distributions and treated as variables in the emulator construction and hence values for them are obtained using Maximum Likelihood convergence. Here $f(\mathbf{x})$and$f(\mathbf{x\prime})$ are distinct data points.

The predefined regression functions $h(.)$ can be combined into a matrix $H = [h(\mathbf{x}_1, \ldots, \mathbf{x}_n)]^T$. The matrix A is defined to be the nxn matrix whose $(i, j)th$ element is the correlation between x_i and x_j, $c(x_i, x_j)$, which can take various forms, such as

$$c(x_i, x_j) = exp(-b(x_i - x_j)^2). \tag{1.7}$$

It is essential that $c(x_i, x_i) = 1$ and that the strength of correlation is proportional to $|x_i - x_j|$. Here b is a parameter quantifying the smoothness of $f(x)$ for the input variable in question. There will be a unique b for each input variable.

1.3.1.4 Training an emulator

The creation of a GP emulator relies upon a training data set, $x_{T_1}, \ldots, x_{T_n}$, that spans the parameter space, being used to obtain objective information, $f(\mathbf{x}_T)$. This objective information is then combined with the subjective information derived from the emulator, $\hat{f}(\mathbf{x}|\beta, \sigma^2)$, to provide estimates of all other output, $y = f(\mathbf{x})$, within the domain (Haylock & O'Hagan, 1996; Saltelli *et al.*, 2000).

The choice of training data is important, since the full model will be run on each input vector $\mathbf{x}$. It has already been established that the model in question is assumed to be computationally expensive, otherwise there would be no need for implementing GP emulator technology, thus what is needed is a suitably small set of data that spans the domain of interest and can be assumed to have no systematic uncertainty (O'Hagan, 2006). The PPEs used in this research were all created using maximin latin hypercubes, where each new training point is calculated so as to maximise the minimum distance between training points.

Extra information becomes available with each training run of the model, since for $\mathbf{x}$ and $\mathbf{x}'$, two neighbouring data points, the value of $f(\mathbf{x}')$ will give us information about the value of $f(\mathbf{x})$ (Oakley & O'Hagan, 2002). By selecting a set of training data which broadly covers the domain, it can be expected that the emulator will provide a reasonable estimation of uncertainty, for any new input value within the domain, so long as the response surface is relatively smooth (Conti & O'Hagan, 2010). Emulator uncertainty increases rapidly for input outside the domain of the training data (O'Hagan, 2006), an example of the R$\hat{u}$nge phenomena (Atkinson, 1989), hence, the training data are selected so that no extrapolation is required.

Having obtained a vector of output values directly from the model for the training data, $(\mathbf{y}_T)$, it is assumed that the joint distribution between this training output and model output, $f(\mathbf{x})$, for any new data, $\mathbf{x}$, is multivariate normal. This assumption allows for the use of standard conditioning techniques on a multivariate normal distribution. Conditional estimates of hyperparameters may be obtained through the use of Bayes' theorem, (1.3). Following Haylock & O'Hagan (1996) and Saltelli *et al.* (2000) and drawing upon (1.5) to (1.7), the posterior GP of the computer model is

$$f(\mathbf{x})|\beta, \sigma^2, \mathbf{y}_T \sim N(m^*(\mathbf{x}), \sigma^2 c^*(\mathbf{x}, \mathbf{x}\prime)), \tag{1.8}$$

where

$$m^*(\mathbf{x}) = h^T(\mathbf{x})\beta + t(\mathbf{x})^T A^{-1}(\mathbf{y}_T - H\beta), \tag{1.9}$$

$$t(\mathbf{x}) = [c(\mathbf{x}, \mathbf{x}_1), \ldots, c(\mathbf{x}, \mathbf{x}_n)]^T \tag{1.10}$$

and

$$c^*(\mathbf{x}, \mathbf{x\prime}) = c(\mathbf{x}, \mathbf{x}') - t(\mathbf{x})^T A^{-1} t(\mathbf{x}'), \tag{1.11}$$

for any input vectors $\mathbf{x}$ and $\mathbf{x\prime}$.

Given a large enough training sample, the value of $f(\mathbf{x})$ can be calculated with high confidence (O'Hagan, 2006).

1.3.1.5 Hyperparameters

As stated in section 1.3.1.5 hyperparameters are typically prescribed starting values using available information and beliefs. During emulator construction, it becomes possible to treat these hyperparameters as variables, using (1.1), to obtain their conditional distributions

$$\beta|\sigma^2, \mathbf{y}_T \sim N(\hat{\beta}, \sigma^2(H^T A^{-1} H)^{-1}) \tag{1.12}$$

and

$$\hat{\sigma}^2 \equiv \sigma^2|\mathbf{y}_T \sim \frac{\mathbf{y}_T^T(A^{-1} - A^{-1}H(H^T A^{-1} H)^{-1} H^T A^{-1})\mathbf{y}_T}{n - q - 2}, \tag{1.13}$$

where q is the rank of H and

$$\hat{\beta} = (H^T A^{-1} H)^{-1} H^T A^{-1} \mathbf{y}_T, \tag{1.14}$$

as per Haylock & O'Hagan (1996). Integrating the product of $f(.)|\mathbf{y}_T, \beta, \sigma^2$ and $\beta|\sigma^2, \mathbf{y}_T$ with respect to β and then integrating the product of $f(.)|\sigma^2, \mathbf{y}_T$ and $\sigma^2|\mathbf{y}_T$ eradicates the conditional dependence of $f(\mathbf{x})$ on β and σ^2. The result is a t distribution from which mean and variance of $f(\mathbf{x})|\mathbf{y}_T$ can be obtained.

Finally, following the method described by Bastos & O'Hagan (2009), the newly constructed GP emulator is obtained, as

$$\hat{f}(.) \equiv f(.)|\mathbf{y}_T \sim \textit{Student } t(n - q, m(.), V(.,.)) \tag{1.15}$$

where

$$m(\mathbf{x}) = h(\mathbf{x})^T \hat{\beta} + t(\mathbf{x})^T A^{-1}(\mathbf{y}_T - H\hat{\beta}) \tag{1.16}$$

and

$$V(\mathbf{x},\mathbf{x}') = \hat{\sigma}^2[c(\mathbf{x},\mathbf{x}') - t(\mathbf{x})^T A^{-1} t(\mathbf{x}') + (h(\mathbf{x}) - t(\mathbf{x})^T A^{-1} H) \\ (H^T A^{-1} H)^{-1}(h(\mathbf{x}') - t(\mathbf{x}')^T A^{-1} H)^T]. \tag{1.17}$$

1.3.1.6 The smoothness parameter

Assuming that the model function, $f(.)$, is smooth allows the correlation to take the form seen in (1.7) and (1.11), where correlation between two data points decreases with the distance between them. Smoothness is a measure of how rapidly the function output changes gradient, across the domain of input values, for a particular variable. It is the inclusion of a smoothness parameter, b, in equation (1.7) that allows for the use of a maximum likelihood procedure to obtain improved estimates of σ^2 and β. Once suitable hyperparameters have been identified, the smoothness parameter is recalculated to provide the best possible representation of model output behaviour. If reliable initial estimates of smoothness parameters are not available, then a larger sample of training data can compensate, since the output uncertainty increases with distance from out training data points (O'Hagan, 2006). In this research estimates of the response surface were unobtainable in advance, hence sufficiently large ensembles were created.

1.3.1.7 Emulator Validation

Before uncertainty analysis is performed, it is important to validate the efficacy of the emulator in approximating the model output at points in parameter space distinct from the training dataset (Bastos & O'Hagan, 2009). All emulators used in this research were formally validated against samples of simulations designed to span the parameter space using the 'augmentLHS' R function (R. Carnell, 2016). Parameter combinations far away from training data points provide the most new information and therefore the greatest test of the emulator's ability to accurately reproduce model output. Validation points close to training points in the multi-dimensional parameter space test the sensitivity of the emulator hyperparameters. The 'augmentLHS' function provides a suitable validation set for the emulators created in this thesis. In each case a new sample of input, $\mathbf{x}_*$, was used to obtain model output, y_*, for comparison with output from the emulator, $\hat{f}(\mathbf{x}_*)$, as conditioned by the training data. For all analyses new emulators were created post-validation using both the original design and validation points, which enhances the emulator performance under the assumption that the new emulators validate as well or better than those created with less data.

1.3.1.8 Sensitivity analysis

Sensitivity analysis is a powerful approach which can highlight those aspects of model functionality which most require improvement in order to reduce model uncertainty (Saltelli *et al.*, 2000; Oakley & O'Hagan, 2004). The method used to calculate the percentage contributions to variance referred to in Chapters 2-5 are described here.

Given the distribution of X, the contributions to output variance made by realisations of individual input data, $\mathbf{X}_i$, can be quantified as

$$V_i = var\{E(Y|X_i)\}. \tag{1.18}$$

This is the expectation of the amount by which uncertainty in Y will be reduced by knowing the true value of the individual input X_i.

The uncertainty that remains after we have realised all values except $\mathbf{X}_i$ is

$$V_{Ti} = var(Y) - var\{E(Y|\mathbf{X}_{-i})\}, \tag{1.19}$$

where $\mathbf{X}_{-i}$ is the vector of input with the variable $\mathbf{X}_i$ omitted. Upon scaling these values by $var(Y)$, the measures become scale invariant and can be compared directly to assess the relative contributions to uncertainty.

It is often critical in practice to compare first order interaction effects between variables, not just their individual contributions (Lee *et al.*, 2011). This is made possible, following the methodology introduced in Satelli *et al.* (2000), by using the input of two variables, $\mathbf{X}_{i,j}$, to calculate

$$V_{i,j} = var\{E(Y|\mathbf{X}_{i,j})\} = var\{z_i(X_i) + z_j(X_j) + z_{i,j}(\mathbf{X}_{i,j})\}, \tag{1.20}$$

where

$$z_k(x_k) = E(Y|x_k) - E(Y) \tag{1.21}$$

and

$$z_{i,j}(\mathbf{x}_{i,j}) = E(Y|\mathbf{x}_{i,j}) - z_j(x_j) - E(Y) \tag{1.22}$$

are the main effects and first order interaction effects respectively. Interactions between parameters do not play a large role in this research because a broad range of uncertain parameters have been perturbed, leading to a reduction of the interaction terms (Lee *et al.*, 2013).

1.3.2 Newtonian relaxation

One of the aims of this research is to determine the relative importance of uncertain aerosol and atmospheric parameters as sources of aerosol ERF forcing variance over different periods. The relative importance of these sources of uncertainty can be used to inform field campaigns and target model development. The largest source of uncertainty in aerosol ERF comes from the ToA shortwave (SW) component (Yokohata *et al.*, 2010) associated with lower tropospheric clouds (Webb *et al.*, 2006; Shiogama *et al.*, 2012). The magnitude of ToA outgoing radiation is dependent on the composition and cloudiness of the atmosphere, particularly the cloud albedo, the spatial position and vertical extent of clouds all of which can be affected by aerosols. Complex aerosol, cloud and dynamical feedbacks are represented in modern GCMs although there is substantial uncertainty about the magnitude of these feedbacks in different and regimes (Seifert *et al.*, 2012; Boucher *et al.*, 2013; Rosenfeld *et al.*, 2014; Johnson *et al.*, 2015).

In order to more fully quantify the relative contributions of aerosol and atmospheric parameters to aerosol ERF variance, the effect of parametric perturbations must be allowed to feedback onto model dynamics. No dynamical feedbacks are included in the model configurations used in Chapters 2-4, where cloud are prescribed using International Satellite Cloud Climatology Project (ISCCP) D2 data and meteorological fields, such as horizontal winds and temperatures, are 'nudged' towards European Center for Medium-Range Weather Forecasting (ECMWF) ERA-Interim reanalysis data using Newtonian relaxation. Controlling atmospheric conditions with nudging allows the effect of aerosols on radiative forcing to be quantified in the absence of significant internal model variability that results from dynamical feedbacks, because pairs of simulations have near-identical atmospheric states.

Nudging of GCMs is typically applied by relaxing model values towards horizontal winds and temperature simultaneously (Telford *et al.*, 2008). Nudging to horizontal winds and not temperature can produce ToA radiative fluxes in better agreement with those from free-running simulations (Zhang *et al.*, 2014). Nudging to horizontal winds and not temperatures increases the number of degrees of freedom with which the model can disperse inconsistencies in atmospheric states during the relaxation process. Phase III of the AeroCom model intercomparison will be conducted using simulations nudged to horizontal winds only.

In Chapter 5 clouds and meteorological values are calculated within the model, with

the exception of horizontal winds above 2.2km which are nudged towards ECMWF ERA-Interim reanalysis data. Using this minimal nudging approach keeps synoptic-scale dynamical features consistent across the ensemble, but allows aerosol and atmospheric parameter perturbations to influence the state of the lower atmosphere, allowing for rapid adjustments to be captured. Without nudging ToA radiative fluxes need to be averaged over many decades in order to produce signals stronger than the noise resulting from internal variability (Kooperman *et al.*, 2012). The inclusion of rapid adjustments to cloud properties, such as lifetime and precipitation efficiency, in the aerosol ERF calculation gives a more complete picture of energy budget change (Boucher *et al.*, 2013) and is especially important for quantifying the climatic effects of anthropogenic aerosols (Wang *et al.*, 2013).

1.4 Aerosol-cloud-radiation dynamical feedbacks

Aerosol and atmospheric parameters are usually perturbed in isolated groups in GCMs because of the computational cost required to include multiple extra parameters in PPEs. Sensitivity analyses conducted using PPEs containing only aerosol or atmospheric parameter perturbations have been used to inform the parameter screening process used to create the PPEs analysed in Chapters 2-5 (described in detail in Appendix 7).

Parameters affecting clouds, such as the rate of entrainment of dry air and the convective mass flux, can significantly influence aerosol ERF (Haerter *et al.*, 2009), by affecting the vertical extent of tropical clouds, atmospheric stability (Tost *et al.*, 2010; Persad *et al.*, 2012) and therefore the poleward transportation of aerosols (Storelvmo, 2012). The vertical distribution of aerosols is also affected by convection in sub-tropical shallow cumulus clouds (Wonaschuetz *et al.*, 2012) affecting the dispersal of aerosols from source regions (Storelvmo, 2012).

Aerosols have the potential to significantly alter precipitation rates, clouds and atmospheric dynamics. Surface air temperature cooling induced by aerosols can reduce convective precipitation (Guo *et al.*, 2013) and increasing within-cloud aerosol concentrations can enhance (Storer & Der Heever, 2013) or suppress (Kim *et al.*, 2007; Planche *et al.*, 2010; Koren *et al.*, 2010) precipitation depending on the cloud regime (Storer & Der Heever, 2013; Johnson *et al.*, 2015). Changing aerosol concentrations can also cause changes in cloud regime (Croft *et al.*, 2012; Jenkins *et al.*, 2013). The aerosol size distribution can also influence the effect of increasing aerosol concentrations on precipitation and

convection (Ekman *et al.*, 2011; Blyth *et al.*, 2013; Johnson *et al.*, 2015). The absorption and re-emission of shortwave energy by carbonaceous aerosols can induce localised heating and cloud evaporation (Guo *et al.*, 2013).

By comprehensively quantifying the sensitivity of aerosol ERF to a broad range of aerosol and atmospheric parameters using a PPE where all parameters are perturbed simultaneously, the research in Chapter 5 is designed to determine if the representation of aerosols or the atmosphere has the greatest influence on ToA radiative fluxes and aerosol ERF. Influence on the state of the atmosphere and the change in state are analysed separately in Chapter 5 because sensitivities in state do not necessarily imply sensitivities in change-of-state (Lee *et al.*, 2016).

1.5 Thesis aims and structure

This thesis will quantify parametric contributions to variance in components of aerosol ERF both globally and regionally over a variety of time periods. In doing so priorities for model development will be identified and the climatic importance of uncertain parameters determined. The thesis will begin by investigating the relative contributions to variance in global mean aerosol cloud-albedo effect (CAE) forcing from natural and anthropogenic aerosol emissions and aerosol process parameters in Chapter 2. The aerosol CAE forcing, often referred to as the first aerosol indirect effect, is the approximation to ACI forcing obtained without accounting for aerosol induced rapid atmospheric adjustments. The time-dependence of CAE sensitivity to parameter perturbations will be established in Chapter 3 by quantifying contributions to CAE forcing variance over the different anthropogenically influenced periods 1850-2008, 1978-2008 and 1998-2008. Analysing sources of CAE forcing variance during periods with fundamentally different anthropogenic emission trends will allow for the broadest possible exploration of forcing period dependence. The period dependence of contributions to variance is analysed using the groupings of aerosol processes and natural and anthropogenic emissions employed in Chapter 2. Quantifying the magnitude of CAE forcing uncertainty in the recent periods will make an analysis of the role of CAE forcing in near-term historical climate change possible. Specifically the hypothesis that aerosol forcing is no longer relevant for present and future climate uncertainty (Stevens, 2013) can be tested.

Regional patterns of aerosol radiative forcing, important for understanding climate

change on decadal timescales (Shindell *et al.*, 2013), will be examined in Chapter 4. Contributions to CAE forcing variance over the 1978-2008 period will be quantified during months where surface temperatures are thought to influence large-scale climate effects. Physically-based arguments for temporal and spatial changes in the magnitude of contributions to CAE forcing variance will be provided. The research in Chapter 4 will aid interpretation of the climatic importance of aerosol forcing uncertainty in recent decades. The effect of cancellation of contributions to global mean CAE forcing variance in regions of positive and negative forcing will be quantified and the effect cancellation has on interpretation of model development priorities determined.

The results from Chapters 2-4 will inform the construction of the PPE used in Chapter 5, which will be used to compare contributions to variance in ToA radiative fluxes and aerosol ERF over the 1850-2008 and 1978-2008 periods. Only if the sources of variance are similar will it be possible to effectively use observed ToA fluxes to constrain aerosol ERF. The reduced capacity for ToA fluxes to be used as a constraint on aerosol ERF, because of model equifinality, will be explicitly tested. Chapter 5 benefits from having a minimal nudging configuration and includes perturbations to both aerosol and atmospheric parameters, allowing for the relative contributions to aerosol ERF variance from these sources to be quantified. Chapter 5 provides the first comprehensive assessment of the extent to which uncertainty in representations of aerosols and the atmosphere influence aerosol ERF.

Supporting information for Chapters 2, 3 and 5 are provided in Appendices 1-3 respectively. The development and recent refinement of GLOMAP model is reviewed in Appendix 4, providing insight into the level of scrutiny the model has been subject to. Testing of anthropogenic emission inventories for potential use in producing the ensembles in this research is summarised in Appendix 5 and tests of structural changes to the GLOMAP model, implemented during the model development period between producing Chapters 2 and 3, are included in Appendix 6. Results from parameter screening tests that informed the inclusion of parameters in the GLOMAP and HadGEM3 PPEs used in chapters 2-4 and 5 respectively are summarised in Appendix 7. Finally an analysis of the parameter combinations that produce the most extreme PI-PD aerosol ERF values in the HadGEM3 PPE used in Chapter 5 is provided in Appendix 8. The analysis in Appendix 8 informed development of the release version of the United Kingdom Earth System Model (UKESM-1).

The research presented in this thesis has the potential to significantly advance scientific

understanding of the relative importance of parametrisations from various components of the earth system in their contributions to uncertainty in aerosol ERF and its components. The combined results within this thesis help address the question of why although scientific knowledge about aerosol-cloud-radiation interactions has increased significantly in recent decades, uncertainty in aerosol ERF remains the largest source of forcing uncertainty, which was the the focus of the 2015 Sackler Colloquium 'Improving Our Fundamental Understanding of the Role of Aerosol-Cloud Interactions in the Climate System' (Seinfeld *et al.*, 2015). A summary of new knowledge arising from this research and proposed future research directions are presented in Chapter 6.

References - Chapter 1

Atkinson, K. E. 1989. *An introduction to numerical analysis*. 2nd edn. Oxford, U.K.: J. Wiley & Sons Ltd.

Bastos, L. S., & O'Hagan, A. 2009. Diagnostics for Gaussian process emulators. *Technometrics*, **51**, 425–438.

Bayes, T. 1958. An essay towards solving a problem in the doctrine of chances. *Biometrika*, **45**, 296–315. First published as: Bayes, T., 1763, An essay towards solving a problem in the doctrine of chances: Philosophical transactions of the Royal Society of London.

Berkson, J. 1930. Bayes' theorem. *The annuls of mathematical statistics*, **1**, 42–56.

Beven, K., & Freer, J. 2001. Equifinality, data assimilation, and uncertainty estimation in mechanistic modelling of complex environmental systems using the GLUE methodology. *J. Hydrol.*, **249**, 11–29.

Blyth, A. M., Lowenstein, J. H., Huang, Y., Cui, Z., Davies, S., & Carslaw, K. S. 2013. The production of warm rain in shallow maritime cumulus clouds. *Quart. J. Roy. Meteor. Soc.*, **139**, 20–31.

Bond, T. C., Doherty, S. J., Fahey, D. W., Forster, P. M., Berntsen, T., DeAngelo, B. J., Flanner, M. G., Ghan, S., Krcher, B., Koch, D., Kinne, S., Kondo, Y., Quinn, P. K., Sarofim, M. C., Schultz, M. G., Schulz, M., Venkataraman, C., Zhang, H., Zhang, S., Bellouin, N., Guttikunda, S. K., Hopke, P. K., Jacobson, M. Z., Kaiser, J. W., Klimont, Z., Lohmann, U., Schwarz, J. P., Shindell, D., Storelvmo, T., Warren, S. G., & Zender, C. S. 2013. Bounding the role of black carbon in the climate system: A scientific assessment. *J. Geo. Res. Atmos.*, **118**, 5380–5552.

Boucher, O., Randall, D., Artaxo, P., Bretherton, C., Feingold, G., Forster, P., Kerminen, V. M., Kondo, Y., Liao, H., Lohmann, U., Rasch, P., Satheesh, S. K., Sherwood, S., Stevens, B., & Zhang, X. Y. 2013. Clouds and aerosols. *In:* Stocker, T. F., Qin, D.,

Plattner, G. K., Tignor, M., Allen, S. K., Boschung, J., Nauels, A., Xia, Y., Bex, V., & Midgley, P. M. (eds), *Climate change 2013: The physical science basis. contribution of working group i to the fifth assessment report of the intergovernmental panel on climate change*. Cambridge, United Kingdom and New York, NY, USA: Cambridge University Press.

Carslaw, K. S., Lee, L. A., Reddington, C. L., Mann, G. W., & Pringle, K. J. 2013. The magnitude of uncertainty in global aerosol. *Farr. Disc.*, **165**, 495–512.

Chalmers, N., Highwood, E. J., Hawkins, E., Sutton, R., & Wilcox, L. J. 2012. Aerosol contribution to the rapid warming of near-term climate under RCP 2.6. *Geophys. Res. Lett.*, **39**.

Collins, M., Booth, B. B. B., Bhaskaran, B., Harris, G. R., Murphy, J. M., Sexton, D. M. H., & Webb, M. J. 2010. Climate model errors, feedbacks and forcings: a comparison of perturbed physics and multi-model ensembles. *Clim. Dyn.*, **36**, 1737–1766.

Collins et al. 2008. Evaluation of the HadGEM2 model. *Met Office Hadley Centre Technical Note no. HCTN 74.*

Conti, S., & O'Hagan, A. 2010. Bayesian emulation of complex multi-output and dynamical computer models. *J. Stat. Plan. Inf.*, **140**, 640–651.

Cooke, R. M. 1991. *Experts in Uncertainty.* Oxford, U.K.: Oxford University Press.

Croft, B., Pierce, J. R., Martin, R. V., Hoose, C., & Lohmann, U. 2012. Uncertainty associated with convective wet removal of entrained aerosols in a global climate model. *Atmos. Chem. Phys.*, **12**, 10725–10748.

Ekman, A. M. L., Engstrom, A., & Soderberg, A. 2011. Impact of Two-Way Aerosol-Cloud Interaction and Changes in Aerosol Size Distribution on Simulated Aerosol-Induced Deep Convection Cloud Sensitivity. *J. Atmos. Sci.*, **68**, 685–698.

Flores, M. J., Nicholson, A. E., Brunskill, A., Orb, K. B., & Mascaro, S. 2011. Incorporating expert knowledge when learning Bayesian network structure: A medical case study. *Artificial intelligence in medicine*, **53**, 181–204.

Forster, P., Ramaswamy, V., Artaxo, P., Berntsen, T., Betts, R., Fahey, D. W., Haywood, J., Lean, J., Lowe, D. C., Myhre, G., Nganga, J., Prinn, R., Raga, G., Shultz, M., & Van Dorland, R. 2007. Changes in Atmospheric Constituents and in Radiative Forcing. *In:*

Solomon, S., Qin, D., Manning, M., Chen, Z., Marquis, M., Averyt, K. B., Tignor, M., & Miller, H. L. (eds), *Climate Change 2007: The Physical Sciene Basis. Contribution of Working Group I to the Fourth Assessment Report of the Intergovernmental Panel on Climate Change*. Cambridge, United Kingdom and New York, NY, USA: Cambridge University Press.

GASSP. 2016. *Global Aerosol Synthesis and Science Project.* ***http://gassp.org.uk/****. Accessed: March 2016.*

Golaz, J. C., Horowitz, L. W., & II, H. Levy. 2013. Cloud tuning in a coupled climate model: impact on 20th century warming. *Geophys. Res. Lett.*, 1–20.

Gosling, J. P., Oakley, J. E., & O'Hagan, A. 2007. Nonparametric elicitation for heavy-tailed prior distributions. *Bayes. Anal.*, **2**, 693–718.

Granier, C., Bessagnet, B., Bond, T., D'Angiola, A., van der Gon, H. D., Frost, G. J., Heli, A., Kaiser, J. W., Kinne, S., Kilmont, Z., Kloster, S., Lamarque, J. F., Liousse, C., Masui, T., Meleux, F., Mieville, A., Ohara, T., Raut, J. C., Riahi, K., Schultz, M. G., Smith, S. J., Thompson, A., van Aardenne, J., van der Werf, G. R., & van Vuuren, D. P. 2011. Evolution of anthropogenic and biomass burning emissions of air pollutants at global and regional scales during the 1980-2010 period. *Climatic change*, **109**, 163–190.

Guo, L., Highwood, E. J., Shaffrey, L. C., & Turner, A. G. 2013. The effect of regional changes in anthropogenic aerosols on rainfall of the East Asian Sumer Monsoon. *Atmos. Chem. Phys.*, **13**, 1521–1534.

HadGEM3. 2016. *Met Office climate prediction model: HadGEM3 family.* ***http://www.metoffice.gov.uk/research/modelling–systems/unified–model/climate–models/hadgem****. Accessed: March 2016.*

Haerter, J. O., Roeckner, E., Tomassini, L., & von Storch, J. S. 2009. Parametric uncertainty effects on aerosol radiative forcing. *Geophys. Res. Lett.*, **36**, 1–5.

Harris, G. R., Sexton, D. M. H., Booth, B. B. B., Collins, M., & Murphy, J. M. 2013. Probabilistic projections of transient climate change. *Clim. Dyn.*

Hawkins, E., & Sutton, R. 2009. The potential to narrow uncertainty in regional climate predictions. *Bull. amer. Meteor. Soc.*, 1097–1107.

Haylock, R. G., & O'Hagan, A. 1996. *Bayesian Statistics 5: On inference for outputs of computationally expensive algorithms with uncertainty on the inputs.* Oxford University Press.

Jenkins, A. K. L., Forster, P. M., & Jackson, L. S. 2013. The effects of timing and rate of marine cloud brightening aerosol injection on albedo changes during the diurnal cycle of marine stratocumulus cloud. *Atmos. Chem. Phys.*, **13**, 1659–1673.

Johnson, J. S., Cui, Z., Lee, L. A., Gosling, J. P., Blyth, A. M., & Carslaw, K. S. 2015. Evaluating uncertainty in convective cloud microphysics using statistical emulation. *J. Adv. Model. Earth Syst.*, **7**, 162–187.

Johnson, S. R., Tomlinson, G. A., Hawker, G. A., & et al. 2010. A valid and reliable belief elicitation method for Bayesian priors. *Journal of clinical epidemiology*, **63**, 370–383.

Jones, G. S., Stott, P. A., & Chistidis, N. 2013. Attribution of observed historical near surface temperature variations in anthropogenic and natural causes using CMIP5 simulations. *J. Geo. Res. Atmos., Online: http://onlinelibrary.wiley.com/doi/10.1002/jgrd.50239/pdf.*

Kim, M. K., Lau, W. K. M., Kim, K. M., & Lee, W. S. 2007. A GCM study of the effects of radiative forcing of sulfate aerosol on large scale circulation and rainfall in East Asia during boreal spring. *Geophys. Res. Lett.*, **34**.

Klocke, D., Pincus, R., & Quass, J. 2011. On constraining estimates of climate sensitivity with present day observations through model weighting. *J. Cli.*, **24**, 6092–6099.

Kooperman, G. J., Pritchard, M. S., Ghan, S. J., Wang, M., Somerville, R. C. J., & Russell, L. M. 2012. Constraining the influence of natural variability to improve estimates of global aerosol indirect effects in a nudged version of the Community Atmosphere Model 5. *J. Geo. Res.*, **117**, 1–16.

Koren, I., Feingold, G., & Remer, L. A. 2010. The invigoration of deep convective clouds over the Atlantic: aerosol effect, meteorology or retrieval artifact. *Atmos. Chem. Phys.*, **10**, 8855–8872.

Lamarque, J. F., Bond, T. C., Eyring, V., Granier, C., Heli, A., Kilmont, Z., Lee, D., Liousse, C., Mieville, A., Owen, B., Schultz, M. G., Shindell, D., Smith, S. J., Stehfest, E., Van Aardenne, J., Cooper, O. R., Kainuma, M., Mahowald, N., McConnell, J. R., Naik, V., Riahi, K., & van Vuuren, D. P. 2010. Historical (1850-2000) gridded anthropogenic and biomass burning emissions of reactive gases and aerosols: methodology and application. *Atmos. Chem. Phys.*, **10**, 7017–7039.

Lambert, F. H., Harris, G. R., Collins, M., Murphy, J. M., Sexton, D. M. H., & Booth, B. B. B. 2012. Interactions between perturbations to different Earth system components simulated by a fully-coupled climate model. *Clim. Dyn.*

Lee, L. A., Carslaw, K. S., Pringle, K. J., Mann, G. W., & Spracklen, D. V. 2011. Emulation of a complex global aerosol model to quantify sensitivity to uncertain parameters. *Atmos. Chem. Phys.*, **11**, 12253–12273.

Lee, L. A., Carslaw, K. S., Pringle, K. J., & Mann, G. W. 2012. Mapping the uncertainty in global CCN using emulation. *Atmos. Chem. Phys.*, **12**, 9739–9751.

Lee, L. A., Pringle, K. J., Reddington, C. L., Mann, G. W., Stier, P., Spracklen, D. V., Pierce, J., & Carslaw, K. S. 2013. The magnitude and causes of uncertainty in global model simulations of cloud condensation nuclei. *Atmos. Chem. Phys.*, **13**, 8879–8914.

Lee, L. A., Reddington, C. L., & Carslaw, K. S. 2016. On the relationship between aerosol model uncertainty and radiative forcing uncertainty. *Proc. Nat. Ac. Sci.*, **Early Edition**, Early Edition.

Lee, P. M. 2004. *Bayesian statistics, an introduction*. 3rd edn. Oxford, U.K.: J. Wiley & sons, Ltd.

Li, J., Wang, W. C., Sun, Z., Wu, G., Liao, H., & Liu, Y. 2014. Decadal variation of East Asian radiative forcing due to anthropogenic aerosols during 1850–2100 and the role of atmospheric moisture. *Clim. Res.*, **61**, 241–257.

Mann, G. W., Carslaw, K. S., Spracklen, D. V., Ridley, D. A., Manktelow, P. T., Chipperfield, M. P., Pickering, S. J., & Johnson, C. E. 2010. Description and evaluation of GLOMAP-mode aerosol microphysics model for the UKCA composition-climate model. *Geosci. Mod. Dev.*, **3**, 519–551.

Mann, G. W., Carslaw, K. S., Ridley, D. A., Merikanto, D. V. Spracklen K. J. Pringle J., Korhonen, H., Schwarz, J. P., Lee, L. A., Manktelow, P. T., Woodhouse, M. T., Schmidt, A., Breider, T. J., Emmerson, K. M., Reddington, C. L., Chipperfield, M. P., & Pickering, S. J. 2012. Intercomparison of modal and sectional aerosol microphysics representations within the same 3-D global chemical transport model. *Atmos. Chem. Phys.*, **12**, 4449–4476.

Mao, K. B., Ma, Y., Xia, L., Chen, W. Y., Shen, X. Y., He, T. J., & Xu, T. R. 2014. Global aerosol change in the last decade: An analysis based on MODIS data. *Atmos. Env.*, **94**, 680–686.

Michibata, T., & Takemura, T. 2015. Evaluation of autoconversion schemes in a single model framework with satellite observations. *J. Geo. Res. Atmos.*, **120**, 1–21.

Mitchell, J. F. B., Senior, C. A., & Ingram, W. J. 1989. CO2 and climate: a missing feedback? *Nat.*, **341**, 132–134.

Myhre, G., Shindell, D., Bréon, F. M., Collins, W., Fuglestvedt, J., Huang, J., Koch, D., Lamarque, J. F., Lee, D., Mendoza, B., Nakajima, T., Robock, A., Stephens, G., Takemura, T., & Zhang, H. 2013. Anthropogenic and Natural Radiative Forcing. *In:* Stocker, T. F., Qin, D., Plattner, G. K., Tignor, M., Allen, S. K., Boschung, J., Nauels, A., Xia, Y., Bex, V., & Midgley, P. M. (eds), *Climate Change 2013: The Physical Science Basis. Contribution of Working Group I to the Fifth Assessment Report of the Intergovernmental Panel on Climate Change*. Cambridge, United Kingdom and New York, NY, USA: Cambridge University Press.

Neubauer, D., Lohmann, U., Hoose, C., & Frontoso, M/ G. 2014. Impact of the representation of marine stratocumulus clouds on the anthropogenic aerosol effect. *Atmos. Chem. Phys.*, **14**, 11997–12022.

Oakley, J. E., & O'Hagan, A. 2002. Bayesian inference for the uncertainty distribution of computer model outputs. *Biometrika*, **89**, 769–784.

Oakley, J. E., & O'Hagan, A. 2004. Probabilistic sensitivity analysis of complex models: a Bayesian approach. *Jrssb*, **66**, 751–769.

Oakley, J. E., & O'Hagan, A. 2007. Uncertainty in prior elicitations: a nonparametric approach. *Biometrika*, **94**, 427–441.

O'Hagan, A. 2006. Bayesian analysis of computer code outputs - A tutorial. *Reliability engineering and system safety*, **91**, 1290–1300.

Pan, W., Tatang, M. A., McRae, G. J., & Prinn, R. G. 1998. Uncertainty analysis of indirect radiative forciny by anthropogenic sulphate aerosols. *J. Geo. Res.*, **103**, 3815–3823.

Pennell, C., & Reichler, T. 2010. On the effective number of climate models. *J. Cli.*, **24**, 2358–2367.

Penner, J. E., Andreae, M., Annegarn, H., Barrie, L., Feichter, J., Hegg, D., Jayaraman, A., Leaitch, R., Murphy, D., Nganga, J., & Pitari, G. 1996. Aerosols, their Direct and Indirect Effects. *In:* Houghton, J. T., Ding, Y., Griggs, D. J., Noguer, M., van der

Linden, P. J., Dai, X., Maskell, K., & Johnson, C. A. (eds), *Climate Change 2001: The Scientific Basis. Contribution of Working Group I to the Third Assessment Report of the Intergovernmental Panel on Climate Change*. Cambridge, United Kingdom and New York, NY, U.S.A.: Cambridge University Press.

Persad, G., Ming, Y., & Ramaswamy, V. 2012. Tropical tropospheric-only responses to absorbing aerosols. *J. Cli.*, **25**, 2471–2480.

Planche, C., Wobrock, W., Flossmann, A. I., Tridon, F., van Baelen, J., Pointin, Y., & Hagen, M. 2010. The influence of aerosol particle number and hygroscopicity on the evolution of convective cloud systems and their precipitation: a numerical study based on the COPS observations on 12 August 2007. *Atmos. Res.*, **98**, 40–56.

Qian, Y., Yan, H., Zhangshuan, H., Gardar, J., Klein, S., Lucas, D., Neale, R., Rasch, P., Swiller, L., Tannahill, J., Wang, H., Wang, M., & Zhao, C. 2015. Parametric sensitivity analysis of precipitation at global and local scales in the Comunity Atmosphere Model CAM5. *J. Adv. Model. Earth Syst.*, **7**, 382–411.

R. Carnell. 2016. *Package 'lhs'*. http://lhs.r-forge.r-project.org.

Rosenfeld, D., Andreae, M. O., Asmi, A., Chin, M., de Leeuw, G., Donovan, D. P., Kahn, R., Kinne, S., Kivekäs, N., Kulmala, M., Lau, W., Schmidt, K. S., Suni, T., Wagner, T., Wild, M., & Quaas, J. 2014. Global observations of aerosol-cloud-precipitation climate interactions. *Rev. Geophys.*, **52**, 750–808.

Rotstayn, L. D., Collier, M., Shindell, D. T., & Boucher, O. 2015. Why does aerosol forcing control historical global-mean surface temperature change in CMIP5 models? *J. Climate.*, **28**, 6608–6625.

Saltelli, A., & Annoni, P. 2010. How to avoid a perfunctory sensitivity analysis. *Environ. Mod. Soft.*, **25**, 1508–1517.

Saltelli, A., Chan, K., & Scott, E. M. 2000. *Sensitivity Analysis*. Oxford, U.K.: Wiley.

Satelli, A., Tarantola, S., & Campolongo, F. 2000. Sensitivity analysis as an ingredient of modelling. *Stat. Sci.*, **15**, 377–395.

Schimel, D., Alves, D., Enting, I., Heimann, M., Joos, F., Raynaud, D., Wigley, T., Prather, M., Derwent, R., Ehhalt, D., Fraser, P., Sanhueza, E., Zhou, X., Jonas, P., Charlson, R., Rodhe, H., Sadasivan, S., Shine, K. P., Fouquart, Y., Ramaswamy, V., Solomon, S., Srinivasan, J., Albritton, D., Derwent, R., Lal, I. Isaksen M., & Wubebbles,

D. 1996. Radiative Forcing of Climate Change. *In:* Houghton, J. T., Meira Filho, L. G., Callander, B. A., Harris, N., Kattenberg, A., & Maskell, K. (eds), *Climate Change 1996: Contribution of Working Group I to the 2nd Assessment Report of the Intergovenmental Panel on Climate Change*. Cambridge, United Kingdom and New York, NY, U.S.A.: Cambridge University Press.

Seifert, A., Köhler, C., & Beheng, K. D. 2012. Aerosol-cloud-precipitation effects over Germany as simulated by a convective-scale numerical weather prediction model. *Atmos. Chem. Phys.*, **12**, 709–725.

Seinfeld, J., Prather, K., Kraucunas, I., Guenther, A., & Dunlea, E. 2015. *Improving our fundamental understanding of the role of aerosol–cloud interactions in the climate system.* ***http://www.nasonline.org/programs/sackler–colloquia/completed_colloquia/Role_of_Aerosol_Cloud_Interactions.html****. Accessed: March 2016.*

Sexton, D. M. H., Murphy, J. M., Collins, M., & Webb, M. J. 2012. Multivariate probabilistic projections using imperfect climate models Part I: outline of methodology. *Clim. Dyn.*, **38**, 2513–2542.

Sexton, David M. H., Karmalkar, A., Murphy, J., Booth, B. B. B., & Regayre, L. A. In prep.. The elicitation of distributions of parameters in HadGEM3 versions GA4 and GA7 for use in perturbed parameter ensembles. *Hadley Centre technical note, Met Office, U.K.*

Shindell, D., Faluvegi, G., Rotstayn, L., & Milly, G. 2015. Spatial patterns of radiative forcing and surface temperature response. *J. Geo. Res. Atmos.*, **120**, 5385–5403.

Shindell, D. T., Lamarque, J. F., Schulz, M., Flaner, M¿, Jiao, C., Chin, M., Young, P.J., Lee, Y.H., Rotstayn, L., Mahowald, N., Milly, G., Faluvegi, G., Balkanski, Y., Collins, W. J., Conley, A. J., Dalsoren, S., Easter, R., Ghan, S., Horowitz, L., Liu, X., Myhre, G., Nagashima, T., Naik, V., Rumbold, S. T., Skeie, R., Sudo, K., Szopa, S., Takemura, T., Voulgarakis, A., Yoon, J. H., & Lo, F. 2013. Radiative forcing in the ACCMIP historical and future climate simulations. *Atmos. Chem. Phys.*, **13**, 2939–2974.

Shiogama, H., Watanabe, M., Yoshimori, M., Yokohata, T., Ogura, T., Annan, J. D., Hargreaves, J. C., Abe, M., Kamae, Y., O'ishi, R., Nobui, R., Emori, S., Nozawa, T., Abe-Ouchi, A., & Kimoto, M. 2012. Perturbed physics ensemble using the MIROC5 coupled atmosphere-ocean GCM without flux corrections: experimental design and results. *Clim. Dyn.*, **39**, 3041–3056.

Skeie, R. B., Bernsten, T. K., Myhre, G., Tanaka, K., Kvalevåg, M. M., & Hoyle, C. R. 2011. Anthropogenic radiative forcing time series from pre-industrial times until 2010. *Atmos. Chem. Phys.*, **11**, 11827–11857.

Smith, S. J., van Aardenne, J., Klimont, Z., Andres, R. J., Volke, A., & Arias, S. Delgado. 2011. Anthropogenic sulfur dioxide emissions: 1850 to 2005. *Atmos. Chem. Phys.*, **11**, 1101–1116.

Spracklen, D. V., Pringle, K. J., Carslaw, K. S., Chipperfield, M. P., & Mann, G. W. 2005. A global off-line model of size-resolved aerosol microphysics: I. Model development and prediction of aerosol properties. *Atmos. Chem. Phys.*, **5**, 2227–2252.

Steir, P., Schutgens, N. A. J., Bian, H., Boucher, O., Chin, M., Ghan, S., Huneeus, N., Kinne, S., Lin, G., Myhre, G., Penner, J. E., Randles, C., Samset, B., Schulz, M., Yu, H., & Zhou, C. 2012. Host model uncertainties in aerosol radiative forcing estimates: results from the AeroCom prescribed intercomparison study. *Atmos. Chem. Phys. Disc.*, **12**, 25487–25549.

Stevens, B. 2013. Aerosols: Uncertain then, irrelevant now. *Nat.*, **503**, 47–48.

Stevens, B. 2015. Rethinking the lower bound on aerosol radiative forcing. *J. Cli.*, **28**, 4794–4819.

Stocker, T. F., Qin, D., Plattner, G. K., Tignor, M., Allen, S. K., Boschung, J., Nauels, A., Xia, Y., Bex, V., & Midgley, P. M. 2013a. *Climate change 2013: The physical science basis. contribution of working group i to the fifth assessment report of the intergovernmental panel on climate change*. Cambridge, United Kingdom and New York, NY, USA: Cambridge University Press.

Stocker, T. F., Qin, D., Plattner, G. K., Tignor, M., Allen, S. K., Boschung, J., Nauels, A., Xia, Y., Bex, V., & Midgley, P. M. 2013b. Summary for policymakers. *In:* Stocker, T. F., Qin, D., Plattner, G. K., Tignor, M., Allen, S. K., Boschung, J., Nauels, A., Xia, Y., Bex, V., & Midgley, P. M. (eds), *Climate change 2013: The physical science basis. contribution of working group i to the fifth assessment report of the intergovernmental panel on climate change*. Cambridge, United Kingdom and New York, NY, USA: Cambridge University Press.

Storelvmo, T. 2012. Uncertainties in aerosol direct and indirect effects attributed to uncertainties in convective transport parameterisations. *Atmos. Res.*, **118**, 357–369.

Storelvmo, T., Lohmann, U., & Bennartz, R. 2009. What governs the spread in shortwave forcings in the transient IPCC AR4 models? *Geophys. Res. Lett.*, **36**, L01806.

Storer, R. L., & Der Heever, S. C. Van. 2013. Microphysical Processes Evident in Aerosol Forcing of Tropical Deep Convective Clouds. *J. Atmos. Sci.*, **70**, 430–446.

Taylor, K. E., Stouffer, R. J., & Meehl, G. A. 2009. A summary of the CMIP5 experimental design. *PCMDI Tech. Rep.*, *online: Available from http* : $//www.cmip-pcmdi.llnl.gov/cmip5/docs/Taylor_CMIP5_design.pdf$.

Tebaldi, C., & Knutti, R. 2007. The use of the multi-model ensemble in probabilistic climate projections. *Philos. Trans. R. Soc. Ser. A.*, **365**.

Telford, P. J., Braesicke, P., Morgenstern, O., & Pyle, J. A. 2008. Technical Note: Description and assessment of a nudged version of the new dynamics Unified Model. *Atmos. Chem. Phys.*, **8**, 1701–1712.

Tost, H., Lawrence, M. G., Brühl, C., & Jöckel, P. 2010. Uncertainties in atmospheric chemistry modelling due to convection parameterisations and subsequent scavenging. *Atmos. Chem. Phys.*, **10**, 1931–1951.

Twomey, S. 1977. Influence of pollution on shortwave albedo of clouds. *J. Atmos. Sci.*, **34**, 1149–1152.

Wang, T., Wang, H. J., Otterå, O. H., Gao, Y. Q., Suo, L. L., Furevik, T., & Yu, L. 2013. Anthropogenic agent implicated as a prime driver of shift in precipitation in eastern China in the late 1970s. *Atmos. Chem. Phys.*, **13**, 12433–12450.

Webb, M. J., Senior, C. A., Sexton, D. M. H., Ingram, W. J., Williams, K. D., Ringer, M. A., McAvaney, B. J., Colman, R., Soden, B. J., Gudgel, R., Knutson, T., Emori, S., Ogura, T., Tsushima, Y., Andronova, N., Li, B., Musat, I., Bony, S., & Taylor, K. E. 2006. On the contribution of local feedback mechanisms to the range of climate sensitivity in two GCM ensembles. *Clim. Dyn.*, **27**, 17–38.

Wilcox, L. J., Highwood, E. J., & Dunstone, N. J. 2013. The influence of anthropogenic aerosol on multi-decadal variations of historical global climate. *Environ. Res. Lett.*, **8**.

Wilcox, L. J., Highwood, E. J., Booth, B. B. B., & Carslaw, K. S. 2015. Quantifying sources of inter-model diversity in the cloud albedo effect. *Geophys. Res. Lett.*, **42**, 1568–1575.

Wonaschuetz, A., Sorooshian, A., Ervens, B., Chuang, P. Y., Feingold, G., Murphy, S. M., de Gouw, J., & Warneke, C. 2012. Aerosol and gas re-distribution by shallow cumulus clouds: An investigation using airborne measurements. *J. Geo. Res.*, **117**, 1–18.

Yokohata, T., Webb, M. J., Collins, M. J., Williams, K. D., Yoshimori, M., Hargreaves, J. C., & Annan, J. D. 2010. Structural similarities and differences in climate responses to CO_2 increase between two perturbed physics ensembles by general circulation models. *J. Cli.*, **23**, 1392–1410.

Zhang, K., Wan, H., Liu, X., Ghan, S. J., Kooperman, G. J., Ma, P. L., Rasch, P. J., Neubauer, D., & Lohmann, U. 2014. Technical Note: On the use of nudging for aerosol-climate model intercomparison studies. *Atmos. Chem. Phys.*, **12**, 8631–8645.

Chapter 2

Large contribution of natural aerosols to uncertainty in indirect forcing

ARTICLE

33

doi:10.1038/nature12674

Large contribution of natural aerosols to uncertainty in indirect forcing

K. S. Carslaw[1], L. A. Lee[1], C. L. Reddington[1], K. J. Pringle[1], A. Rap[1], P. M. Forster[1], G. W. Mann[1,2], D. V. Spracklen[1], M. T. Woodhouse[1]†, L. A. Regayre[1] & J. R. Pierce[3]

The effect of anthropogenic aerosols on cloud droplet concentrations and radiative properties is the source of one of the largest uncertainties in the radiative forcing of climate over the industrial period. This uncertainty affects our ability to estimate how sensitive the climate is to greenhouse gas emissions. Here we perform a sensitivity analysis on a global model to quantify the uncertainty in cloud radiative forcing over the industrial period caused by uncertainties in aerosol emissions and processes. Our results show that 45 per cent of the variance of aerosol forcing since about 1750 arises from uncertainties in natural emissions of volcanic sulphur dioxide, marine dimethylsulphide, biogenic volatile organic carbon, biomass burning and sea spray. Only 34 per cent of the variance is associated with anthropogenic emissions. The results point to the importance of understanding pristine pre-industrial-like environments, with natural aerosols only, and suggest that improved measurements and evaluation of simulated aerosols in polluted present-day conditions will not necessarily result in commensurate reductions in the uncertainty of forcing estimates.

The impact of aerosol changes on cloud albedo (called the aerosol first indirect forcing)[1] is estimated[2] to exert a global mean radiative forcing of climate over the industrial period between $-0.4\ \mathrm{W\,m^{-2}}$ and $-1.8\ \mathrm{W\,m^{-2}}$. Other aerosol–cloud interaction effects, involving rapid adjustments, may be of comparable magnitude[3] but their radiative effects are even less well understood on a global scale[3,4]. The uncertainty in the aerosol forcing is much larger than the uncertainty in the well-constrained positive forcing of $1.7 \pm 0.2\ \mathrm{W\,m^{-2}}$ that is due to carbon dioxide change. The aerosol indirect forcing therefore has a highly uncertain influence on climate change and has the potential to mask a significant portion of greenhouse gas warming[5].

The magnitude of the forcing caused by aerosol–cloud interactions depends on several poorly modelled aspects of the climate, but is broadly understood to stem from different treatments of aerosols, clouds and radiation[3,6–8]. Nevertheless, the fundamental driver is the change in aerosols from the pre-industrial period to the present day, which controls the change in cloud droplet concentrations. It is recognized that quantification of aerosol indirect forcing requires an understanding of both the pre-industrial aerosol state[9–12] and the effect of the substantial anthropogenic perturbation. However, because of the complexity of processes that determine cloud-forming aerosol concentrations[10] and the computational expense of global aerosol models which explicitly simulate their production and loss processes[13–16], a comprehensive assessment of the magnitude and leading causes of uncertainty in indirect forcing has not been attempted.

Perturbed parameter simulations

Here we carry out a variance-based sensitivity analysis of a global aerosol model to attribute the uncertainty in the aerosol first indirect forcing to uncertainties in the emissions and processes that control changes in aerosol over the industrial period. We perform an ensemble of perturbed parameter global aerosol microphysical model simulations using present-day (PD) and pre-industrial (PI) emissions (PD is defined as the year 2000 and PI is defined[17] as 1750, with additional PI simulations to test the effect of using alternative reference years of 1850 or 1900). The 168 1-year model simulations in the PI and PD periods cover the full expert-elicited uncertainty space of 28 parameters describing natural and anthropogenic aerosol emissions, aerosol precursor gas emissions, microphysical processes and structures of the aerosol model (see Methods). To characterize fully the magnitude and causes of model uncertainty we use Bayesian emulators conditioned on the ensemble data to generate continuous model output across the parameter space[18,19]. This approach enables a Monte Carlo sampling of the model uncertainty space[20] so that a full variance-based sensitivity analysis of the model outputs can be performed.

Radiative forcing uncertainty

Figure 1 shows the annual mean first indirect radiative forcing and the associated 1σ uncertainty when assuming the 1750 reference state. The global annual mean indirect forcing is $-1.16\ \mathrm{W\,m^{-2}}$ ($\sigma = 0.22\ \mathrm{W\,m^{-2}}$, 95% confidence interval $-0.7\ \mathrm{W\,m^{-2}}$ to $-1.6\ \mathrm{W\,m^{-2}}$), compared to the multi-model range reported in ref. 2 of $-0.4\ \mathrm{W\,m^{-2}}$ to $-1.8\ \mathrm{W\,m^{-2}}$ (best estimate, $-0.7\ \mathrm{W\,m^{-2}}$) and an estimate ($-0.6 \pm 0.4\ \mathrm{W\,m^{-2}}$) based on assimilated PD aerosol optical depth[21]. Our estimated 95% confidence interval is slightly narrower than the multi-model ensemble range, most probably because the latter includes structural differences in the host model aerosol, cloud and radiation schemes[2,3,6]. Nevertheless, improved understanding of the aerosol processes and emissions would clearly help to reduce uncertainty in model forcing calculations.

The seasonal variation of global mean forcing and the contributions of different parameters to the uncertainty are shown in Fig. 2a and b (see the Methods and Extended Data Table 3 for the definition and elicited range of each parameter). The eight most important parameters account for 92% of the forcing variance: volcanic SO_2 emissions, anthropogenic SO_2 emissions, dimethyl sulphide (DMS) emissions from marine biota, the width of the accumulation mode, dry deposition of accumulation mode aerosol, sub-grid sulphate particle formation, the width of the Aitken mode, and the diameter of emitted fossil fuel combustion particles. Several parameters that have a large effect on uncertainties in PD concentrations of cloud condensation nuclei (CCN)[18]

[1]School of Earth and Environment, University of Leeds, Leeds, LS2 9JT, UK. [2]National Centre for Atmospheric Science, University of Leeds, Leeds, LS2 9JT, UK. [3]Department of Atmospheric Science, Colorado State University, Fort Collins, Colorado 80523, USA. †Present address: CSIRO Marine and Atmospheric Research, Aspendale, Victoria 3195, Australia.

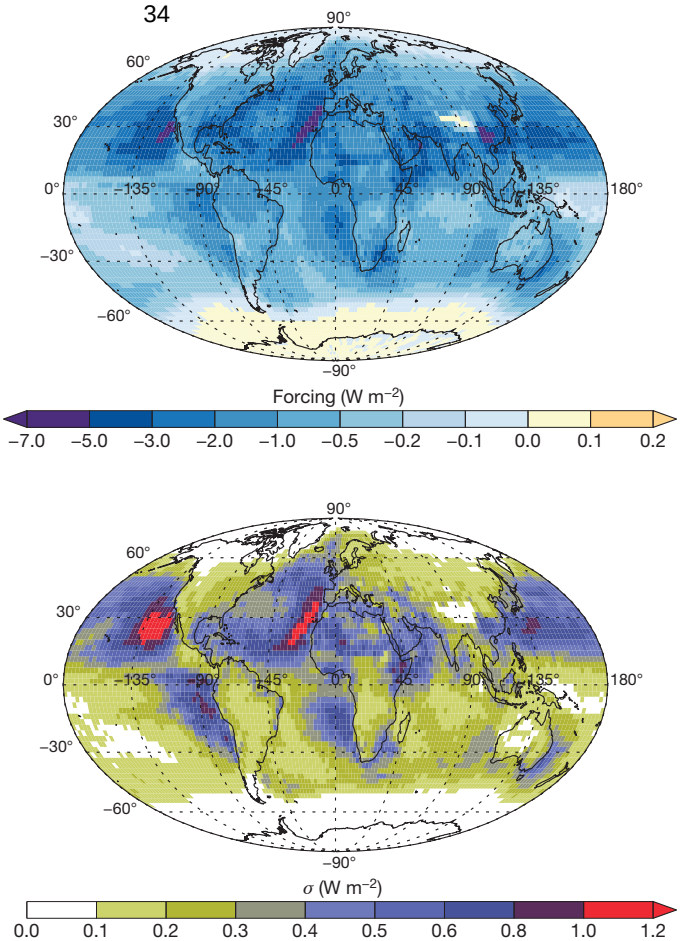

Figure 1 | The global distribution of annual mean aerosol first indirect forcing and associated uncertainty. **a**, First indirect forcing; **b**, standard deviation σ of forcing. The maps were computed from a Monte Carlo sampling of an emulator of forcing in each grid cell of the model.

have a small effect on forcing uncertainty, which is related to the way they perturb PI and PD CCN, as we discuss below.

A striking aspect of the results is the large contribution to the global mean forcing uncertainty from emissions of natural aerosol and precursor gases. Together, emissions of volcanic SO_2, marine DMS, biogenic volatile organic carbon (forming secondary organic aerosol), biomass burning and sea spray account for 45% of the global annual mean forcing variance (Fig. 2b). This compares with 34% of the annual mean forcing variance that is due to the eight parameters associated with anthropogenic fossil fuel, biofuel, SO_2 and sulphate particle emissions. The biomass burning emissions were perturbed as a single parameter and not separated into natural wildfires and anthropogenic biomass burning. However, the annual mean 2% contribution of biomass burning to the forcing variance means that the natural–anthropogenic split is not important to our overall conclusions. Moreover, the seasonality of the uncertainty caused by biomass burning suggests that it can be attributed mostly to northern mid-latitude emissions associated with natural fires (see Methods).

The relative contribution of different parameters to the uncertainty depends on the sampled range in the ensemble (Extended Data Table 3). The range for DMS (−50%/+100%) is consistent with assessments of multiple emission parameterizations[22] and the same range for volcanic SO_2 is plausible given the uncertainty in sources[23]. However, our assumed range of −40%/+50% for the main anthropogenic aerosol uncertainty (SO_2 emissions) is high compared to the most recent inventories. Thus, it is likely that our estimate of the natural aerosol effect on forcing uncertainty is an underestimate.

It is important to note that most of the natural emissions do not, by themselves, cause a forcing over the industrial period because the emission source strengths were defined to be the same in the PI and PD simulations (except for biomass burning); that is, a high setting of the emissions in the PI simulation was paired with the same high setting in the PD. However, natural emissions affect the uncertainty in the aerosol first indirect forcing because they affect the background aerosol state upon which the forcing is calculated (see below).

Because our variance-based approach considers parameter interactions, we are able to establish that the large contribution of natural aerosol emissions to forcing uncertainty is not strongly dependent on the magnitude of the other parameters. This is important information because, for example, the large sensitivity of forcing to natural sulphur emissions could be overemphasized if particle formation rates due to sulphuric-acid-driven nucleation were too high in the model. However, such parameter interactions can be quantified as the difference between the sum of the main effect variances (coloured bars in Fig. 2b) and the total variance (100% in Fig. 2b); see the Methods. Interactions generally account for less than 10% of the total forcing variance, demonstrating that the ranked uncertainty results are robust to uncertainties in the model set-up.

The effect of some parameters on forcing uncertainty could be underestimated if the parameter varied in an unknown way between the PI and PD eras, which we have not accounted for here. For example, if DMS or volcanic emissions were at the low end of the uncertainty range in the PI and at the higher end in the PD then the resulting increase in sulphate aerosol over this period would constitute an additional uncertainty in the forcing[23]. It is plausible that natural emissions change over time, implying that the uncertainty attributable to these parameters could be underestimated. Whether other parameters behave in this way depends on the extent to which the model processes represent an absolute understanding or whether they have been inadvertently tuned to conditions in the PD atmosphere.

Alternative reference years

The contribution of natural emissions to the forcing uncertainty will depend on the reference year that is used. The 1750 reference, used here, is commonly assumed to represent a pristine PI state, whereas early industrial decades from the 1850s onwards have also been used[24]. To test the effect of using alternative years for forcing, we repeated our calculations for the periods 1850–2000, 1850–1980 and 1900–2000 (limited to June to reduce computational cost). For the alternative reference years we used the same natural emissions as in 1750, but different anthropogenic emissions (see Methods). As expected, the indirect forcing is lower when a slightly polluted reference year is used (a June mean of $-1.30\ W\ m^{-2}$ for 1850 and $-0.96\ W\ m^{-2}$ for 1900, versus $-1.42\ W\ m^{-2}$ for 1750). The uncertainty analysis shows that the standard deviation of forcing is slightly larger when the reference year is 1850 ($\sigma = 21\%$ of mean) than for 1750 ($\sigma = 19\%$ of mean); see Extended Data Table 4. However, the uncertainties in 1850 emissions are likely to be larger than for the year 2000, which we have not attempted to account for, so we expect our estimate of 1850–2000 forcing uncertainty to be an underestimate. The contribution of anthropogenic emissions to the forcing uncertainty is also greater using an 1850 reference (46% of variance, versus 38% using 1750). This change compared to 1750 is mainly caused by the increased contribution from fossil fuel and sulphate particle emissions. These results show that natural emissions remain a substantial part of the forcing uncertainty even when slightly polluted reference years are used. They also confirm that the uncertainty in forcing is strongly sensitive to the assumed PI emissions, whether natural or anthropogenic: the large absolute change in anthropogenic emissions between 1980 and 2000 causes hardly any change in the contribution of anthropogenic emissions to the uncertainty in forcing referenced to 1850 (47% versus 46% of variance; see Extended Data Table 4), but the small absolute change in emissions

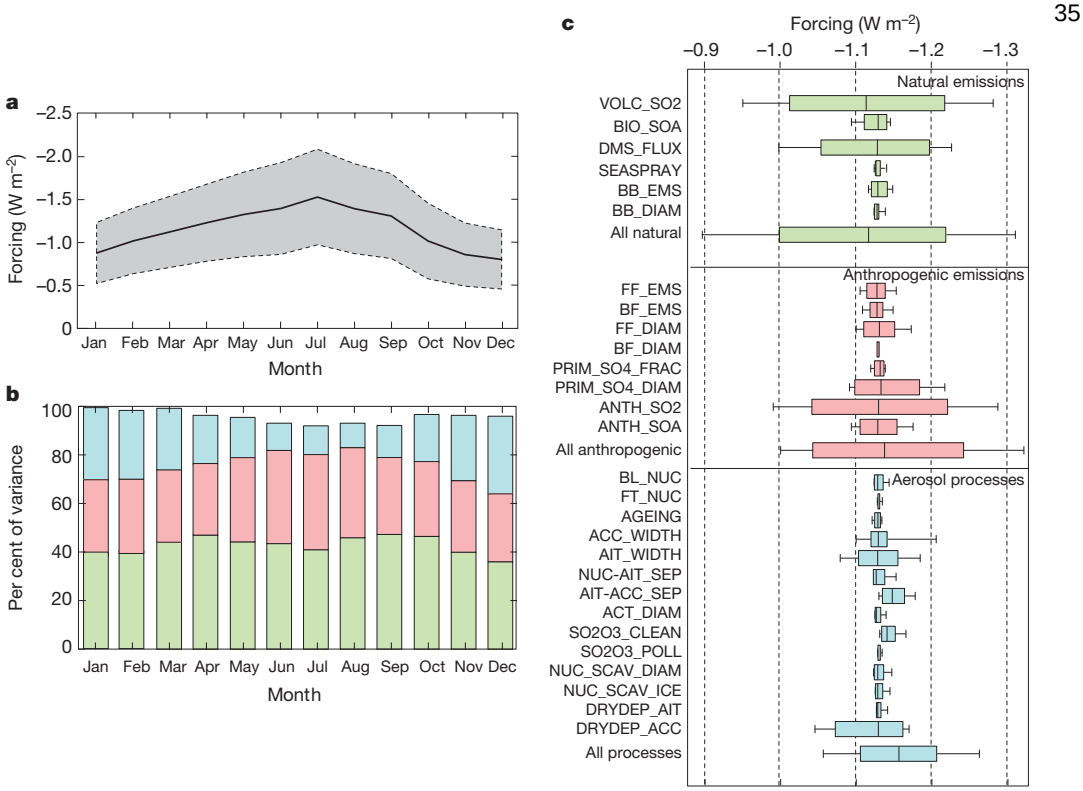

Figure 2 | Magnitude and sources of uncertainty in global mean aerosol first indirect forcing. **a**, Global mean forcing and two-standard-deviation uncertainty range. **b**, Seasonal cycle of the contribution of different groups of parameters to global monthly mean forcing variance (green, natural emissions; pink, anthropogenic emissions; blue, aerosol processes). The difference between the sum of variances and 100% is accounted for by parameter interactions. **c**, Global annual mean forcing uncertainty range due to specific parameters and groups of parameters. The box shows the interquartile range and the whisker shows the 9%–91% confidence interval. The definition of each parameter is given in Extended Data Table 3.

between 1750 and 1850 causes a large change in the anthropogenic contribution (38% to 46%).

Although not a focus of this work, our results also suggest that most of the aerosol–cloud forcing has probably been realized by 1980 and has changed little between 1980 and 2000 (comparing 1850–1980 and 1850–2000 time periods; see Extended Data Table 4). This, combined with the uncertainty analysis, indicates that it may be possible to place a relatively tight constraint on the aerosol forcing over recent decades (compared to the PI-to-PD period), which would help determine the forcing contribution to the reduction in warming trend.

Importance of natural aerosols

The large contribution of natural aerosol emissions to forcing uncertainty is caused by three factors (Fig. 3a–d). First, the 1σ response of CCN to changing DMS emissions is 44% higher in the PI period than in the PD period ($\sigma = 12.9\ \mathrm{cm}^{-3}$ versus $9.0\ \mathrm{cm}^{-3}$) between 60° S and 60° N in July, caused by the more efficient nucleation of new particles in the cleaner PI atmosphere. Second, cloud droplet number concentrations increase more steeply with CCN when concentrations are low in the PI era. This effect occurs because high droplet concentrations limit the in-cloud supersaturation. Third, cloud albedo sensitivity to changes in cloud droplet concentrations (the susceptibility[1]) is higher in the PI era because the dependence of albedo A on droplet number N is approximately $\mathrm{d}A/\mathrm{d}N = A(1 - A)/3N$. The combined effect of these three factors means that the forcing uncertainty is more strongly affected by natural aerosol (which affects PI cloud albedo in a near-linear way) than PD anthropogenic aerosol (which affects PD albedo in a sub-linear way). For the region of high forcing off the coast of Chile, CCN concentrations rise in our model by a factor of 6.6 ($75\ \mathrm{cm}^{-3}$ in the PI period to $500\ \mathrm{cm}^{-3}$ in the PD). Under these conditions, and with a cloud albedo of 0.5, the sensitivity of albedo to CCN is about 15 times higher in the PI period than in the PD.

Although natural aerosol emissions cause only a small uncertainty in PI and PD CCN, they can have a disproportionate effect on forcing uncertainty compared to some process parameters, which we illustrate for typical conditions in Fig. 3e. For example, aerosol deposition processes were identified as a major uncertainty in PD CCN[18]. However, uncertainty in such a process causes an uncertainty in CCN that is in proportion to the aerosol abundance (so the absolute error in CCN will be higher in the PD than in the PI). In contrast, the uncertainty in DMS emissions causes approximately the same absolute error in CCN in the PI and PD. As shown in Fig. 3e, the relationship between CCN, cloud droplet concentrations and albedo means that there is some degree of cancellation of errors in the case where the CCN error is proportional to the amount of aerosol. For the illustrative conditions used in Fig. 3e, when PD CCN concentrations are about double the PI levels, the uncertainty in forcing is a factor of ten higher in the absolute case than in the proportional case.

Implications

Our study provides the first assessment of how aerosol processes and emissions affect the uncertainty in indirect forcing between the PI and PD periods and provides quantitative support for previous studies that have highlighted the importance of understanding PI aerosol[9–12]. There are several implications. First, it will prove difficult to constrain the sources of forcing uncertainty by making observations in the PD atmosphere[11,21], because the low sensitivity of PD clouds to these emissions[18,22] is unrepresentative of the PI atmosphere. We would need to understand the effects of natural emissions on PI-like aerosol. The nearest equivalent we have to PI conditions in the PD atmosphere is in very clean environments[9], but the spread of perturbed particle concentrations[10,25] may make it difficult to observe sufficiently pristine environments, except over very remote marine locations[26]. Second, because the magnitude of the PI emissions themselves (notably volcanic and DMS) are now unmeasurable, some of the forcing uncertainty in

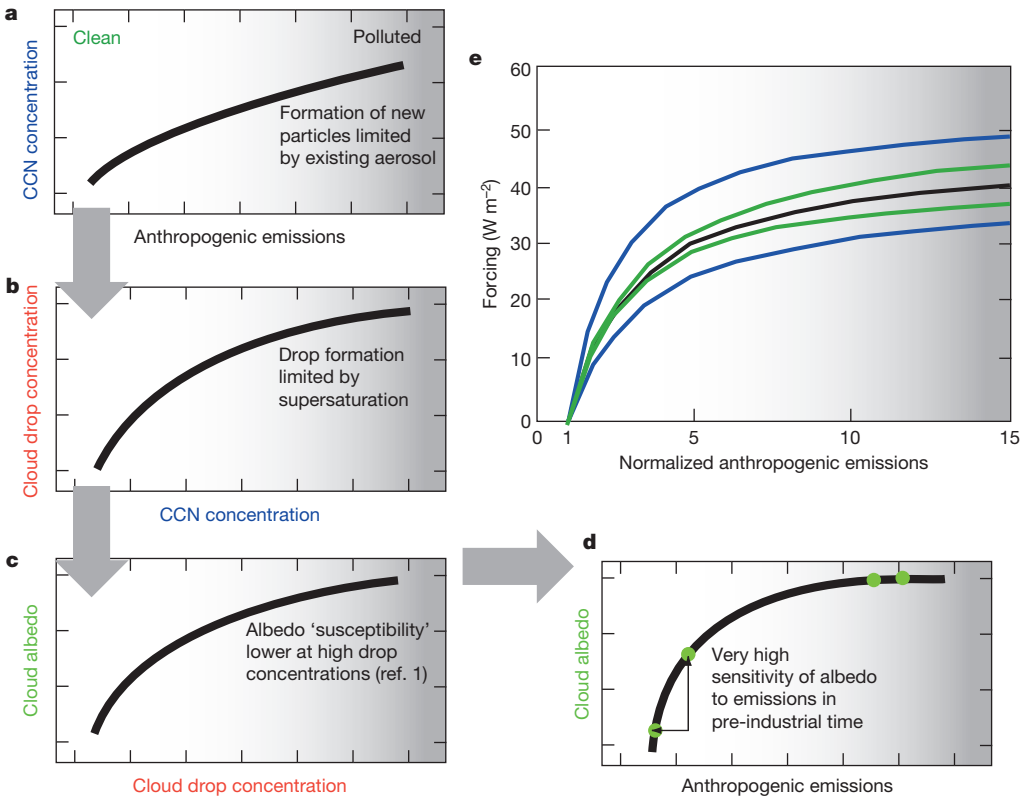

Figure 3 | Schematic explaining the importance of natural emissions for forcing uncertainty. **a**, CCN concentrations are more sensitive to emissions of sulphur precursor gases in the PI era because the condensation sink of the nucleating sulphuric acid vapour onto existing aerosol is lower. **b**, Cloud droplet concentrations are more sensitive to changes in CCN when droplet concentrations are low because higher droplet concentrations suppress in-cloud supersaturation and limit the activation of additional aerosol particles. **c**, Cloud albedo is more susceptible to changes in cloud droplet concentration when concentrations are low[1]. **d**, All three effects in **a**–**c** lead to a much higher sensitivity of albedo to precursor gas emissions in the PI era. **e**, Calculated effect of how the uncertainty in modelled aerosol affects the uncertainty in forcing. In this example, it is assumed that the CCN concentration scales in direct proportion with anthropogenic emissions (horizontal axis), as occurs approximately in the model. Uncertainties are then applied to CCN ($\pm\Delta$CCN). The green lines shows the uncertainty in forcing when ΔCCN is proportional to the CCN concentration and the blue lines shows a case where ΔCCN is constant and independent of the anthropogenic emissions. The initial PI CCN concentration is 50 cm^{-3}, rising to a maximum of 750 cm^{-3} in the PD. The cloud droplet number concentration (CDNC) is calculated as CDNC = $375 \times (1 - \exp(-0.0025 \times \mathrm{CCN}))$ (ref. 28). The albedo A of the baseline cloud is assumed to be 0.5 and the albedo versus CDNC is $dA/d\ln(\mathrm{CDNC}) = A(1-A)/3A$ (ref 1). The forcing is calculated according to $-F_0 T_a^2 \Delta A$, where ΔA is the change in albedo from the PI value (0.5), T_a is the transmission of the atmosphere (assumed to be 0.75) and F_0 is the radiative flux, assumed to be 340 W m^{-2}. The black line shows the calculated forcing assuming the baseline aerosol number concentration. The green line shows the calculated forcing assuming $\pm$30% uncertainty in CCN (35–65 cm^{-3} in the PI era to 525–975 cm^{-3} maximum in the PD). This calculation represents an uncertainty in aerosol concentrations due to a process that affects PI and polluted aerosol concentrations by the same factor, such as dry deposition. The blue line shows the calculated forcing assuming $\pm$15 cm^{-3} uncertainty in CCN (35–65 cm^{-3} in the PI era, as in the scaled calculation, to a maximum polluted concentration of 735–765 cm^{-3}). This calculation represents an uncertainty in aerosol concentrations due to a process or emission that affects PI and polluted aerosol by approximately the same absolute amount, such as caused by uncertainty in DMS or volcanic SO_2 emissions. The small absolute change in aerosol has a much larger effect on forcing uncertainty than the scaled aerosol change.

climate simulations may be irreducible[27]. Therefore, empirical estimates of PI-to-PD forcing based on observations of aerosol and aerosol–cloud relations under PD conditions[21,28] may not be accurate. Third, efforts to constrain the magnitude of equilibrium climate sensitivity based on net forcing and ocean heat content relative to a PI reference[24] will always be hampered by our limited ability to constrain the natural aerosol state. Although it makes sense to define the forcing relative to a PI reference period when the forcing was zero and the Earth was approximately in energy balance, this does not imply zero error contribution from the reference state. We have shown that the uncertainties in PI-to-PD forcing are strongly affected by the PI aerosol. Other reference periods could be considered, but equilibrium climate sensitivity studies would need to account for uncertainties in ocean heat content. A final implication is that the major sources of uncertainty will depend on the period over which forcing is calculated, so future aerosol indirect forcing may be sensitive to a different set of parameters. Therefore, accurate simulation of past forcing, if this could be achieved, may not guarantee accurate future estimates. Furthermore, other aerosol–cloud interaction effects not considered here[3,4] may also depend nonlinearly on aerosol between the PI period and the PD, and the uncertainties could be dominated by a different set of parameters.

Future efforts to reduce the uncertainty in simulated aerosol forcing need to combine measurements and models in ways that target sources of uncertainty, rather than relying on good model–observation agreement of PD aerosol as a measure of model fidelity. This means that models need to be based on sound microphysical processes and must not be reliant on tuning to PD aerosol levels. It is also essential for climate models and other models used for long-term simulations to include accurate representations of all natural aerosols, even if they have a small effect on PD aerosol levels in polluted environments. Even as future simulations of aerosol–cloud interaction become increasingly spatially resolved and able to capture more aerosol–cloud interaction processes and associated uncertainties, the uncertainty introduced from a poorly constrained pristine aerosol state will remain.

METHODS SUMMARY

The GLObal Model of Aerosol Processes (GLOMAP)[15,16] calculates the time-dependent global distribution of size-resolved aerosol particles, including the

microphysical processes of particle nucleation, growth, coagulation, cloud cycling and deposition. The model transport is prescribed in terms of three-dimensional gridded wind speed, temperature and humidity fields from the European Centre for Medium-Range Weather Forecasts analyses. Anthropogenic emissions (from fossil fuel, biofuel and biomass burning) were set to their 1750 (plus alternative 1850 and 1900) values in the PI era and year 2000 values for the PD and were perturbed by a given factor (see Extended Data Tables 1 and 2). The uncertainty range for each parameter was chosen on the basis of expert elicitation[18]. The model was run for 168 combinations of parameter settings from among 28 parameters representing aerosol and precursor gas emissions, microphysical processes and aerosol model structures (see Extended Data Table 3).

The radiative forcing between the PI era and the PD was calculated using a radiative transfer model[29] and a monthly and geographically varying data set of cloud optical depth[30]. The diurnal cycle of incoming solar radiation was accounted for, but no diurnal cycle of cloud cover was assumed. Cloud droplet concentrations were calculated from the aerosol size distribution assuming a characteristic updraft speed of 0.15 m s^{-1} over ocean and 0.3 m s^{-1} over land. The albedo change in each grid cell was then calculated in terms of the change in cloud droplet effective radius at constant liquid water path[31]. Global mean forcings were calculated for 1750–2000, 1850–2000, 1900–2000 and 1850–1980 (see Extended Data Table 4).

A Gaussian process emulator was built to describe the monthly and global mean PI-to-PD change in top-of-the-atmosphere radiation across the space of the 28 uncertain parameters[18], and then a Monte Carlo sampling of the emulator was used to generate a probability distribution of global mean forcing. Variance decomposition was used to quantify the fraction of variance attributable to the uncertain parameters. The forcing and uncertainty maps (Fig. 1) were generated by performing a similar analysis on separate emulators for each model grid cell.

Online Content Any additional Methods, Extended Data display items and Source Data are available in the online version of the paper; references unique to these sections appear only in the online paper.

Received 29 March; accepted 16 September 2013.

1. Twomey, S. Aerosols, clouds, and radiation. *Atmos. Environ. A* **25,** 2435–2442 (1991).
2. Forster, P. *et al.* in *Climate Change 2007: The Physical Science Basis, Contribution of Working Group I to the Fourth Assessment Report of the Intergovernmental Panel on Climate Change* (eds Solomon, S. *et al.*) 129–234 (Cambridge Univ. Press, 2007).
3. Lohmann, U. & Feichter, J. Global indirect aerosol effects: a review. *Atmos. Chem. Phys.* **5,** 715–737 (2005).
4. Stevens, B. & Feingold, G. Untangling aerosol effects on clouds and precipitation in a buffered system. *Nature* **461,** 607–613 (2009).
5. Andreae, M. O., Jones, C. D. & Cox, P. J. Strong present-day aerosol cooling implies a hot future. *Nature* **435,** 1187–1190 (2005).
6. Quaas, J. *et al.* Aerosol indirect effects—general circulation model intercomparison and evaluation with satellite data. *Atmos. Chem. Phys.* **9,** 8697–8717 (2009).
7. Lohmann, U. & Ferrachat, S. Impact of parametric uncertainties on the present-day climate and on the anthropogenic aerosol effect. *Atmos. Chem. Phys.* **10,** 11373–11383 (2010).
8. Pan, W. W., Tatang, M. A., McRae, G. J. & Prinn, R. G. Uncertainty analysis of indirect radiative forcing by anthropogenic sulfate aerosols. *J. Geophys. Res.* **103,** 3815–3823 (1998).
9. Andreae, M. O. Aerosols before pollution. *Science* **315,** 50–51 (2007).
10. Andreae, M. O. & Rosenfeld, D. Aerosol–cloud–precipitation interactions. Part 1. The nature and sources of cloud-active aerosols. *Earth Sci. Rev.* **89,** 13–41 (2008).
11. Penner, J. E., Xu, L. & Wang, M. H. Satellite methods underestimate indirect climate forcing by aerosols. *Proc. Natl Acad. Sci. USA* **108,** 13404–13408 (2011).
12. Hoose, C. *et al.* Constraining cloud droplet number concentration in GCMs suppresses the aerosol indirect effect. *Geophys. Res. Lett.* **36,** L12807 (2009).
13. Adams, P. J. & Seinfeld, J. H. Predicting global aerosol size distributions in general circulation models. *J. Geophys. Res.* **107,** 4370, doi: 10.1029/2001JD001010 (2002).
14. Liu, X., Penner, J. E. & Herzog, M. Global modeling of aerosol dynamics: model description, evaluation, and interactions between sulfate and nonsulfate aerosols. *J. Geophys. Res.* **110,** D18206, doi: 10.1029/2004JD005674 (2005).
15. Spracklen, D. V. *et al.* A global off-line model of size-resolved aerosol microphysics. I. Model development and prediction of aerosol properties. *Atmos. Chem. Phys.* **5,** 2227–2252 (2005).
16. Mann, G. W. *et al.* Description and evaluation of GLOMAP-mode: a modal global aerosol microphysics model for the UKCA composition-climate model. *Geosci. Model Dev.* **3,** 519–551 (2010).
17. Dentener, F. *et al.* Emissions of primary aerosol and precursor gases in the years 2000 and 1750 prescribed data-sets for AeroCom. *Atmos. Chem. Phys.* **6,** 4321–4344 (2006).
18. Lee, L. A. *et al.* The magnitude and causes of uncertainty in global model simulations of cloud condensation nuclei. *Atmos. Chem. Phys.* **13,** 8879–8914 (2013).
19. Lee, L. A., Carslaw, K. S., Pringle, K. J. & Mann, G. W. Mapping the uncertainty in global CCN using emulation. *Atmos. Chem. Phys.* **12,** 9739–9751 (2012).
20. Saltelli, A., Tarantola, S. & Chan, K. P.-S. A quantitative model-independent method for global sensitivity analysis of model output. *Technometrics* **41,** 39–56 (1999).
21. Bellouin, N., Quaas, J., Morcrette, J.-J. & Boucher, O. Estimates of aerosol radiative forcing from the MACC re-analysis. *Atmos. Chem. Phys.* **13,** 2045–2062 (2013).
22. Woodhouse, M. T. *et al.* Low sensitivity of cloud condensation nuclei to changes in the sea-air flux of dimethyl-sulphide. *Atmos. Chem. Phys.* **10,** 7545–7559 (2010).
23. Schmidt, A. *et al.* Importance of tropospheric volcanic aerosol for indirect radiative forcing of climate. *Atmos. Chem. Phys.* **12,** 7321–7339 (2012).
24. Otto, A. *et al.* Energy budget constraints on climate response. *Nature Geosci.* **6,** 415–416 (2013).
25. Manktelow, P. T., Carslaw, K. S., Mann, G. W. & Spracklen, D. V. Variable CCN formation potential of regional sulfur emissions. *Atmos. Chem. Phys.* **9,** 3253–3259 (2009).
26. Penner, J. E., Zhou, C. & Xu, L. Consistent estimates from satellites and models for the first aerosol indirect forcing. *Geophys. Res. Lett.* **39,** L13810 (2012).
27. Neelin, J. D., Bracco, A., Luo, H., McWilliams, J. C. & Meyerson, J. E. Considerations for parameter optimization and sensitivity in climate models. *Proc. Natl Acad. Sci. USA* **107,** 21349–21354 (2010).
28. Jones, A. *et al.* Indirect sulphate aerosol forcing in a climate model with an interactive sulphur cycle. *J. Geophys. Res.* **106,** 20293–20310 (2001).
29. Edwards, J. M. & Slingo, A. Studies with a flexible new radiation code. I. Choosing a configuration for a large scale model. *Q. J. R. Meteorol. Soc.* **122,** 689–719 (1996).
30. Rossow, W. B. &. Schiffer, R. A. Advances in understanding clouds from ISCCP. *Bull. Am. Meteorol. Soc.* **80,** 2261–2287 (1999).
31. Rap, A. *et al.* Natural aerosol direct and indirect radiative effects. *Geophys. Res. Lett.* **40,** 3297–3301 (2013).

Acknowledgements This research has received funding from the Natural Environment Research Council AEROS project (project number NE/G006172/1) and GASSP project (project number NE/J024252/1), the EC Seventh Framework Programme under grant agreement FP7-ENV-2010-265148 (Integrated Project PEGASOS), and the National Centre for Atmospheric Science. K.S.C. and P.M.F. are currently Royal Society Wolfson Merit Award holders.

Author Contributions K.S.C. wrote the manuscript. L.A.L. did the statistical analysis. C.L.R., K.J.P. and G.W.M. performed the aerosol modelling. M.T.W., L.A.R. and K.J.P. prepared the emissions. K.S.C., L.A.L. and C.L.R. did the data interpretation. A.R. and P.M.F. did the forcing calculations. All authors contributed to the editing of the manuscript.

Author Information Reprints and permissions information is available at www.nature.com/reprints. The authors declare no competing financial interests. Readers are welcome to comment on the online version of the paper. Correspondence and requests for materials should be addressed to K.S.C. (k.s.carslaw@leeds.ac.uk).

Chapter 3

Uncertainty in the magnitude of aerosol-cloud radiative forcing over recent decades

AGU PUBLICATIONS

41

Geophysical Research Letters

RESEARCH LETTER

10.1002/2014GL062029

Key Points:
- Forcing sensitivity to aerosol parameters is strongly period dependent
- Understanding near-future climate is limited if a single period is considered
- In recent decades, parametric uncertainty is smaller than model diversity

Supporting Information:
- Readme
- Table S1
- Table S2
- Table S3
- Figure S1
- Figure S2
- Figure S3

Correspondence to:
L. A. Regayre,
L.A.Regayre11@leeds.ac.uk

Citation:
Regayre, L. A., K. J. Pringle, B. B. B. Booth, L. A. Lee, G. W. Mann, J. Browse, M. T. Woodhouse, A. Rap, C. L. Reddington, and K. S. Carslaw (2014), Uncertainty in the magnitude of aerosol-cloud radiative forcing over recent decades, *Geophys. Res. Lett.*, *41*, 9040–9049, doi:10.1002/2014GL062029.

Received 26 SEP 2014
Accepted 17 NOV 2014
Accepted article online 24 NOV 2014
Published online 16 DEC 2014

Uncertainty in the magnitude of aerosol-cloud radiative forcing over recent decades

L. A. Regayre[1], K. J. Pringle[1], B. B. B. Booth[2], L. A. Lee[1], G. W. Mann[1,3], J. Browse[1], M. T. Woodhouse[4], A. Rap[1], C. L. Reddington[1], and K. S. Carslaw[1]

[1]School of Earth and Environment, University of Leeds, Leeds, UK, [2]UK Hadley Centre Met Office, Exeter, UK, [3]National Centre for Atmospheric Science, University of Leeds, Leeds, UK, [4]CSIRO Oceans and Atmosphere, Aspendale, Victoria, Australia

Abstract Aerosols and their effect on the radiative properties of clouds are one of the largest sources of uncertainty in calculations of the Earth's energy budget. Here the sensitivity of aerosol-cloud albedo effect forcing to 31 aerosol parameters is quantified. Sensitivities are compared over three periods; 1850–2008, 1978–2008, and 1998–2008. Despite declining global anthropogenic SO_2 emissions during 1978–2008, a cancelation of regional positive and negative forcings leads to a near-zero global mean cloud albedo effect forcing. In contrast to existing negative estimates, our results suggest that the aerosol-cloud albedo effect was likely positive (0.006 to 0.028 W m^{-2}) in the recent decade, making it harder to explain the temperature hiatus as a forced response. Proportional contributions to forcing variance from aerosol processes and natural and anthropogenic emissions are found to be period dependent. To better constrain forcing estimates, the processes that dominate uncertainty on the timescale of interest must be better understood.

1. Introduction

Aerosols directly reflect sunlight and affect cloud properties such as albedo [*Twomey*, 1977]. Other rapid adjustments to cloud properties in response to changes in aerosol concentrations can also occur, yet these remain poorly understood and poorly represented in global climate models (GCMs) [*Boucher et al.*, 2013]. Uncertainty in the magnitude of aerosol-cloud interaction (ACI) forcing in response to changing anthropogenic emissions is the dominant source of uncertainty in net aerosol radiative forcing within current GCMs [*Skeie et al.*, 2011; *Stocker et al.*, 2013]. The cloud albedo effect (CAE) [*Boucher et al.*, 2013], an effect characterized by a decrease in cloud drop effective radius that results from an increase in cloud droplet number concentration for a fixed amount of liquid water [*Twomey*, 1977], remains the largest component of the ACI.

The greatest source of uncertainty in global CAE forcing between the preindustrial and the present-day is the state of the preindustrial atmosphere [*Carslaw et al.*, 2013a]. This arises because cloud albedo responds, to a first-order approximation, logarithmically to increasing aerosol concentrations, so a large proportion of the uncertainty in cloud radiative change over the industrial period is associated with low aerosol concentrations in the preindustrial [*Schmidt et al.*, 2012; *Carslaw et al.*, 2013a; *Ghan et al.*, 2013]. *Carslaw et al.* [2013a] found that 45% of CAE forcing variance, calculated between 1750 and 2000, was attributable to uncertain and potentially unconstrainable natural aerosol emissions, suggesting a substantial component of climate model forcing uncertainty may be irreducible.

CO_2 concentrations are the main source of uncertainty in radiative forcing of future climate, when calculated to 2100, because CO_2 is a long-lived greenhouse gas for which emissions vary substantially in emission scenarios [*van Vuuren et al.*, 2011]. By the end of the century, aerosol forcing is likely to be negligible compared to CO_2 forcing [*Smith and Bond*, 2014]. On decadal timescales however, uncertainty in the change in aerosol forcing due to the representation of aerosol processes and emissions is comparable to the change in CO_2 forcing and can strongly influence radiative forcing calculations [*Hawkins and Sutton*, 2009; *Kirtman et al.*, 2013].

It is important to know the sign and magnitude of changes in CAE forcing in recent decades because changes in near-term historical forcing will inform the interpretation of near-future climate changes. Reducing forcing uncertainty in near-future projections is critical, yet the sources of CAE forcing uncertainty within global models are unknown, which limits individual model development and hinders the interpretation of

model intercomparison studies. Here we quantify uncertainty in CAE forcing attributable to 31 uncertain aerosol parameters, within a single global model for the periods 1850–2008, 1978–2008, and 1998–2008. This statistical analysis allows for areas of research to be prioritized for further model development, so that uncertainty in near-term climate projections may be reduced and makes an analysis of the role of CAE forcing in near-term historical climate change possible.

2. Methods

2.1. Time Periods

The three periods 1850–2008, 1978–2008, and 1998–2008 were chosen to provide the greatest contrast in changing anthropogenic aerosol emissions. By considering CAE forcing sensitivities across the three periods simultaneously, it is assumed that all parameters with the potential to strongly influence near-future climates will be identified.

Historical radiative forcing is usually calculated from preindustrial to present day, where an overall increase in global emissions of anthropogenic aerosols occurs. The period 1850–2008 is therefore included in this study for consistency. Global SO_2 emissions peaked in the late 1970s at approximately 120 Tg per year in 1978 [*Lamarque et al.*, 2010], then experienced several periods of decline, with Asian emissions causing further increases in the early part of this century [*Smith et al.*, 2011] resulting in approximately 103 Tg being emitted in 2008 [*Lamarque et al.*, 2010]. The overall decline in global anthropogenic emissions since the late 1970s coincides with a period of relatively rapid warming of surface temperatures [*Hartmann et al.*, 2013]. The period 1978–2008 can therefore be considered as distinct from 1850 to 2008, with the potential to produce CAE forcing values that are influenced by a unique set of parameters.

The 10 year period 1998–2008 can also be considered as a distinct period of anthropogenic emissions. In 1998, approximately 108 Tg of SO_2 was emitted globally [*Lamarque et al.*, 2010] hence between 1998 and 2008 global SO_2 emissions declined more gradually than in previous decades [*Granier et al.*, 2011]. The multidecadal trend in declining SO_2 emissions eased in Europe, yet became stronger in North America, during the 1998–2008 period. Asian emissions increased more rapidly than in the 1978–2008 period. The 1998–2008 period is also of interest because of the hiatus in global surface temperature rise which has been noted in the observational record since the late 1990s [*Brohan et al.*, 2006]. Identifying the sign and magnitude of CAE forcing, along with the associated variance, will shed light on the role of CAE forcing during the hiatus period.

The choice of 2008 as the end point for each period is based on an interest in evaluating decadal forcings and is thus constrained by our choice to use 1978 and 1998 as the start of the most recent periods. The experimental design outlined in section 2.2 is such that the choice of end year is largely arbitrary and is not expected to affect the results or conclusions.

2.2. Perturbed Parameter Ensemble

Thirty-one parameters related to aerosol processes as well as natural and anthropogenic aerosol emissions were identified and perturbed simultaneously within the GLObal Model of Aerosol Processes (GLOMAP) [*Spracklen et al.*, 2005; *Mann et al.*, 2010, 2012], at a horizontal resolution of $2.8° \times 2.8°$ with 31 vertical levels between the surface and 10 h Pa. GLOMAP is an extension to the TOMCAT three dimensional chemical transport model [*Stockwell and Chipperfield*, 1999]. Maximin Latin Hypercube sampling was used to create a parameter combination design, of 187 points, that spans the uncertain parameter space.

The parameters perturbed in this ensemble are similar to those used in *Lee et al.* [2013] and *Carslaw et al.* [2013a] with some new or adjusted parametrisations that relate to uncertain aspects of a newer version of the model. Particle formation within the continental boundary layer now uses a parametrisation that is enhanced in the presence of organic material [*Metzger et al.*, 2010]. Parametrisations for the dry deposition of SO_2, the emission flux of dust aerosol and two parameters relating to the wet removal of aerosols in low-level drizzling clouds have been included. The probability distributions for the uncertain parameters were identified through expert elicitation updated from *Lee et al.* [2013].

In this version of the model, three-dimensional meteorological fields and distribution of clouds obtained from the European Centre for Medium-Range Weather Forecasts (ECMWF) ERA-Interim reanalysis for 2008 are used for all years. Low-level stratiform clouds are prescribed from the International Satellite Cloud Climatology Project (ISCCP) D2 data [*Rossow and Schiffer*, 1999]. Modeled aerosols do not affect the

meteorology, transport, and presence of cloud, although the aerosols themselves are affected by cloud processing and precipitation. Changes in simulated CAE forcing across the ensemble, for each period, can therefore be attributed solely to the parameter perturbations.

Emission scenarios prepared for the Atmospheric Chemistry and Climate Model Intercomparison Project (ACCMIP) [*Lamarque et al.*, 2010] and prescribed in some of the Coupled Model Intercomparison Project Phase 5 (CMIP5) experiments [*Taylor et al.*, 2012] were used here to prescribe anthropogenic aerosol emissions for the years 1850, 1978, 1998, and 2008.

Pairs of simulations were used in the calculation of radiative forcing. Identical model configurations were used for each pair with the exception of anthropogenic aerosol emissions which were prescribed according to the years at either end of the periods examined. CAE forcing is defined here to be the difference in top of atmosphere net radiative fluxes between years and was quantified by modifying the cloud drop effective radius (r_e) for low- and middle-level clouds up to 6×10^2 h Pa, within the offline version of the Edwards and Slingo radiative transfer model [*Edwards and Slingo*, 1996]. This is the same approach used to calculate forcing in *Carslaw et al.* [2013a]. Surface albedo and cloud optical depths from ISCCP D2 for the year 2000 were used, and therefore, r_e was modified relative to values derived for that year, denoted here using the "ref" superscript:

$$r_e = r_e^{\mathrm{ref}} \times \left(\frac{\mathrm{CDNC}^{\mathrm{ref}}}{\mathrm{CDNC}} \right)^{1/3}, \tag{1}$$

where CDNC is the monthly mean cloud drop number concentration within each model grid box. A fixed value of $r_e^{\mathrm{ref}} = 10\,\mu\mathrm{m}$ was used to ensure consistency with the ISCCP retrievals, and CAE forcing over a given period was taken as the difference between forcings for each year relative to the year 2000. The net cloud radiative effect from our year 2000 reference simulation is $-25.7\ \mathrm{W\,m^{-2}}$. *Calisto et al.* [2014] use 10 years of satellite retrievals to calculate an average cloud radiative effect of $-18.8\ \mathrm{W\,m^{-2}}$. While our reference cloud radiative effect is higher than determined from satellite retrievals, it is in agreement with CMIP5 models [*Calisto et al.*, 2014].

A cloud droplet activation parametrisation [*Fountoukis and Nenes*, 2005; *Barahona et al.*, 2010] was used to calculate CDNCs using the monthly mean aerosol distribution and composition in each grid box. Global, annual averages of CAE forcing for the 187 ensemble members were used to construct a statistical approximation to the model output and perform a sensitivity analysis.

2.3. Sensitivity Analysis

A variance-based sensitivity analysis [*Saltelli et al.*, 2000] of CAE forcing is made possible using validated Bayesian emulators [*Oakley and O'Hagan*, 2002] that are conditioned on the 187 member ensemble for each period to provide a statistical approximation of model output at any point in the 31-dimensional parameter space. The Bayesian emulation approach has been successfully applied to GLOMAP model output by *Lee et al.* [2011, 2012, 2013] and *Carslaw et al.* [2013a, 2013b].

The generation of a complete parametric response surface allows for contributions to variance, from each parameter and interactions between parameters, to be quantified explicitly across the entire surface. Nonlinear variations within the response surface are accounted for automatically and can be examined as required. These advantages cannot be obtained using one-at-a-time parameter perturbations, as is standard practice in climate model development. The results of the CAE forcing sensitivity analyses are provided in section 3.2. Sensitivity analyses were conducted using probability distributions of forcing that were obtained using the extended-FAST sampling method [*Saltelli et al.*, 1999], with 10^4 emulator sample points per parameter. These samples were also used to calculate 90% credible intervals of CAE forcing that account for variation across the parameter space.

3. Results

3.1. Ensemble Mean Aerosol-Cloud Radiative Forcing

Figure 1 shows the mean CAE forcing of the 187 member ensemble, for each period, within each model grid box. In Figure 1a, the well-documented negative anthropogenic aerosol forcing between the early-industrial to present-day period can be seen. The CAE forcing is strongest in the Northern Hemisphere where anthropogenic aerosol emissions increased significantly since 1850. The majority of the atmosphere changes from clean to polluted during this period.

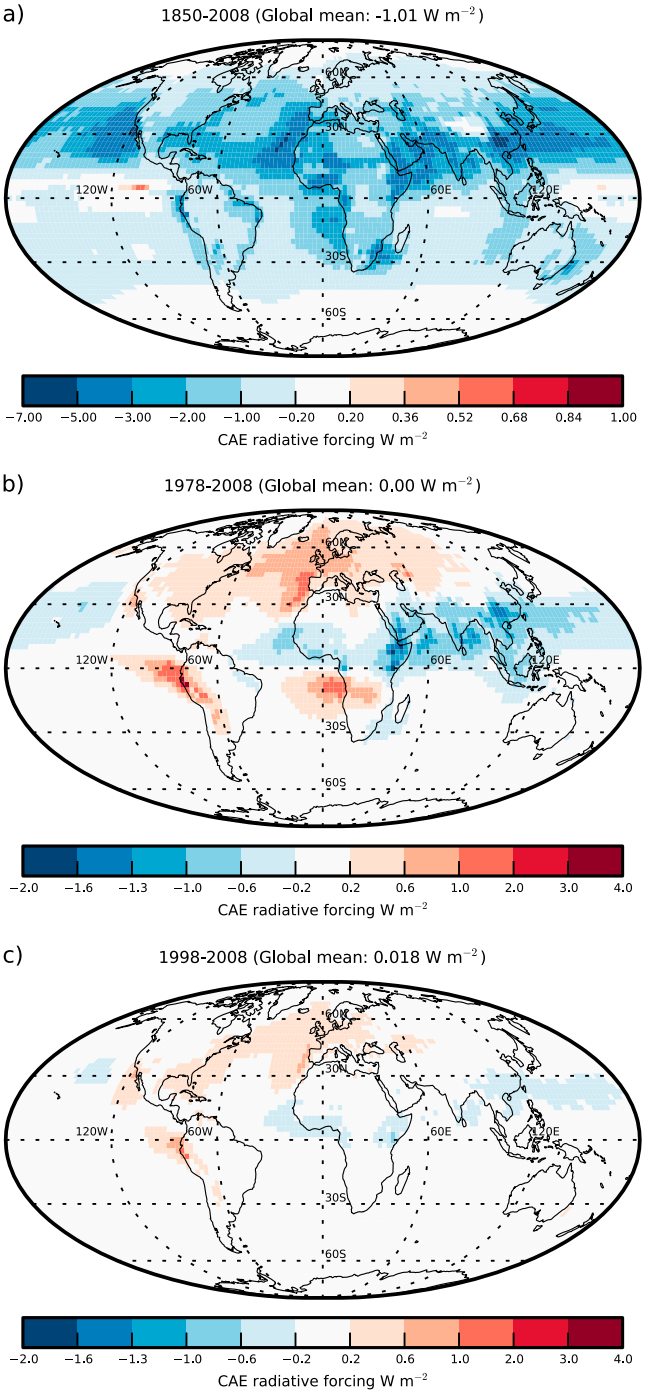

Figure 1. Average CAE radiative forcing for (a) 1850–2008, (b) 1978–2008, and (c) 1998–2008 in W m^{-2}. Forcing values for all ensemble members are averaged within individual grid boxes. The global means are calculated using 10^4 values sampled from the emulator for each period.

In recent decades, the effect of the regional changes in emissions outlined in section 1 become evident. There are regions of strong positive forcing where the CAE is smaller in 2008 than in 1978 in response to declining anthropogenic aerosol emissions. The patterns of regional forcing in the 1978–2008 period closely resemble those detected by *Andrews* [2013], in aerosol effective radiative forcing and changes in aerosol optical depth, over a similar period using a GCM with dynamic meteorology. Regional CAE forcings of opposite sign cancel out when calculating the global mean forcing. In the 1978–2008 period, ensemble mean CAE forcings in individual model grid boxes range from −1.8 to 3.0 W m^{-2} and from −0.8 to 1.1 W m^{-2} in the 1998–2008 period.

The spatial pattern of CAE forcing is similar between 1978–2008 and 1998–2008 (Figures 1b and 1c). The regions of positive and negative forcing are considerably smaller in the most recent decade, which is to be expected since the 1998–2008 period is much shorter and also because the rates of change in SO_2 emissions in these regions during this period are generally smaller than in previous decades. Differences in the spatial patterns of ensemble mean CAE forcing confirm that the magnitude and sign of changes in anthropogenic emissions lead to distinct cloud albedo responses in the three periods.

3.2. Sensitivity Analysis of Each Period

3.2.1. Magnitude and Diversity of CAE Forcing Estimates

Effective radiative forcing due to aerosol-cloud interactions for the 1750–2011 period is calculated by *Myhre et al.* [2013], using a multimodel ensemble, to be −0.45 W m^{-2} with a credible interval of (−1.2 to 0.0 W m^{-2}). Our mean emulated global CAE forcing for 1850–2008 is −1.01 W m^{-2} with a credible interval of (−1.235 W m^{-2}, −0.782 W m^{-2}). Individual ensemble members produce values ranging from −1.817 to − 0.461 W m^{-2}. The breadth of CAE forcing values is sufficient to provide a useful framework for exploring parametric sources of uncertainty.

The strong negative global mean forcing in the 1850–2008 period is not present in 1978–2008 where the mean emulated CAE forcing is zero with a credible interval of (−0.035 W m^{-2}, 0.033 W m^{-2}). The global

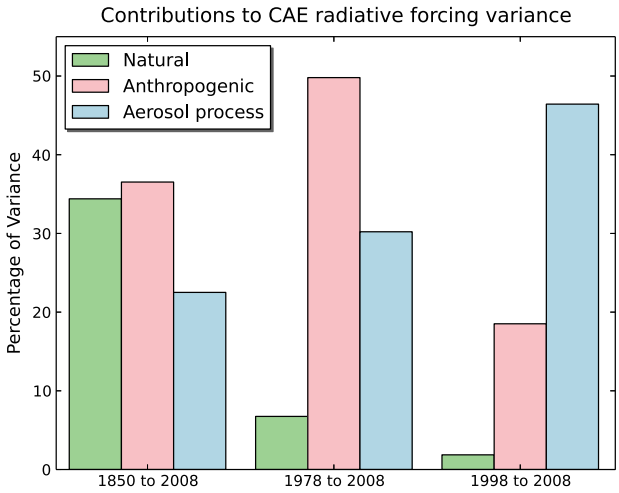

Figure 2. Contributions to globally averaged CAE forcing variance from aerosol process parameters and natural and anthropogenic emissions, for the three periods 1850–2008, 1978–2008, and 1998–2008. Percentages are obtained by Monte Carlo sampling from independent emulators of forcing for each period. Note that the total variance changes substantially between periods.

mean CAE forcing magnitude and credible range for the 1978–2008 period are both small compared to a CO_2 forcing of 0.7 W m^{-2} over the same period [*Myhre et al.*, 2013], resulting from compensating positive and negative regional forcings of up to 3 W m^{-2}. The relatively small uncertainty around zero that we calculate does not alter the conclusion that increasing concentrations of CO_2 and other well-mixed greenhouse gases produced the observed rapid warming of global mean surface temperature, which started in the late 1970s [*Hartmann et al.*, 2013].

The small credible forcing range calculated here suggests a confidence in the zero 1978–2008 emulated mean CAE forcing which is in contrast with other studies. *Skeie et al.* [2011] calculate a CAE forcing during the 1978–2008 period of approximately −0.093 W m^{-2} and *Shindell et al.* [2013] use three CMIP5 GCMs to calculate combined CAE and rapid adjustment forcings of approximately −0.04, −0.15, and −0.67 W m^{-2} between 1980 and 2000. The magnitude of global CAE forcing diversity between models is the same order of magnitude as the CO_2 forcing over recent decades [*Myhre et al.*, 2013]. Our results isolate the uncertainty attributable to aerosol parameters and emissions within a global model and suggest that these factors are a smaller source of CAE forcing uncertainty than the uncertainty arising from the representation of atmospheric physics within models and the structural choices of aerosol and atmospheric physics parametrisations, at least for the globally averaged CAE forcing. Our small global mean CAE forcing uncertainty for the 1978–2008 period is the result of compensating uncertainties in positive and negative regional forcings. A large part of the difference between our small parametric uncertainty and model diversity in global CAE forcing over recent decades may be caused by differences in the extent to which regional forcings truly cancel within models.

In the 1998–2008 period, there is an overall positive forcing of 0.018 W m^{-2} with a credible interval of (0.006 W m^{-2}, 0.028 W m^{-2}). The continued decline in global anthropogenic emissions during this period, although smaller per decade than the period 1978–2008, produces a positive CAE forcing. The small, likely positive CAE forcing suggests that CAE forcing is unlikely to be the cause of the hiatus in global surface temperature rise, which would require a forcing of the order of −0.35 W m^{-2} [*Solomon et al.*, 2007]. The positive global CAE forcing calculated here contrasts with the −0.06 W m^{-2} potential contribution of CAE forcing to recent changes in surface temperatures calculated by *Schmidt et al.* [2014]. The positive 1998–2008 global CAE forcing is a small but nonnegligible 2–11% of the 0.25 W m^{-2} CO_2 forcing over the same period [*Myhre et al.*, 2013]. When CAE forcing and its parametric sensitivities are accounted for the magnitude of forcing per decade that would need to be explained by other external forcings increases. Approximately half of current GCMs exclude the CAE [*Wilcox et al.*, 2013] and are therefore unable to account for this important process and its inherent uncertainty when calculating forcing over recent decades.

3.2.2. Changes in the Sources of Uncertainty

Uncertainty in global mean CAE forcing can be decomposed into uncertainty arising from aerosol process parameters and from natural and anthropogenic emissions, using a variance-based sensitivity analysis [*Saltelli et al.*, 2000]. Proportional reductions in total variance that can be expected if all parameters within a group were known precisely, are presented for each period in Figure 2. The CAE forcing variance is smaller in the two most recent periods than in the 1850–2008 period, and the contributions to variance should be interpreted in this context. Because the emulators produce results in a fraction of the time required for

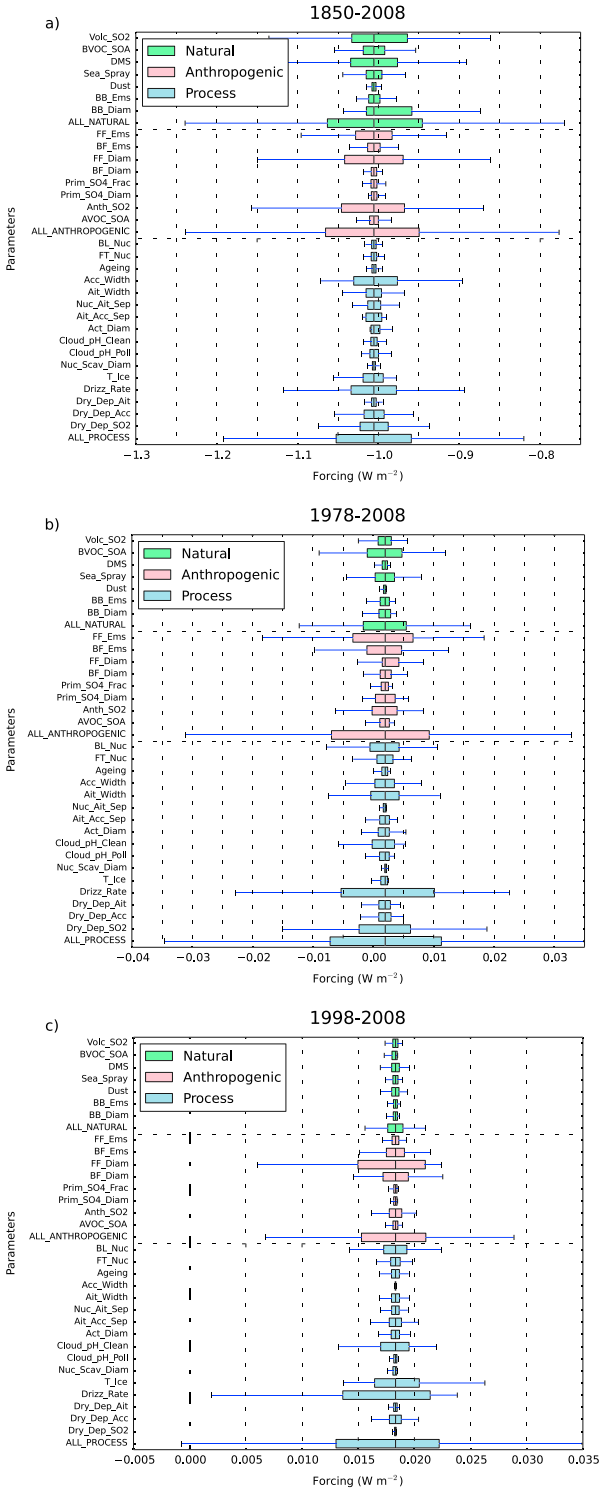

Figure 3. Box-and-whisker plots of CAE radiative forcing for individual parameters and groups of parameters during the periods (a) 1850–2008, (b) 1978–2008, and (c) 1998–2008. The probability density of each parameter is obtained by Monte Carlo sampling from the emulators for each period. The 25th, 50th, and 75th percentiles are used to create each box, and the whiskers extend to the most extreme sample point within 1.5 times the interquartile range. All box-and-whisker plots are centered on the mean emulated forcing value for that period. The range of emulated CAE forcing changes within each period.

the global model, sufficiently large samples can be taken from the multidimensional response surface to produce meaningful statistical summaries, such as those provided in Figure 2.

Each of the anthropogenic aerosol emission periods produces a distinct mix of contributions to variance, with substantial changes in the influence of parametric uncertainties on global CAE forcing variance between periods. Natural aerosol contributions to forcing variance decline from 34.4% in 1850–2008 to only 6.8% and 1.9% in 1978–2008 and 1998–2008, respectively. This decline was predicted by *Carslaw et al.* [2013a], who showed that using a relatively polluted baseline in the forcing calculation reduces the importance of uncertainty in natural aerosol emissions. Note that the parametric contributions presented here differ from those in *Carslaw et al.* [2013a] because a different early-industrial period start year was used and furthermore model results are influenced by the structural changes implemented in this version of the model, as described in section 2.2.

Uncertainties in anthropogenic emissions dominate forcing uncertainty during the 1978–2008 period, contributing 49.8% of the global CAE forcing variance, compared to a 30.2% contribution from aerosol process parameters. Anthropogenic emission uncertainties determine both the magnitude and the sign of CAE forcing during the 1978–2008 period. Strong regional forcings of opposite sign have the potential to be canceled out, and the anthropogenic emission uncertainties control the relative importance of regional contributions to the global CAE forcing.

Aerosol process parameters dominate the 1998–2008 forcing uncertainty, contributing 46.4% of the global CAE forcing variance, with anthropogenic emissions accounting for only 18.5%. Global CAE forcing during this period is controlled by those regions experiencing a decline in anthropogenic

emissions, leading to an overall positive forcing. Aerosol process parameter uncertainties take on a larger role in controlling global CAE forcing during this period, because uncertainties in parameters controlling the growth and removal of aerosol are more important than the uncertainties in the emissions themselves when changes in emissions are small. The uncertainties in aerosol process parameters contribute to the forcing variance in each period, although their influence is strongest in the absence of large changes in anthropogenic aerosol emissions. The dominance of aerosol process parameters as a source of global mean CAE forcing variance in the near-term suggests that aerosol model structural uncertainty is likely to make an important contribution to near-future climate projection uncertainty.

The changing proportional contributions to global CAE forcing variance from the three sources of parametric uncertainty suggest that the periods examined here are diverse enough to enable the identification of those uncertain aerosol parameters which may influence future CAE forcing uncertainty. Changes in the contributions from individual parameters are discussed further in section 3.2.3.

3.2.3. Changes in Contributions From Individual Parameters

Individual aerosol parameter contributions to CAE forcing variance over the three periods are summarized using box-and-whisker plots in Figure 3. Each box and whisker plot is generated by sampling from the emulator 10^4 times with the parameter in question allowed to vary across the parameter space and all other parameters held fixed at their median values, making these plots comparable to those in *Carslaw et al.* [2013a].

Some parameters such as the drizzle rate (Drizz_ rate), defined as the precipitation rate in low-level stratocumulus clouds within a 6 h period [*Browse et al.*, 2012], contribute to CAE forcing variance regardless of emission period. Other parameters make small contributions to variance in some periods and substantial contributions in others. For some parameters, such as the magnitude of anthropogenic SO_2 emissions (Anth_ SO_2) and global fossil fuel and global biofuel emission fluxes (FF_ Ems and BF_ Ems), the parametric contributions to forcing variance are correlated with the magnitude of emissions. Anthropogenic emission fluxes change less dramatically in 1998–2008 than in the other periods [*Bond et al.*, 2007; *Lamarque et al.*, 2010], and as such the associated parameters make smaller contributions to forcing variance.

The period dependence of individual parametric contributions to CAE forcing variance suggests that studies that are designed to quantify aerosol model uncertainty from a single time period, such as the preindustrial to present-day, may not be informative of model sensitivities in near-future climates of interest.

4. Conclusions

The most striking result of our study is that the parametric uncertainty of global mean CAE forcing over recent decades is much smaller than the range predicted by other climate models. Regional positive and negative forcings of up to 3 $W\,m^{-2}$ cancel each other in calculations of global CAE forcing over recent decades. Our analysis suggests that uncertainties in aerosol processes and emissions in a single global model (if spatially and temporally correlated as we assume) are less important than structural differences between models over recent decades. In contrast, over the 1850–2008 period, the forcing is almost everywhere negative, and aerosol parameters and emissions account for a substantial fraction of the multimodel range [*Carslaw et al.*, 2013a]. Thus, in historical or future periods in which regional patterns of forcing of opposite sign can occur, the true uncertainty in global mean forcing may be largely determined by the extent to which regional forcing cancelation occurs. That is, an understanding of regional patterns of forcing across multiple models becomes paramount.

The small global mean CAE uncertainty attributable to aerosol parameters and emissions over recent decades hides much larger regional forcing uncertainties. Causes of regional forcing uncertainty are likely to be highly variable, and an analysis of them may provide insight into the cause of model diversity. One method for understanding the sources of multimodel diversity in global and regional CAE forcing over recent decades would be to incorporate a perturbed parameter framework into multimodel intercomparison projects. The design of such experiments would benefit from being informed by the results here, which highlight those aerosol processes and emissions that are likely to influence multimodel global CAE forcing diversity on different timescales.

Despite the small calculated uncertainties in global mean CAE forcing, our analysis clearly shows that the causes of uncertainty in forcing over recent decades are very different to those associated with forcing

48

referenced to the preindustrial state [*Carslaw et al.*, 2013a]. Natural emission uncertainty was shown by *Carslaw et al.* [2013a] to substantially influence CAE forcing uncertainty since the preindustrial era. Here natural emission uncertainty has been shown to play only a minor role in controlling global CAE forcing variance in recent decades, where the atmosphere at both the start and end of the forcing period can be considered polluted relative to the preindustrial atmosphere. In order to identify parameters that have the potential to influence the near-future climate forcing, it is essential to perform sensitivity analyses using a range of diverse anthropogenic aerosol emission periods. Reducing uncertainty in these parameters will likely lead to improved near-future climate projections. The implication of the period dependence of CAE forcing sensitivity to uncertain aerosol parameters and emissions is that multimodel intercomparison projects may benefit from a design structure that utilizes historic periods over which anthropogenic emissions most closely resemble those used in the near-future climates they are to inform.

If the historical period under consideration contains relatively large regional and global changes in anthropogenic aerosol emissions, such as the 1978–2008 period, then uncertainties in these emissions contribute most to global CAE forcing uncertainty. Addressing the causes of anthropogenic emission inventory diversity during the 1978–2008 period is shown here to be a priority for reducing uncertainty in CAE forcing calculations over recent decades and therefore warrants further research.

Aerosol process parameters influence global CAE forcing variance much more strongly in periods where the forcing is controlled by relatively small changes in anthropogenic aerosol emissions, as is the case in the 1998–2008 period. This decade contrasts with the 1978–2008 period when there were relatively large regional increases and decreases in anthropogenic emissions. The CAE forcing uncertainty for the 1998–2008 period can be viewed as the lower limit that could be expected in near-future climates because first, the anthropogenic aerosol emission changes during the most recent decade are so small, and second, our results highlight the importance of aerosol process parameters over recent decades suggesting that uncertainties in the structural representation of aerosols between models may also have the greatest impact on uncertainty during these periods. Furthermore, we assume that anthropogenic aerosol emission fluxes are perfectly correlated, both temporally and spatially, so that anthropogenic emissions are systematically scaled high/low and regional positive and negative forcings can cancel in the calculation of the global mean forcing. If anthropogenic aerosol emissions were underestimated at one end of a period and overestimated at the other, for example, then anthropogenic emission uncertainty would be a larger source of CAE forcing variance during that period which would inflate the credible ranges of CAE forcing.

Here we show that the credible range of CAE forcing during the 1998–2008 period is (0.006 W m^{-2}, 0.028 W m^{-2}), indicating that a positive CAE forcing is likely during the 1998–2008 period. In contrast to existing negative estimates of aerosol indirect forcing, our results suggest that the aerosol-cloud albedo effect was likely positive during the last decade, indicating that the hiatus in surface warming cannot be attributed to CAE forcing. A likely positive CAE forcing during this period reframes the role of CAE forcing in explaining model overestimation of recent warming using external forcings. The attribution of the present pause in surface warming as a forced response [*Kaufmann et al.*, 2011; *Estrada et al.*, 2013; *Haywood et al.*, 2013; *Kosaka and Xie*, 2013; *Santer et al.*, 2014] is more difficult given the present results. The existing role of aerosols in explaining the hiatus therefore needs to be reevaluated.

Acknowledgments
Data can be made available upon request from the corresponding author. L.A. Regayre is funded by a Doctoral Training Grant from the Natural Environment Research Council (NERC) and a CASE studentship with the UK Met Office Hadley Centre. Ben Booth was supported by the Joint UK DECC/Defra Met Office Hadley Centre Climate Programme (GA01101). Ken Carslaw acknowledges funding from the Royal Society Wolfson Award. We acknowledge funding from NERC under grants AEROS and GASSP (NE/G006172/1 and NE/J024252/1). This work made use of the facilities of N8 HPC provided and funded by the N8 consortium and EPSRC (grant EP/K000225/1). The Centre is coordinated by the Universities of Leeds and Manchester. Thanks to those experts who participated in the elicitation exercise and L. Rotstayn at CSIRO Oceans and Atmosphere for an insightful review of this article. The authors thank two anonymous reviewers for their helpful comments.

The Editor thanks two anonymous reviewers for their assistance in evaluating this paper.

References

Andrews, T. (2013), Using an AGCM to diagnose historical effective radiative forcing and mechanisms of recent decadal climate change, *J. Clim.*, *27*, 1193–1209, doi:10.1175/JCLI-D-13-00336.1.

Barahona, D., R. E. L. West, P. Stier, S. Romakkaniemi, and A. Nenes (2010), Comprehensively accounting for the effect of giant CCN in cloud activation parameterizations, *Atmos. Chem. Phys.*, *10*, 2467–2473, doi:10.5194/acp-10-2467-2010.

Bond, T. C., E. Bhardwaj, R. Dong, R. Jogani, S. Jung, C. Roden, D. G. Streets, and N. M. Trautmann (2007), Historical emissions of black and organic carbon aerosol from energy-related combustion, 1850–2000, *Global Biogeochem. Cycles*, *21*, GB2018, doi:10.1029/2006GB002840.

Boucher, O., et al. (2013), Clouds and aerosols, in *Climate Change 2013: The Physical Science Basis. Contribution of Working Group I to the Fifth Assessment Report of the Intergovernmental Panel on Climate Change*, edited by T. F. Stocker et al., pp. 574, 578, 609–610, Cambridge Univ. Press, Cambridge, U. K., and New York.

Brohan, P., J. J. Kennedy, I. Harris, S. F. B. Tett, and P. D. Jones (2006), Uncertainty estimates in regional and global observed temperature changes: A new data set from 1850, *J. Geophys. Res.*, *111*, D12106, doi:10.1029/2005JD006548.

Browse, J., K. S. Carslaw, S. R. Arnold, K. J. Pringle, and O. Boucher (2012), The scavenging processes controlling the seasonal cycle in Arctic sulphate and black carbon aerosol, *Atmos. Chem. Phys.*, *12*, 6775–6798, doi:10.5194/acp-12-6775-2012.

Calisto, M., D. Folini, M. Wild, and L. Bengtsson (2014), Cloud radiative forcing intercomparison between fully coupled CMIP5 models and CERES satellite data, *Ann. Geophys.*, *32*, 793–807, doi:10.5194/angeo-32-793-2014.

Carslaw, K. S., et al. (2013a), Large contribution of natural aerosols to uncertainty in indirect forcing, *Nature*, *503*, 67–71, doi:10.1038/nature12674.

Carslaw, K. S., L. A. Lee, C. L. Reddington, G. W. Mann, and K. J. Pringle (2013b), The magnitude of uncertainty in global aerosol, *Faraday Discuss.*, *165*, 495–512, doi:10.1039/C3FD00043E.

Edwards, J. M., and A. Slingo (1996), Studies with a flexible new radiation code: I. Choosing a configuration for a large scale model, *Q. J. R. Meteorol. Soc.*, *122*, 689–719, doi:10.1256/smsqj.53106.

Estrada, F., P. Perron, and B. Martínez-López (2013), Statistically derived contributions to diverse human influences to twentieth-century temperature change, *Nat. Geosci.*, *6*, 1050–1055, doi:10.1038/ngeo1999.

Fountoukis, C., and A. Nenes (2005), Continued development of a cloud droplet formation parameterization for global climate models, *J. Geophys. Res.*, *110*, D11212, doi:10.1029/2004JD005591.

Ghan, S. J., S. J. Smith, M. Wang, K. Zhang, K. J. Pringle, K. S. Carslaw, J. Pierce, S. Bauer, and P. Adams (2013), A simple model of global aerosol indirect effects, *J. Geophys. Res. Atmos.*, *118*, 6688–6707, doi:10.1002/jgrd.50567.

Granier, C., et al. (2011), Evolution of anthropogenic and biomass burning emissions of air pollutants at global and regional scales during the 1980–2010 period, *Clim. Change*, *109*, 163–190, doi:10.1007/s10584-011-0154-1.

Hartmann, D. L., et al. (2013), Observations: Atmosphere and surface, in *Climate Change 2013: The Physical Science Basis. Contribution of Working Group I to the Fifth Assessment Report of the Intergovernmental Panel on Climate Change*, edited by T. F. Stocker et al., p. 193, Cambridge Univ. Press, Cambridge, U. K., and New York.

Hawkins, E., and R. Sutton (2009), The potential to narrow uncertainty in regional climate predictions, *Bull. Am. Meteorol. Soc.*, *90*, 1097–1107, doi:10.1175/2009BAMS2607.1.

Haywood, J. M., A. Jones, and G. S. Jones (2013), The impact of volcanic eruptions in the period 2000–2013 on global mean temperature trends evaluated in the HadGEM2-ES climate model, *Atmos. Sci. Lett.*, *15*, 92–96, doi:10.1002/asl2.471.

Kaufmann, R., H. Kauppi, M. Mann, and J. Stock (2011), Reconciling anthropogenic climate change with observed temperature 1998–2008, *Proc. Natl. Acad. Sci. U.S.A.*, *108*, 11,790–11,793, doi:10.1073/pnas.1102467108.

Kirtman, B., et al. (2013), Near-term climate change: Projections and predictability, in *Climate Change 2013: The Physical Science Basis. Contribution of Working Group I to the Fifth Assessment Report of the Intergovernmental Panel on Climate Change*, edited by T. F. Stocker et al., pp. 1002–1007, Cambridge Univ. Press, Cambridge, U. K., and New York.

Kosaka, Y., and S. P. Xie (2013), Recent global-warming hiatus tied to equatorial Pacific surface cooling, *Nature*, *501*, 403–407, doi:10.1038/nature12534.

Lamarque, J. F., et al. (2010), Historical (1850–2000) gridded anthropogenic and biomass burning emissions of reactive gases and aerosols: Methodology and application, *Atmos. Chem. Phys.*, *10*, 7017–7039, doi:10.5194/acp-10-7017-2010.

Lee, L. A., K. S. Carslaw, K. J. Pringle, G. W. Mann, and D. V. Spracklen (2011), Emulation of a complex global aerosol model to quantify sensitivity to uncertain parameters, *Atmos. Chem. Phys.*, *11*, 12,253–12,273, doi:10.5194/acp-11-12253-2011.

Lee, L. A., K. S. Carslaw, K. J. Pringle, and G. W. Mann (2012), Mapping the uncertainty in global CCN using emulation, *Atmos. Chem. Phys.*, *12*, 9739–9751, doi:10.5194/acp-12-9739-2012.

Lee, L. A., K. J. Pringle, C. L. Reddington, G. W. Mann, P. Stier, D. V. Spracklen, J. Pierce, and K. S. Carslaw (2013), The magnitude and causes of uncertainty in global model simulations of cloud condensation nuclei, *Atmos. Chem. Phys.*, *13*, 8879–8914, doi:10.5194/acp-13-8879-2013.

Mann, G. W., K. S. Carslaw, D. V. Spracklen, D. A. Ridley, P. T. Manktelow, M. P. Chipperfield, S. J. Pickering, and C. E. Johnson (2010), Description and evaluation of GLOMAP-mode aerosol microphysics model for the UKCA composition-climate model, *Geosci. Model Dev.*, *3*, 519–551, doi:10.5194/gmd-3-519-2010.

Mann, G. W., et al. (2012), Intercomparison of modal and sectional aerosol microphysics representations within the same 3-D global chemical transport model, *Atmos. Chem. Phys.*, *12*, 4449–4476, doi:10.5194/acp-12-4449-2012.

Metzger, A., et al. (2010), Evidence for the role of organics in aerosol particle formation under atmospheric conditions, *Proc. Natl. Acad. Sci. U.S.A.*, *107*, 6646–6651, doi:10.1073/pnas.0911330107.

Myhre, G., et al. (2013), Anthropogenic and natural radiative forcing, in *Climate Change 2013: The Physical Science Basis. Contribution of Working Group I to the Fifth Assessment Report of the Intergovernmental Panel on Climate Change*, edited by T. F. Stocker et al., p. 677, Cambridge Univ. Press, Cambridge, U. K., and New York.

Oakley, J. E., and A. O'Hagan (2002), Bayesian inference for the uncertainty distribution of computer model outputs, *Biometrika*, *89*, 769–784, doi:10.1093/biomet/89.4.769.

Rossow, W. B., and R. A. Schiffer (1999), Advances in understanding clouds from ISCCP, *Bull. Am. Meteorol. Soc.*, *80*, 2261–2288, doi:10.1175/1520-0477(1999)080<2261:AIUCFI>2.0.CO;2.

Saltelli, A., S. Tarantola, and K. P. S. Chan (1999), A quantitative model-independent method for global sensitivity analysis of model output, *Technometrics*, *41*, 39–56, doi:10.2307/1270993.

Saltelli, A., K. Chan, and E. M. Scott (2000), *Sensitivity Analysis*, Wiley, Hoboken, N. J.

Santer, B. D., et al. (2014), Volcanic contribution to decadal changes in tropospheric temperature, *Nat. Geosci.*, *7*, 185–189, doi:10.1038/ngeo2098.

Schmidt, A., K. S. Carslaw, G. W. Mann, A. Rap, K. J. Pringle, D. V. Spracklen, M. Wilson, and P. M. Forster (2012), Importance of tropospheric volcanic aerosol for indirect radiative forcing of climate, *Atmos. Chem. Phys.*, *12*, 7321–7339, doi:10.5194/acp-12-7321-2012.

Schmidt, G. A., D. T. Shindell, and K. Tsigaridis (2014), Reconciling warming trends, *Nat. Geosci.*, *7*, 158–160, doi:10.1038/ngeo2105.

Shindell, D. T., et al. (2013), Radiative forcing in the ACCMIP historical and future climate simulations, *Atmos. Chem. Phys.*, *13*, 2939–2974, doi:10.5194/acp-13-2939-2013.

Skeie, R. B., T. K. Bernsten, G. Myhre, K. Tanaka, M. M. Kvalevàg, and C. R. Hoyle (2011), Anthropogenic radiative forcing time series from pre-industrial times until 2010, *Atmos. Chem. Phys.*, *11*, 11,827–11,857, doi:10.5194/acp-11-11827-2011.

Smith, S. J., and T. C. Bond (2014), Two hundred fifty years of aerosols and climate: The end of the age of aerosols, *Atmos. Chem. Phys.*, *14*, 537–549, doi:10.5194/acp-14-537-2014.

Smith, S. J., J. van Aardenne, Z. Klimont, R. J. Andres, A. Volke, and S. D. Arias (2011), Anthropogenic sulfur dioxide emissions: 1850 to 2005, *Atmos. Chem. Phys.*, *11*, 1101–1116, doi:10.5194/acp-11-1101-2011.

Solomon, S., D. Qin, M. Manning, Z. Chen, M. Marquis, K. B. Averyt, M. Tignor, and H. L. Miller (Eds.) (2007), *IPCC, 2007: The Physical Science Basis. Contribution of Working Group I to the Fourth Assessment Report of the Intergovernmental Panel on Climate Change*, Cambridge Univ. Press, Cambridge, U. K., and New York.

Spracklen, D. V., K. J. Pringle, K. S. Carslaw, M. P. Chipperfield, and G. W. Mann (2005), A global off-line model of size-resolved aerosol microphysics: I. Model development and prediction of aerosol properties, *Atmos. Chem. Phys.*, *5*, 2227–2252.

50

Stocker, T. F., D. Qin, G. K. Plattner, M. Tignor, S. K. Allen, J. Boschung, A. Nauels, Y. Xia, V. Bex, and P. M. Midgley (2013), Summary for policymakers, in *Climate Change 2013: The Physical Science Basis. Contribution of Working Group I to the Fifth Assessment Report of the Intergovernmental Panel on Climate Change*, edited by T. F. Stocker et al., pp. 13–14, Cambridge Univ. Press, Cambridge, U. K., and New York.

Stockwell, D. Z., and M. P. Chipperfield (1999), A tropospheric chemical-transport model: Development and validation of the model transport schemes, *Q. J. R. Meteorol. Soc.*, *125*, 1747–1783, doi:10.1256/smsqj.55713.

Taylor, K. E., R. J. Stouffer, and G. A. Meehl (2012), An overview of CMIP5 and the experiment design, *Bull. Am. Meteorol. Soc.*, *93*, 485–498, doi:10.1175/BAMS-D-11-00094.1.

Twomey, S. (1977), Influence of pollution on shortwave albedo of clouds, *J. Atmos. Sci.*, *34*, 1149–1152.

van Vuuren, D. P., et al. (2011), The representative concentration pathways: An overview, *Clim. Change*, *109*, 5–31, doi:10.1007/s10584-011-0148-z.

Wilcox, L. J., E. J. Highwood, and N. J. Dunstone (2013), The influence of anthropogenic aerosol on multi-decadal variations of historical global climate, *Environ. Res. Lett.*, *8*, 024033, doi:10.1088/1748-9326/8/2/024033.

Chapter 4

The climatic importance of uncertainties in regional aerosol-cloud radiative forcing over recent decades

The Climatic Importance of Uncertainties in Regional Aerosol–Cloud Radiative Forcings over Recent Decades

LEIGHTON A. REGAYRE, KIRSTY J. PRINGLE, LINDSAY A. LEE, ALEXANDRU RAP, JO BROWSE, GRAHAM W. MANN,* CARLY L. REDDINGTON, AND KEN S. CARSLAW

Institute for Climate and Atmospheric Science, School of Earth and Environment, University of Leeds, Leeds, United Kingdom

BEN B. B. BOOTH

Met Office Hadley Centre for Climate Change, Exeter, United Kingdom

MATTHEW T. WOODHOUSE

CSIRO Oceans and Atmosphere, Aspendale, Victoria, Australia

(Manuscript received 10 February 2015, in final form 1 May 2015)

ABSTRACT

Regional patterns of aerosol radiative forcing are important for understanding climate change on decadal time scales. Uncertainty in aerosol forcing is likely to vary regionally and seasonally because of the short aerosol lifetime and heterogeneous emissions. Here the sensitivity of regional aerosol cloud albedo effect (CAE) forcing to 31 aerosol process parameters and emission fluxes is quantified between 1978 and 2008. The effects of parametric uncertainties on calculations of the balance of incoming and outgoing radiation are found to be spatially and temporally dependent. Regional uncertainty contributions of opposite sign cancel in global-mean forcing calculations, masking the regional importance of some parameters. Parameters that contribute little to uncertainty in Earth's global energy balance during recent decades make significant contributions to regional forcing variance. Aerosol forcing sensitivities are quantified within 11 climatically important regions, where surface temperatures are thought to influence large-scale climate effects. Substantial simulated uncertainty in CAE forcing in the eastern Pacific leaves open the possibility that apparent shifts in the mean ENSO state may result from a forced aerosol signal on multidecadal time scales. A likely negative aerosol CAE forcing in the tropical North Atlantic calls into question the relationship between Northern Hemisphere aerosol emission reductions and CAE forcing of sea surface temperatures in the main Atlantic hurricane development region on decadal time scales. Simulated CAE forcing uncertainty is large in the North Pacific, suggesting that the role of the CAE in altering Pacific tropical storm frequency and intensity is also highly uncertain.

1. Introduction

Aerosols affect Earth's climate by absorbing and scattering solar and terrestrial radiation (Twomey 1977; Boucher et al. 2013). The cloud albedo effect (CAE) (Boucher et al. 2013), characterized by a decrease in cloud drop effective radius that results from an increase in cloud droplet number concentration for a given amount of liquid water (Twomey 1977), is the largest component of the aerosol–cloud interaction. Uncertainty in the magnitude of CAE forcing remains the dominant source of uncertainty in net aerosol radiative forcing within current global climate models (Skeie et al. 2011; IPCC 2013).

Anthropogenic aerosol emission fluxes and aerosol process parameters were identified by Regayre et al. (2014) as the largest sources of simulated global-mean

Denotes Open Access content.

* Current affiliation: National Centre for Atmospheric Science, University of Leeds, Leeds, United Kingdom.

Corresponding author address: Leighton A. Regayre, Institute for Climate and Atmospheric Science, School of Earth and Environment, University of Leeds, Leeds, LS2 9JT, United Kingdom.
E-mail: laregayre11@leeds.ac.uk

DOI: 10.1175/JCLI-D-15-0127.1

CAE forcing variance in recent decades; however, credible ranges of global-mean CAE forcing were found to be small compared to the magnitude of forcing resulting from changes in atmospheric CO_2 concentrations. Regayre et al. (2014) hypothesized that a large component of multimodel CAE forcing diversity during recent decades is determined by the extent to which regional positive and negative forcings cancel in individual models when calculating global-mean CAE forcing.

The magnitude of large-scale climatic responses, such as global-mean surface temperature, are sensitive to the spatial position of regional forcings (Shindell et al. 2013), making it important to understand CAE forcing at the regional scale. In this paper we aim to identify the aerosol process parameters and emission fluxes, hereafter referred to as parameters, which are the largest sources of regional-mean CAE forcing variance and also have potential to be influential on global-mean forcing in near-future climates.

We compare the Regayre et al. (2014) global-mean CAE forcing results with an analysis that accounts for cancellation of positive and negative regional forcings. The CAE forcing sensitivity to the 31 aerosol parameters is quantified within 11 regions where CAE forcing potentially influences large-scale climate effects such as monsoon intensity, tropical storm development, and precipitation. The statistical analyses conducted here highlight aspects of aerosol research and model development that should be prioritized in order to reduce the impact of uncertainty in regional CAE forcings on near-term climate projections.

2. Methods

a. Perturbed parameter ensemble

The Global Model of Aerosol Processes (GLOMAP) (Spracklen et al. 2005; Mann et al. 2010, 2012) was used by Regayre et al. (2014) to create the perturbed parameter ensemble used in this research. Each ensemble member has a horizontal resolution of 2.8° × 2.8° with 31 vertical levels between the surface and 10 hPa. GLOMAP is an extension of the TOMCAT chemical transport model (Stockwell and Chipperfield 1999). To create each ensemble member, 31 aerosol process parameters and emission fluxes were perturbed simultaneously. Maximin Latin hypercube sampling was used to create a parameter combination design, of 186 points, that spans the 31-dimensional uncertain parameter space. The probability distributions for the uncertain parameters used in Regayre et al. (2014) were identified through expert elicitation updated from Lee et al. (2013). A further simulation with all parameters set to their median values was included in the ensemble to ensure coverage of what experts believed to be an important region of parameter space.

In the version of the GLOMAP model used to create the ensemble, three-dimensional meteorological fields and cloud distributions for all years were obtained from the European Centre for Medium-Range Weather Forecasts (ECMWF) interim reanalysis (ERA-Interim) for 2008. Low-level stratiform clouds were prescribed from the International Satellite Cloud Climatology Project (ISCCP) D2 data (Rossow and Schiffer 1999). Modeled aerosols are affected by cloud processing and precipitation, although changes in modeled aerosols do not affect the meteorology, transport, or presence of cloud. Emission scenarios prepared for the Atmospheric Chemistry and Climate Model Intercomparison Project (ACCMIP) (Lamarque et al. 2010) and prescribed in some of the experiments from phase 5 of the Coupled Model Intercomparison Project (CMIP5) (Taylor et al. 2012) were used to prescribe anthropogenic aerosol emissions in these simulations. The experimental design is such that parameter perturbations are the sole cause of changes in simulated CAE forcing for each ensemble member.

Pairs of 1-yr simulations were used to calculate monthly and annual-mean CAE forcing. Identical model configurations were used for each pair of simulations with the exception of anthropogenic aerosol emissions, which were prescribed distinctly for each year. The definition of CAE forcing used here is identical to that of Carslaw et al. (2013) and Regayre et al. (2014), where it is regarded as the difference in top-of-atmosphere net radiative fluxes between years. CAE forcing values are calculated by modifying the cloud drop effective radius r_e for low- and midlevel clouds up to 6×10^2 hPa, within the offline version of the Edwards and Slingo (1996) radiative transfer model. Because year-2000 values of surface albedo and cloud optical depths from ISCCP D2 were used, r_e was modified relative to values derived for that year, denoted here using the superscript ref:

$$r_e = r_e^{\mathrm{ref}} \left(\frac{\mathrm{CDNC}^{\mathrm{ref}}}{\mathrm{CDNC}} \right)^{1/3}, \tag{1}$$

where CDNC is the monthly mean cloud drop number concentration within each model grid box. A cloud droplet activation parameterization (Fountoukis and Nenes 2005; Barahona et al. 2010) was used to calculate CDNC for each ensemble member in each model grid box using the monthly mean aerosol distribution and composition. A fixed value of $r_e^{\mathrm{ref}} = 10\,\mu$m was used to

ensure consistency with the ISCCP retrievals. CAE forcing over the 1978–2008 period was taken as the difference between forcings for each year relative to the year 2000. Regayre et al. (2014) show that the net cloud radiative effect from the year-2000 reference simulation is in agreement with CMIP model output (Calisto et al. 2014).

b. Sensitivity analysis

A sensitivity analysis (Saltelli et al. 2000; Lee et al. 2013) of CAE forcing in each model grid box is made possible using validated Bayesian emulators (O'Hagan 2006) that are conditioned on output from the 187 perturbed parameter simulations. The emulator of each model grid box provides a statistical approximation of CAE forcing at any point in the 31-dimensional parameter space. A further emulator is constructed using global-mean absolute CAE forcing, where the absolute value of CAE forcing for each model grid box is used in the calculation of the global mean to remove the effect of canceling regional forcings of opposing sign. This approach allows us to use a single global value to quantify the importance of individual parameters, even if changes in the parameter cause positive and negative forcings that cancel in the global-mean calculation.

The Bayesian emulation approach has been successfully applied to GLOMAP model output by Lee et al. (2011, 2012, 2013), Carslaw et al. (2013), Hamilton et al. (2014), and Regayre et al. (2014). Contributions to variance from each parameter and statistical interactions between parameters can be explicitly quantified across the multidimensional response surface. This is made possible because the emulators produce output in a fraction of the time required to produce a simulation. Large samples of output can therefore be obtained and used to produce probability distributions. The extended Fourier amplitude sensitivity test (FAST) sampling method (Saltelli et al. 1999), with 10^4 emulator sample points, was used here to obtain the data for each Monte Carlo–style sensitivity analysis.

The results of the global-mean absolute CAE forcing sensitivity analyses are contrasted with the results of the global CAE forcing sensitivity analysis of Regayre et al. (2014) in section 3a. Regional sensitivity analysis results and their climatic importance are discussed in section 3b. Here the sensitivity analysis is conducted using monthly, rather than annual, mean CAE forcing to avoid cancellation of forcings of opposite sign in different months or seasons. The statistic considered most in the discussion of these results is the percentage reduction in monthly mean CAE forcing variance that could be expected if the parameter in question were known exactly. Mean regional contributions to forcing are obtained for each month by weighting contributions to CAE forcing variance within each model grid box by the proportion of total regional forcing evident within that grid box. The CAE forcing uncertainty within regions is quantified using mean 90% credible intervals (CIs) of CAE forcing. The means of the 5th and 95th percentiles within each model grid box are used to calculate mean CIs. Regional-mean forcings and CIs are calculated using only the months where CAE forcing has been identified as climatically important, as summarized in section 2d.

c. Time period

The ensemble of 187 paired perturbed parameter simulations for the period 1978–2008 used by Regayre et al. (2014) to analyze global CAE forcing uncertainty is used here to analyze regional CAE forcing uncertainty. The 1978–2008 period produces distinct regions of positive and negative CAE forcing that result from spatial heterogeneity in the long-term trends of anthropogenic emissions. In 1978, global anthropogenic sulfate emissions peaked (Lamarque et al. 2010) then decreased in Europe and North America while increasing significantly in Asia (Smith et al. 2011). Current satellite observations reveal a persistence of these regional trends in anthropogenic emissions (Mao et al. 2014), and simulations suggest that peak regional aerosol forcing from Asian anthropogenic emissions relative to the preindustrial era may not be reached for several decades (Li et al. 2014), indicating that a sensitivity analysis of 1978–2008 CAE forcing will be informative about near-future climate uncertainties. A time series of global CAE forcing relative to the year 1850, constructed using simulations where all parameters were set to their median values, is presented in Fig. 1. The global-mean CAE forcing trend plateaus in the 1980s, making the change in forcing relative to 1850 near neutral during the 1978–2008 period.

d. Large-scale climate effects

Global models initialized with prescribed SSTs based on observations show enhanced interannual predictability of regional temperatures and precipitation (Hermanson and Sutton 2010; Robson et al. 2013). Confident prediction of large-scale climate effects relies on well-simulated SST, which in turn requires the reliable simulation of the CAE. Changing anthropogenic aerosol emissions have the potential to induce aerosol-specific changes in regional atmospheric circulation and precipitation (Kirtman et al. 2013).

Large regional uncertainties in CAE forcing will strongly influence SST and thus hinder the accurate simulation of climate effects, which affect much of

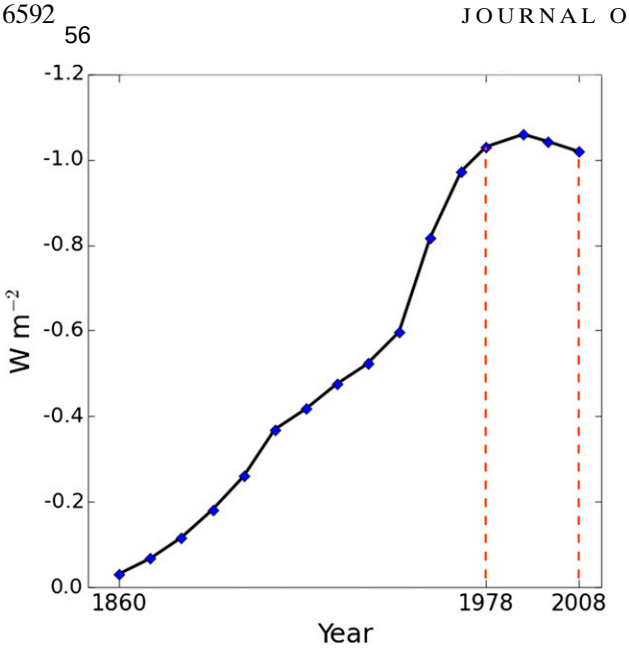

FIG. 1. Global-mean CAE forcing relative to 1850 (W m^{-2}). Simulations with all parameters in the Regayre et al. (2014) design set to their median values were used to calculate the global-mean CAE forcing values.

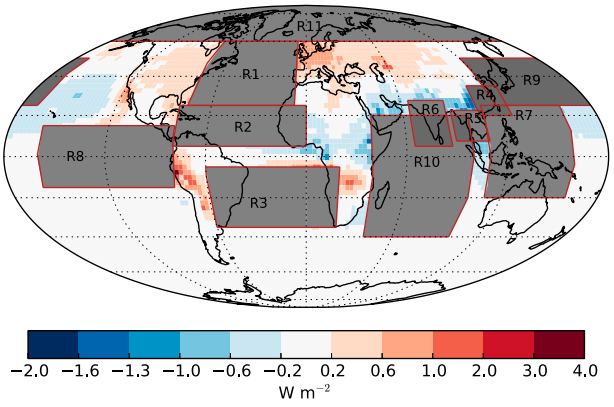

FIG. 2. Regions of climatic importance, as summarized in Table 1, overlaid onto annual-mean CAE forcing for the 1978–2008 period, taken from the simulation where all aerosol process parameters and emission fluxes are set to their median elicited values.

Earth's population. Table 1 and Fig. 2 indicate the location of the 11 regions (R1–R11) used in the regional component of this research. Regions were chosen based on the potential for changes in SST and/or surface air temperature (SAT) to influence large-scale climatic effects. The regional CAE forcing sensitivity analyses presented in section 3b are individually restricted to either marine or continental land environments. External forcings in tropical regions are more likely to induce a global temperature response than polar forcings (Roe et al. 2015). However, it is assumed that reducing uncertainty in the simulation of the climate effects outlined in this section, by reducing uncertainty in CAE forcing, will improve near-future climate projections.

1) INTERTROPICAL CONVERGENCE ZONE AND SAHEL PRECIPITATION

Ascending air near the equator is advected poleward and descends in the subtropical dry zones forming the Hadley cell. The structure of the Hadley cell determines the position of subtropical dry zones, which are important for Earth's hydrological cycle and energy balance (Seidel et al. 2008). Observational evidence suggests that the Hadley cell has widened in recent decades (Allen et al. 2012; Choi et al. 2014), which cannot be explained by greenhouse gas–induced warming (Lu et al. 2007). The width and position of the ITCZ, within which the ascending air that contributes to the Hadley cell resides, plays an important role in determining the structure of the Hadley cell (Kang and Lu 2012).

TABLE 1. Latitude and longitude ranges used to define regions where CAE forcing is known to influence SST and therefore has the potential to indirectly influence climate effects. The months indicate when SST has the greatest influence on climatic effects.

Key	Location	Lat range	Lon range	Climate effect	Relevant months
R1	Extratropical North Atlantic	25°–60°N	7°–75°W	North Atlantic tropical storms	Apr–Oct
				Sahel precipitation	All year
R2	Tropical North Atlantic	5°–25°N	0°–80°W	North Atlantic tropical storms	Apr–Oct
				Atlantic ITCZ and Sahel precipitation	All year
R3	Tropical South Atlantic	5°–35°S	60°W–20°E	Atlantic ITCZ and Sahel precipitation	All year
R4	East China	20°–35°N	107.5°–125°E	Asian summer monsoon	Jun–Sep
R5	Southeast Asia	7.5°–22.5°N	90°–107.5°E	Asian summer monsoon	Jun–Sep
R6	Indian subcontinent	5°–27.5°N	65°–87.5°E	Asian summer monsoon	Jun–Sep
R7	Western Pacific	20°S–25°N	107.5°–160°E	Asian summer monsoon	Jun–Sep
R8	Tropical eastern Pacific	15°S–15°N	160°–80°W	ENSO	Oct–Feb
R9	Northwestern Pacific	25°–50°N	120°E–170°W	Pacific tropical storms	Jan–Jul
R10	Indian Ocean	40°S–20°N	40°–100°E	Asian summer monsoon	Jun–Sep
R11	Arctic	60°–90°N	All lon	Arctic warming	May–Sep

The gradient in interhemispheric tropical SSTs determines the position and width of the Atlantic ITCZ (Chang et al. 2011; Cvijanovic and Chiang 2013), which affects precipitation patterns in neighboring regions (Zhang et al. 2007; Hwang et al. 2013). Anomalously cold North Atlantic SSTs relative to SSTs in the South Atlantic are correlated with a southward shift in ITCZ position and with periods of drought in the Sahel over the last century (Folland et al. 1986; Mulitza et al. 2008; Shanahan et al. 2009). A strong contrast between tropical and extratropical North Atlantic SSTs is found by Liu et al. (2014) to be an integral component of the teleconnection that allows SSTs to influence precipitation in neighboring regions. Anthropogenic aerosol emissions have prevented North Atlantic SST from warming as rapidly as South Atlantic SST in response to increasing greenhouse gas concentrations over the last century (Rotstayn and Lohmann 2002), yet since the late 1970s the gradient between Atlantic Ocean basins has declined as a result of anthropogenic aerosol emission reduction strategies in the Northern Hemisphere (Chang et al. 2011; Chiang et al. 2013; Friedman et al. 2013).

Booth et al. (2012) argue that aerosol forcing may decouple North Atlantic SSTs from Atlantic meridional overturning circulation (AMOC)-driven changes, suggesting that changing aerosol concentrations since the preindustrial period may be the dominant influence on SSTs. The relative importance of anthropogenic aerosols and the AMOC in determining North Atlantic SSTs remains unknown (Zhang et al. 2013); however, Dunstone et al. (2013, Fig. S8 in their supplementary information) revealed a correlation between the magnitude of CAE forcing in models and the degree to which CAE forcing determines Atlantic SSTs. Exploring the sources of uncertainty in CAE forcing in the Atlantic will therefore inform the possible sources of multimodel SST diversity.

2) TROPICAL STORM DEVELOPMENT REGIONS

Tropical storms have the potential to cause considerable socioeconomic damage (Pielke et al. 2008), and thus there is value in reducing uncertainty in the simulation of near-future events. Climate model simulations that make use of observed North Atlantic SSTs are capable of reproducing tropical storm frequency variance (Trenberth and Shea 2006; Zhao and Held 2012), and anthropogenic aerosols have been implicated as causing decadal changes in North Atlantic SSTs (Mann and Emanuel 2006; Evan et al. 2009; Dunstone et al. 2013). Evidence suggests that uncertainty in near-future tropical storm frequency can be reduced by improving the representation of aerosol radiative forcing within models (Villarini and Vecchi 2013).

Tropical storm development in the North Atlantic is influenced by SSTs in regions that also influence ITCZ position and Sahel precipitation as described in section 2d(1), compounding the importance of quantifying CAE forcing uncertainty in these regions. Pacific Ocean SSTs are also affected by changes in anthropogenic aerosol emissions (Boo et al. 2015), particularly from Asia (Yeh et al. 2013). The metrics used to determine the phase of the Pacific decadal oscillation and the width of the tropical storm belt contain large uncertainties that are associated with anthropogenic aerosol forcing (Allen et al. 2014). Changing atmospheric temperatures and SSTs in the northwestern Pacific in response to increasing Asian anthropogenic aerosol emissions are a likely cause of increased Pacific tropical storm frequency and intensity in recent decades, according to Wang et al. (2014a,b).

3) ASIAN SUMMER MONSOON

The Asian summer monsoon (ASM) is characterized by heavy rainfall across much of the Asian continent, providing as much as 70% of the annual rainfall to some Asian regions over the summer months (Gong and Ho 2003). The intensity of contrast between SST and continental SAT is correlated with the strength of the ASM (Webster 1987), and in recent decades a weakening of the land–sea contrast, largely attributable to anthropogenic aerosol emissions, has to a large extent counteracted the intensification of the ASM expected to result from the positive forcing associated with increasing atmospheric greenhouse gas (GHG) concentrations (Wang et al. 2013; Guo et al. 2013; Salzmann et al. 2014). Observational evidence suggests that a greater proportion of ASM precipitation occurs over southern China than in the north as a result of a weaker ASM (Ding et al. 2008; Ye et al. 2013), with flood risks and increased air pollution likely outcomes (Li et al. 2011).

Substantial anthropogenic sulfate aerosol concentrations are transported from Asian continents over the Indian Ocean during the early part of each year (Verma et al. 2013), and Fadnavis et al. (2013) established that ASM precipitation over India declines in response to anthropogenic emissions. The CAE significantly affects SST in the Indian Ocean (Yun et al. 2014), largely countering the positive CO_2 forcing in this region since the early industrial period (Dong and Zhou 2014). CAE forcing is therefore partially responsible for the early onset of the ASM resulting in heavy precipitation over the Indian subcontinent at the start of the monsoon season and reduced precipitation during the remainder of the Northern Hemisphere summer (Bollasina et al. 2013; Henriksson et al. 2014).

4) EL NIÑO–SOUTHERN OSCILLATION

Aside from the seasonal cycle, the El Niño–Southern Oscillation (ENSO) is the largest mode of climate variability (Diaz et al. 2001; McPhaden et al. 2006). The El Niño phase of the ENSO results in anomalously warm SSTs in the eastern equatorial Pacific accompanying a reversal of trade winds and a slowing down of circulation within the Pacific basin (Rasmusson and Carpenter 1982).

The magnitude of aerosol forcing and its uncertainty in the region where the dominant ENSO signal manifests are considered in this paper because, although there are no established links between CAE forcing and ENSO variability, aerosols appear to project strongly onto SSTs on multidecadal time scales (Shindell et al. 2013; Regayre et al. 2014). Changes in mean SSTs interpreted as a shift toward a more El Niño or La Niña state may in fact reflect changes due to local forcing. Quantifying the uncertainty in CAE forcing in these regions will establish the potential for shifts in the ENSO mean state on decadal time scales to be a result of a forced aerosol signal.

5) ARCTIC

The Arctic region has experienced anomalous warming compared to the rest of Earth's surface over recent decades (Serreze et al. 2009). Much of the warming in the Arctic is attributable to the ice–albedo feedback (Screen and Simmonds 2010), where melt pools reduce the albedo of the surface, allowing for greater warming. Gillett et al. (2008) identify anthropogenic emissions as playing an essential role in warming the Arctic in recent decades. Decreasing anthropogenic aerosol concentrations transported to the Arctic from North America and Europe generate a positive CAE forcing, which has been shown to be a major cause of the observed warming (Shindell and Faluvegi 2009; Chylek et al. 2014).

e. Regional aerosol radiative forcing

The effect of each parameter perturbation on the 1978–2008 CAE forcing at each location depends on the relative changes in aerosol distributions (and hence CDNCs) in the two years. CAE forcing depends nonlinearly on CDNC changes and is more sensitive when CDNCs are low (Carslaw et al. 2013). Furthermore, the effect of aerosol parameter perturbations on forcing must be interpreted in the context of the sign of regional CAE forcing.

Six representative scenarios (S1–S6) are depicted in Fig. 3 to assist with interpreting the effect of changing CDNCs through aerosol parameter perturbations on

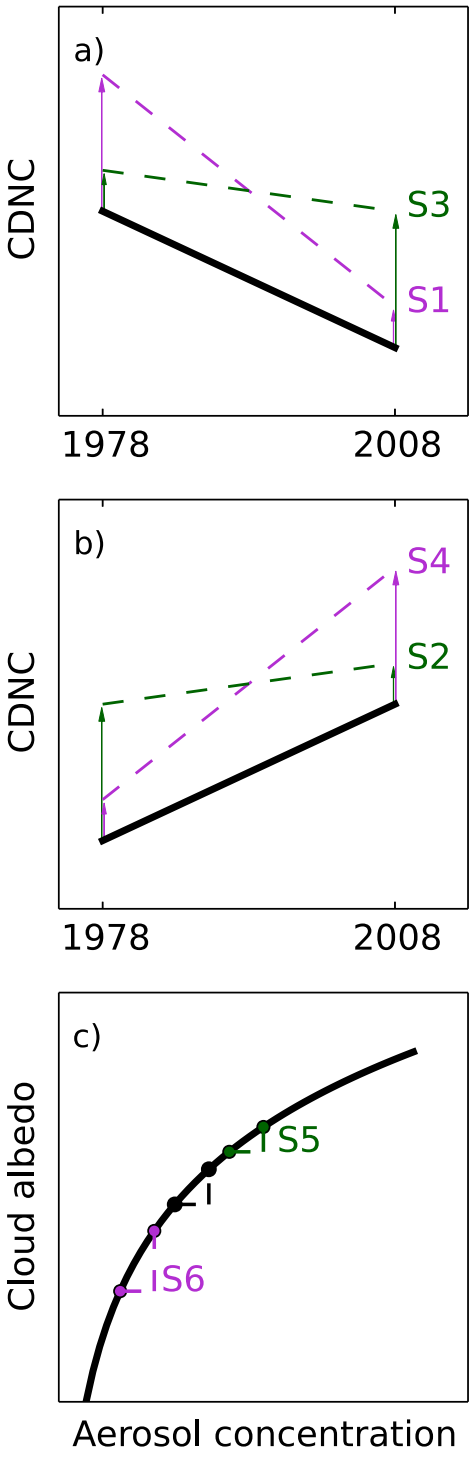

FIG. 3. Theoretical effects of perturbing parameters on (a) declining CDNC (positive CAE forcing), (b) increasing CDNC (negative CAE forcing), and (c) albedo between 1978 and 2008. Black lines represent the baseline case with no parameter perturbations. Six scenarios representing perturbed parameter cases are labeled S1–S6. Purple indicates an amplification and green indicates a suppression of CAE forcing regardless of the sign of the underlying forcing within an individual model grid box.

CAE forcing. Amplification of positive and negative CAE forcing (steeper gradient) occurs in scenarios S1 and S4, respectively, as a result of changing a parameter. In S1 the change in CDNC is largest in 1978, thereby strengthening the positive CAE forcing between 1978 and 2008 (caused by a larger net decrease in CDNC than in the baseline case). In S4 the change in CDNC is largest in 2008, thereby strengthening the negative forcing. In scenarios S2 and S3 the relative changes in CDNCs in 1978 and 2008 are identical to the changes in S1 and S4, respectively; however, the sign of forcing is reversed, and therefore in these cases the parameter perturbation causes a suppression of the CAE forcing (making the slope of the line in the perturbed case shallower than the line in the baseline case).

Absolute changes in CDNCs within a given model grid box, resulting from a parameter perturbation, may be the same in the two simulated years, but because of the nonlinear relationship between aerosol concentration and albedo (Fig. 3c) a forcing will still occur. The importance of the baseline aerosol concentration in radiative forcing calculations is discussed in Carslaw et al. (2013). A more polluted baseline is associated with a smaller temporal change in albedo; hence, scenario S5 represents a decrease in CAE forcing (relative to the baseline case) resulting from an increase in aerosol concentrations in both years. Scenario S6 represents the case where a parameter perturbation causes CDNCs in both years to decrease (relative to the baseline case), leading to a greater difference in albedo between the two years and therefore stronger CAE forcing.

Scenarios S1–S4 are all based on the assumption that CDNC increases in a region in both years as a result of the parameter perturbation. Mirror images of scenarios S1–S4 where CDNCs decrease are not shown, nor are more extreme cases where CDNCs increase in one year and decrease in the other; however, scenarios S1–S4 provide a suitable framework for examining the cancellation of regional contributions to global-mean CAE forcing variance.

3. Results

a. Global forcing sensitivities

Because contributions of opposing signs cancel, parameter perturbations that act to enhance CAE forcing in regions of both positive and negative forcing could make significant contributions to regional CAE forcing variance that are not detected in a sensitivity analysis of global-mean CAE forcing variance. Regions of substantial positive and negative forcing are evident in each of the maps in Fig. 4. Similarly, a parameter perturbation that acts to suppress CAE forcing (as described by scenarios S2 and S3) will make contributions to both positive and negative regional forcing that cancel in a global forcing calculation, whereas a parameter perturbation that acts to amplify positive regional forcings (S1) and conversely suppress negative regional forcings (S2) will not have its contribution to global-mean CAE forcing variance affected by regional forcing cancellation.

The percentage contributions to global-mean CAE forcing and global-mean absolute CAE forcing, calculated between 1978 and 2008 as described in section 2b, are compared in Fig. 5. There is no correlation evident between the global-mean forcing and global-mean absolute forcing measures. No parameter contributes more than 10% of the CAE forcing variance in both cases, suggesting that substantial cancellation of important regional contributions to global-mean CAE forcing occurs.

Contributions to CAE forcing in individual model grid boxes are presented in Fig. 6 for two parameters that contribute a substantial percentage of variance in either global-mean CAE forcing or global-mean absolute CAE forcing. The spatial pattern of CAE forcing sensitivities to parameter perturbations varies temporally, and the months displayed in Fig. 6 are representative of months where the parameters in question contribute substantially to CAE forcing variance. Only percentage contributions to variance in model grid boxes where the absolute ensemble-mean CAE forcing is greater than $0.1\,\mathrm{W\,m^{-2}}$ have been plotted (shaded purple where an increase in the value of the parameter acts to amplify CAE forcing and shaded green where forcing is suppressed, matching the shading used in Fig. 3). The spatial patterns of contributions to variance need to be analyzed in the context of the underlying spatial pattern of CAE forcing represented in Fig. 4 in order to understand the global-mean effect of perturbing a parameter.

The emission flux of organic carbon and black carbon aerosols from fossil fuel sources (FF_Ems) and the diameter of emitted particles (FF_Diam) are the largest sources of global-mean CAE forcing uncertainty (Fig. 5). Contributions to CAE forcing variance from FF_Ems for May are presented in Fig. 6a. Increasing FF_Ems typically amplifies negative CAE forcing in regions where CDNCs have increased between 1978 and 2008 (S4) yet suppresses positive CAE forcing in regions where CDNCs have declined (S3). Fossil fuel emissions are a large component of the increase in Asian CDNC, and positively perturbing FF_Ems amplifies the negative CAE forcing in this region (S4). In contrast, the positive forcing is suppressed (S3) in regions where the decrease in CDNC is not driven by carbonaceous

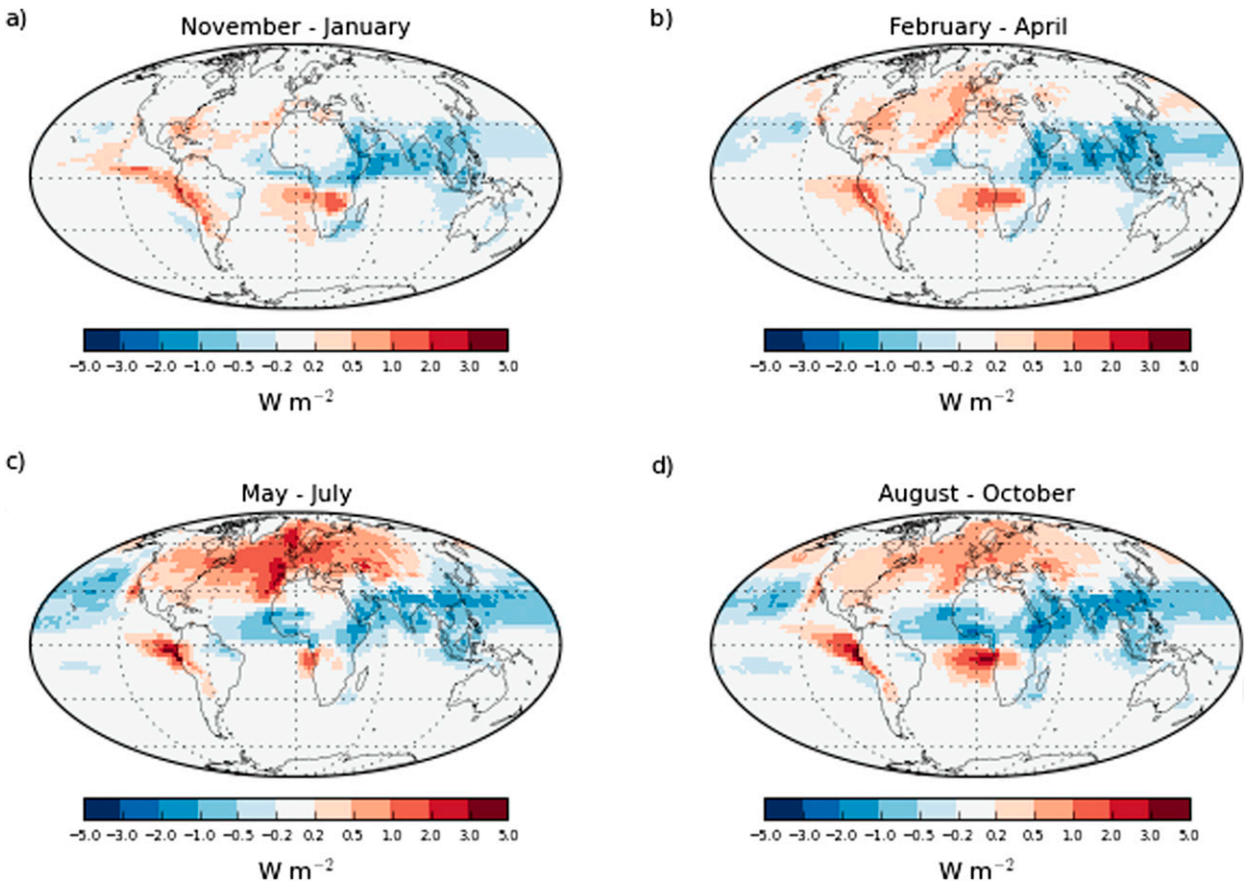

FIG. 4. Ensemble-mean CAE forcing within individual model grid boxes for (a) November–January, (b) February–April, (c) May–July, and (d) August–October during the 1978–2008 period.

aerosol emissions from fossil fuel sources (Lamarque et al. 2010; Granier et al. 2011), such as North America, because the relatively low 2008 CDNCs are more sensitive to positive FF_Ems perturbations than the higher 1978 CDNCs (S5).

Perturbing FF_Ems produces a shift in CAE forcing in the same direction for both positive and negative forcing regions. Therefore, when forcing is amplified (suppressed) in a positive forcing region, it is suppressed (amplified) in a region of negative forcing. Increasing FF_Diam produces an inverse pattern of forcing response to increasing FF_Ems because increases in the size of emitted particles reduce their number concentration (for a fixed value of FF_Ems). The globally consistent sign of forcing response to parameter perturbations makes fossil fuel emission parameters the dominant sources of global-mean CAE forcing variance, despite making relatively small percentage contributions to regional forcing variance. The decline in importance of fossil fuel emission parameters as sources of global-mean CAE forcing uncertainty when adjusted for the cancellation of positive and negative regional forcings (Fig. 5), suggests that other parameters make far larger regionally important contributions to uncertainty in CAE forcing.

The pattern of contributions to variance for the emission flux of SO_2 aerosols from continuously degassing and sporadically erupting volcanoes (Volc_SO2; Fig. 6b) contrasts with the FF_Diam pattern. Increasing Volc_SO2 in regions where it contributes to CAE forcing variance suppresses the magnitude of both positive and negative forcing, simply because the volcanic aerosol raises the natural background CDNC against which anthropogenic forcing is defined (S5). Volc_SO2 makes its largest contribution to variance in regions of relatively low aerosol concentrations (Schmidt et al. 2012); however, in some regions aerosol concentrations are lowest in 1978 and in other regions in 2008. The cancellation of positive and negative regional forcings in global CAE forcing calculations masks the importance of Volc_SO2 as a source of aerosol forcing uncertainty. The lower importance of this natural emission parameter to the uncertainty in recent decadal forcing (Regayre et al. 2014) versus forcing since the preindustrial era (Carslaw et al. 2013) is mostly related to regional cancellation in the Regayre et al. (2014) study.

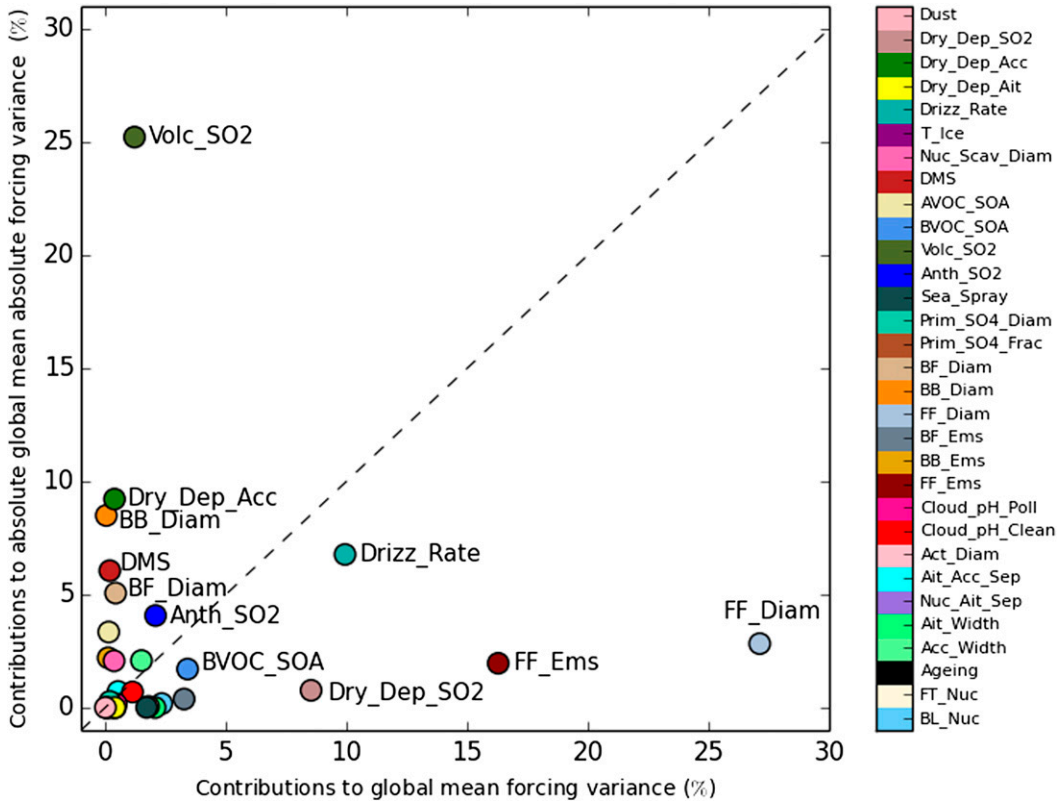

FIG. 5. Global-mean CAE forcing and global-mean absolute CAE forcing percentage contributions to variance for each aerosol parameter. The dashed diagonal line is the 1:1 line.

b. *Regional forcing sensitivities*

A sensitivity analysis that quantifies contributions to CAE forcing variance from aerosol parameters is conducted here for each of the regions identified as being influential on the climate effects outlined in section 2d. Figures 7–9 summarize the mean regional percentage contributions to variance during the 1978–2008 period. Regional-mean forcings and mean 90% CIs (calculated as outlined in section 2b for months where SSTs are

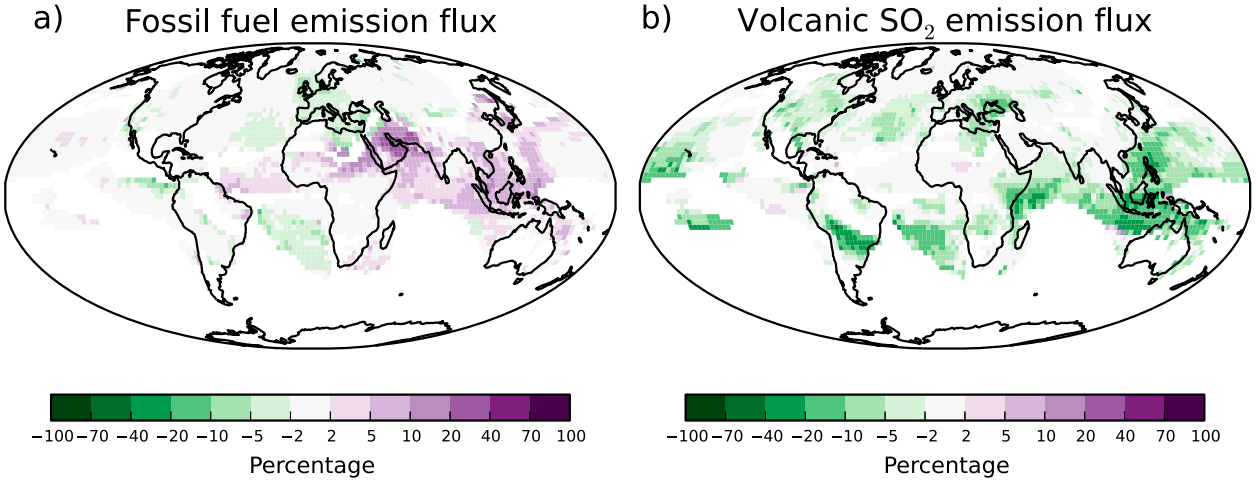

FIG. 6. Percentage contributions to CAE forcing variance for (a) fossil fuel emission flux in May and (b) continuously degassing and sporadically erupting volcanic SO_2 emission flux in June. Purple shading is used to indicate that increasing the parameter amplifies CAE forcing (positive or negative) within individual model grid boxes, and green shading indicates that increasing the parameter suppresses CAE forcing.

climatically important) are summarized in Table 2. While the global-mean simulated CAE forcing is a small fraction of the forcing caused by changes in anthropogenic CO_2 emissions (Regayre et al. 2014), Fig. 10 illustrates that in many climatically important regions the uncertainty in CAE forcing, arising from uncertainty in aerosol emissions and process parameters, is at least as important as forcing arising from changing CO_2 emissions during this period. Very similar spatial response patterns result when the Myhre et al. (2013) global-mean value of $0.7\,W\,m^{-2}$ is used to represent the forcing caused by changes in anthropogenic CO_2 emissions in the ratio calculation.

1) Intertropical convergence zone and Sahel precipitation

A negative mean CAE forcing in the tropical North Atlantic (R2) of $-0.05\,W\,m^{-2}$ contrasts with the positive forcing of $0.25\,W\,m^{-2}$ in the tropical South Atlantic (R3). On their own these results suggest that CAE forcing has exacerbated the interhemispheric differences in SSTs in recent decades. The mean CAE forcing in the extratropical North Atlantic (R1) is $0.51\,W\,m^{-2}$, which is the largest annual-mean forcing of the regions examined here. Sources of CAE forcing uncertainty are examined in each Atlantic region (R1–R3) with regard to their potential influence on uncertainty in ITCZ position and Sahel precipitation.

Uncertainty in CAE forcing is of a similar magnitude in all three regions with credible values ranging from 0.37 to $0.65\,W\,m^{-2}$ in the extratropical North Atlantic, from -0.21 to $0.11\,W\,m^{-2}$ in the tropical North Atlantic and from 0.06 to $0.41\,W\,m^{-2}$ in the tropical South Atlantic. The sign of CAE forcing is uncertain in the tropical North Atlantic because negative forcing in the eastern part of this region competes with positive forcing in the west. Positive CAE forcing in the extratropical North Atlantic and negative CAE forcing in the tropical North Atlantic suggest that there may be less hemispheric consensus in the sign of the forcing resulting from reductions in anthropogenic aerosol emissions than previously appreciated.

In each of the regions where CAE forcing is thought to have an influence on the position of the ITCZ (R2 and R3) and Sahel precipitation (R1–R3), CAE forcing variance is determined by a distinct combination of parameters; however, anthropogenic emission fluxes and aerosol process parameters account for the majority of the variance in each case. In the tropical North Atlantic (R2) the largest CAE forcing uncertainty sources in the Northern Hemisphere summer months (when the mean forcing is negative) are the rate of dry deposition of aerosols in the accumulation mode (Dry_Dep_Acc) and FF_Diam. The rate of dry deposition of SO_2 (Dry_Dep_SO2), anthropogenic SO_2 emissions (Anth_SO2), and the formation of secondary organic aerosols (SOA) from anthropogenic volatile organic compounds (VOCs) (AVOC_SOA) are important sources of CAE forcing uncertainty in the tropical North Atlantic during the months where forcing is negative. These same parameters contribute substantially to CAE forcing variance in the extratropical North Atlantic (R1) for much of the year, suggesting that, during the Northern Hemisphere winter, uncertainty in North American anthropogenic emissions is influential on SST in the tropical North Atlantic.

Contributions to CAE forcing variance in the tropical South Atlantic (R3) are diverse; however, the majority are accounted for by the emitted particle diameter of aerosols from biomass burning sources (BB_Diam), the rate of precipitation scavenging in warm low-level stratocumulus clouds (Drizz_Rate), and Anth_SO2. Uncertainty sources in the tropical South Atlantic are so varied that constraining all aerosol parameters that contribute to CAE forcing variance on decadal time scales is unrealistic. Instead, representations of ITCZ position could be more readily improved by reducing the uncertainty in Drizz_Rate, which is the largest source of uncertainty in October when the mean regional forcing is largest.

2) North Atlantic tropical storm development

Contributions to CAE forcing uncertainty in the extratropical and tropical North Atlantic (R1 and R2) are examined here, as in section 3b(1). Analysis is restricted to the warmest Northern Hemisphere months when tropical storms predominate.

The tropical North Atlantic (R2) has a smaller absolute-mean regional CAE forcing and uncertainty range, between April and October, than the extratropical North Atlantic (R1). Credible values range from -0.33 to $0.02\,W\,m^{-2}$ in the tropical North Atlantic and range from 0.54 to $0.95\,W\,m^{-2}$ in the extratropical North Atlantic. The mean simulated CAE forcing in the tropical North Atlantic (R2) is negative ($-0.14\,W\,m^{-2}$). The positive CAE forcing in the wider North Atlantic (e.g., $0.75\,W\,m^{-2}$ in R1) supports the hypothesis that reductions in Northern Hemispheric aerosol emissions have warmed SSTs and acted as one of the drivers of recent decadal increases in Atlantic tropical storms (Booth et al. 2012). However, the simulated CAE forcing in the tropical North Atlantic ($-0.14\,W\,m^{-2}$), which roughly aligns with the main Atlantic hurricane development region, is of the opposite sign from that suggested by Dunstone et al. (2013) as being consistent with an aerosol driver of tropical storm changes. The

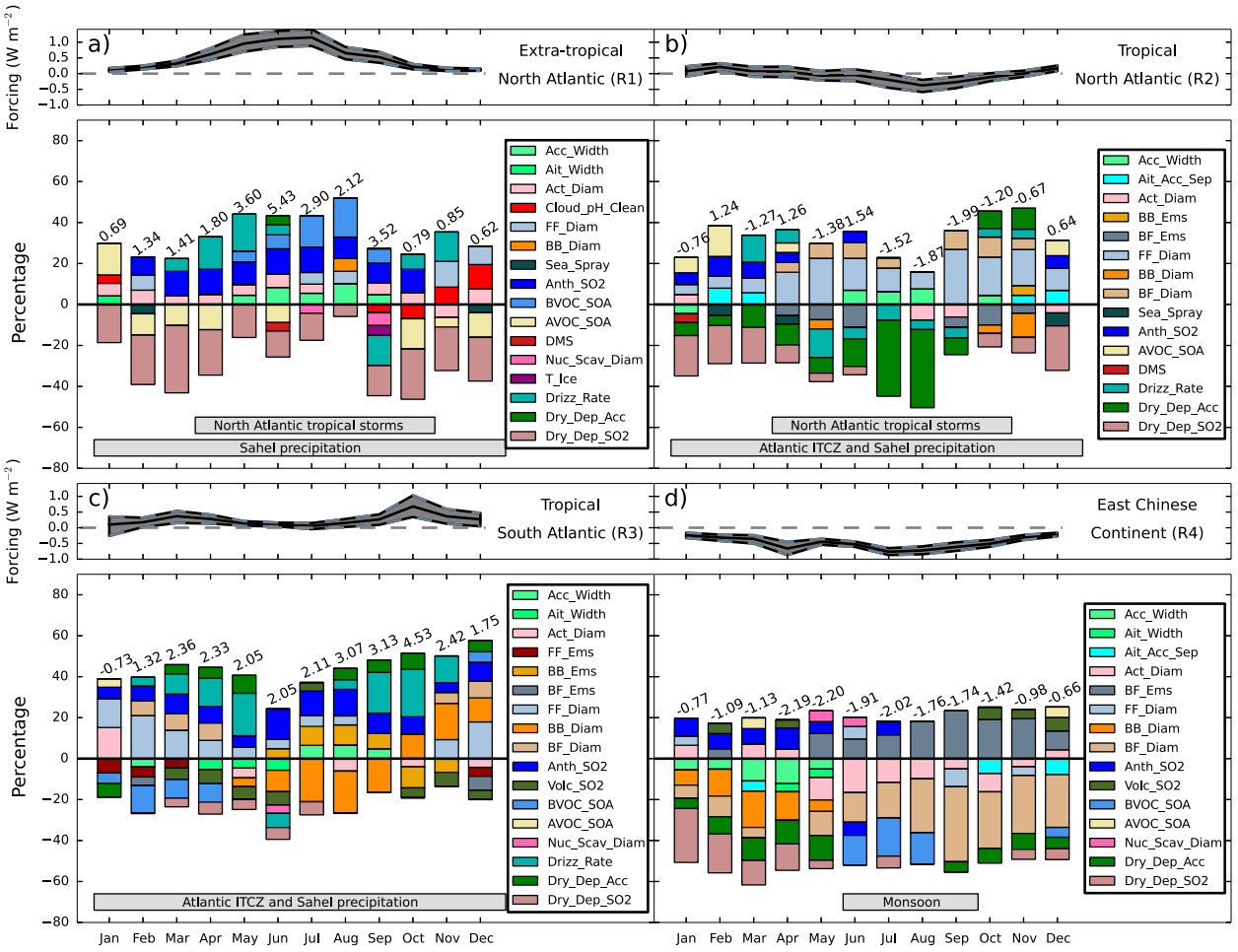

FIG. 7. Regional-mean percentage contributions to CAE forcing variance for R1–R4. Contributions of less than 4% of the CAE forcing variance are omitted. A reminder of climatically important effects is provided using shaded text under the appropriate months. Where increasing a parameter leads to an amplification of positive or negative CAE forcing (S1, S4, and S6 in Fig. 3), the percentage contributions are above the *x* axis. If a parameter increase leads to suppression of CAE forcing in the region (S2, S3, and S5), then the contributions are below the *x* axis. A time series of average forcing values is included in a panel at the top of each plot with mean regional 90% CIs shaded gray. CAE forcing in the model grid box where absolute CAE forcing is strongest is presented above the bar for each month.

credible range of simulated tropical North Atlantic CAE forcing includes positive values. However, unless physical grounds are found for ruling out parameter combinations that lead to mean CAE forcing values in the lower part of this range, these results call into question the relationship between Northern Hemisphere aerosol emission reductions and CAE forcing of SSTs in the main Atlantic hurricane development region on decadal time scales.

In the tropical North Atlantic (R2) Dry_Dep_Acc and FF_Diam contribute most to forcing variance in months relevant to tropical storm development, while Anth_SO2 and Dry_Dep_SO2 contribute most to variance in the extratropical North Atlantic (R1). Uncertainty in tropical storm development in the Atlantic Ocean in recent decades, insofar as it is affected by CAE forcing on SST, is largely determined by uncertainties in aerosol deposition process parameters and anthropogenic emission fluxes.

3) PACIFIC TROPICAL STORM DEVELOPMENT

The northwestern Pacific Ocean (R9) has a simulated-mean CAE forcing of $-0.20\,\mathrm{W\,m^{-2}}$ with credible values ranging from -0.33 to $-0.06\,\mathrm{W\,m^{-2}}$, making the magnitude of its role in Pacific tropical storm development in recent decades highly uncertain. Figure 9a shows that the magnitude and uncertainty in CAE forcing are largest in the Northern Hemisphere summer months when a negative forcing will reduce SSTs and therefore potentially suppress tropical storm development. During January and February when anthropogenic aerosol emissions may alter the Pacific

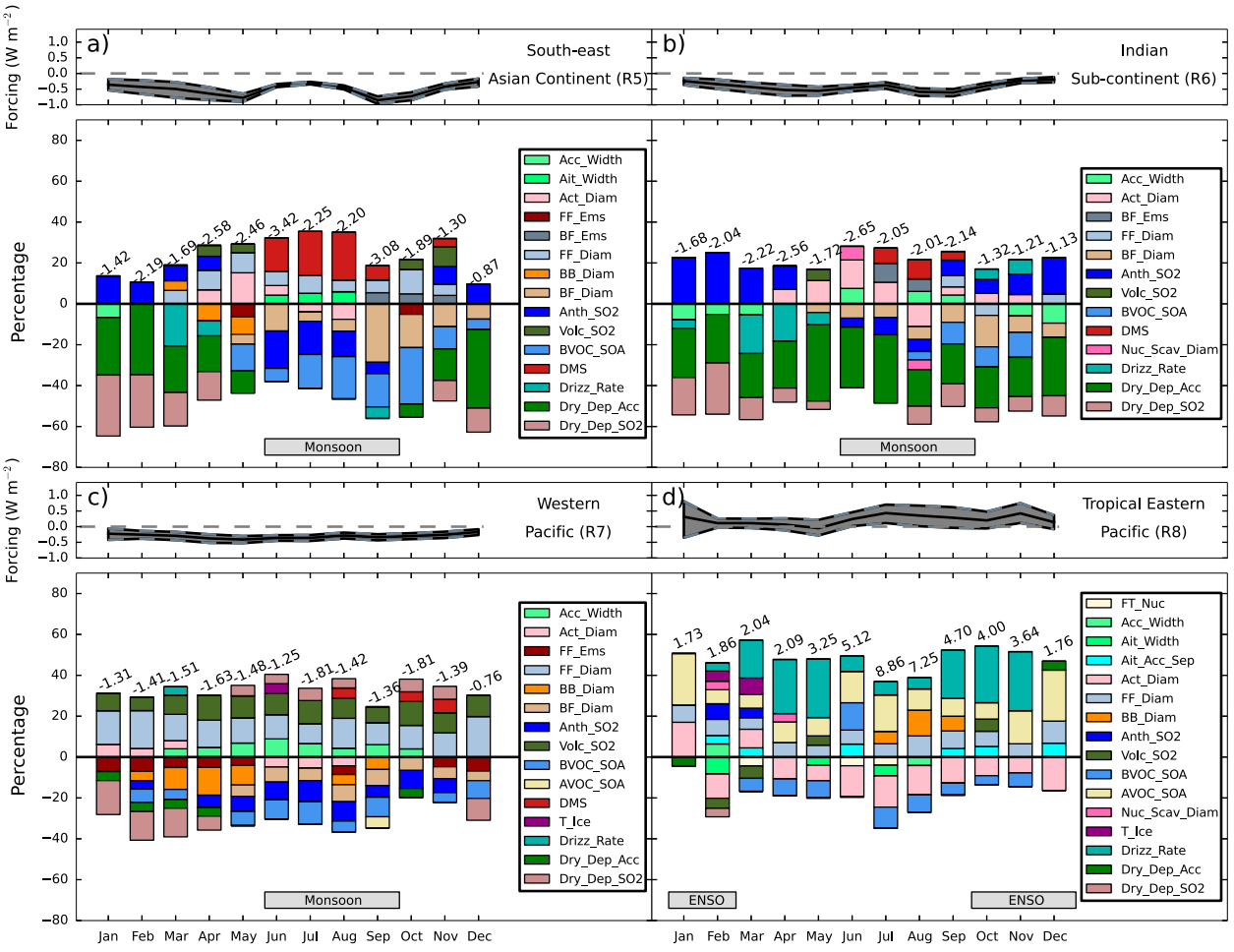

FIG. 8. Regional-mean percentage contributions to CAE forcing variance for R5–R8. Features are identical to Fig. 7.

storm track (Wang et al. 2014a), the magnitude of CAE forcing is near zero with relatively little uncertainty, suggesting that, if anthropogenic aerosol emissions do affect the Pacific storm track, it is through aerosol feedbacks on clouds and meteorology not modeled here.

The sources of CAE forcing uncertainty in the northwestern Pacific (R9) are numerous and temporally dependent. Dry_Dep_SO2 makes the largest contribution to CAE forcing variance during the early months of the year, relevant to the potential influence of aerosols on the Pacific storm track. The sources of CAE forcing uncertainty are diverse during other months, indicating that reducing uncertainty in the role of CAE forcing in Pacific tropical storm development will require a combination of developments in the representation of aerosol emission fluxes and aerosol process parameters.

4) ASIAN SUMMER MONSOON

The gradient in land–sea surface temperatures influences ASM development; hence, the relative magnitudes of CAE forcing in neighboring regions are considered here. Mean CAE forcing between June and September is negative in all regions examined here, and the contrast in forcing is largest between the Chinese continental and marine regions (R4 and R7). The continental CAE forcing is $-0.67\,\mathrm{W\,m^{-2}}$ compared to only $-0.33\,\mathrm{W\,m^{-2}}$ in the neighboring marine region, suggesting that CAE forcing plays an important role in reducing the land–sea thermal contrast. The negative CAE forcing is also stronger in continental Southeast Asia (R5) and India (R6) than in the neighboring Indian Ocean (R10), having respective values of -0.47, -0.51, and $-0.18\,\mathrm{W\,m^{-2}}$. In each of the regions relevant to ASM prediction, the land–sea surface temperature contrast is weakened as a result of CAE forcing, implying CAE forcing contributed to the weakened ASM observed in these regions in recent decades, as outlined in section 2d(3).

Contributions to CAE forcing variance are considered simultaneously for neighboring continental and marine regions in China (R4 and R7), Southeast Asia

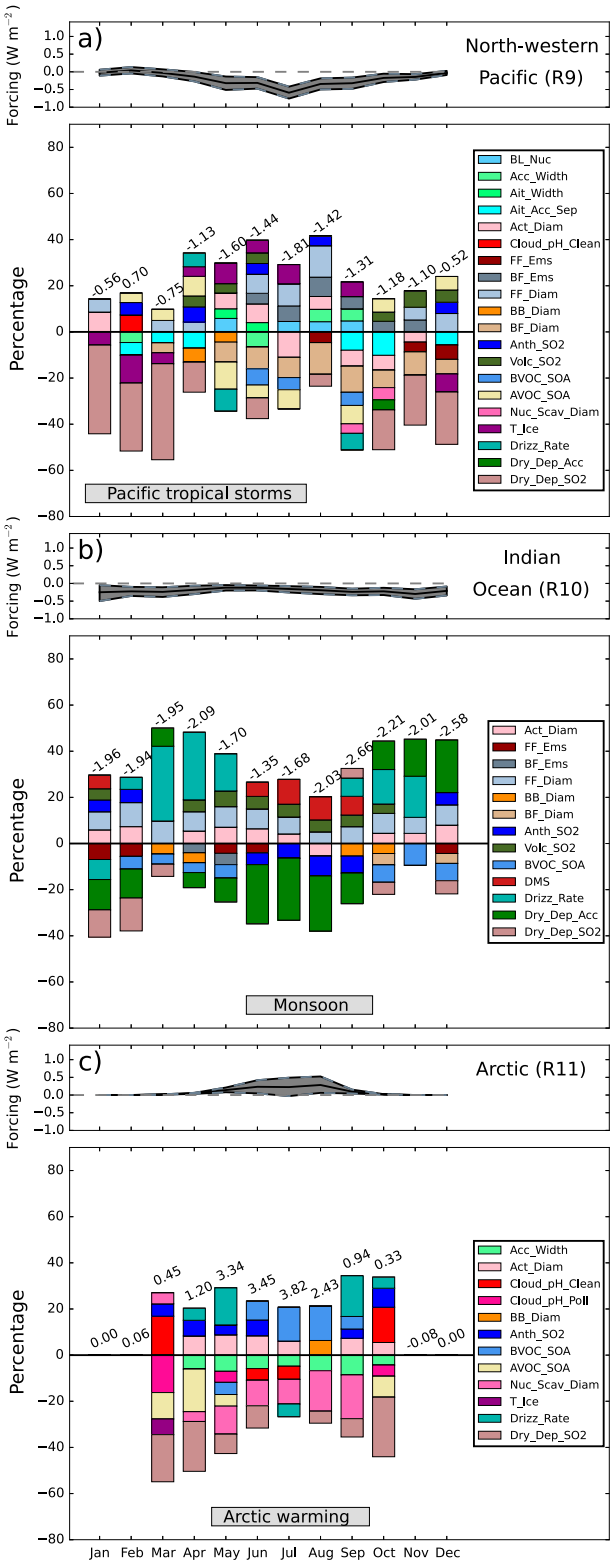

FIG. 9. Regional-mean percentage contributions to CAE forcing variance for R9–R11. Features are identical to Fig. 7.

(R5 and R10), and India (R6 and R10). In continental China (R4) CAE forcing uncertainty is largely determined by biofuel emission flux (BF_Ems) and emitted particle diameter (BF_Diam), and to a lesser extent by SOA formation from biogenic VOCs (BVOC_SOA). In the western Pacific bordering China (R7) FF_Diam, Volc_SO2, and Anth_SO2 make substantial contributions to CAE forcing variance. BVOC_SOA is the only parameter to contribute substantially to uncertainty in CAE forcing in the marine and continental regions.

In Southeast Asia (R5) the largest sources of CAE forcing uncertainty are the emission flux of dimethyl sulfide (DMS), BF_Diam, Anth_SO2, and BVOC_SOA. Many of the important uncertainty sources in Southeast Asia (R5) also contribute to CAE forcing variance in the Indian Ocean (R10). The aerosol removal process parameters Dry_Dep_Acc and Drizz_Rate are the largest sources of CAE forcing uncertainty over the Indian Ocean. Dry_Dep_Acc also makes the largest contribution to CAE forcing variance over the Indian continent (R6), with smaller contributions coming from DMS, BF_Ems, BF_Diam, and the diameter at which aerosols are considered large enough to have the potential to act as cloud condensation nuclei (CCN) (Act_Diam).

The importance of biofuel carbonaceous aerosol parameters BF_Ems and BF_Diam as sources of CAE forcing uncertainty is largely restricted to the continental regions where they are produced. Uncertainty in the magnitude of CAE forcing in the Indian Ocean and Indian continent can be reduced by improving the representation of Dry_Dep_Acc. Anth_SO2 also plays an important role in both continental and marine regions, confirming the results of Verma et al. (2013). Neighboring land and marine regions in Southeast Asia and China are sensitive to noticeably different combinations of aerosol parameters. Wang et al. (2014) show that CMIP5 models typically underestimate CAE forcing in the western Pacific and over China. The aerosol emission fluxes and model processes identified here provide a foundation for examining the cause of CAE forcing underestimation and for reducing the effect of uncertainty in CAE forcing on ASM prediction.

5) EL NIÑO–SOUTHERN OSCILLATION

Changes in SSTs in the tropical eastern Pacific Ocean (R8), where anomalously warm or cold SSTs in the Pacific Ocean typically initially develop, are used to determine changes to the mean state of the ENSO (Rasmusson and Carpenter 1982). The sign of forcing is likely positive in the tropical eastern Pacific with mean CAE forcing of 0.24 W m^{-2} and simulated credible values ranging from −0.08 to 0.53 W m^{-2}. The upper

TABLE 2. Regional-mean CAE forcings and mean 90% CIs for months where CAE forcing influences climatic effects. The largest absolute individual model gridbox mean CAE forcings within each region are provided for the months of interest (indicated in Table 1). Ratios of mean regional CAE forcing 90% credible interval range to the forcing caused by changes in anthropogenic CO_2 emissions, using the months of interest, provide context for the relative importance of regional CAE forcing uncertainties.

Key	Location	Climate effect	Mean forcing ($W\,m^{-2}$)	Mean 90% CI ($W\,m^{-2}$)	Largest absolute-mean forcing ($W\,m^{-2}$)	Ratio of mean forcings (CAE:CO_2)
R1	Extratropical North Atlantic	North Atlantic tropical storms	0.75	(0.54, 0.95)	2.88	0.59
R1	Extratropical North Atlantic	Sahel precipitation	0.51	(0.37, 0.66)	2.09	0.41
R2	Tropical North Atlantic	North Atlantic tropical storms	−0.14	(−0.33, 0.02)	−0.96	0.32
R2	Tropical North Atlantic	Atlantic ITCZ and Sahel precipitation	−0.05	(−0.21, 0.11)	−0.63	0.44
R3	Tropical South Atlantic	Atlantic ITCZ and Sahel precipitation	0.25	(0.06, 0.41)	2.20	0.50
R4	East China	Asian summer monsoon	−0.66	(−0.77, −0.54)	−1.86	0.33
R5	Southeast Asia	Asian summer monsoon	−0.47	(−0.57, −0.43)	−2.74	0.20
R6	Indian subcontinent	Asian summer monsoon	−0.51	(−0.63, −0.40)	−2.22	0.32
R7	Western Pacific	Asian summer monsoon	−0.33	(−0.43, −0.24)	−1.46	0.27
R8	Tropical eastern Pacific	ENSO development	0.24	(−0.08, 0.53)	2.60	0.88
R9	Northwestern Pacific	Pacific tropical storms	−0.20	(−0.33, −0.06)	−0.94	0.38
R10	Indian Ocean	Asian summer monsoon	−0.18	(−0.27, −0.10)	−1.93	0.25
R11	Arctic	Arctic warming	0.20	(0.04, 0.36)	2.80	0.57

credible CAE forcing value indicates that there may have been as much as 1×10^{11} J of energy entering the tropical eastern Pacific between 1978 and 2008 as a result of positive CAE forcing. The positive CAE forcing in the eastern Pacific is consistent with the shift toward conditions more suitable for El Niño events that occurred at the end of the twentieth century (Trenberth and Hoar 1996). This raises the possibility that past aerosol changes may have influenced the mean ENSO state. The likely positive CAE forcing simulated here suggests that it may be possible that apparent multidecadal shifts in the mean ENSO state in the tropical eastern Pacific, resulting from changing SSTs, are the result of a forced aerosol signal.

The dominant sources of uncertainty in the tropical eastern Pacific (R8) are Drizz_Rate, which contributes most to CAE forcing variance in November when mean forcing is largest, and AVOC_SOA, which contributes in the early months of the year when CAE forcing uncertainty is relatively large. Act_Diam and FF_Diam are also important sources of CAE forcing uncertainty. Improving the representation of these aerosol process

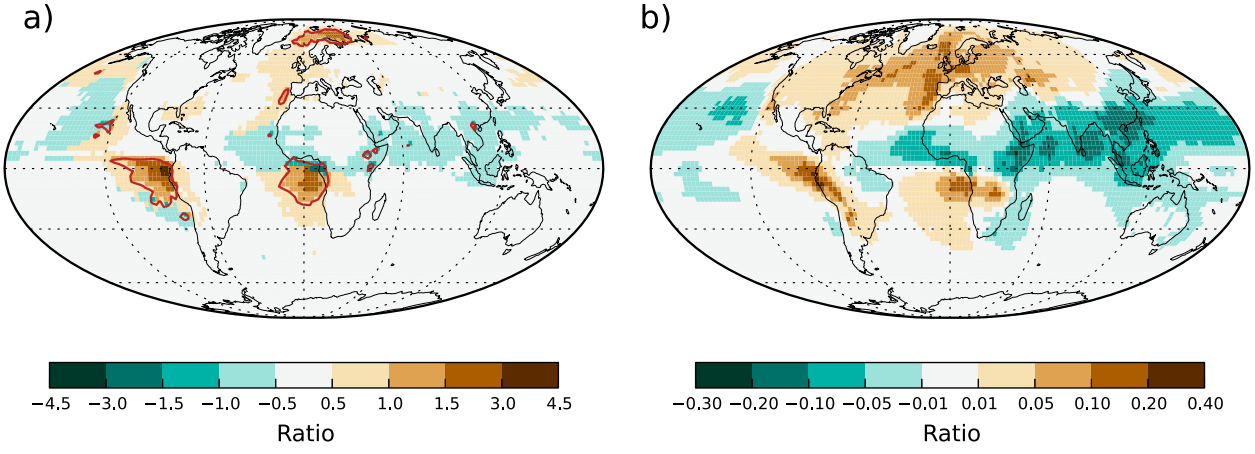

FIG. 10. Regional uncertainty in CAE forcing. (a) Ratio of the annual-mean absolute 90% credible range of CAE forcing to the forcing caused by changes in anthropogenic CO_2 emissions, calculated within individual model grid boxes. The contours indicate locations where the regional CAE forcing credible range and global-mean CO_2 change forcing are equal. Ratios are calculated independently within individual model grid boxes and credible ranges have been multiplied by −1 where global-mean CAE forcing is negative. (b) Ratio of annual-mean CAE forcing to simulated CO_2 induced forcing.

and emission flux parameters will reduce uncertainty in the magnitude of the CAE forcing in recent decades, allowing further research into the potential for an aerosol-forced signal to influence the mean ENSO state on multidecadal time scales conducted with better constrained CAE forcing values.

6) ARCTIC

The sign of CAE forcing in the Arctic (R11) is likely positive with credible values ranging from 0.04 to 0.36 $W m^{-2}$. A positive CAE forcing in the Arctic agrees with the results of Shindell and Faluvegi (2009) and Chylek et al. (2014), which suggest that decreasing North American and European anthropogenic emissions in recent decades have contributed to Arctic warming.

The pH of water within clouds in relatively clean (Cloud_pH_Clean) and polluted (Cloud_pH_Poll) atmospheric environments affects the rate of secondary sulfate formation, and both parameters are important sources of CAE forcing uncertainty in the Arctic, where anthropogenic emissions have often been transported relatively long distances from Northern Hemisphere continental regions (Law et al. 2014). Cloud_pH_Poll contributes more to CAE forcing variance than Cloud_pH_Clean in the Northern Hemisphere summer months when the forcing is strongest.

The important contributions of aerosol process parameters to CAE forcing in the Arctic is indicative that the uncertainties are related to the processing of aerosols during transport into this region. Furthermore, the dominance of aerosol process parameters in this region suggests that multimodel CAE forcing diversity in the Arctic is likely to be larger than in other regions.

4. Conclusions

During the 1978–2008 period, changes in anthropogenic CO_2 emissions cause a global-mean forcing of 0.7 $W m^{-2}$ (Myhre et al. 2013). Regayre et al. (2014) calculated a near-zero global-mean CAE forcing with high confidence during the 1978–2008 period. However, it is shown here that substantial regional aerosol CAE forcing uncertainties of climatic importance exist. The disparity between the magnitudes and degree of uncertainty in global and regional mean CAE forcings is explained by the cancellation of positive and negative regional forcings.

Performing a sensitivity analysis on global-mean absolute CAE forcing has revealed a number of parametric contributions to CAE forcing variance that were not identified in the sensitivity analysis of global CAE forcing conducted by Regayre et al. (2014). Continuously degassing and sporadically erupting volcanic SO_2 emissions, the rate of dry deposition of aerosols in the accumulation mode, and the diameter of carbonaceous aerosols emitted from biomass burning sources all contributed very little to global-mean CAE forcing uncertainty, yet here it is shown that across the globe these parameters are the main sources of uncertainty on the regional scale. The drizzle rate within low-level stratocumulus clouds is an important source of uncertainty for global-mean CAE forcing with and without the cancellation of positive and negative regional forcings. The emission flux and diameter of organic carbon and black carbon aerosols from fossil fuel sources cause most of the uncertainty in global-mean CAE forcing, yet they are relatively small sources of uncertainty in global-mean absolute CAE forcing, each explaining less than 5% of the variance. The large contributions of fossil fuel parameters to global-mean CAE forcing arise because other parameters experience a greater degree of regional forcing cancellation in the global-mean calculation.

Aerosol parameter contributions to regional CAE forcing variance have been analyzed in 11 regions where CAE forcing is believed to influence large-scale climate effects. Within the climatically important regions examined, anthropogenic aerosol emission fluxes and aerosol process parameters are typically the largest sources of CAE forcing uncertainty. However, in many regions there is at least one natural aerosol emission flux that plays an important role. When attempting to constrain regional CAE forcing over recent decades, uncertainties in natural emission fluxes cannot be ignored. In particular the emission flux of SO_2 from continuously degassing and sporadically erupting volcanoes and the formation of SOA from biogenic VOCs contribute a small percentage of CAE forcing variance in almost all regions.

Quantifying the magnitude and uncertainty in regional CAE forcing provides insight into the potential for CAE forcing to influence large-scale climate effects. Our calculated uncertainty ranges leave open the possibility that CAE forcing may act against, rather than drive, the observed reduction in interhemispheric SST gradient in the Atlantic since the late 1970s. Considering the broader North Atlantic, the strong positive CAE forcing in the extratropical North Atlantic may influence ITCZ position and width. A negative CAE forcing in the tropical North Atlantic during recent decades calls into question whether further reductions in Northern Hemisphere anthropogenic aerosol emissions will lead to further increases in Atlantic storminess. CAE forcing is unlikely to be the cause of recent changes in the Pacific storm track although it has the potential to affect SSTs and therefore storm frequency in summer months. Our results support the hypothesis

that the observed changes in the ASM in recent decades are in part driven by CAE forcing that weakens the SAT/SST gradient in China, Southeast Asia, and India. CAE forcing in the eastern Pacific and uncertainty in the forcing are shown here to be substantial, allowing us to speculate that apparent shifts in the mean ENSO state, determined using changes in SST, may result from a forced aerosol signal on multidecadal time scales. Our results also support the hypothesis that CAE forcing was positive in the Arctic in recent decades. Uncertainty in simulated CAE forcing is substantial in the Arctic and therefore so is its role in the observed rapid warming of Arctic surface temperatures.

In the atmosphere, aerosols feed back onto meteorology and clouds; however, our experiment was designed to quantify the effect of uncertain aerosol emission fluxes and process parameters on CAE forcing in isolation. The additional uncertainty arising from the representation of atmospheric physics within global models has the potential to affect regional and global CAE forcing calculations. Fasullo and Trenberth (2012) provide clear evidence that teleconnections and feedbacks must be adequately modeled in order to reduce uncertainty in the simulation of climate effects. Furthermore, using a dynamic ocean, rather than prescribing SSTs, in global climate models can produce markedly different climatic responses to external forcings (Ocko et al. 2014; Andrews et al. 2015). Research into the relative importance of uncertainties in aerosol and atmospheric physics parameterizations as sources of CAE forcing uncertainty using global climate models that include representations of aerosol–cloud meteorology and atmosphere–ocean feedbacks is essential. The sources of aerosol parametric uncertainty identified as globally and regionally important here can be used to inform future research where the reduction of CAE forcing variance is a priority.

Acknowledgments. Data can be made available upon request from the corresponding author. L. A. Regayre is funded by a Doctoral Training Grant from the Natural Environment Research Council (NERC) and a CASE studentship with the Met Office Hadley Centre. B. B. B. Booth was supported by the Joint UK DECC/Defra Met Office Hadley Centre Climate Programme (GA01101). K. S. Carslaw acknowledges funding from the Royal Society Wolfson Award. We acknowledge funding from NERC under AEROS and GASSP Grants NE/G006172/1 and NE/J024252/1. This work made use of the facilities of N8 HPC provided and funded by the N8 consortium and EPSRC (EP/K000225/1). The Met Office Hadley Centre is coordinated by the University of Leeds and the University of Manchester. The authors thank three anonymous reviewers for their constructive comments on this article.

REFERENCES

Allen, R. J., S. C. Sherwood, J. R. Norris, and C. S. Zender, 2012: The equilibrium response to idealized thermal forcings in a comprehensive GCM: Implications for recent tropical expansion. *Atmos. Chem. Phys.,* **12,** 4795–4816, doi:10.5194/acp-12-4795-2012.

——, J. R. Norris, and M. Kovilakam, 2014: Influence of anthropogenic aerosols and the Pacific decadal oscillation on tropical belt width. *Nat. Geosci.,* **7,** 270–274, doi:10.1038/ngeo2091.

Andrews, T., J. M. Gregory, and M. J. Webb, 2015: The dependence of radiative forcing and feedback on evolving patterns of surface temperature change in climate models. *J. Climate,* **28,** 1630–1648, doi:10.1175/JCLI-D-14-00545.1.

Barahona, D., R. E. L. West, P. Stier, S. Romakkaniemi, and A. Nenes, 2010: Comprehensively accounting for the effect of giant CCN in cloud activation parameterizations. *Atmos. Chem. Phys.,* **10,** 2467–2473, doi:10.5194/acp-10-2467-2010.

Bollasina, M. A., Y. Ming, and V. Ramaswamy, 2013: Earlier onset of the Indian monsoon in the late twentieth century: The role of anthropogenic aerosols. *Geophys. Res. Lett.,* **40,** 3715–3720, doi:10.1002/grl.50719.

Boo, K. O., B. B. B. Booth, Y. H. Byun, J. Lee, C. Cho, S. Shim, and K. T. Kim, 2015: Influence of aerosols in multidecadal SST variability simulations over the North Pacific. *J. Geophys. Res. Atmos.,* **120,** 517–531, doi:10.1002/2014JD021933.

Booth, B. B. B., N. J. Dunstone, P. R. Halloran, T. Andrews, and N. Bellouin, 2012: Aerosols implicated as a prime driver of twentieth-century North Atlantic climate variability. *Nature,* **484,** 228–232, doi:10.1038/nature10946.

Boucher, O., and Coauthors, 2013: Clouds and aerosols. *Climate Change 2013: The Physical Science Basis,* T. F. Stocker et al., Eds., Cambridge University Press, 571–657. [Available online at http://www.climatechange2013.org/images/report/WG1AR5_Chapter07_FINAL.pdf.]

Calisto, M., D. Folini, M. Wild, and L. Bengtsson, 2014: Cloud radiative forcing intercomparison between fully coupled CMIP5 models and CERES satellite data. *Ann. Geophys.,* **32,** 793–807, doi:10.5194/angeo-32-793-2014.

Carslaw, K. S., and Coauthors, 2013: Large contribution of natural aerosols to uncertainty in indirect forcing. *Nature,* **503,** 67–71, doi:10.1038/nature12674.

Chang, C. Y., J. C. H. Chiang, M. F. Wehner, A. Friedman, and R. Ruedy, 2011: Sulfate aerosol control of tropical Atlantic climate over the twentieth century. *J. Climate,* **24,** 2540–2555, doi:10.1175/2010JCLI4065.1.

Chiang, J. C. H., C. Y. Chang, and M. F. Wehner, 2013: Long-term behavior of the Atlantic interhemispheric SST gradient in the CMIP5 historical simulations. *J. Climate,* **26,** 8628–8640, doi:10.1175/JCLI-D-12-00487.1.

Choi, J., S. W. Son, J. Lu, and S. K. Min, 2014: Further observational evidence of Hadley cell widening in the Southern Hemisphere. *Geophys. Res. Lett.,* **41,** 2590–2597, doi:10.1002/2014GL059426.

Chylek, P., N. Hengartner, G. Lesins, J. D. Klett, O. Humlum, M. Wyatt, and M. Dubey, 2014: Isolating the anthropogenic component of Arctic warming. *Geophys. Res. Lett.,* **41,** 3569–3576, doi:10.1002/2014GL060184.

Cvijanovic, I., and J. C. Chiang, 2013: Global energy budget changes to high latitude North Atlantic cooling and the tropical ITCZ response. *Climate Dyn.,* **40,** 1435–1452, doi:10.1007/s00382-012-1482-1.

Diaz, H. F., M. P. Hoerling, and J. K. Eischeid, 2001: ENSO variability, teleconnections and climate change. *Int. J. Climatol.,* **21,** 1845–1862, doi:10.1002/joc.631.

Ding, Y., Z. Wang, and Y. Sun, 2008: Inter-decadal variation of the summer precipitation in east China and its association with decreasing Asian summer monsoon. Part I: Observed evidences. *Int. J. Climatol.,* **28,** 1139–1161, doi:10.1002/joc.1615.

Dong, L., and T. Zhou, 2014: The Indian Ocean sea surface temperature warming simulated by CMIP5 models during the twentieth century: Competing forcing roles of GHGs and anthropogenic aerosols. *J. Climate,* **27,** 3348–3362, doi:10.1175/JCLI-D-13-00396.1.

Dunstone, N. J., D. M. Smith, B. B. B. Booth, L. Hermanson, and R. Eade, 2013: Anthropogenic aerosol forcing of Atlantic tropical storms. *Nat. Geosci.,* **6,** 534–539, doi:10.1038/ngeo1854.

Edwards, J. M., and A. Slingo, 1996: Studies with a flexible new radiation code. I: Choosing a configuration for a large-scale model. *Quart. J. Roy. Meteor. Soc.,* **122,** 689–719, doi:10.1002/qj.49712253107.

Evan, A. T., D. J. Vimont, A. K. Heidinger, J. P. Kossin, and R. Bennartz, 2009: The role of aerosols in the evolution of tropical North Atlantic Ocean temperature anomalies. *Science,* **324,** 778–781, doi:10.1126/science.1167404.

Fadnavis, S., K. Semeniuk, L. Pozzoli, M. G. Schultz, S. D. Ghude, S. Das, and R. Kakatkar, 2013: Transport of aerosols into the UTLS and their impact on the Asian monsoon region as seen in a global model simulation. *Atmos. Chem. Phys.,* **13,** 8771–8786, doi:10.5194/acp-13-8771-2013.

Fasullo, J. T., and K. E. Trenberth, 2012: A less cloudy future: The role of subtropical subsidence in climate sensitivity. *Science,* **338,** 792–794, doi:10.1126/science.1227465.

Folland, C. K., T. N. Palmer, and D. E. Parker, 1986: Sahel rainfall and worldwide sea temperatures, 1901–85. *Nature,* **320,** 602–607, doi:10.1038/320602a0.

Fountoukis, C., and A. Nenes, 2005: Continued development of a cloud droplet formation parameterization for global climate models. *J. Geophys. Res.,* **110,** D11212, doi:10.1029/2004JD005591.

Friedman, A. R., Y. T. Hwang, J. C. H. Chiang, and D. M. W. Frierson, 2013: Interhemispheric temperature asymmetry over the twentieth century and in future projections. *J. Climate,* **26,** 5419–5433, doi:10.1175/JCLI-D-12-00525.1.

Gillett, N. P., D. A. Stone, P. A. Stott, T. Nozawa, A. Yu. Karpechko, G. C. Hegerl, M. F. Wehner, and P. D. Jones, 2008: Attribution of polar warming to human influence. *Nat. Geosci.,* **1,** 750–754, doi:10.1038/ngeo338.

Gong, D. Y., and C. H. Ho, 2003: Arctic oscillation signals in the East Asian summer monsoon. *J. Geophys. Res.,* **108,** 4066, doi:10.1029/2002JD002193.

Granier, C., and Coauthors, 2011: Evolution of anthropogenic and biomass burning emissions of air pollutants at global and regional scales during the 1980–2010 period. *Climatic Change,* **109,** 163–190, doi:10.1007/s10584-011-0154-1.

Guo, L., E. J. Highwood, L. C. Shaffrey, and A. G. Turner, 2013: The effect of regional changes in anthropogenic aerosols on rainfall of the East Asian summer monsoon. *Atmos. Chem. Phys.,* **13,** 1521–1534, doi:10.5194/acp-13-1521-2013.

Hamilton, D. S., L. A. Lee, K. J. Pringle, C. L. Reddington, D. V. Spracklen, and K. S. Carslaw, 2014: Occurrence of pristine aerosol environments on a polluted planet. *Proc. Natl. Acad. Sci. USA,* **111,** 18 466–18 471, doi:10.1073/pnas.1415440111.

Henriksson, S. V., and Coauthors, 2014: Spatial distributions and seasonal cycles of aerosol climate effects in India seen in a global climate–aerosol model. *Atmos. Chem. Phys.,* **14,** 10 177–10 192, doi:10.5194/acp-14-10177-2014.

Hermanson, L., and R. T. Sutton, 2010: Case studies in interannual to decadal climate predictability. *Climate Dyn.,* **35,** 1169–1189, doi:10.1007/s00382-009-0672-y.

Hwang, Y. T., D. M. W. Frierson, and S. M. Kang, 2013: Anthropogenic sulfate aerosol and the southward shift of tropical precipitation in the late 20th century. *Geophys. Res. Lett.,* **40,** 2845–2850, doi:10.1002/grl.50502.

IPCC, 2013: Summary for policymakers. *Climate Change 2013: The Physical Science Basis,* T. F. Stocker et al., Eds., Cambridge University Press, 1–29. [Available online at https://www.ipcc.ch/pdf/assessment-report/ar5/wg1/WGIAR5_SPM_brochure_en.pdf.]

Kang, S. M., and J. Lu, 2012: Expansion of the Hadley cell under global warming: Winter versus summer. *J. Climate,* **25,** 8387–8393, doi:10.1175/JCLI-D-12-00323.1.

Kirtman, B., and Coauthors, 2013: Near-term climate change: Projections and predictability. *Climate Change 2013: The Physical Science Basis,* T. F. Stocker et al., Eds., Cambridge University Press, 953–1028. [Available online at https://www.ipcc.ch/pdf/assessment-report/ar5/wg1/WG1AR5_Chapter11_FINAL.pdf.]

Lamarque, J. F., and Coauthors, 2010: Historical (1850–2000) gridded anthropogenic and biomass burning emissions of reactive gases and aerosols: Methodology and application. *Atmos. Chem. Phys.,* **10,** 7017–7039, doi:10.5194/acp-10-7017-2010.

Law, K. S., and Coauthors, 2014: Arctic air pollution: New insights from POLARCAT-IPY. *Bull. Amer. Meteor. Soc.,* **95,** 1873–1895, doi:10.1175/BAMS-D-13-00017.1.

Lee, L. A., K. S. Carslaw, K. J. Pringle, G. W. Mann, and D. V. Spracklen, 2011: Emulation of a complex global aerosol model to quantify sensitivity to uncertain parameters. *Atmos. Chem. Phys.,* **11,** 12 253–12 273, doi:10.5194/acp-11-12253-2011.

——, ——, ——, and ——, 2012: Mapping the uncertainty in global CCN using emulation. *Atmos. Chem. Phys.,* **12,** 9739–9751, doi:10.5194/acp-12-9739-2012.

——, K. J. Pringle, C. L. Reddington, G. W. Mann, P. Stier, D. V. Spracklen, J. Pierce, and K. S. Carslaw, 2013: The magnitude and causes of uncertainty in global model simulations of cloud condensation nuclei. *Atmos. Chem. Phys.,* **13,** 8879–8914, doi:10.5194/acp-13-8879-2013.

Li, J., W. C. Wang, Z. Sun, G. Wu, H. Liao, and Y. Liu, 2014: Decadal variation of East Asian radiative forcing due to anthropogenic aerosols during 1850–2100, and the role of atmospheric moisture. *Climate Res.,* **61,** 241–257, doi:10.3354/cr01236.

Li, Z., and Coauthors, 2011: East Asian Studies of Tropospheric Aerosols and their Impact on Regional Climate (EAST-AIRC): An overview. *J. Geophys. Res.,* **116,** D00K34, doi:10.1029/2010JD015257.

Liu, Y., J. C. H. Chiang, C. Chou, and C. M. Patricola, 2014: Atmospheric teleconnection mechanisms of extratropical North Atlantic SST influence on Sahel rainfall. *Climate Dyn.,* **43,** 2797–2811, doi:10.1007/s00382-014-2094-8.

Lu, J., G. A. Vecchi, and T. Reichler, 2007: Expansion of the Hadley cell under global warming. *Geophys. Res. Lett.,* **34,** L06805, doi:10.1029/2006GL028443.

Mann, G. W., K. S. Carslaw, D. V. Spracklen, D. A. Ridley, P. T. Manktelow, M. P. Chipperfield, S. J. Pickering, and C. E. Johnson, 2010: Description and evaluation of GLOMAP-mode: A modal global aerosol microphysics model for the UKCA composition-climate model. *Geosci. Model Dev.,* **3,** 519–551, doi:10.5194/gmd-3-519-2010.

——, and Coauthors, 2012: Intercomparison of modal and sectional aerosol microphysics representations within the same 3-D global chemical transport model. *Atmos. Chem. Phys.,* **12,** 4449–4476, doi:10.5194/acp-12-4449-2012.

Mann, M. E., and K. A. Emanuel, 2006: Atlantic hurricane trends linked to climate change. *Eos, Trans. Amer. Geophys. Union,* **87,** 233–241, doi:10.1029/2006EO240001.

Mao, K. B., Y. Ma, L. Xia, W. Y. Chen, X. Y. Shen, T. J. He, and T. R. Xu, 2014: Global aerosol change in the last decade: An analysis based on MODIS data. *Atmos. Environ.,* **94,** 680–686, doi:10.1016/j.atmosenv.2014.04.053.

McPhaden, M. J., S. E. Zeibak, and H. M. Glantz, 2006: ENSO as an integrating concept in earth science. *Science,* **314,** 1740–1745, doi:10.1126/science.1132588.

Mulitza, S., and Coauthors, 2008: Sahel megadroughts triggered by glacial slowdowns of Atlantic meridional overturning. *Paleoceanography,* **23,** PA4206, doi:10.1029/2008PA001637.

Myhre, G., and Coauthors, 2013: Anthropogenic and natural radiative forcing. *Climate Change 2013: The Physical Science Basis,* T. F. Stocker et al., Eds., Cambridge University Press, 659–740. [Available online at https://www.ipcc.ch/pdf/assessment-report/ar5/wg1/WG1AR5_Chapter08_FINAL.pdf.]

Ocko, I. B., V. Ramaswamy, and Y. Ming, 2014: Contrasting climate responses to the scattering and absorbing features of anthropogenic aerosol forcings. *J. Climate,* **27,** 5329–5345, doi:10.1175/JCLI-D-13-00401.1.

O'Hagan, A., 2006: Bayesian analysis of computer code outputs: A tutorial. *Reliab. Eng. Syst. Saf.,* **91,** 1290–1300, doi:10.1016/j.ress.2005.11.025.

Pielke, R. A, J. Gratz, C. W. Landsea, D. Collins, M. A. Saunders, and R. Musulin, 2008: Normalized hurricane damage in the United States: 1900–2005. *Nat. Hazards Rev.,* **9,** 29–42, doi:10.1061/(ASCE)1527-6988(2008)9:1(29).

Rasmusson, E. M., and T. H. Carpenter, 1982: Variations in tropical sea surface temperature and surface wind fields associated with the Southern Oscillation/El Niño. *Mon. Wea. Rev.,* **110,** 354–384, doi:10.1175/1520-0493(1982)110<0354:VITSST>2.0.CO;2.

Regayre, L. A., and Coauthors, 2014: Uncertainty in the magnitude of aerosol-cloud radiative forcing over recent decades. *Geophys. Res. Lett.,* **41,** 9040–9049, doi:10.1002/2014GL062029.

Robson, J., R. Sutton, and D. Smith, 2013: Predictable climate impacts of the decadal changes in the ocean in the 1990s. *J. Climate,* **26,** 6329–6339, doi:10.1175/JCLI-D-12-00827.1.

Roe, G. H., N. Feldl, K. C. Armour, Y. T. Hwang, and D. M. W. Frierson, 2015: The remote impacts of climate feedbacks on regional climate predictability. *Nat. Geosci.,* **8,** 135–139, doi:10.1038/ngeo2346.

Rossow, W. B., and R. A. Schiffer, 1999: Advances in understanding clouds from ISCCP. *Bull. Amer. Meteor. Soc.,* **80,** 2261–2287, doi:10.1175/1520-0477(1999)080<2261:AIUCFI>2.0.CO;2.

Rotstayn, L. D., and U. Lohmann, 2002: Tropical rainfall trends and the indirect aerosol effect. *J. Climate,* **15,** 2103–2116, doi:10.1175/1520-0442(2002)015<2103:TRTATI>2.0.CO;2.

Saltelli, A., S. Tarantola, and K. P. S. Chan, 1999: A quantitative model-independent method for global sensitivity analysis of model output. *Technometrics,* **41,** 39–56, doi:10.1080/00401706.1999.10485594.

——, K. Chan, and E. M. Scott, 2000: *Sensitivity Analysis.* Wiley, 504 pp.

Salzmann, M., H. Weser, and R. Cherian, 2014: Robust response of Asian summer monsoon to anthropogenic aerosols in CMIP5 models. *J. Geophys. Res. Atmos.,* **119,** 11 321–11 337, doi:10.1002/2014JD021783.

Schmidt, A., K. S. Carslaw, G. W. Mann, A. Rap, K. J. Pringle, D. V. Spracklen, M. Wilson, and P. M. Forster, 2012: Importance of tropospheric volcanic aerosol for indirect radiative forcing of climate. *Atmos. Chem. Phys.,* **12,** 7321–7339, doi:10.5194/acp-12-7321-2012.

Screen, J. A., and I. Simmonds, 2010: The central role of diminishing sea ice in recent Arctic temperature amplification. *Nature,* **464,** 1334–1337, doi:10.1038/nature09051.

Seidel, D. J., F. Qiang, W. J. Randel, and T. J. Reichler, 2008: Widening of the tropical belt in a changing climate. *Nat. Geosci.,* **1,** 21–24, doi:10.1038/ngeo.2007.38.

Serreze, M. C., A. P. Barrett, J. C. Stroeve, D. N. Kindig, and M. M. Holland, 2009: The emergence of surface-based Arctic amplification. *Cryosphere,* **3,** 11–19.

Shanahan, T. M., and Coauthors, 2009: Atlantic forcing of persistent drought in West Africa. *Science,* **324,** 377–380, doi:10.1126/science.1166352.

Shindell, D., and G. Faluvegi, 2009: Climate response to regional radiative forcing during the twentieth century. *Nat. Geosci.,* **2,** 294–300, doi:10.1038/ngeo473.

——, and Coauthors, 2013: Radiative forcing in the ACCMIP historical and future climate simulations. *Atmos. Chem. Phys.,* **13,** 2939–2974, doi:10.5194/acp-13-2939-2013.

Skeie, R. B., T. K. Berntsen, G. Myhre, K. Tanaka, M. M. Kvalevåg, and C. R. Hoyle, 2011: Anthropogenic radiative forcing time series from pre-industrial times until 2010. *Atmos. Chem. Phys.,* **11,** 11 827–11 857, doi:10.5194/acp-11-11827-2011.

Smith, S. J., J. van Aardenne, Z. Klimont, R. J. Andres, A. Volke, and S. D. Arias, 2011: Anthropogenic sulfur dioxide emissions: 1850–2005. *Atmos. Chem. Phys.,* **11,** 1101–1116, doi:10.5194/acp-11-1101-2011.

Spracklen, D. V., K. J. Pringle, K. S. Carslaw, M. P. Chipperfield, and G. W. Mann, 2005: A global off-line model of size-resolved aerosol microphysics: I. Model development and prediction of aerosol properties. *Atmos. Chem. Phys.,* **5,** 2227–2252, doi:10.5194/acp-5-2227-2005.

Stockwell, D. Z., and M. P. Chipperfield, 1999: A tropospheric chemical-transport model: Development and validation of the model transport schemes. *Quart. J. Roy. Meteor. Soc.,* **125,** 1747–1783, doi:10.1002/qj.49712555714.

Taylor, K. E., R. J. Stouffer, and G. A. Meehl, 2012: An overview of CMIP5 and the experiment design. *Bull. Amer. Meteor. Soc.,* **93,** 485–498, doi:10.1175/BAMS-D-11-00094.1.

Trenberth, K. E., and T. J. Hoar, 1996: The 1990–1995 El Niño-Southern Oscillation event: Longest on record. *Geophys. Res. Lett.,* **23,** 57–60, doi:10.1029/95GL03602.

——, and D. J. Shea, 2006: Atlantic hurricanes and natural variability in 2005. *Geophys. Res. Lett.,* **33,** L12704, doi:10.1029/2006GL026894.

Twomey, S., 1977: Influence of pollution on shortwave albedo of clouds. *J. Atmos. Sci.,* **34,** 1149–1152, doi:10.1175/1520-0469(1977)034<1149:TIOPOT>2.0.CO;2.

Verma, S., O. Boucher, H. C. Upadhyaya, and O. Sharma, 2013: Variations in sulphate aerosols concentration during winter

monsoon season for two consecutive years using a general circulation model. *Atmósfera,* **26,** 359–367.

Villarini, G., and G. A. Vecchi, 2013: Projected increases in North Atlantic tropical cyclone intensity from CMIP5 models. *J. Climate,* **26,** 3231–3240, doi:10.1175/JCLI-D-12-00441.1.

Wang, F., S. Yang, and T. Wu, 2014: Radiation budget biases in AMIP5 models over the East Asian monsoon region. *J. Geophys. Res. Atmos.,* **119,** 13 400–13 426, doi:10.1002/2014JD022243.

Wang, T., H. J. Wang, O. H. Otterå, Y. Q. Gao, L. L. Suo, T. Furevik, and L. Yu, 2013: Anthropogenic agent implicated as a prime driver of shift in precipitation in eastern China in the late 1970s. *Atmos. Chem. Phys.,* **13,** 12 433–12 450, doi:10.5194/acp-13-12433-2013.

Wang, Y., R. Zhang, and R. Saravanan, 2014a: Asian pollution climatically modulates mid-latitude cyclones following hierarchical modelling and observational analysis. *Nat. Commun.,* **5,** 3098, doi:10.1038/ncomms4098.

——, and Coauthors, 2014b: Assessing the effects of anthropogenic aerosols on Pacific storm track using a multiscale global climate model. *Proc. Natl. Acad. Sci. USA,* **111,** 6894–6899, doi:10.1073/pnas.1403364111.

Webster, P. J., 1987: The elementary monsoon. *Monsoons,* J. S. Fein and P. L. Stephens, Eds., Wiley, 3–32.

Ye, J., W. Li, L. Li, and F. Zhang, 2013: ''North drying and south wetting'' summer precipitation trend over China and its potential linkage with aerosol loading. *Atmos. Res.,* **125–126,** 12–19, doi:10.1016/j.atmosres.2013.01.007.

Yeh, S. W., W. M. Kim, Y. H. Kim, B. K. Moon, R. J. Park, and C. K. Song, 2013: Changes in the variability of the North Pacific sea surface temperature caused by direct sulfate aerosol forcing in China in a coupled general circulation model. *J. Geophys. Res. Atmos.,* **118,** 1261–1270, doi:10.1029/2012JD017947.

Yun, K. S., J. Y. Lee, and K. J. Ha, 2014: Recent intensification of the South and East Asian monsoon contrast associated with an increase in the zonal tropical SST gradient. *J. Geophys. Res. Atmos.,* **119,** 8104–8116, doi:10.1002/2014JD021692.

Zhang, R., and Coauthors, 2013: Have aerosols caused the observed Atlantic multidecadal variability? *J. Atmos. Sci.,* **70,** 1135–1144, doi:10.1175/JAS-D-12-0331.1.

Zhang, X., F. W. Zwiers, G. C. Hegerl, F. H. Lambert, N. P. Gillett, S. Solomon, P. A. Stott, and T. Nozawa, 2007: Detection of human influence on twentieth-century precipitation trends. *Nature,* **448,** 461–465, doi:10.1038/nature06025.

Zhao, M., and I. M. Held, 2012: TC-permitting GCM simulations of hurricane frequency response to sea surface temperature anomalies projected for the late-twenty-first century. *J. Climate,* **25,** 2995–3009, doi:10.1175/JCLI-D-11-00313.1.

Chapter 5

Observed planetary energy balance does not constrain aerosol radiative forcing

Observed planetary energy balance does not constrain aerosol radiative forcing

Leighton A. Regayre[1*], Jill S. Johnson[1], Masaru Yoshioka[1],

Kirsty J. Pringle[1], David M. H. Sexton[2], Ben B. B. Booth[2],

Graham W. Mann[1,3], Lindsay A. Lee[1], Nicolas Bellouin[4],

Grenville M. S. Lister[5], Colin E. Johnson[3], Ben Johnson[3],

James D. P. Mollard[4]and Kenneth S. Carslaw[1]

1. Institute for Climate and Atmospheric Science, School of Earth and Environment, University of Leeds, Leeds, LS2 9JT, UK.
2. UK Hadley Centre Met Office, Exeter, Fitzroy Road, Exeter, Devon, EX1 3PB, UK.
3. Current affiliation: National Centre for Atmospheric Science, University of Leeds, Leeds, LS2 9JT, UK.
4. Department of Meteorology, School of Mathematical & Physical Sciences, Faculty of Science, University of Reading, Reading, RG6 6BB, UK.
5. National Centre for Atmospheric Science, University of Reading, Reading, RG6 6BB, UK.
*Corresponding author email: L.A.Regayre11@leeds.ac.uk

Changes in aerosols cause a change in net top-of-the-atmosphere (ToA) short-wave and long-wave radiative fluxes and rapid adjustments in clouds, water vapour and temperature, causing an effective radiative forcing (ERF) of the planetary energy budget. Aerosol ERF has persisted as the largest uncertain component of net anthropogenic forcing over the industrial period (Boucher *et al.*, 2013). The diverse sources of uncertainty and the computational cost of running climate models make it difficult to isolate the main causes of aerosol ERF uncertainty and to understand how observations can be used to constrain it. Here we use model emulation and sensitivity analyses to show that while most of the uncertainty in present-day radiative flux is caused by uncertainty in the physical atmosphere model, particularly parameters related to clouds, most of the uncertainty in aerosol ERF is caused by the representation of aerosols. Although ToA fluxes and aerosol ERF share some common sources of uncertainty, tight observational constraint of present-day ToA fluxes has almost no effect on the uncertainty in aerosol ERF over the industrial period or over recent decades.

Reduction of uncertainty in aerosol ERF is important, not least because it would improve estimates of climate sensitivity (Collins *et al.*, 2013; Tett *et al.*, 2013), but remains challenging for two reasons: First, ERF is usually quantified with reference to a period pre-dating the satellite era (usually referenced to 1850 or 1750) meaning it is not a directly observable quantity. Second, aerosol ERF depends on many poorly understood interactions of aerosols with components of the physical climate system. Important sources of uncertainty are known to be aerosol emission fluxes (Granier *et al.*, 2011), representations of complex sub-grid processes such as clouds (Haerter *et al.*, 2009; Lohmann & Ferrachat, 2010; Golaz *et al.*, 2013; Neubauer *et al.*, 2014), precipitation responses (Tost *et al.*, 2010; Croft *et al.*, 2012; Michibata & Takemura, 2015), aerosol processes (Textor *et al.*, 2006, 2007; Storelvmo *et al.*, 2009; Croft *et al.*, 2012), radiation calculations (Steir *et al.*, 2012; Wilcox *et al.*, 2015) and subsequent feedbacks on atmospheric dynamics. Although a credible lower limit to the global mean aerosol ERF can be found using a 'top-down' approach and historical temperature trends (Stevens, 2015), model structural choices affect the resulting inferences made about the climate system (Knutti *et al.*, 2008). Furthermore, such methods do not provide a model with which to make improved climate projections and neglect important sources of uncertainty in the specified model components.

Ultimately, although the total impact of changes in aerosol emissions combine many complex processes, the net effect (aerosol ERF) is manifested as a change in planetary radiation balance. Some of the ERF uncertainty may be irreducible because it depends on the unobservable state of aerosols in the pre-industrial (PI) era (Carslaw *et al.*, 2013). But a large fraction of the uncertainty is known to be caused by aerosol and cloud physics processes that also determine the radiative state of the present-day (PD) atmosphere (Haerter *et al.*, 2009; Lohmann & Ferrachat, 2010). There are grounds, therefore, to expect that confronting the full range of potential climate simulations with observations of the present-day radiation balance will help reduce uncertainty in historical aerosol forcing. In fact, a previous study (Lohmann & Ferrachat, 2010) showed that tuning combinations of four cloud physics parameters to obtain observed radiation balance resulted in a 56% reduction in the range of aerosol ERF values. However, there are many more important sources of uncertainty in radiation balance and aerosol ERF than were simulated in this study. Other attempts to quantify the uncertainty in the ToA radiative flux caused by aerosols (Tett *et al.*, 2013; Shiogama *et al.*, 2012) explored only the current state of the atmosphere, not how it changes over time.

Here we create a perturbed parameter ensemble (PPE) of a variant of the HadGEM3

model and use model emulation (Lee *et al.*, 2013; Sexton *et al.*, 2012) to enable the combined effects of uncertainties in aerosol, cloud and other atmospheric processes to be quantified. HadGEM3 capably represents changes in cloud regime (Nam *et al.*, 2012); one of the requirements for simulating rapid adjustments to aerosol perturbations (Stevens & Feingold, 2009; Zhang *et al.*, 2015). We perturb parameters in the physical atmosphere model known to influence the properties and distribution of clouds and humidity (atmospheric parameters) (Sexton *et al.*, In prep.) in combination with aerosol emission, deposition and process parameters (aerosol parameters) (Lee *et al.*, 2013; Regayre *et al.*, 2014) (SI Extended Data Tables 1 and 2). By combining PPEs with statistical emulation and Monte Carlo sampling we are able to perform a sensitivity analysis that fully samples output across multi-dimensional parameter space (Lee *et al.*, 2013), which enables the variance to be decomposed into individual components.

Fig. 1 summarises the causes of variance in present-day global annual mean reflected shortwave radiation (RSR), outgoing longwave radiation (OLR), as well as the clear and cloudy sky components of RSR. Uncertainty in the 27 aerosol and atmospheric parameters results in a present-day RSR uncertainty of around ± 10 W m^{-2} (Extended Data Fig 2.) and OLR uncertainty of about ± 5 W m^{-2}. Observable ToA radiative flux variances are largely determined by parameters affecting atmospheric cloudiness and humidity. The majority of the RSR variance is determined by just four parameters (Rad_Mcica_Sigma, Sea_Spray, Sig_W and Ent_Fac_Dp). Rad_Mcica_Sigma and Ent_Fac_Dp are also significant sources of OLR variance. The sources of RSR and OLR variance are not dependent on the time period examined (Extended Data Fig. 3 and 4).

By far the largest source of variance in both RSR and OLR is Rad_Mcica_Sigma. This parameter affects the homogeneity of simulated clouds, altering, amongst other things, cloud fraction and tropospheric temperature profiles. Nevertheless, when we neglect uncertainty in this parameter the variances are still dominated by atmospheric parameters related to cloud processes (Extended Data Table 3). The dominant role of a cloud radiative parameter in determining ToA flux variance suggests that constraining this parameter to a very narrow range should constrain radiative fluxes and consequentially aerosol ERF (Haerter *et al.*, 2009; Lohmann & Ferrachat, 2010).

Contributions to variance in PI (here 1850) to PD aerosol ERF and the separate components due to changes in aerosol-radiation interaction (ARI) and aerosol-cloud interaction (ACI) are summarised in Fig. 2. Natural aerosol emissions (here, sea spray and dimethylsulphide, DMS) persist as important sources of 1850-PD ACI forcing variance (Fig. 2b), as in previous studies of several climate models (Wilcox *et al.*, 2015) and the aerosol-only component of a global model (Carslaw *et al.*, 2013). However, these results suggest that natural emissions are insignificant for direct aerosol (ARI) forcing uncertainty (Fig. 2c) because this forcing component responds linearly to changes in aerosol concentration.

Fig. 2d summarises the relative contributions of atmospheric and aerosol parameters to RSR, OLR and aerosol ERFs over the periods 1978-PD and 1850-PD. Atmospheric parameters cause the majority (79%) of the variance in present-day ToA RSR, but only 36% of the variance in 1850-PD aerosol ERF, and less than 10% of the 1978-PD aerosol ERF variance (Extended Data Fig. 5) with the rest of the uncertainty attributable to the aerosol model. This analysis shows that uncertainties in aerosol parameters are of secondary importance for determining present-day ToA radiative flux, but they are the dominant source of uncertainty in the change in atmospheric radiative balance on multi-century and multi-decadal timescales. The contributions to variance in aerosol ERF depend on how parameters influence the atmospheres response to the *change* in anthropogenic emissions, while ToA RSR variance depends on how they influence the

state of the atmosphere.

We now explore the extent to which present-day measurements of global mean ToA radiative flux can help constrain the change in flux between two time periods, which defines the ERF. What can be expected based on the common causes of uncertainty in ToA RSR and aerosol ERF? First, although the variance in ToA RSR is mostly caused by uncertainty in the physical atmosphere model and the variance in aerosol ERF by uncertainty in the aerosol model, there is actually substantial overlap in the combinations of parameters causing uncertainty. About 40% of the aerosol ERF variance is determined by parameters that also account for about 70% of the RSR variance (Rad_Mcica_Sigma, Sea_Spray and Sig_W.) It might therefore be expected that tight constraint of present-day RSR will have some effect on the range of modelled aerosol ERF. Second, although atmospheric parameters cause the majority of present-day RSR uncertainty, the aerosol parameters alone produce a 95% ToA RSR credible interval of 97.7 - 106.1 $\mathrm{W\,m^{-2}}$ (around 40% of the original credible range). This large contribution of aerosols to the uncertainty in present-day RSR makes it reasonable to assume that observations of RSR will provide at least some constraint on aerosol ERF by reducing the component of RSR variance attributable to aerosols.

Fig. 3 shows the effect of constraining the modelled present-day RSR to within $\pm 0.25\mathrm{W\,m^{-2}}$ and $\pm 0.5\,\mathrm{W\,m^{-2}}$ of $98.3\,\mathrm{W\,m^{-2}}$, the multi-year average of the Clouds and the Earth's Radiant Energy System (CERES) observations (Loeb *et al.*, 2009). The ± 0.25 W $\mathrm{m^{-2}}$ provides a very tight constraint on the model: it represents just 2% of the modelled RSR range and includes only around 5% of the 270000 emulator-sampled model variants used to generate the full RSR probability density function. Consequentially, the smaller set of observationally constrained model variants also predicts reasonably constrained 1978 and 1850 RSR ranges. However, Fig. 3 shows that the 1978-PD and 1850-PD aerosol ERFs are essentially unconstrained when the near-CERES RSR variants are used compared to using the full sample of credible model variants. Very negative 1850-PD forcings (lower than around -2.2 $\mathrm{W\,m^{-2}}$) can be ruled out, but this represents only ($\sim$10%) of the credible aerosol ERF range.

Very dense sampling of multi-dimensional parameter space produces many model variants with very similar present-day ToA RSR values but vastly different aerosol ERF values. This diversity of credible model variants would be overlooked had we perturbed parameters individually. Constraining the parameter space to match observations significantly reduces the likelihood of low Rad_Mcica_Sigma values (Extended Data Fig. 7), suggesting that the lack of constraint of aerosol ERF despite tight RSR constraint is partly due to model equifinality (Beven & Freer, 2001; Lee *et al.*, 2016), where numerous parameter combinations in a complex model produce equally plausible output because of error compensation. To try to overcome the multi-dimensionality of the problem, we restricted the near-CERES sample further by limiting the allowed range of the dominant source of uncertainty for both RSR and aerosol ERF (Rad_Mcica_Sigma). Observationally constraining the largest source of variance in present-day *state* of the atmosphere (RSR in this case) is expected to provide a constraint on the *change* in state (Lee *et al.*, 2016). However, restricting Rad_Mcica_Sigma to within 2% of its original range and constraining the parameter space with CERES observations has no appreciable effect on the aerosol ERF uncertainty range (Extended Data Table 3).

Our results give an insight into the difficulty of reducing multi-model diversity in aerosol ERF and in reaching a consensus on the extent to which aerosols have contributed to historical changes in the planetary energy balance. The ToA radiative flux is the global measurement most closely related to ERF, and these two model quantities share common sources of uncertainty. Nevertheless, observational constraint of ToA flux

representing just 2% of the model's prior range has very little impact on the models ability to calculate aerosol ERF. Climate models are routinely evaluated against present-day radiative fluxes so as to ensure accurate characterisation of the present-day state of the atmosphere. By highlighting how different parameters and processes control the change in planetary radiative balance in one state-of-the-art model our results point to one reason why uncertainty in aerosol ERF has persisted through the various generations of climate model development. Our results, combined with those of other studies that have comprehensively sampled model uncertainties (Calisto *et al.*, 2014; Lee *et al.*, 2016; Ghan *et al.*, 2016), suggest that multi-decadal aerosol ERF uncertainty may only be reduced by simultaneously applying a large number of observational constraints (Sexton *et al.*, 2012; Sanderson, 2010; Collins *et al.*, 2012) covering pristine and polluted environments, targeting the specific processes identified here. Although PD RSR observations are not important for constraining multi-decadal , multi-century aerosol ERF they may be important for constraining other parts of the climate system. Equifinality limits the effect of each individual observed variable on model spread, and the challenge now is to find optimum combinations of constraints that overcome this problem. Reducing the uncertainty in multi-decadal aerosol ERF will require extensive collaboration between modelling and observational groups and a focus on uncertainty reduction, rather than quantification.

5.1 Methods

Methods and associated references are available in the online version of this letter.

5.2 Acknowledgments

Data can be made available upon request from the corresponding author. L. A. Regayre is funded by a Doctoral Training Grant from the Natural Environment Research Council (NERC) and a CASE studentship with the UK Met Office Hadley Centre. B. B. B. Booth was supported by the Joint UK DECC/Defra Met Office Hadley Centre Climate Programme (GA01101). K. S. Carslaw acknowledges funding from the Royal Society Wolfson Award. We acknowledge funding from NERC under grants AEROS, ACID-PRUF and GASSP (NE/G006172/1, NE/I020059/1 and NE/J024252/1). This work used the ARCHER UK National Supercomputing Service (http://www.archer.ac.uk). ARCHER project allocation n02-FREEPPE was used to create the present-day ensemble and the Leadership Project allocation n02-CCPPE was used to create the pre-industrial ensemble. The authors appreciate the commitment given by all those who participated in the expert elicitation exercise which supported this research, particularly S. Turnock, D. Hamilton, A. Schmidt, C. Scott, R. Stevens, E. Butt, C. Reddington, M. Woodhouse, D. Spracklen and O. Wild.

Author contributions

Leighton Regayre tested the model configuration, designed and prepared the ensemble and analysed the results. Leighton Regayre and Ken Carslaw wrote the letter. Ken Carslaw, Ben Booth, Kirsty Pringle, David Sexton and Jill Johnson contributed to the analysis and interpretation of results. Ken Carslaw, Masaru Yoshioka, Kirsty Pringle, Graham Mann, Jill Johnson, Grenville Lister, Nicolas Bellouin, James Mollard and Ben Johnson helped prepare the model configuration that served as the template for the ensemble. The screening of atmospheric parameters was conducted by Leighton Regayre, David Sexton and Ken Carslaw. Leighton Regayre and Jill Johnson elicited probability

density functions of all aerosol parameters. Ken Carslaw, Nicolas Bellouin, Colin Johnson, Graham Mann, Kirsty Pringle, Ben Johnson, James Mollard, Masaru Yoshioka and Lindsay Lee participated in the formal elicitation. Jill Johnson contributed to the statistical design. Grenville Lister and Masaru Yoshioka advised on computational aspects of the ensemble creation.

Competing Financial Interests
The authors declare no competing financial interests.

References - Chapter 5

Beven, K., & Freer, J. 2001. Equifinality, data assimilation, and uncertainty estimation in mechanistic modelling of complex environmental systems using the GLUE methodology. *J. Hydrol.*, **249**, 11–29.

Boucher, O., Randall, D., Artaxo, P., Bretherton, C., Feingold, G., Forster, P., Kerminen, V. M., Kondo, Y., Liao, H., Lohmann, U., Rasch, P., Satheesh, S. K., Sherwood, S., Stevens, B., & Zhang, X. Y. 2013. Clouds and aerosols. *In:* Stocker, T. F., Qin, D., Plattner, G. K., Tignor, M., Allen, S. K., Boschung, J., Nauels, A., Xia, Y., Bex, V., & Midgley, P. M. (eds), *Climate change 2013: The physical science basis. contribution of working group i to the fifth assessment report of the intergovernmental panel on climate change*. Cambridge, United Kingdom and New York, NY, USA: Cambridge University Press.

Calisto, M., Folini, D., Wild, M., & Bengtsson, L. 2014. Cloud radiative forcing intercomparison between fully coupled CMIP5 models and CERES satellite data. *Ann. Geophys.*, **32**, 793–807.

Carslaw, K. S., Lee, L. A., Reddington, C. L., Pringle, K. J., Rap, A., Forster, P. M., Mann, G. W., Spracklen, D. V., Woodhouse, M., Regayre, L. A., & Pierce, J. R. 2013. Large contribution of natural aerosols to uncertainty in indirect forcing. *Nat.*, **503**, 67–71.

Collins, M., Chandler, R. E., Cox, P. M., Huthnance, J. M., Rougier, J., & Stephenson, D. B. 2012. Quantifying future climate change. *Nat. Clim. Ch.*, **2**, 403–409.

Collins, M., Knutti, R., Arblaster, J., Dufresne, J. L., Fichefet, D., Friedlingstein, P., Gao, X., Gutowski, W. J., Johns, T., Krinner, G., Shongwe, M., Tebaldi, C., Weaver, A. J., & Wehner, M. 2013. Long-term climate change: Projections commitments and irreversibility. *In:* Stocker, T. F., Qin, D., Plattner, G. K., Tignor, M., Allen, S. K., Boschung, J., Nauels, A., Xia, Y., Bex, V., & Midgley, P. M. (eds), *Climate change 2013: The physical science basis. contribution of working group i to the fifth assessment report of the intergovernmental panel on climate change*. Cambridge, United Kingdom and New York, NY, USA: Cambridge University Press.

Croft, B., Pierce, J. R., Martin, R. V., Hoose, C., & Lohmann, U. 2012. Uncertainty associated with convective wet removal of entrained aerosols in a global climate model. *Atmos. Chem. Phys.*, **12**, 10725–10748.

Ghan, S. J., Wang, M., Zhang, S., Ferrachat, S., Gettleman, A., Griesfeller, J., Kipling, Z., Lohmann, U., Morrison, H., Neubauer, D., Partridge, D. G., Stier, P., Takemura, T., Wang, H., & Zhang, K. 2016. Challenges in constraining anthropogenic aerosol effects on cloud radiative forcing using present-day spatiotemporal variability. *Proc. Nat. Ac. Sci.*, **Early Edition**, Early Edition.

Golaz, J. C., Horowitz, L. W., & II, H. Levy. 2013. Cloud tuning in a coupled climate model: impact on 20th century warming. *Geophys. Res. Lett.*, 1–20.

Granier, C., Bessagnet, B., Bond, T., D'Angiola, A., van der Gon, H. D., Frost, G. J., Heli, A., Kaiser, J. W., Kinne, S., Kilmont, Z., Kloster, S., Lamarque, J. F., Liousse, C., Masui, T., Meleux, F., Mieville, A., Ohara, T., Raut, J. C., Riahi, K., Schultz, M. G., Smith, S. J., Thompson, A., van Aardenne, J., van der Werf, G. R., & van Vuuren, D. P. 2011. Evolution of anthropogenic and biomass burning emissions of air pollutants at global and regional scales during the 1980-2010 period. *Climatic change*, **109**, 163–190.

Haerter, J. O., Roeckner, E., Tomassini, L., & von Storch, J. S. 2009. Parametric uncertainty effects on aerosol radiative forcing. *Geophys. Res. Lett.*, **36**, 1–5.

Knutti, R., Krähenmann, S., Frame, D. J., & Allen, M. R. 2008. Comment on "Heat capacity, time constant, and sensitivity of earth's climate system" by SE Schwartz.". *J. Geo. Res. Atmos.*, **113**, 1984–2012.

Lee, L. A., Pringle, K. J., Reddington, C. L., Mann, G. W., Stier, P., Spracklen, D. V., Pierce, J., & Carslaw, K. S. 2013. The magnitude and causes of uncertainty in global model simulations of cloud condensation nuclei. *Atmos. Chem. Phys.*, **13**, 8879–8914.

Lee, L. A., Reddington, C. L., & Carslaw, K. S. 2016. On the relationship between aerosol model uncertainty and radiative forcing uncertainty. *Proc. Nat. Ac. Sci.*, **Early Edition**, Early Edition.

Loeb, N. G., Wielicki, B. A., Doelling, D. R., Smith, G. L., Keyes, D. F., Kato, S., Manalo-Smith, N., & Wong, T. 2009. Toward optimal closure of the Earth's top-of-atmosphere radiation budget. *J. Climate.*, **22**, 748–766.

Lohmann, U., & Ferrachat, S. 2010. Impact of parametric uncertainties on the present-day climate and on the anthropogenic aerosol effect. *Atmos. Chem. Phys.*, **10**, 11373–11383.

Michibata, T., & Takemura, T. 2015. Evaluation of autoconversion schemes in a single model framework with satellite observations. *J. Geo. Res. Atmos.*, **120**, 1–21.

Nam, C., Bony, S., Dufresne, J. L., & Chepfer, H. 2012. The 'too few, too bright' tropical low-cloud problem in CMIP5 models. *Geophys. Res. Lett.*, **39**, L21801.

Neubauer, D., Lohmann, U., Hoose, C., & Frontoso, M/ G. 2014. Impact of the representation of marine stratocumulus clouds on the anthropogenic aerosol effect. *Atmos. Chem. Phys.*, **14**, 11997–12022.

Regayre, L. A., Pringle, K. J., Booth, B. B. B., Lee, L. A., Mann, G. W., Browse, J., Woodhouse, M. T., Rap, A., Reddington, C. L. S., & Carslaw, K. S. 2014. Uncertainty in the magnitude of aerosol-cloud radiative forcing over recent decades. *Geophys. Res. Lett.*, **41**, 9040–9049.

Sanderson, B. M. 2010. A multimodel study of parametric uncertainty in predictions of climate response to rising greenhouse gas concentrations. *J. Climate.*, **24**, 1362–1377.

Sexton, D. M. H., Murphy, J. M., Collins, M., & Webb, M. J. 2012. Multivariate probabilistic projections using imperfect climate models Part I: outline of methodology. *Clim. Dyn.*, **38**, 2513–2542.

Sexton, David M. H., Karmalkar, A., Murphy, J., Booth, B. B. B., & Regayre, L. A. In prep.. The elicitation of distributions of parameters in HadGEM3 versions GA4 and GA7 for use in perturbed parameter ensembles. *Hadley Centre technical note, Met Office, U.K.*

Shiogama, H., Watanabe, M., Yoshimori, M., Yokohata, T., Ogura, T., Annan, J. D., Hargreaves, J. C., Abe, M., Kamae, Y., O'ishi, R., Nobui, R., Emori, S., Nozawa, T., Abe-Ouchi, A., & Kimoto, M. 2012. Perturbed physics ensemble using the MIROC5 coupled atmosphere-ocean GCM without flux corrections: experimental design and results. *Clim. Dyn.*, **39**, 3041–3056.

Steir, P., Schutgens, N. A. J., Bian, H., Boucher, O., Chin, M., Ghan, S., Huneeus, N., Kinne, S., Lin, G., Myhre, G., Penner, J. E., Randles, C., Samset, B., Schulz, M., Yu, H., & Zhou, C. 2012. Host model uncertainties in aerosol radiative forcing estimates: results from the AeroCom prescribed intercomparison study. *Atmos. Chem. Phys. Disc.*, **12**, 25487–25549.

Stevens, B. 2015. Rethinking the lower bound on aerosol radiative forcing. *J. Cli.*, **28**, 4794–4819.

Stevens, B., & Feingold, G. 2009. Untangling aerosol effects on clouds and precipitation in a buffered system. *Nat.*, **461**, 607–613.

Storelvmo, T., Lohmann, U., & Bennartz, R. 2009. What governs the spread in shortwave forcings in the transient IPCC AR4 models? *Geophys. Res. Lett.*, **36**, L01806.

Tett, S. F. B., Rowlands, D. J., Mineter, M. J., & Cartis, C. 2013. Can top-of-atmosphere radiation measurements constrain climate predictions? part II: Climate sensitivity. *J. Climate.*, **26**, 9367–9383.

Textor, C., Schulz, M., Guibert, S., Kinne, S., Balkanski, Y., Bauer, S., Berntsen, T., Berglen, T., Boucher, O., Chin, M., Dentener, F., Diehl, T., Easter, R., Feichter, H., Fillmore, D., Ghan, S., Ginoux, P., Gong, S., Grini, A., Hendricks, J., Horowitz, L., Huang, P., Isaksen, I., Iversen, I., Kloster, S., Koch, D., Kirkevåg, A., Kristjansson, J. E., Krol, M., Lauer, A., Lamarque, J. F., Liu, X., Montanaro, V., Myhre, G., Penner, J., Pitari, G., Reddy, S., Seland, O., Stier, P., Takemura, T., & Tie, X. 2006. Analysis and quantification of the diversities of aerosol life cycles within AeroCom. *Atmos. Chem. Phys.*, **6**, 1777–1813.

Textor, C., Schulz, M., Guibert, S., Kinne, S., Balkanski, Y., Bauer, S., Berntsen, T., Berglen, T., Boucher, O., Chin, M., Dentener, F., Diehl, T., Feichter, J., Fillmore, D., Ginoux, P., Gong, S., Grini, A., Hendricks, J., Horowitz, L., Huang, P., Isaksen, I. S. A., Iversen, T., Kloster, S., Koch, D., Kirkevåg, A., Kristjansson, J. E., Kro, M., Lauer, A., Lamarque, J. F., Liu, X., Montanaro, V., Myhre, G., Penner, J. E., Pitari, G., Reddy, M. S., Seland, O., Stier, P., Takemura, T., & Tie, X. 2007. The effect of harmonized emissions on aerosol properties in global models - an AeroCom experiment. *Atmos. Chem. Phys.*, **7**, 4489–4501.

Tost, H., Lawrence, M. G., Brühl, C., & Jöckel, P. 2010. Uncertainties in atmospheric chemistry modelling due to convection parameterisations and subsequent scavenging. *Atmos. Chem. Phys.*, **10**, 1931–1951.

Wilcox, L. J., Highwood, E. J., Booth, B. B. B., & Carslaw, K. S. 2015. Quantifying sources of inter-model diversity in the cloud albedo effect. *Geophys. Res. Lett.*, **42**, 1568–1575.

Zhang, S., Wang, M., Ghan, S.J., Ding, A., Wang, H., Zhang, K., Neubauer, D., Lohmann, U., Ferrachat, S., Takeamura, T., Gettleman, A., Morrison, H., Lee, Y. H., Shindell, D. T., Partridge, D. G., Stier, P., Kipling, Z., & Fu, C. 2015. On the characteristics of aerosol indirect effect based on dynamic regimes in climate models. *Atmos. Chem. Phys. Disc.*, **15**, 23683–23729.

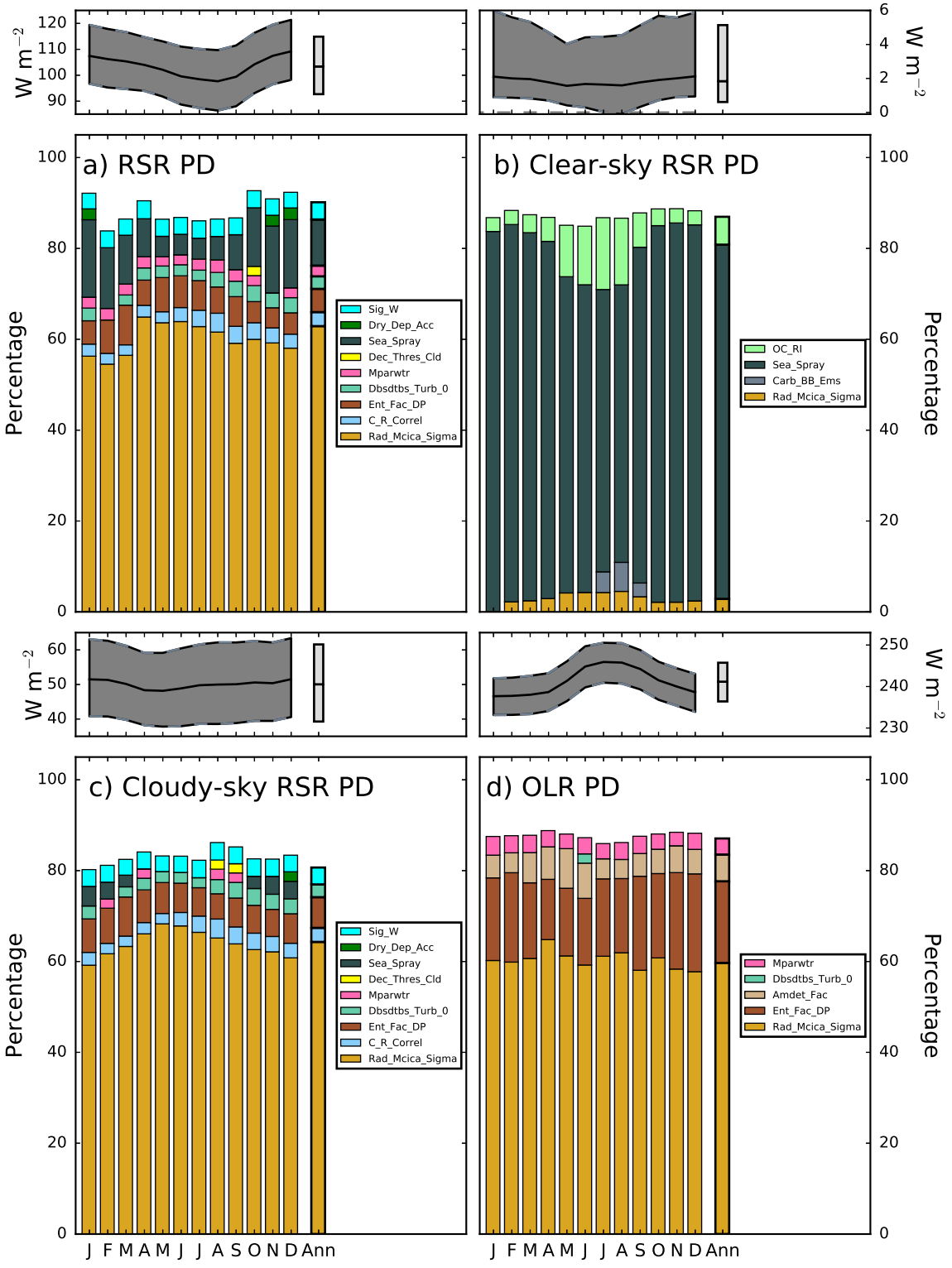

Fig. 1. Percentage contributions to variance in PD global, monthly and annual mean ToA a) RSR, b) Clear-sky RSR c) Cloudy-sky RSR and d) OLR. Each bar contains only those parametric contributions larger than 2%. The monthly and annual medians and 95% credible intervals from the Monte Carlo samples are displayed in the top panels of a)-d). The monthly median values are connected using bold lines and the credible intervals are shaded grey.

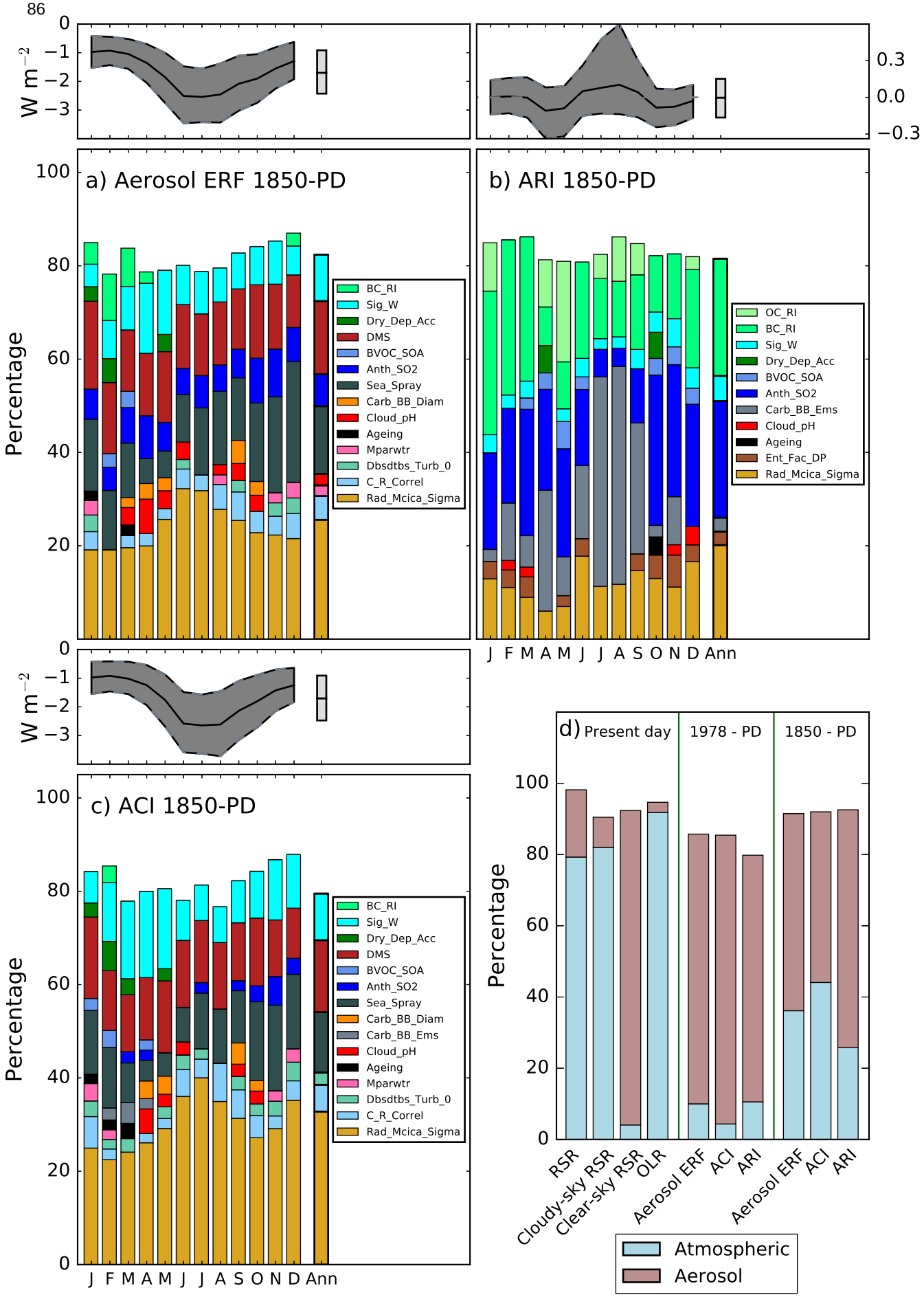

Fig 2. Percentage contributions to variance in 1850-PD global, monthly and annual mean a) Aerosol ERF, b) ARI and c) ACI and d) the relative contributions from atmospheric and aerosol parameters to variance in ToA radiative fluxes and 1978-PD and 1850-PD radiative forcing. Graphical features for a)-c) are identical to those in Fig. 1.

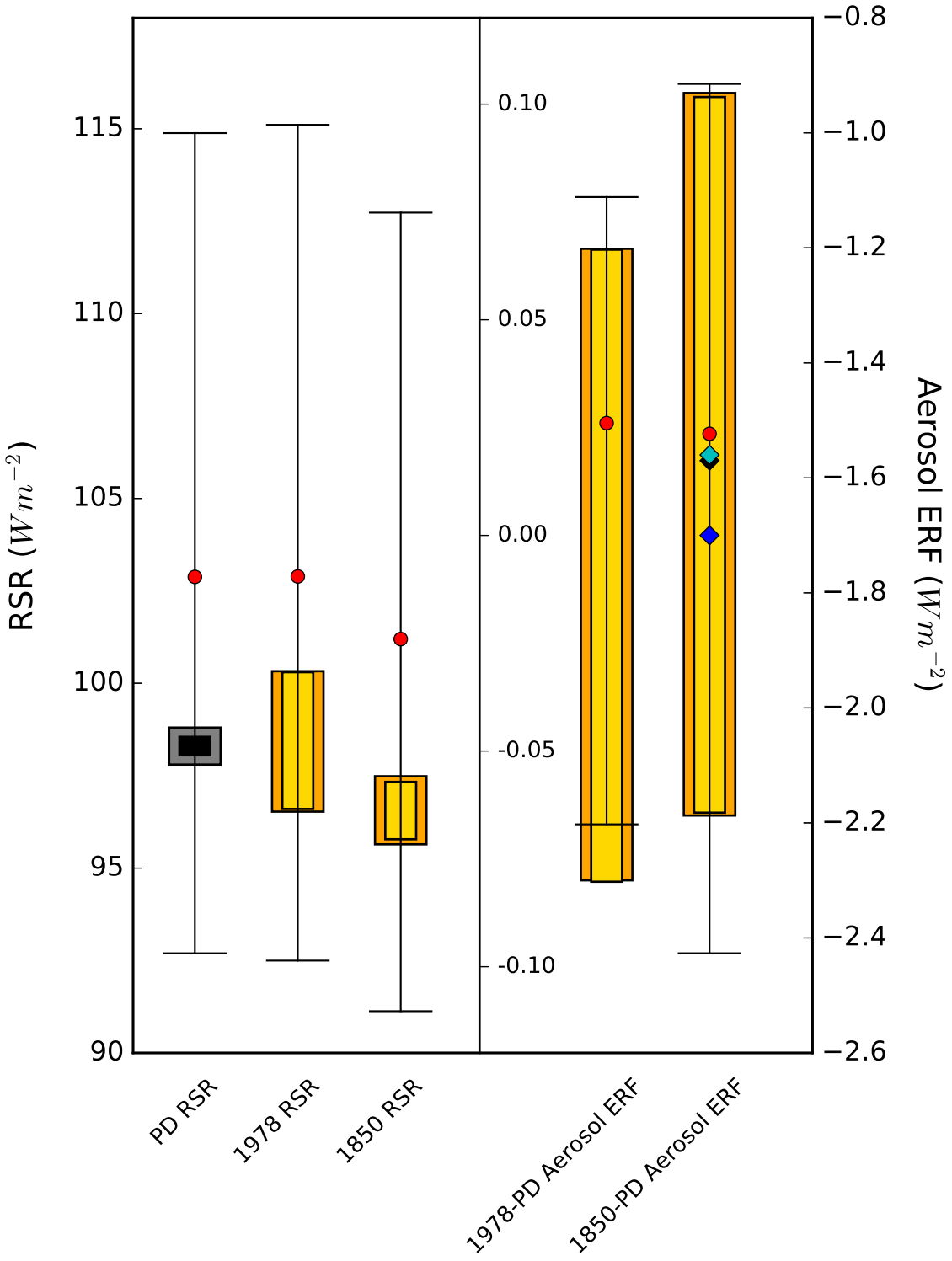

Fig. 3. The range of 1978 and 1850 ToA RSR and 1978-PD and 1850-PD aerosol ERF values resulting from model variants matching observationally constrained present-day ToA RSR. Present-day samples are represented as black and grey boxes. The black box contains all model variants within +/-0.25 Wm^{-2} of the CERES-observed global annual mean present-day ToA RSR. Yellow boxes represent the 95% credible interval of values using the model variants in this sample. The grey box contains all model variants within +/-0.5 Wm^{-2} of the CERES-observed global annual mean ToA RSR and the orange boxes are the 95% credible intervals obtained using these model variants. The black lines show 95% credible intervals of the full 270000 member Monte Carlo sample for each output variable. The middle and right-hand axes are aerosol ERF for 1978-PD and 1850-PD respectively. Output from the simulation with all parameters set to their median values is shown as red dots. The median 1850-PD aerosol ERF from the full 270000 member sample is displayed with a blue diamond. The median of the tightest observationally constrained sample is represented with a black diamond and the median of the same sample restricted further by narrowing the Rad_Mcica_Sigma range with a cyan diamond.

Chapter 6

Overview and Discussion

Parametric contributions to uncertainty in aerosol ERF and its components have been quantified within the size resolving global aerosol model GLOMAP and the global climate model HadGEM3. This study is the first to assess the regional, seasonal and temporal dependence of parametric sources of aerosol forcing uncertainty. Furthermore, priorities for model development targeting the reduction of aerosol ERF uncertainty have been identified, many of which are applicable to other models. Sources of aerosol forcing uncertainty in climatically important regions have been identified and interpreted in the context of recent changes to regional climates. Finally, a comprehensive analysis of the relative importance of aerosol and physical atmosphere (atmospheric) parameters on the atmospheric state and change-of-state has been conducted revealing that improved understanding of both aerosol and atmospheric parameters is required but will reduce uncertainty in different aspects of climate modelling.

6.1 Summary of major results

The following is a summary of the major results of this thesis in the context of the aims outlined in Chapter 1.

1. **The forcing period dependence of parametric contributions to aerosol forcing variance have been quantified using four periods with distinct anthropogenic aerosol emissions: 1750-PD, 1850-PD, 1978-PD and 1998-PD.**

   a) Natural aerosol emission parameters are the largest source of forcing uncertainty over the industrial period causing 45% of the global annual mean CAE forcing variance since 1750. The role of natural aerosol emission uncertainty in causing forcing variance arises because of the non-linear relationship between cloud albedo and aerosol concentrations. Natural aerosols are predominant in the relatively clean pre-industrial atmosphere, hence uncertainty in this source of aerosols significantly affects the forcing calculation (Chapter 2).

   b) Natural aerosols are a weaker source of forcing uncertainty when 1850, rather than 1750, is used to define the start of the industrial period because the baseline atmospheric state is relatively polluted reducing the effect of uncertainty in the natural emissions on the forcing calculation. In the 1850 case natural aerosols cause between 34% and 37% of the CAE forcing variance compared to 45% in the 1750 case (Chapters 2 and 3).

c) Uncertain anthropogenic aerosol emission parameter contributions to CAE forcing variance increase from 34% to 46% when changing the start of the industrial era from 1750 to the relatively polluted 1850 (Chapter 2). Anthropogenic aerosol emissions play a far greater role in determining CAE forcing in the 1978-2008 period contributing nearly 50% of the variance. During the 1978-2008 period substantial regional changes in emissions compensate to produce a near-zero global annual mean forcing, reducing the importance of the baseline aerosol state in the forcing calculation and hence the contribution to forcing variance from natural aerosols. (Chapter 3). The importance of anthropogenic aerosol emission uncertainty relative to natural aerosol emission uncertainty in recent decades is greatly reduced when the cancellation of positive and negative regional forcings is accounted for (Chapter 4).

d) Aerosol process parameters are the largest source of CAE forcing uncertainty in the most recent decade. Over the ten year forcing period 1998-2008 changes in regional and global anthropogenic emissions are relatively small. Therefore anthropogenic emission parameter uncertainty is of reduced importance for forcing than in the 1978-2008 period. In the absence of important anthropogenic and natural emission uncertainties the most uncertain process-based aspects of the GLOMAP model become apparent. (Chapter 3).

e) The period dependence of parametric contributions to CAE forcing variance suggests that the similarity of the forcing period to be simulated and the periods analysed here can inform the choice of model development priorities. For near-term climate projections uncertainty in anthropogenic emission and model process parameters need to be reduced. However for longer-term climate projections into atmospheres relatively clear of anthropogenic aerosols, the reduction of natural emission uncertainty will be priority (Chapters 2, 3 and 5).

2. **The key parametric sources of aerosol forcing uncertainty have been identified by statistically analysing contributions to variance attained through sampling from statistical emulators created using PPEs. PPEs have been created for aerosol ERF and its components using increasingly sophisticated versions of the GLOMAP model and finally in the HadGEM3 model. In all model versions, specific parameters have been identified as priorities for model development that targets the reduction of aerosol forcing uncertainty.**

   a) The emission flux of SO_2 from continuously degassing and sporadically erupting volcanoes and dimethyl sulphide emissions are the largest parametric sources of aerosol forcing uncertainty over the industrial period (Chapters 2 and 3). Sea spray emissions contribute more to industrial period ACI forcing variance than volcanic emissions in the HadGEM3 model (Chapter 5). However, volcanic SO_2 emissions are by far the largest source of the compensation-corrected forcing uncertainty in the 1978-2008 period accounting for more than 25% of the variance (Chapter 4).

   b) Of the anthropogenic aerosol emission parameters anthropogenic SO_2 emission uncertainty is most important over the industrial period. However, carbonaceous aerosol emissions are the main source of anthropogenic emission uncertainty in recent decades.(Chapters 2, 3 and 4).

   c) In the 1998-2008 period when aerosol process parameter uncertainties are the dominant cause of aerosol forcing variance, the removal of aerosols from the atmosphere through wet deposition and the pH dependent production of

aerosol sulphate from the oxidation of sulphur dioxide by ozone are key sources of CAE forcing uncertainty (Chapter 3). The Sig_W parameter, which controls the distribution of sub-grid vertical velocities used to calculate aerosol activation into cloud droplets, directly affects cloud droplet formation in the HadGEM3 model and is therefore an important source of ACI forcing uncertainty regardless of the forcing period. Dry deposition velocities of aerosols in the Accumulation mode and SO_2 are also significant contributors to ACI forcing variance in recent decades (Chapter 5 and Appendix 3).

3. **The magnitude of aerosol forcing uncertainty in climatically important regions over the 1978-2008 period have been quantified and the potential for aerosols to influence large-scale climate effects in recent decades analysed.**

   a) A likely negative forcing in the tropical North Atlantic and positive forcing in the tropical South Atlantic indicate that CAE forcing may have exacerbated the inter-hemispheric difference in sea surface temperatures in recent decades, affecting the position of the regional inter-tropical convergence zone and precipitation in the Sahel. The sign of forcing in the tropical North Atlantic is uncertain with dry deposition rates and the size of carbonaceous aerosol emissions largely determining the values. Tropical South Atlantic CAE forcing in Southern Hemispheric Summer months is also affected by deposition rates, though wet deposition parameters control the variance in that region (Chapter 4).

   b) Uncertainty in the extent to which aerosols may influence North Atlantic tropical storm development via CAE forcing on sea surface temperatures is largely determined by anthropogenic emission and aerosol process parameters. Therefore positive emulated CAE forcing in the extra-tropical North Atlantic (0.51 $\mathrm{W\,m^{-2}}$) is consistent with the theory that reductions in Northern Hemispheric anthropogenic aerosol emissions have warmed sea surface temperatures. However, the negative CAE forcing (-0.14 $\mathrm{W\,m^{-2}}$) over the main hurricane development region during months relevant for hurricane development calls into question the role of Northern Hemispheric aerosol reductions in forcing tropical sea surface temperatures and influencing hurricane development and frequency on decadal time scales (Chapter 4).

   c) CAE forcing in response to changing Asian anthropogenic aerosol emissions has been ruled out as an influence on the position of the Pacific topical storm track. However competing parametric sources of CAE forcing variance, in particular carbonaceous aerosol emission parameters, make the broader extent of CAE forcing influence on tropical Pacific storms less certain (Chapter 4).

   d) The contrast between continental and marine CAE forcing in Asian regions suggests that aerosols play an important role in suppressing development of the East-Asian and Indian Monsoons by reducing the land-sea thermal contrast during early monsoon development. CAE forcing in continental and marine regions are subject to distinct sources of parametric uncertainty, providing insight into the potential causes of the multi-model CAE forcing positive bias in the region (Chapter 4).

   e) The largest annual mean CAE forcing in recent decades is in the region where observed sea surface temperatures are used to predict changes in the El Niño Southern Oscillation. In this region CAE forcing uncertainty is up to 5 times larger than the known forcing resulting from anthropogenic CO_2 emissions. The regional mean CAE forcing (0.24 $\mathrm{W\,m^{-2}}$) is consistent with observed end-of-century change towards conditions more suited to El Ninõ events,

suggesting that an aerosol forced signal may influence the mean ENSO state on multi-decadal time scales (Chapter 4).

f) An entirely positive credible interval of Arctic CAE forcing (0.04, 0.36 $\mathrm{W\,m^{-2}}$) supports the hypothesis that Northern Hemispheric anthropogenic aerosol emission reductions have caused warming in the Arctic in recent decades. Aerosol process parameters are the dominant source of Arctic CAE forcing uncertainty, suggesting that multi-model CAE forcing diversity is likely to be larger than in other regions (Chapter 4).

4. **The relative importance of aerosol emission, deposition and process parameters and atmospheric parameters that affect the properties and distribution of clouds and humidity, as sources of aerosol ERF uncertainty in the HadGEM3 model have been quantified.**

   a) Atmospheric parameters control ToA radiative fluxes in 1850, 1978 and present-day atmospheres accounting for nearly 80% of the ToA RSR variance. The majority of the variance in each year is caused by uncertainty in Rad_Mcica_Sigma the parameter controlling the shape of sub-grid clouds, and therefore the amount of cloud passed to the radiation code. Atmospheric parameters still cause around 50% of the ToA RSR variance when uncertainty in Rad_Mcica_Sigma is neglected. (Chapter 5 and Appendix 3).

   b) Aerosol parameter uncertainty is an important source of ToA RSR variance but less so than uncertainty in atmospheric parameters. The 95% credible interval of ToA RSR calculated by neglecting uncertainty in all atmospheric parameters is (97, 106 $\mathrm{W\,m^{-2}}$); almost 40% of the credible range (93, 115 $\mathrm{W\,m^{-2}}$) from perturbing both aerosol and atmospheric parameters (Chapter 5 and Appendix 3).

   c) Aerosol parameters are the dominant source of aerosol ERF uncertainty over the industrial period and in recent decades. Atmospheric parameters contribute only 36% and around 5% of the variance in 1850-PD and 1978-PD aerosol ERF respectively. Aerosol and atmospheric parameters are both important sources of model uncertainty. However, reducing aerosol ERF uncertainty requires an improved understanding of the processes causing aerosol parameter uncertainty.

5. **The extent to which present-day observations of ToA radiative fluxes can be used to constrain aerosol ERF over the industrial period and in recent decades has been quantified.**

   a) Observations of present-day ToA RSR, with assumed observational uncertainty at the lower end of published values, are able to constrain ToA RSR in the 1850 and 1978 atmospheres. The range of credible ToA RSR values is broader in the 1850 and 1978 cases by several $\mathrm{W\,m^{-2}}$ because atmospheric responses to parameter perturbations differ between environments with different aerosol concentrations and compositions. The credible interval range from each constrained sample is at most 18% of the credible interval range in the unconstrained case, significantly narrowing the emulated ToA RSR range in historical atmospheres (Chapter 5).

   b) Observations of present-day ToA RSR provide almost no constraint on aerosol ERF over the industrial period or in recent decades. In the best case scenario RSR observations reduce 1850-PD aerosol RSR by at most around 10%, ruling out only the most extreme forcings. These results suggest that aerosol ERF forcing uncertainty may only be reduced by applying optimum combinations of multiple observational constraints (Chapter 5).

6.2 Necessary simplifications

This section explores the impact of this research given the simplifications that were necessary due to computational restrictions. The statistical methods outlined in Chapter 1 reduce the computational expense required to perform comprehensive sensitivity analyses, reducing the required number of simulations from tens of thousands to just a few hundred per anthropogenic emission period. Even so more than 1300 full year simulations were needed to create the GLOMAP and HadGEM3 PPEs. The research conducted in this thesis has utilised substantial super-computing resource for conducting and analysing the large ensembles of simulations (e.g. Regayre *et al.* 2016).

The GLOMAP PPEs used in Chapters 2, 3 and 4 were relaxed towards ECMWF climatological values and ISCCP clouds prescribed so as to isolate the aerosol forced signal from other sources of uncertainty, as described in Chapter 1. The HadGEM3 PPE simulations created for Chapter 5 were relaxed towards horizontal winds above around 2km only, as described in Appendix 3, to retain synoptic-scale dynamical features whilst ensuring aerosol forced signals could be detected. The use of prescribed meteorological values in the PPE creation means that no information has been captured regarding the dependence of aerosol forcing parametric sensitivity on meteorological conditions. The vertical extent of convection varies significantly between meteorological years, as does the fraction of natural aerosols in the global distribution (Feng *et al.*, 2011), with potentially large implications for forcing (Liu *et al.*, 2007). Furthermore feedbacks between components of the HadGEM3 model may be underestimated using the 'nudging' approach (Chrastansky & Rotstayn, 2012). Ideally the PPEs would have been created using multi-year averages to calculate forcing values. However even with century-long simulations forced signals can not be isolated as readily as they can from 'nudged' simulations (Kooperman *et al.*, 2012). The PPEs would also have benefited from including a dynamic ocean, rather than prescribing sea surface temperatures (Ocko *et al.*, 2014; Andrews *et al.*, 2015), which would allow the regional climatic effects of aerosol ERF to be directly quantified. Because the analyses conducted in this thesis are either of global annual mean values or are in regions with established relationships between aerosol forcing and climatic responses, the results can be generalised to other meteorological years without significant risk of their being misinterpreted.

All perturbations applied in this research have been to global parameter values. These is no reason to believe that uncertainty in parameters such as anthropogenic SO_2 and carbonaceous emissions should scale globally, rather than regionally as is the case with attribution studies (for example Jones *et al.*, 2013). Anthropogenic influences on uncertainty in emissions (for example Mahowald *et al.* 2010) are also neglected in our experiments. The inclusion of spatially and temporally dependent parameter perturbations was considered during expert elicitation exercises but rejected in favour of perturbing a broader range of uncertain parameters relating to different model processes.

6.3 Future research directions

The breadth of model output produced by the large PPEs used in this thesis gives rise to applications beyond their designed use. The present-day component of the GLOMAP PPE analysed in Chapters 3 and 4 has been used to develop an aerosol climatology for running the HadGEM3 model uncoupled from the GLOMAP model. The results from Chapters 2, 3 and 4, as well as the elicitation exercise and model configuration tests conducted for Chapter 5, informed the Global Aerosol Synthesis and Science Project (GASSP) (GASSP, 2016) experimental design. In the GASSP project output from the

HadGEM and other PPEs will be challenged using a broad range of observational datasets. Chapter 2-5 results have also been used to inform the design of the U.K. Hadley Center Met Office ensemble prediction system currently under development (Sexton *et al.*, In prep.) as part of the Climate Science for Service Partnership (CSSP) - China project (CSSP, 2016).

The HadGEM3 PPE created for Chapter 5 has additional benefits over those from earlier Chapters in that rapid atmospheric adjustments to aerosol and atmospheric parameters have been captured. Preliminary investigations of regional changes in cloud fraction and precipitation in response to parameter perturbations suggest that this PPE has significant potential for use in testing hypotheses about dynamical responses to aerosols. The aerosol forcing of climate effects at the regional level, explored using established relationships in Chapter 4, could be investigated in far greater detail using the HadGEM3 PPE. The ensemble is eminently suitable for informing investigations into recent decadal changes in North Atlantic atmospheric composition (ACSIS, 2016) and the role of aerosols in causing observed surges and temporary slowdowns in global mean surface temperatures (SMURPHS, 2016) for example. The PPE could be used to identify specific observations that could help reduce uncertainty in climatic responses to aerosol forcing over Africa (CLARIFY, 2016). Furthermore, the range of global annual mean aerosol ERF values produced by the ensemble suggests it could be used to investigate the causes of common GCM biases such as Southern Ocean shortwave radiation bias (Nam *et al.*, 2012).

In Chapter 5 ToA RSR observations were shown to be a poor constraint of aerosol ERF over multiple decades. Trends in regional anthropogenic emissions do not change greatly during the 1998-2008 period suggesting that there may be value in investigating the use of recent decadal aerosol ERF observations as a constraint on aerosol ERF in other periods. This is one strategy for reducing uncertainty in multi-decadal aerosol ERF but in practice, as indicated in the concluding paragraph in Chapter 5, this task will require extensive collaboration between modelling and observational groups and a shift in focus from uncertainty quantification to uncertainty reduction.

References - Chapter 6

ACSIS. 2016. *Atmospheric Observations Model Simulations.* ***https://www.ncas.ac.uk/index.php/en/climate–science–programme/climate–projects/353–acsis–ltsm****. Accessed: March 2016.*

Andrews, T., Gregory, J. M., & Webb, M. J. 2015. The dependence of radiative forcing and feedback on evolving patterns of surface temperature change in climate models. *J. Climate.*, **28**, 1630–1648.

Chrastansky, A., & Rotstayn, L. D. 2012. The effect of ENSO-induced rainfall and circulation changes on the direct and indirect radiative forcing from Indonesian biomass-burning aerosols. *Atmos. Chem. Phys.*, **12**, 11395–11416.

CLARIFY. 2016. *Cloud–Aerosol–Radiation Interactions and Forcing: Year 2016 (CLARIFY 2016).* ***http://gtr.rcuk.ac.uk/projects?ref=NE/L013746/1****. Accessed: March 2016.*

CSSP. 2016. *Climate Science for Service Partnership China.* ***http://www.metoffice.gov.uk/research/collaboration/csspChina****. Accessed: March 2016.*

Feng, W., Chipperfield, M. P., Domse, S., Monge-Sanz, B. M., Yang, X., & Ramonet, M. 2011. Evaluation of cloud convection and tracer transport in a three-dimensional chemical transport model. *Atmos. Chem. Phys.*, **11**, 5783–5803.

GASSP. 2016. *Global Aerosol Synthesis and Science Project.* ***http://gassp.org.uk/****. Accessed: March 2016.*

Jones, G. S., Stott, P. A., & Chistidis, N. 2013. Attribution of observed historical near surface temperature variations in anthropogenic and natural causes using CMIP5 simulations. *J. Geo. Res. Atmos., Online: http://onlinelibrary.wiley.com/doi/10.1002/jgrd.50239/pdf.*

Kooperman, G. J., Pritchard, M. S., Ghan, S. J., Wang, M., Somerville, R. C. J., & Russell, L. M. 2012. Constraining the influence of natural variability to improve estimates of global aerosol indirect effects in a nudged version of the Community Atmosphere Model 5. *J. Geo. Res.*, **117**, 1–16.

Liu, X., Penner, J., Das, B., Bergmann, D., Rodriguez, J., Strathan, S., Wand, M., & Feng, Y. 2007. Uncertainties in global aerosol simulations: Assessment using three meteorological datasets. *J. Geo. Res.*, **112**.

Mahowald, N. M., Kloster, S., Engelstaedter, S., Moore, J. K., Mukhopadhyay, S., McConnell, J. R., Albani, S., Doney, S. C., Bhattacharya, A., Curran, M. A. J., Flanner, M. G., Hoffman, F. M., Lawrence, D. M., Lindsay, K., Mayewski, P. A., Neff,

J., Rothenberg, D., Thomas, E., Thornton, P. E., & Zender, C. S. 2010. Observed 20th century dust variability: impact on climate and biogeochemistry. *Atmos. Chem. Phys.*, **10**, 10875–10893.

Nam, C., Bony, S., Dufresne, J. L., & Chepfer, H. 2012. The 'too few, too bright' tropical low-cloud problem in CMIP5 models. *Geophys. Res. Lett.*, **39**, L21801.

Ocko, I. B., Ramaswamy, V., & Ming, Y. 2014. Contrasting climate responses to the scattering and absorbing features of anthropogenic aerosol forcings. *J. Climate.*, **27**, 5329–5345.

Regayre, L .A., Carslaw, K.S., Pringle, K. J., Lee, L. A., & Booth, B. B. B. 2016. *The Climatic Importance of Aerosol Uncertainty - N8 Case study,* ***http://n8hpc.org.uk/the–climatic–importance–of–aerosol–uncertainty–3/****. Accessed: March 2016.*

Sexton, David M. H., Karmalkar, A., Murphy, J., Booth, B. B. B., & Regayre, L. A. In prep.. The elicitation of distributions of parameters in HadGEM3 versions GA4 and GA7 for use in perturbed parameter ensembles. *Hadley Centre technical note, Met Office, U.K.*

SMURPHS. 2016. *Securing Multidisciplinary UndeRstanding and Prediction of Hiatus and Surge events (SMURPHS).* ***http://www.smurphs.leeds.ac.uk/****. Accessed: March 2016.*

Chapter 7

Appendices

Appendix 1 - Supporting Information for Chapter 2

METHODS

Model description. The GLObal Model of Aerosol Processes (GLOMAP-mode)[15,16] is a three-dimensional global aerosol microphysics model that simulates the evolution of the particle size distribution and size-resolved chemical composition of aerosol particles on a global three-dimensional grid. The model has previously been evaluated against observations[16] and improved by comparing aerosol simulations against a more detailed version of the model that treats the aerosol size distribution using a sectional approach[32]. The GLOMAP models have been widely used and evaluated against global measurements of particle number concentrations[33,34], CCN[35,36], aerosol chemical components[37–39], and cloud droplets[40]. The aerosol module is run within the TOMCAT global three-dimensional offline chemistry transport model[41]. The aerosol and chemical species are transported by three-dimensional meteorological fields read in from the European Centre for Medium-Range Weather Forecasts (ECMWF) ERA-Interim reanalyses for 2008. Aerosol transport is advanced every 30 min by interpolating between the analyses, which are updated every 6 h and the aerosol microphysical/chemical processes are calculated on a range of shorter time-steps of less than 30 min. Uncoupling the aerosol from the model transport and meteorology in the chemistry transport model (so that aerosol does not affect meteorology) is equivalent to the commonly used "double-call" approach in a climate model[42] in which the aerosol radiative effects are decoupled from the model physics so that particular radiative forcings can be diagnosed using pairs of model runs. The model was run at a horizontal resolution of $2.8^\circ \times 2.8^\circ$ with 31 vertical levels between the surface and 10 hPa.

The aerosol size distribution is defined by seven log-normal modes: one nucleation mode and soluble and insoluble modes covering the Aitken, accumulation and coarse size ranges. The aerosol chemical components are sulphate, sea salt, black carbon, particulate organic matter and dust. Secondary organic aerosol is produced from the first stage oxidation products of biogenic monoterpenes and anthropogenic volatile-organic-carbon compounds, and is assumed to have zero vapour pressure. It is combined with the particulate-organic-matter component after kinetic condensation on the aerosol. The model includes dust emissions, but we do not perturb them because we focus on the effect on CCN concentrations, which we have previously shown are not strongly affected by dust particles even in intense dust storms[43].

The microphysical model resolves the main processes that shape the particle size distribution on a global scale: new particle formation, coagulation, gas-to-particle transfer, cloud processing, and dry and wet deposition. Wet deposition of particles occurs by two processes. In-cloud nucleation scavenging in which activated particles form cloud droplets and are removed in precipitation and below-cloud impaction scavenging by falling raindrops. ECMWF meteorological fields are used to diagnose large-scale frontal precipitation and sub-grid convective precipitation is assumed to occur in 30% of the affected grid box area. Low-level stratiform clouds are read in separately from International Satellite Cloud Climatology Project (ISCCP) D2 data[30]. In these clouds we assume that aerosol particles are activated and subsequently undergo 'cloud processing' in which sulphate mass is added to activated aerosol owing to the aqueous-phase oxidation of sulphur dioxide.

Concentrations of the oxidants OH, O_3, H_2O_2 and NO_3 and HO_2 were specified on the three-dimensional grid using six-hourly monthly mean concentrations from a TOMCAT simulation with detailed tropospheric chemistry[44]. Concentrations of H_2O_2 are depleted through the aqueous-phase reaction with SO_2 and replenished through the reaction $HO_2 + HO_2$ (ref. 15). A spin-up period of six months was performed (three months of which had parameters set at their median value and formed the basis of a further three-month spin for each of the runs with the changed parameter settings).

Emissions. The emission fluxes were perturbed by scaling baseline values, which are specified in Extended Data Table 1 for the 1750–2000 simulations, and in Extended Data Table 2 for the 1850–2000, 1900–2000 and 1850–1980 simulations. The Aerosol Comparisons between Observations and Models (AeroCom) emissions scenarios used for 1750 and 2000 are not available for the intermediate years. For the three additional time periods we therefore used the emissions prepared for the Atmospheric Chemistry and Climate Model Intercomparison Project (ACCMIP[45]) for 1850, 1900, 1980 and 2000. For the sensitivity runs, we show results for June after two months of spin-up after the perturbations were applied.

Cloud droplet number concentrations. CDNCs were calculated as a post-processing step using an activation parameterization[46] and the modelled monthly mean aerosol size distribution and composition in each grid cell for each perturbed parameter run. These calculations account for the coupling between the uncertain aerosol particle size distribution (and composition) and the number of particles activated into cloud droplets.

An updraught speed of 0.15 m s^{-1} was used over marine regions and 0.3 m s^{-1} over land, which is typical of cloud-base speeds in low-level stratus and stratocumulus clouds. Because updraft is highly variable in clouds it is normal to report updraft measurements as the standard deviation σ of a probability density function of updrafts (normally centred on zero). However, it is possible to calculate CDNC using a single characteristic updraft speed (w^*) that gives comparable results to using a probability density function of updrafts[47]. The characteristic speed is given by $w^* = B\sigma$, where B is a conversion factor constrained through closure studies to be in the range 0.65–0.8 (refs 47, 48). Here, we use $w^* = 0.15$ m s^{-1} over marine regions, which equates to $\sigma = 0.19$–0.23 m s^{-1}, and $w^* = 0.3$ m s^{-1} over land, which equates to $\sigma = 0.38$–0.46 m s^{-1}. The updrafts used to calculate CDNC should be representative of cloud base, where activation primarily occurs. Updrafts at cloud base are typically smaller than in-cloud updrafts as the latent heat released by condensation onto cloud droplets fuels higher in-cloud updrafts[49,50]. For example, in measurements during the Marine Stratus/Stratocumulus Experiment (MASE) experiment[51] the standard deviation rises from 0.3 m s^{-1} at cloud base to 0.6 m s^{-1} at cloud top. Thus, we consider our updraft velocities to be appropriate for cloud base.

To test the effect of higher updraft speeds, we recalculated CDNC for July using $w^* = 0.25$ m s^{-1} over oceans and 0.4 m s^{-1} over land. We then built a new emulator for global annual mean forcing. The global mean forcing changes negligibly at the higher speeds. The fractional contributions to variance change from low to high updraft speed as follows: natural aerosol changes from 45% to 42%, anthropogenic emissions decrease from 34% to 33% and processes rise from 19% to 21%.

Radiative forcing. The forcing was calculated as the difference of top-of-the-atmosphere net short-wave plus long-wave radiative fluxes between the PD and the PI periods. The PD and PI runs were performed using identical meteorological analyses. Each parameter perturbation run in the PI period was paired with its equivalent setting in the PD period. The PI and PD simulations are therefore identical in every respect except for the anthropogenic emissions. The modelled aerosol properties were then used to calculate the CDNC values in the PI and PD periods, from which the forcing was calculated for each two-dimensional grid point of the model.

We used the off-line version of the Edwards and Slingo radiative transfer model[29] with six bands in the short-wave and nine bands in the long-wave, with a delta-Eddington two-stream scattering solver at all wavelengths. We used a monthly mean climatology for water vapour, temperature and ozone based on ECMWF reanalysis data, together with surface albedo and cloud optical depth fields from the International Satellite Cloud Climatology Project (ISCCP-D2)[30] for the year 2000. The diurnal cycle of incoming solar radiation was accounted for, but no diurnal cycle of cloud cover was assumed. The sensitivity of our forcing estimates to the cloud climatology is very small[31], according to an extra set of calculations performed using the 1983–2008 multi-annual ISCCP cloud climatology.

The cloud albedo forcing between the PI and PD experiments is quantified by modifying the cloud droplet effective radius r_e for low- and mid-level water clouds up to 600 hPa:

$$r_e^{PI} = r_e^{PD} \times \left(\frac{CDNC^{PD}}{CDNC^{PI}}\right)^{1/3}$$

where CDNC is the monthly mean cloud droplet number concentration in each grid cell. A fixed value for $r_e^{PD} = 10$ μm is used in order to ensure consistency with the ISCCP cloud retrievals. This overestimates the strength of the forcing because clouds with more droplets tend, on average, to have less water for reasons that are physically understood[52]. However, our conclusions about the relative sources of uncertainty are not affected.

Perturbed parameters. The ensemble of model runs was designed to enable an emulator to be built. The ensemble consists of 168 combinations of parameter settings from 28 parameters representing aerosol and precursor gas emissions, microphysical processes and aerosol model structures. The uncertainty range for each parameter was chosen based on expert elicitation[18] (see Extended Data Table 3 for a complete list). Parameter combinations within the uncertainty range were defined by a maximin Latin Hypercube sampling of the parameter space. Paired simulations were run for one year for 1750 and 2000 using the AeroCom emissions (336 runs in total) and for one month for 1850, 1900, 1980 and 2000 using the ACCMIP emissions. Each parameter setting in the PI era was paired with the same parameter setting in the PD. Anthropogenic emissions (from fossil fuel, biofuel and biomass burning) were set to their 1750, 1850 or 1900 values in the PI era and the year 1980 and 2000 values for the PD and were perturbed by the same factor.

Parameters 1 to 14 define aerosol microphysical processes and the definition of the size distribution modal parameters, whereas parameters 15 to 28 define the emission of aerosols and precursor gases. Full details about the parameter ranges and the process of expert elicitation are provided in ref. 18. Here we summarize the main aspects of the perturbed parameters.

The boundary-layer nucleation parameterization (P1) assumes a rate $j = A[H_2SO_{4(g)}]$, with A (in units of s^{-1}) being the perturbed parameter. Throughout the atmosphere (but important only in the free troposphere) we use a binary homogeneous H_2SO_4–H_2O nucleation rate model scaled by an uncertain factor (P2).

Ageing is the process by which freshly emitted carbonaceous particles (for example, from biomass burning) can become increasingly water soluble as they accumulate water-soluble compounds during transport. The controlling parameter, as used in many global models[53], is the number of monolayers of soluble material required to convert the particles into water-soluble particles, which can then act as CCN. The lower limit of our assumed ageing means that initially insoluble particles become soluble on the timescale of hours in polluted regions. This process affects the number of aerosol particles able to form cloud droplets in the forcing calculation, and also affects the cloud processing of aerosol during run time of the model.

The activation diameter (P4) defines the dry-equivalent diameter at which particles are able to activate to cloud droplets during run time of the model. A single value of activation diameter is used globally in a given run. The activation diameter controls the formation of cloud droplets in all low-level clouds, and thereby controls which particles undergo cloud processing (sulphate production on the particles due to oxidation of sulphur dioxide) and removal in precipitation, and therefore shapes the particle size distribution. Cloud droplet concentrations from run-time of the model are not used in the forcing calculations (they are only used as a physical process that shapes the particle size distribution). For the forcing (see previous section) cloud droplet concentrations are quantified as a post-processing step based on the uncertain particle size distributions and an assumed updraft speed. In reality, the activation diameter in a given cloud updraft is controlled by the particle size distribution, solubility and updraft speed. The updraft speed was not included as a perturbed parameter because the chemical transport model does not have a parameterization of updrafts in different cloud types and environments. Perturbation of the activation diameter accounts approximately for the uncertainty in updraft speed, but by prescribing a value in each simulation it ignores the way that the diameter is coupled to the properties of the aerosol size distribution in a given grid cell. This approach is likely to overestimate the uncertainty because it allows a larger variation in the number of aerosol particles that can be cloud processed, which would otherwise be damped by the coupling of particle number and activation diameter. Nevertheless, activation diameter makes a small contribution to global forcing uncertainty (Fig. 2c).

The parameters SO2O3_CLEAN and SO2O3_POLL (P5 and P6) control the cloud droplet pH, which affects the production rate of aerosol sulphate from oxidation of sulphur dioxide by ozone. The pH is the perturbed parameter and can cause a change in rate by a factor of 10^5 for pH between 3 and 6. One parameter is used for clean (lower acidity) environments (sulphur dioxide less than 0.5 parts per billion) and one for polluted environments.

The in-cloud scavenging diameter offset (P7) controls the diameter of aerosols that can be removed by in-cloud nucleation scavenging. This allows some particles to be activated but not scavenged, assuming that the largest droplets initiate precipitation. The lower limit of P7 (zero nanometres) assumes all activated particles are subject to removal during precipitation.

The scavenging efficiency in ice-containing clouds (P8) controls the fraction of particles accessible to nucleation scavenging when air is below −10 °C. Our previous work has shown this parameter to be important in controlling aerosol transport to the Arctic[38]. Dry deposition of Aitken and accumulation mode particles (P9 and P10) is scaled for each particle size by a given factor. GLOMAP calculates the wind speed and size-dependent deposition velocity due to Brownian diffusion, impaction and interception. The accumulation and Aitken mode width parameters (P11 and P12) define prescribed, globally constant geometric standard deviations of the log-normal size distribution modes. The mode separation diameters (P13 and P14) define the ranges over which the geometric mean radius can vary while staying in a particular mode.

Fossil fuel, biofuel and biomass burning particle emission flux parameters (P15, P16 and P17) scale the mass emission fluxes in the PI based on the 1750, 1850 or 1900 emissions and in the PD based on the year 2000 emissions. The spatial distribution of emissions is different in the PI and PD. Our perturbation accounts for uncertainty in the monthly mean flux but does not account for uncertainty in the spatial pattern or temporal variability in the emissions. Thus, for wildfires we are not able to separate the effects of more intense fires versus more frequent fires, which might have different effects on forcing uncertainty. The biomass burning from open fires was not separated into natural and anthropogenic emissions, so we cannot apportion the uncertainty. Examination of the variation of uncertainty due to these parameters shows a clear seasonal cycle, with a peak contribution to global mean variance of 5% in July and August, which can be attributed to northern mid-latitude wildfires, versus generally less than 1% at other times. The tropical fires are important for CCN[18] but the uncertainty in forcing is limited by the low sensitivity of cloud albedo at very high CCN concentrations. Because most of the northern mid-latitude emissions can be associated with natural fires[54], we have associated the biomass burning uncertainties with the natural emissions.

Fossil fuel, biofuel and biomass burning particle emission sizes (P18, P19 and P20) directly control the number of emitted particles for a given mass flux, and therefore directly influence the CCN population. The sub-grid scale sulphate particle production parameters (P21 and P22) define the formation of particles in sub-grid scale power plant plumes[55,56]. P21 defines the fraction of the emitted sulphur dioxide mass that enters the model grid square as new sulphate particles and P22 defines the dry size of these particles (and hence their number concentration for fixed mass) when emitted into the global grid box.

The sea spray particle mass flux (P23) is scaled by a factor. GLOMAP-mode simulates sea spray particles between 35 nm and 20 μm dry diameter. This parameter conflates multiple sources of uncertainty associated with the wind-speed dependence of the flux such as processes not unaccounted for in the parameterizations (for example, fetch), the wind speed, and the limited spatial resolution of the wind fields in the model.

Anthropogenic sulphur dioxide emissions (P24) are scaled by a factor based on the emissions in 1750, 1850, 1900 and 2000, as described above. Continuously degassing volcanic sulphur dioxide emissions (P25) are scaled based on a global inventory widely used in global models[57]. Time-averaged sporadic emissions are also included. Volcanic emissions are assumed to be the same in the PI and PD simulations.

DMS emissions (P26) are controlled by the sea-water concentration of DMS[58] and the wind-driven transfer velocity parameterization[59]. We conflate these uncertainties by perturbing the calculated sea-air transfer flux by a given factor. This leads to identical absolute perturbations to the DMS flux in the PI era and the PD. We do not account for uncertainty in the spatial pattern of DMS seawater concentration, which is likely to be an important factor in the overall uncertainty[60].

The biogenic secondary-organic-aerosol production parameter (P27) conflates the uncertainty in the emissions of the precursor gases (biogenic volatile organic carbons) and the uncertainty in the yield of secondary-organic-aerosol material following oxidation reactions into a single parameter. P27 scales the volatile organic carbon emissions (with fixed chemical yield) such that global annual secondary-organic-aerosol production lies between the values given in the table. There are also uncertainties in the volatility of different compounds that we do not account for here. The range of emissions used here has been shown to span the range of global *in situ* measurements of organic aerosol[37].

Anthropogenic secondary organic aerosol production (P28) is treated in a similar way to biogenic secondary organic aerosol, by conflating the uncertainty in emissions and yield into a single emission uncertainty. We used the same approach as in ref. 37 by scaling gridded carbon monoxide emissions over a range known to span the range of observed organic aerosol in the PD atmosphere. The range is then scaled further to account for the changes in carbon monoxide emissions in 1850, 1900 and 1980.

Model emulation. Gaussian process emulation[18–20] was used to estimate model predictions at untried points throughout the space of the uncertain model parameters. An emulator was built for the monthly mean first indirect radiative forcing for every two-dimensional grid point (to produce Fig. 1 in the main text) and for the global annual mean and monthly mean forcings to generate Fig. 2 in the main text. The emulator was validated in each case using 84 additional model runs (Extended Data Fig. 1) to ensure that the emulator uncertainty around its mean is low compared to the parametric uncertainty. Twenty-eight of the validation runs were designed to lie near the training points and 64 were defined using a separate Latin Hypercube design[61]. The coefficient of determination (r^2) of the global annual mean emulator forcing versus simulated forcing is 0.94.

Variance-based sensitivity analysis. Variance-based sensitivity analysis is used to decompose the uncertainty in the model predictions to the uncertainty in the model parameters. The total variance of the forcing was calculated by sampling from the emulator mean function using the extended-FAST method[20]. We sampled 5,000 points per parameter (140,000 in total) from the emulator to obtain a probability distribution of forcing. Two measures of sensitivity were calculated: the main effect index measures by how much the variance will be reduced if the parameter can be learnt precisely, and the total effect index measures both the individual effect and the interaction effect of each parameter with all others. The two sensitivity measures are compared to assess the sensitivity of the model output to interactions. Figure 2b (see main text) shows that parameter interactions account for generally less than 10% of the monthly global mean forcing variance (shown as the residual white space above each coloured bar). We note that a nonlinear response of the model output to a parameter across the specified range is accounted for in the main effect variance.

Uncertainty results using different reference periods. Extended Data Table 4 presents results for the additional simulations in which alternative reference years were used for the calculation of forcing (1850 and 1900 instead of 1750), as well as for the period 1850–1980.

32. Mann, G. W. *et al.* Intercomparison of modal and sectional aerosol microphysics representations within the same 3-D global chemical transport model. *Atmos. Chem. Phys.* **12,** 4449–4476 (2012).

33. Spracklen, D. V. *et al.* Explaining global surface aerosol number concentrations in terms of primary emissions and particle formation. *Atmos. Chem. Phys.* **10,** 4775–4793 (2010).
34. Reddington, C. L. *et al.* Primary versus secondary contributions to particle number concentrations in the European boundary layer. *Atmos. Chem. Phys.* **11,** 12007–12036 (2011).
35. Korhonen, H. *et al.* Influence of oceanic dimethyl sulfide emissions on cloud condensation nuclei concentrations and seasonality over the remote Southern Hemisphere oceans: a global model study. *J. Geophys. Res.* **113,** D15204 (2008).
36. Spracklen, D. V., Carslaw, K. S., Poschl, U., Rap, A. & Forster, P. M. Global cloud condensation nuclei influenced by carbonaceous combustion aerosol. *Atmos. Chem. Phys.* **11,** 9067–9087 (2011).
37. Spracklen, D. V. *et al.* Aerosol mass spectrometer constraint on the global secondary organic aerosol budget. *Atmos. Chem. Phys.* **11,** 12109–12136 (2011).
38. Browse, J., Carslaw, K. S., Arnold, S. R., Pringle, K. & Boucher, O. The scavenging processes controlling the seasonal cycle in Arctic sulphate and black carbon aerosol. *Atmos. Chem. Phys.* **12,** 6775–6798 (2012).
39. Schmidt, A. *et al.* Excess mortality in Europe following a future Laki-style Icelandic eruption. *Proc. Natl Acad. Sci. USA* **108,** 15710–15715 (2011).
40. Pringle, K. J. *et al.* A multi-model assessment of the impact of sea spray geoengineering on cloud droplet number. *Atmos. Chem. Phys.* **12,** 11647–11663 (2012).
41. Chipperfield, M. P. New version of the TOMCAT/SLIMCAT off-line chemical transport model: intercomparison of stratospheric tracer experiments. *Q. J. R. Meteorol. Soc.* **132,** 1179–1203 (2006).
42. Bellouin, N. *et al.* Impact of the modal aerosol scheme GLOMAP-mode on aerosol forcing in the Hadley Centre Global Environmental Model. *Atmos. Chem. Phys.* **13,** 3027–3044 (2013).
43. Manktelow, P. T., Carslaw, K. S., Mann, G. W. & Spracklen, D. V. The impact of dust on sulfate aerosol, CN and CCN during an East Asian dust storm. *Atmos. Chem. Phys.* **10,** 365–382 (2010).
44. Arnold, S. R., Chipperfield, M. P. & Blitz, M. A. A three-dimensional model study of the effect of new temperature-dependent quantum yields for acetone photolysis. *J. Geophys. Res.* **110,** D22305, doi: 10.1029/2005JD005998 (2005).
45. Lamarque, J.-F. *et al.* Historical (1850–2000) gridded anthropogenic and biomass burning emissions of reactive gases and aerosols: methodology and application. *Atmos. Chem. Phys.* **10,** 7017–7039 (2010).
46. Fountoukis, C. & Nenes, A. Continued development of a cloud droplet formation parameterization for global climate models. *J. Geophys. Res.* **110,** D11212 (2005).
47. Morales, R. & Nenes, A. Characteristic updrafts for computing distribution-averaged cloud droplet number, autoconversion rate and effective radius. *J. Geophys. Res.* **115,** D18220, doi: 10.1029/2009JD013233 (2010).
48. Peng, Y., Lohmann, U. & Leaitch, R. Importance of vertical velocity variations in cloud droplet nucleation process of marine stratus clouds. *J. Geophys. Res. Atmos.* **110,** D21213, doi:10.1029/2004JD004922 (2005).
49. Lu, M. & Seinfeld, J. H. Study of the aerosol indirect effect by large-eddy simulation of marine stratocumulus. *J. Atmos. Sci.* **62,** 3909–3932 (2005).
50. Hill, A. A., Feingold, G. & Jiang, H. The influence of entrainment and mixing assumption on aerosol-cloud interactions in marine stratocumulus. *J. Atmos. Sci.* **66,** 1450–1464 (2009).
51. Guo, H., Liu, Y. & Daum, P. H. Senum, G. I. & Tao, W.-K. Characteristics of vertical velocity in marine stratocumulus: comparison of large eddy simulations with observations. *Environ. Res. Lett.* **3,** 045020 (2008).
52. Ackerman, A. S. *et al.* The impact of humidity above stratiform clouds on indirect climate forcing. *Nature* **432,** 1014–1017 (2004).
53. Wilson, J., Cuvelier, C. & Raes, F. A modeling study of global mixed aerosol fields. *J. Geophys. Res.* **106,** 34081–34092 (2001).
54. Stocks, B. J. *et al.* Large forest fires in Canada, 1959–1997. *J. Geophys. Res.* **107,** 8149, doi: 10.1029/2001JD000484 (2002).
55. Luo, G. & Yu, F. Sensitivity of global cloud condensation nuclei concentrations to primary sulfate emission parameterizations. *Atmos. Chem. Phys.* **11,** 1949–1959 (2011).
56. Stevens, R. G. *et al.* Nucleation and growth of sulfate aerosol in coal-fired power plant plumes: sensitivity to background aerosol and meteorology. *Atmos. Chem. Phys.* **12,** 189–206 (2012).
57. Andres, R. J. & Kasgnoc, A. D. A time-averaged inventory of subaerial volcanic sulfur emissions. *J. Geophys. Res.* **103,** 25251–25262 (1998).
58. Kettle, A. J. & Andreae, M. O. Flux of dimethylsulfide from the oceans: a comparison of updated data sets and flux models. *J. Geophys. Res.* **105,** 26793–26808 (2000).
59. Nightingale, P. D. *et al.* In situ evaluation of air-sea gas exchange parameterizations using novel conservative and volatile tracers. *Glob. Biogeochem. Cycles* **14,** 373–387 (2000).
60. Woodhouse, M. T. *et al.* Sensitivity of cloud condensation nuclei to regional changes in dimethyl-sulphide emissions. *Atmos. Chem. Phys.* **13,** 2723–2733 (2013).
61. Bastos, L. & O'Hagan, A. Diagnostics for Gaussian process emulators. *Technometrics* **4,** 425–438 (2011).
62. Cofala, J., Amann, M., Klimont, Z. & Schopp, W. *Scenarios of World Anthropogenic Emissions of SO_2, NO_x and CO up to 2030.* Internal report of the Transboundary Air Pollution Programme (International Institute for Applied Systems Analysis, Laxenburg, 2005).
63. Bond, T. C. *et al.* A technology-based global inventory of black and organic carbon emissions from combustion. *J. Geophys. Res.* **109,** D14203, doi:10.1029/2003JD003697 (2004).
64. van der Werf, G. R., Randerson, J. T., Collatz, G. J. & Giglio, L. Carbon emissions from fires in tropical and subtropical ecosystems. *Glob. Change Biol.* **9,** 547–562 (2003).
65. Gong, S. A parameterization of sea-salt aerosol source function for sub and super-micron particles. *Glob. Biogeochem. Cycles* **17,** 1097, doi: 10.1029/2003GB002079 (2003).
66. Guenther, A. *et al.* A global model of natural volatile organic compound emissions. *J. Geophys. Res.* **100,** 8873–8892 (1995).

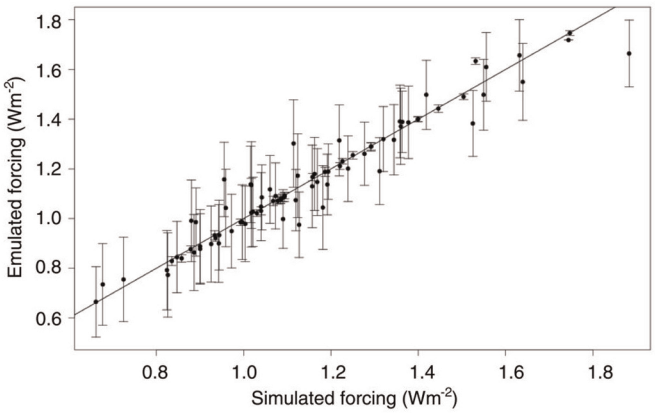

Extended Data Figure 1 | Validation of the global annual mean forcing emulator. The error bars show the emulator 95% uncertainty range around the mean prediction. The 1:1 line is shown.

Extended Data Table 1 | Emissions of aerosols and precursor gases used in the 1750–2000 simulations

Aerosol source	Emitted species	PD (2000) flux	PI (1750) flux	Ref.
Fossil fuel	BC / Tg C per year	3.0	0.0	17
	POM / Tg POM per year	3.2	0.0	17
Power stations	SO_2 / Tg S per year	24.2	0.0	17, 62
Industrial processes	SO_2	19.6	0.0	17, 62
Transportation	SO_2	4.8	0.0	17, 62
Off-road	SO_2	0.8	0.0	17, 62
Biofuel	BC / Tg C per year	1.6	0.4	17, 63
	POM / Tg POM per year	9.1	1.6	17, 63
Domestic	SO_2 / Tg S per year	4.8	0.12	17, 63
Wildfires	BC / Tg C per year	3.1	1.03	17, 64
	POM / Tg POM per year	34.7	12.8	17, 64
	SO_2 / Tg S per year	2.1	1.46	17, 64
Volcanoes	SO_2 / Tg S per year	12.6	12.6	57
Marine dimethyl sulphide	DMS* / Tg S per year	17.1	17.1	58
Sea spray	Salt	Wind-dependent flux	Wind-dependent flux	65
Biogenic volatile organic carbon	Monoterpenes (α-pinene) / Tg POM produced per year	5-360	5-360	37, 66 (for spatial/temporal variation)
Anthropogenic volatile organic carbon	VOC / Tg POM produced per year	2-112	0.0	37

* The DMS emission flux is a global annual value but emissions are calculated at each time step based on the seawater DMS concentration field[58] and a sea–air transfer velocity[59]. These baseline emissions were perturbed according to the factors given in Extended Data Table 3, except for the volatile organic carbon emissions, which were perturbed over the absolute range indicated in this table and in Extended Data Table 3.
BC, black carbon; POM, particulate organic matter; VOC, volatile organic carbon.

Extended Data Table 2 | Emissions of aerosols and precursor gases used in the 1850–2000, 1900–2000 and 1850–1980 simulations.

Aerosol source	Emitted species	2000 flux	1980 flux	1900 flux	1850 flux	Ref.
Fossil fuel	BC / Tg C per year	3.0	2.1	0.4	0.1	45
	POM / Tg POM per year	5.8	3.5	0.8	0.2	45
Power stations	SO_2 / Tg S per year	24.8	30.7	1.8	0.0	45
Industrial processes	SO_2	8.8	11.3	5.6	0.6	45
Transportation	SO_2	7.7	6.9	0.9	0.0	45
Off-road	SO_2	5.6	3.6	0.9	0.0	45
Biofuel	BC / Tg C per year	2.2	2.5	2.0	1.0	45
	POM / Tg POM per year	12.1	12.0	8.9	6.4	45
Domestic	SO_2 / Tg S per year	4.3	6.2	2.6	0.4	45
Wildfires	BC / Tg C per year	1.03	1.03	1.03	1.03	17, 64
	POM / Tg POM per year	12.8	12.8	12.8	12.8	17, 64
	SO_2 / Tg S per year	1.46	1.46	1.46	1.46	17, 64
Volcanoes	SO_2 / Tg S per year	12.6	12.6	12.6	12.6	57
Marine dimethyl sulphide	DMS / Tg S per year	17.1	17.1	17.1	17.1	58
Sea spray	Salt	Wind-dependent flux	Wind-dependent flux	Wind-dependent flux	Wind-dependent flux	65
Biogenic volatile organic carbon	Monoterpenes (α-pinene) / Tg POM produced per year	5-360	5-360	5-360	5-360	37, 66
Anthropogenic volatile organic carbon	VOC / Tg POM produced per year	2.7-145.0	2.6-150.0	0.5-26.5	0.3-15.0	37, 45 (CO emissions)

Extended Data Table 3 | Parameters and their maximum ranges used in the model simulations.

Parameter number	Parameter name	Description	Uncertainty range	Effect
Process parameters				
P1	BL_NUC	Boundary layer nucleation rate	3.2×10^{-7}–2×10^{-4} s^{-1}	Absolute
P2	FT_NUC	Free troposphere nucleation rate	0.01 – 10	Scaled
P3	AGEING	Ageing 'rate' from insoluble to soluble	0.3 – 5 monolayer	Absolute
P4	ACT_DIAM	Cloud drop activation dry diameter	50 – 100 nm	Absolute
P5	SO2O3_CLEAN	pH of cloud drops (controls SO_2 + O_3)	pH 4 – 6.5	Absolute
P6	SO2O3_POLL	pH of cloud drops (SO_2 + O_3)	pH 3.5 – 5	Absolute
P7	NUC_SCAV_DIAM	Nucleation scavenging offset dry diameter	0 – 50 nm	Absolute
P8	NUC_SCAV_ICE	Nucleation scavenging fraction (accumulation mode) in mixed and ice clouds (T< –15 °C)	0 – 1	Scaled
P9	DRYDEP_AIT	Dry deposition velocity of Aitken mode aerosol	0.5 – 2	Scaled
P10	DRYDEP_ACC	Dry deposition velocity of accumulation mode aerosol	0.1 – 10	Scaled
P11	ACC_WIDTH	Mode width (accumulation soluble/insoluble mode)	1.2 – 1.8	Absolute
P12	AIT_WIDTH	Mode width (Aitken soluble/insoluble)	1.2 – 1.8	Absolute
P13	NUC-AIT_SEP	Mode separation diameter (nucleation/Aitken)	9 – 18 nm	Absolute
P14	AIT-ACC_SEP	Mode separation diameter (Aitken/accumulation)	0.9 –2×ACT_DIAM	Scaled
Aerosol and precursor gas emissions				
P15	FF_EMS	BCOC mass emission rate (fossil fuel)	0.5 – 2	Scaled
P16	BB_EMS	BCOC mass emission rate (biomass burning)	0.25 – 4	Scaled
P17	BF_EMS	BCOC mass emission rate (biofuel)	0.25 – 4	Scaled
P18	FF_DIAM	BCOC emitted number median dry diameter (fossil fuel)	30 – 80 nm	Absolute
P19	BB_DIAM	BCOC emitted number median dry diameter (biomass burning)	50 – 200 nm	Absolute
P20	BF_DIAM	BCOC emitted number median dry diameter (biofuel)	50 – 200 nm	Absolute
P21	PRIM_SO4_FRAC	Mass fraction of SO_2 converted to new sulphate particles in sub-grid plumes	0 – 1%	Scaled
P22	PRIM_SO4_DIAM	Emitted number median dry diameter of sub-grid sulphate particles	20 – 100 nm	Absolute
P23	SEASPRAY	Sea spray mass flux (coarse/accumulation)	0.2 – 5	Scaled
P24	ANTH_SO2	SO_2 emission flux (anthropogenic)	0.6 – 1.5	Scaled
P25	VOLC_SO2	SO_2 emission flux (volcanic)	0.5 – 2	Scaled
P26	DMS_FLUX	DMS emission flux	0.5 – 2	Scaled
P27	BIO_SOA	Biogenic monoterpene production of SOA	5 – 360 Tg POM per year *	Absolute
P28	ANTH_SOA	Anthropogenic VOC production of SOA	2 – 112 Tg POM per year *	Absolute

The Latin Hypercube sampling of parameter combinations was designed to lie within these ranges. In the 'effect' column, for the scaled parameters the magnitude of the parameter was multiplied by a factor lying between the maximum and minimum given in the 'uncertainty range' column and for absolute adjustments, the parameter was set to a value within the range of absolute values in the 'uncertainty range' column. BCOC, black carbon/organic carbon; SOA, secondary organic aerosol. *The values given refer to the mass of POM produced, although the perturbations were actually applied to the emitted VOCs. The POM range refers to year 2000. For other years see Extended Data Table 2. The baseline emissions are given in Extended Data Tables 1 and 2.

Extended Data Table 4 | Results for the different periods.

Period	Emissions	Forcing ($W\ m^{-2}$)	Forcing standard deviation ($W\ m^{-2}$)	Forcing standard deviation divided by forcing	Percentage of variance due to natural emissions	Percentage of variance due to anthropogenic emissions	Percentage of variance due to aerosol processes
Annual mean values							
1750–2000	AeroCom	−1.16	0.22	0.18	45	34	14
June mean values							
1750–2000	AeroCom	−1.42	0.27	0.19	45	38	13
1850–2000	ACCMIP	−1.30	0.28	0.22	37	46	11
1900–2000	ACCMIP	−0.96	0.20	0.21	37	43	13
1850–1980	ACCMIP	−1.29	0.27	0.21	38	47	11

All numbers refer to global means. The last three columns refer to percentage of variance.

Appendix 2 - Supporting Information for Chapter 3

110

Auxiliary material for

Uncertainty in the magnitude of aerosol-cloud radiative forcing over recent decades

L. A. Regayre,[1] K. J. Pringle,[1] B. B. B. Booth,[2] L. A. Lee,[1]
G. W. Mann,[1,3] J. Browse,[1] M. T. Woodhouse,[4] A. Rap,[1]
C. L. Reddington[1] and K. S. Carslaw[1]

[1]School of Earth and Environment, University of Leeds, Leeds, LS2 9JT, UK.
[2]UK Hadley Centre Met Office, Exeter, Fitzroy Road, EX1 3PB, Exeter, UK.
[3]National Centre for Atmospheric Science, University of Leeds, Leeds, LS2 9JT, UK.
[4]CSIRO Oceans and Atmosphere, 107-121 Station Street, Aspendale, VIC 3195, Australia.

Geophysical Research Letters

Introduction

The auxiliary information is comprised of three tables and three figures. Table "ts01.pdf" provides a summary of the uncertain aerosol process and emission parameters used to construct the perturbed parameter ensemble that informs the results. Table "ts02.pdf" contains a summary of ensemble mean cloud drop number concentration differences and cloud-albedo effect forcings for all periods. Table "ts03.pdf" compares global annual LW, SW and Net cloud radiative effects for our reference simulation with ten year average Clouds and the Earth's Radiant Energy System (CERES) and Coupled Model Intercomparison Project Phase 5 (CMIP5) values. Figures "fs01.eps" and "fs02.eps" provide detail on the validation of the Gaussian Process emulators for the 1978-2008 and the 1850-2008 and 1998-2008 periods respectively. Figure "fs03.eps" shows average ensemble cloud drop number concentration differences for all periods and corresponds to Figure 1.

1 ts01.pdf Summary of uncertain aerosol process and emission parameters used to create the perturbed parameter ensemble. Parameters are grouped according to their source type and are ordered to match Figure 3. Parameters in bold font replace or are additional to those used in Lee et al. [2013] and Carslaw et al. [2013]. Expert elicitation was used to identify parameter ranges updated from Lee et al. [2013], where descriptions of parameter functionality within GLOMAP are also described. The parameters "T_Ice" and "Drizz_Rate" are described in Browse et al. [2012].

1.1 Column "Parameter key", abbreviated parameter labels used in Figure 3.

1.2 Column "Group", uncertainty source groupings used to color Figures 2 and 3.

1.3 Column "Parameter description", concise parameter descriptions.

1.4 Column "Lower Bound", lower limit used in the ensemble design, below which experts agreed the optimal parameter value was very unlikely to occur.

1.5 Column "Median Value", median value from the elicited parameter range.

1.6 Column "Upper Bound", upper limit used in the ensemble design, above which experts agreed the optimal parameter value was very unlikely to occur.

2 ts02.pdf Ensemble mean cloud drop number concentration (CDNC) differences (m^{-3}) and cloud-albedo effect (CAE) forcings (Wm^{-2}) for all periods. All values are means of the 187 ensemble members. By design the ensemble contains a disproportionately high concentration of extreme perturbed parameter combinations that allows the emulators to interpolate rather than extrapolate parameter influence on CAE forcing. The values in this table are representative of the ensemble used to create the emulators and are not expected to represent typical model behaviour. Vertical column CDNC totals within each model grid box are annually averaged. For each ensemble member annual mean CDNC values for the period start year are subtracted from the corresponding value for 2008 within each model grid box, then CDNC global, Hemisphere and surface type area weighted means are calculated. Absolute CDNC differences are provided for the periods 1978-2008 and 1998-2008. Absolute differences are calculated within each model grid box prior to calculating the area weighted means.

2.1 Column "Quantity", description of the quantity under consideration, being CDNC differences and CAE forcing for each period, with absolute values also provided for the periods 1978-2008 and 1998-2008.

2.2 Column "Global", globally, annually averaged values.

2.3 Column "Southern Hemisphere" annually averaged values for the Southern Hemisphere only.

2.4 Column "Northern Hemisphere" annually averaged values for the Northern Hemisphere only.

2.5 Column "Land" annually averaged values for model gridboxes where 50% or more of the surface is represented as land within the model.

2.6 Column "Marine" annually averaged values for model gridboxes less than 50% of the surface is represented as land within the model.

3 ts03.pdf Global annual LW, SW and Net cloud radiative effects (Wm^{-2}) for our reference simulation. Clouds for the year 2000 were sourced from the International Satellite Cloud Climatology Project (ISCCP) D2 data [Rossow and Schiffer, 1999] and the effective radius was fixed at $r_e = 10\mu m$ for this simulation. Ten year averages of Clouds and the Earth's Radiant Energy System (CERES) and Coupled Model Intercomparison Project Phase 5 (CMIP5) values are taken from Calisto et al. [2014].

3.1 Column "Source", The source from which values in the table are derived.

3.2 Column "LW", Long Wave (LW) cloud radiative effect (Wm^{-2}).

3.3 Column "SW", Short Wave (SW) cloud radiative effect (Wm^{-2}).

3.4 Column "Net", Net cloud radiative effect (Wm^{-2}).

4 fs01.eps Validation of the emulator of CAE forcing for the 1978-2008 period. Ninety-three values from extra full-year paired simulations, with identical perturbed parameter settings chosen randomly from across the multi-dimensional parameter space, are compared to output from the emulator constructed using the ensemble of 187 paired simulations for each year. Emulator predictions and GLOMAP simulated values for the 93 new simulations are represented by points in the scatterplot. The 95% confidence intervals around each emulator mean give an indication of the

emulator's ability to reproduce globally, annually averaged CAE forcing values with sufficient precision. Of the 93 new simulations only seven, coloured red, have confidence intervals that do not cross the 1:1 line. For reference purposes output from the simulation where all parameter values are set to their medians is represented using a blue triangle.

5 fs02.eps Retrospective validation of the emulators of CAE forcing for the periods a) 1850-2008 and b) 1998-2008. For each period a randomly selected subset of 163 of the original 187 ensemble members were used to create a new emulator and the remaining 24 used to validate the emulator in a retrospective fashion. Using fewer ensemble members in the creation of the emulator is expected to produce highly similar results since in each period there are several parameters that contribute insignificantly to CAE forcing variance, reducing the number of simulations required to achieve a suitably dense space-filling design. Emulator predictions and GLOMAP simulated values for the 24 new simulations are represented by points in the scatterplots. The 95% confidence intervals around each emulator mean gives an indication of the emulator's ability to reproduce globally, annually averaged CAE forcing values with sufficient precision. Of the 24 new simulations only three, coloured red, have confidence intervals that do not cross the 1:1 line in the 1850-2008 period and only two do not cross in the 1998-2008 period. For reference purposes output from the simulations where all parameter values are set to their medians are represented using blue triangles.

6 fs03.eps (Figure 1) Ensemble mean cloud drop number concentration (CDNC) differences (m^{-3}) between 2008 and a) 1850, b) 1978 and c) 1998. All values are means of annually averaged vertical column totals in each model gridbox for the 187 ensemble members. By design the ensemble contains a disproportionately high concentration of extreme perturbed parameter combinations that allows the emulators to interpolate rather than extrapolate parameter influence on CAE forcing. The values in this figure are representative of the ensemble used to create the emulator in each period and are not expected to represent typical model behaviour.

References

- Browse, J., K. S. Carslaw, S. R. Arnold, K. Pringle, and O. Boucher (2012), The scavenging processes controlling the seasonal cycle in Arctic sulphate and black carbon aerosol, *Atmos. Chem. Phys., 12*, 6775-6798, doi:10.5194/acp-12-6775-2012.

- Calisto, M., D. Folini, M. Wild, and L. Bengtsson (2014), Cloud radiative forcing intercomparison between fully coupled CMIP5 models and CERES satellite data, *Ann. Geophys., 32*, 793-807, doi:10.5194/angeo-32-793-2014.

- Carslaw, K. S., L. A. Lee, C. L. Reddington, K. J. Pringle, A. Rap, P. M. Forster, G. W. Mann, D. V. Spracklen, M. Woodhouse, L. Regayre, and J. R. Pierce (2013), Large contribution of natural aerosols to uncertainty in indirect forcing, *Nat., 503*, 67-71, doi:10.1038/nature12674.

- Lee, L. A., K. S. Carslaw, K. J. Pringle, G. W. Mann, and D. V. Spracklen (2011), Emulation of a complex global aerosol model to quantify sensitivity to uncertain parameters, *Atmos. Chem. Phys., 11*, 12,253-12,273, doi:10.5194/acp-11-12253-2011.

- Rossow, W. B., and R. A. Schiffer (1999), Advances in understanding clouds from ISCCP, *B. Am. Meteorol. Soc., 80*, 2261-2288, doi:10.1175/1520-0477(1999)080<2261:AIUCFI>2.0.CO;2.

Parameter key	Group	Parameter description	Lower bound	Median value	Upper bound
Volc_SO2	Natural	Volcanic SO_2 emission flux scale factor	0.5	1	2
BVOC_SOA	Natural	Production of secondary organic aerosols (SOA) from biogenic volatile organic compounds (VOC) scale factor	0.27	2.7	20
DMS	Natural	Dimethyl-sulfide emission flux scale factor	0.5	1	2
Sea_Spray	Natural	Sea spray emission flux scale factor	0.2	1	5
Dust	**Natural**	**Dust emission flux scale factor**	**0.387**	**0.774**	**1.548**
BB_Ems	Natural	Black carbon (BC) and organic carbon (OC) from biomass burning (BB) sources emission flux scale factor	0.25	1	4
BB_Diam	Natural	BB aerosol diameter at emission (nm)	50	110	200
FF_Ems	Anthropogenic	BC and OC from fossil fuel (FF) sources emission flux scale factor	0.5	1	2
BF_Ems	Anthropogenic	BC and OC from biofuel (BF) sources emission flux scale factor	0.25	1	4
FF_Diam	Anthropogenic	FF aerosol diameter at emission (nm)	30	56	80
BF_Diam	Anthropogenic	BF aerosol diameter at emission (nm)	50	110	200
Prim_SO4_Frac	Anthropogenic	Fraction of SO_2 emitted as particulate SO_4	0	$1.2x10^{-3}$	0.01
Prim_SO4_Diam	Anthropogenic	Diameter of SO_4 particles at emission (nm)	20	40	100
Anth_SO2	Anthropogenic	Anthropogenic SO_2 emission flux scale factor	0.6	1	1.5
AVOC_SOA	Anthropogenic	Production of SOA from anthropogenic VOC scale factor	0	0.8	1.6
BL_Nuc	Process	**Continental boundary layer nucleation rate scale factor**	**0.01**	**1**	**10**
FT_Nuc	Process	Free troposphere nucleation rate scale factor	0.01	1	10
Ageing	Process	Number of insoluble monolayers that must be 'aged' for an aerosol to become soluble	0.3	1	5
Acc_Width	Process	Accumulation mode width (nm)	1.2	1.5	1.8
Ait_Width	Process	Aitken mode width (nm)	1.2	1.5	1.8
Nuc_Ait_Sep	Process	Nucleation and Aitken mode separation diameter (nm)	$9x10^{-9}$	$1x10^{-8}$	$1.8x10^{-8}$
Ait_Acc_Sep	Process	Aitken and accumulation mode separation diameter scale factor	0.9	1.5	2
Act_Diam	Process	Cloud drop activation diameter (nm)	50	75	100
Cloud_pH_Clean	Process	pH of cloud drops in 'clean' environments	4	5	6.5
Cloud_pH_Poll	Process	pH of cloud drops in 'polluted' environments	3.5	4	5
Nuc_Scav_Diam	Process	Off set diameter to be added to cloud drops before nucleation scavenging is initiated (nm)	0	25	50
T_Ice	**Process**	**Temperature threshold for the suppression of scavenging of insoluble and soluble particles in mixed-phase clouds (K^0)**	**253**	**258**	**268**
Drizz_Rate	**Process**	**Precipitation rate in low-level stratocumulus clouds scale factor**	**0**	**0.5**	**1**
Dry_Dep_Ait	Process	Dry deposition velocity Aitken mode aerosol scale factor	0.5	1	2
Dry_Dep_Acc	Process	Dry deposition velocity of accumulation mode aerosol scale factor	0.1	1	10
Dry_Dep_SO2	**Process**	**Dry deposition velocity of SO_2 scale factor**	**0.1**	**1**	**10**

116

Quantity	Global	Southern Hemisphere	Northern Hemisphere	Land	Marine
2008-1850 CDNC (m^{-3})	698	258	1069	537	774
2008-1978 CDNC (m^{-3})	-23.1	15.9	-50.6	-94.3	10.7
2008-1978 absolute CDNC (m^{-3})	212.4	54.9	341.4	172.2	231.5
2008-1998 CDNC (m^{-3})	-31.0	-0.5	-55.7	-45.0	-24.3
2008-1998 absolute CDNC (m^{-3})	82.3	23.3	130.8	71.9	87.2
2008-1850 CAE forcing (Wm^{-2})	-0.671	-0.124	-0.566	-0.516	-0.743
2008-1978 CAE forcing (Wm^{-2})	-0.012	0.000	0.063	0.037	-0.034
2008-1978 absolute CAE forcing (Wm^{-2})	0.138	0.016	0.138	0.091	0.160
2008-1998 CAE forcing (Wm^{-2})	0.013	0.006	0.036	0.022	0.008
2008-1998 absolute CAE forcing (Wm^{-2})	0.056	0.009	0.059	0.042	0.063

Source	LW	SW	Net
This study (year 2000)	23.8	-49.5	-25.7
CERES 10-yr average (2000-2010)	29.5	-47.5	-18.8
CMIP5 range 10-yr average (1995-2005)	(20.7,30.7)	(-40.8,-54.7)	(-19.9,-28.9)

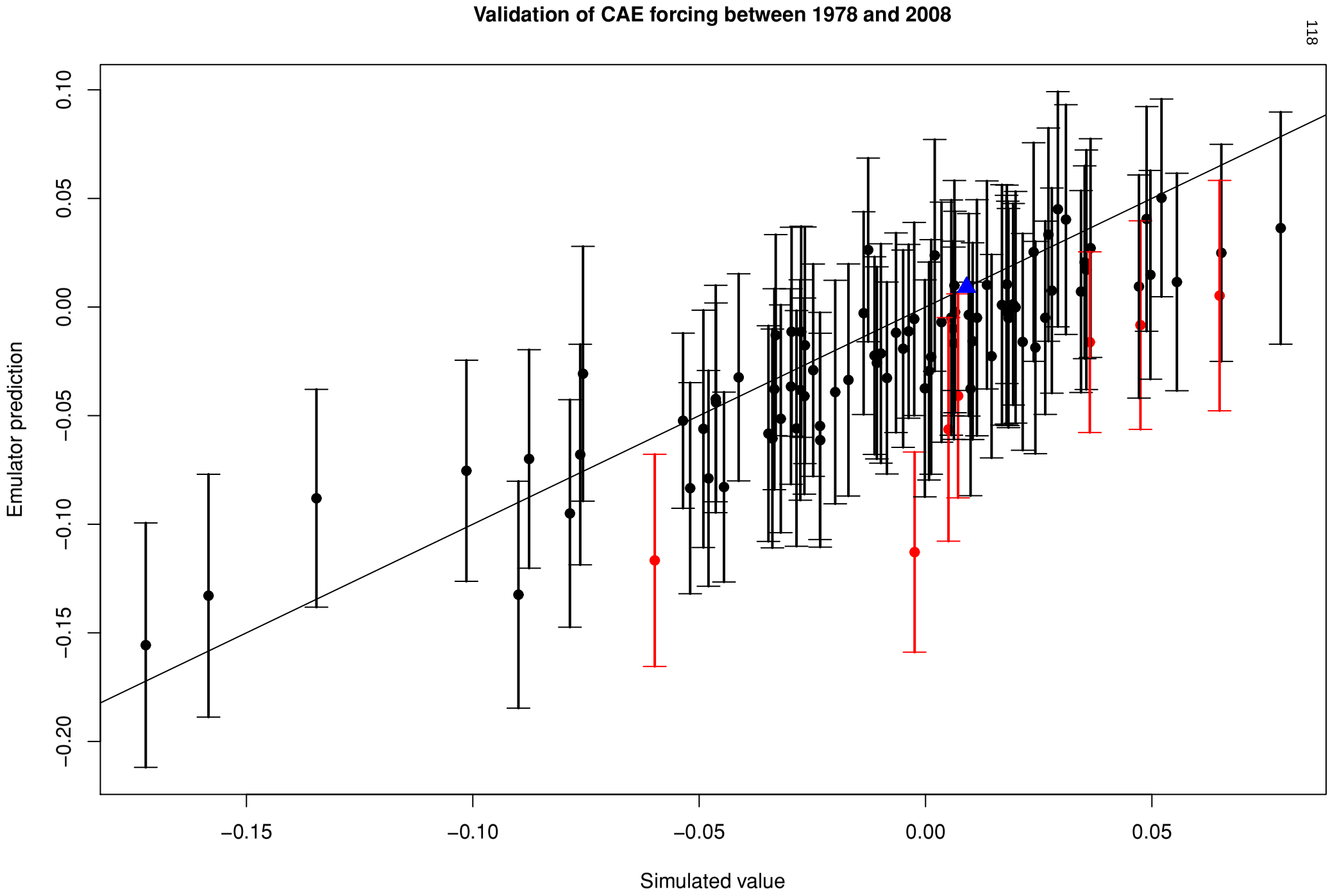
Validation of CAE forcing between 1978 and 2008
118
Emulator prediction
0.10
0.05
0.00
−0.05
−0.10
−0.15
−0.20
−0.15
−0.10
−0.05
0.00
0.05
Simulated value

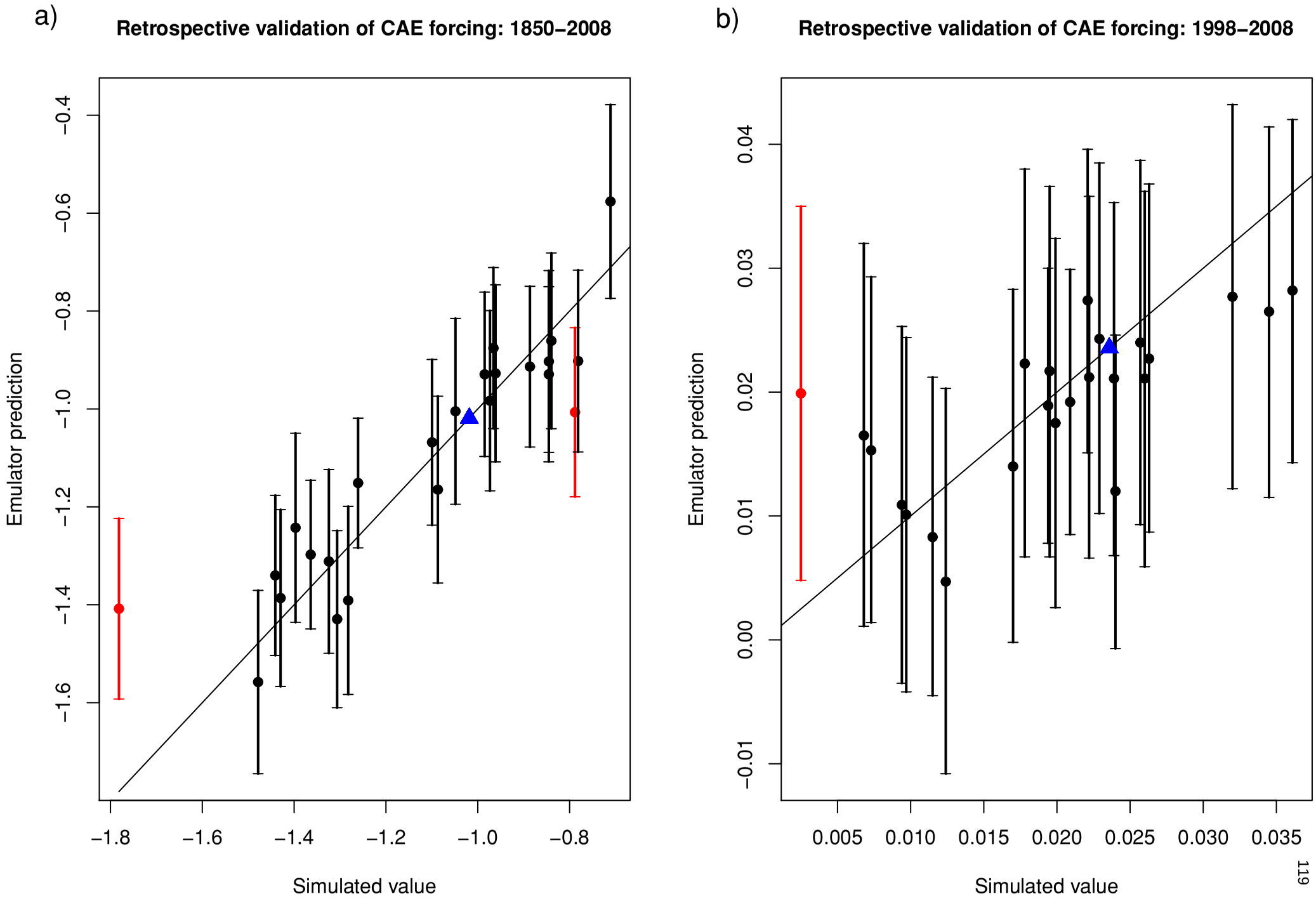
a)
Retrospective validation of CAE forcing: 1850–2008
Emulator prediction
−0.4
−0.6
−0.8
−1.0
−1.2
−1.4
−1.6
−1.8
−1.6
−1.4
−1.2
−1.0
−0.8
Simulated value
b)
Retrospective validation of CAE forcing: 1998–2008
Emulator prediction
0.04
0.03
0.02
0.01
0.00
−0.01
0.005
0.010
0.015
0.020
0.025
0.030
0.035
Simulated value

a)

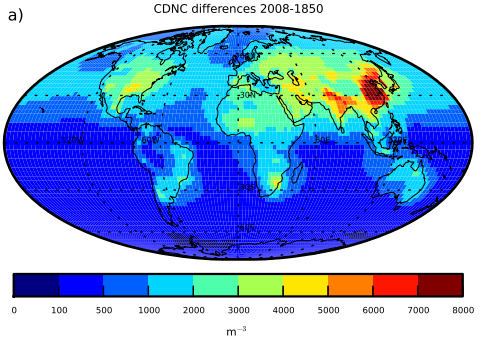
CDNC differences 2008-1850
30N
120W
60W
30E
60E
90E
30S
60S
0
100
500
1000
2000
3000
4000
5000
6000
7000
8000
m^{-3}

b)

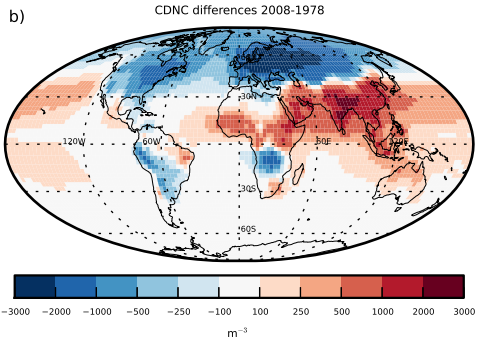
CDNC differences 2008-1978
30N
120W
60W
30E
60E
90E
30S
60S
−3000
−2000
−1000
−500
−250
−100
100
250
500
1000
2000
3000
m^{-3}

c)

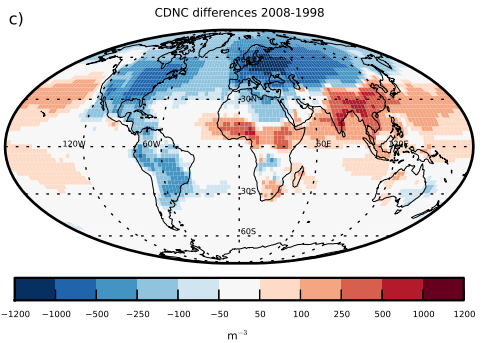
CDNC differences 2008-1998
30N
120W
60W
30E
60E
90E
30S
60S
−1200
−1000
−500
−250
−100
−50
50
100
250
500
1000
1200
m^{-3}

Appendix 3 - Supporting Information for Chapter 5

Observed planetary energy balance does not constrain aerosol radiative forcing

Supporting Information

Leighton A. Regayre[1*], Jill S. Johnson[1], Masaru Yoshioka[1],

Kirsty J. Pringle[1], David M. H. Sexton[2], Ben B. B. Booth[2],

Graham W. Mann[1,3], Lindsay A. Lee[1], Nicolas Bellouin[4],

Grenville M. S. Lister[5], Colin E. Johnson[3], Ben Johnson[3],

James D. P. Mollard[4]and Kenneth S. Carslaw[1]

1. Institute for Climate and Atmospheric Science, School of Earth and Environment, University of Leeds, Leeds, LS2 9JT, UK.

2. UK Hadley Centre Met Office, Exeter, Fitzroy Road, Exeter, Devon, EX1 3PB, UK.

3. Current affiliation: National Centre for Atmospheric Science, University of Leeds, Leeds, LS2 9JT, UK.

4. Department of Meteorology, School of Mathematical & Physical Sciences, Faculty of Science, University of Reading, Reading, RG6 6BB, UK.

5. National Centre for Atmospheric Science, University of Reading, Reading, RG6 6BB, UK.

*Corresponding author email: L.A.Regayre11@leeds.ac.uk

Supporting Information

Model description

The UK Hadley Centre Met Office Unified Model (HadGEM3) (HadGEM3, 2016) is a three-dimensional global atmosphere model. HadGEM3 simulations can make use of the UK Chemistry and Aerosol (UKCA) model, within which the evolution of particle size distribution and size-resolved chemical composition of aerosols are calculated using the GLObal Model of Aerosol Processes (GLOMAP) (Spracklen *et al.*, 2005a; Mann *et al.*, 2010, 2012). The simulations that form the ensemble members used here make use of release version 8.4 of UKCA, run using 1.25°x1.875° horizontal resolution and 85 vertical hybrid pressure levels. Successive versions of the GLOMAP model have been widely evaluated against global measurements of particle number concentration (Spracklen *et al.*, 2010; Reddington *et al.*, 2011), chemical compositions (Spracklen *et al.*, 2011a; Browse *et al.*, 2012; Schmidt *et al.*, 2011) and cloud active aerosol concentrations (Korhonen *et al.*, 2008; Spracklen *et al.*, 2011b; Pringle *et al.*, 2012). The HadGEM models are subject to constant monitoring for their use in numerical weather prediction and have informed successive Coupled Model Inter-comparison Project (CMIP) experiments (Taylor *et al.*, 2012).

The aerosol size distribution is defined by seven log-normal modes: one soluble nucleation mode and both soluble and insoluble Aitken, accumulation and coarse modes. The aerosol chemical components are sulphate, sea salt, black carbon, particulate organic carbon and dust. Secondary organic carbon is produced from the first stage oxidation products of biogenic monoterpenes under the assumption of zero vapour pressure. Secondary organic carbon is combined with particulate organic matter after kinetic condensation on the aerosol.

The GLOMAP model resolves new particle formation, coagulation, gas-to-particle transfer, cloud processing and deposition of gasses and aerosols. The activation of aerosols into cloud droplets is calculated using distributions of sub-grid vertical velocities (West *et al.*, 2014) and the removal of cloud droplets is calculated by the host model. Aerosols are also removed by impaction scavenging of falling raindrops according to the parametrisation of clouds and precipitation collocation (Lebsock *et al.*, 2013; Boutle *et al.*, 2014). Aerosol water uptake efficiency is determined by 'Köhler theory' (Köhler *et al.*, 2006) using size and composition dependent hygroscopicity factors (κ) (Petters & Kreidenweis, 2007).

Anthropogenic emission scenarios prepared for the Atmospheric Chemistry and Climate Model Inter-comparison Project (ACCMIP) (Lamarque *et al.*, 2010) and prescribed in some of the CMIP Phase 5 experiments (Taylor *et al.*, 2012) are prescribed here. Carbonaceous aerosol emissions were prescribed using a ten year average of 2002 to 2011 monthly mean data from the Global Fire and Emissions Database (GFED3) (der Werf *et al.*, 2010).

Top-of-the-atmosphere (ToA) clear-sky reflected shortwave radiation (RSR) calculations account for above-cloud scattering and absorption of aerosol (Ghan, 2013). Biases in clear- and cloudy-sky RSR calculations resulting from the horizontal collocation of aerosols and clouds at different altitudes were removed using diagnostics from a "double-call" configuration where aerosols and radiation are decoupled in the second call to the radiation code.

Each simulation was subject to a seven month spin-up period, with parameters set to their median values for the first four months before perturbations were applied to individual ensemble members. The output analysed in this research comprises the full year of data for each simulation following the spin-up period. All results discussed in the main article all for global, annual mean values. Results for monthly mean values are provided to indicate the temporal dependence of aerosol and atmospheric parameter influence on seasonally varying model output.

Nudging

Newtonian relaxation was used in these simulations to 'nudge' calculated model horizontal winds towards European Centre for Medium-Range Weather Forecasts (ECMWF) ERA-Interim reanalysis values for 2006 between model vertical levels 17-80 (approximately 2.15 to 60 km) using a six hour relaxation timescale. Nudging of atmospheric states is used primarily to validate output from global models (Jeuken *et al.*, 1996; Telford *et al.*, 2008) or to ensure that pairs of simulations have near-identical atmospheric states, so that aerosol and/or chemistry perturbations can be applied and their effects quantified using single realisations of each simulation (van Aalst *et al.*, 2004; Spracklen *et al.*, 2005b). Without nudging radiative fluxes need to be averaged over many decades in order to produce signals stronger than the noise resulting from internal variability (Kooperman *et al.*, 2012).

Nudging towards horizontal winds from ECMWF reanalyses allows low-level cloud

responses to parametric perturbations to be captured, whilst removing much of the spatial heterogeneity in 'free-running' simulations. By nudging to horizontal winds above 2km, synoptic-scale dynamical features are consistent across the ensemble.

Nudging in GCMs is typically applied to horizontal winds and temperature simultaneously (Telford *et al.*, 2008). Nudging to horizontal winds and not temperature can produce ToA radiative fluxes that are in better agreement with those from free-running simulations (Zhang *et al.*, 2014). Phase III of the AeroCom model intercomparison is scheduled to be conducted using simulations nudged to horizontal winds only. By adopting this nudging configuration liquid water path and atmospheric humidity can respond to aerosol-induced changes in temperature in our simulations, allowing more of the rapid responses of clouds and radiation to aerosol perturbations to be captured. Furthermore nudging to horizontal winds and not temperature increases the number of degrees of freedom with which the model can disperse inconsistencies in atmospheric states during the relaxation process.

Parameter perturbations

The 27 parameters perturbed in the ensembles analysed here are presented in Extended Data Tables 1 and 2. Parameters are categorized as either aerosol or atmospheric according to their role in the model.

The atmospheric parameters perturbed in this research were identified as being those with the potential to contribute to uncertainty in a broad range of observational metrics (Sexton *et al.*, In prep.). A number of parameters elicited but not previously tested in a sensitivity analysis framework are included here because they significantly influence clouds and/or precipitation in one-at-a-time perturbation screening experiments, where parameters are individually perturbed to their maximum or minimum value and the output compared to that from the simulation with median parameter values. The role of all parameters in the model are briefly described in Extended Data Tables 1 and 2.

Aerosol parameters included in the ensemble either contribute significantly to uncertainty in cloud drop number concentrations (Lee *et al.*, 2013) and/or aerosol cloud-albedo effect forcing (the ACI without accounting for rapid adjustments) at the global (Regayre *et al.*, 2014) or regional scale (Regayre *et al.*, 2015). Some parameters have been included in the ensemble because they represent structural advances in the model about which there is sufficient uncertainty. An example of this is the refractive

indicies of carbonaceous aerosols which are important for ARI forcing and atmospheric temperatures (Bond *et al.*, 2013).

The probability density functions used here to represent expert beliefs about parameter uncertainty are predominantly trapezoidal distributions. Using trapezoidal distributions to represent parameter uncertainty avoids having an overly-centralised Monte-Carlo sample of the multi-dimensional parameter space. Furthermore, experts converged on agreement about parameter uncertainty using trapezoidal distributions faster than they did when attempting to use other types of distribution. Where elicited distributions were not suitable for computationally efficient sampling using the extended-FAST sensitivity analysis approach (Saltelli *et al.*, 1999), they were closely approximated using trapezoidal distributions.

The trapezoidal distributions (Hetzel, 2012) in Extended Data Tables 1 and 2 are specified using six or seven values. The first four represent the minimum, left vertex, right vertex and maximum parameter values. The next two values represent the slope of the left and right side of the trapezoid, determining it's concave or convex nature. A value of two produces a straight-sided trapezoid. Where a seventh value is present it represents the gradient of the top of the trapezoid.

Perturbed parameter ensemble

Eighteen aerosol emission, deposition and process parameters and nine atmospheric parameters were perturbed simultaneously in pairs of simulations. Global annual mean radiative forcings were calculated as the difference in ToA radiative flux for each pair of simulations, with identical perturbed parameter values but different emission inventories.

Maximin Latin Hypercube sampling was used to create a parameter combination design, of 162 points, that spans the 27-dimensional parameter uncertainty space. A simulation with all parameters set to their median values was included in the ensemble to ensure coverage of what experts believed to be an important region of parameter space. A further set of 54 simulations, with parameter combinations that augment the original design, was created to test the validity of the statistical approach (Bastos & O'Hagan, 2009). The extended-FAST sampling method (Saltelli *et al.*, 1999), with 10^4 sample points per parameter drawn from the statistical emulator for the model, was used to obtain data for conducting sensitivity analysis.

In total 217 perturbed parameter simulations were created for each anthropogenic emission period. Twenty-five simulations did not complete an annual cycle in at least one of the ensembles (with 1850, 1978 and PD emissions) because the combinations of parameters produced values that exceeded model performance thresholds. The ensemble of simulations for each period was made up of the remaining 191 simulations.

Preliminary parameter combination tests revealed that combinations of Entrain_Amp larger than 1.8 and Mix_Detrain larger than 8.0 caused problems with model evolution, with no detectable dependence on the value of other parameter values. The corner of this 2D plane within the 27-dimensional parameter space was removed from the ensemble design and analysis. Combinations of these two parameters were chosen that provided a denser design in the remaining 2D space. The extended-FAST sampling method was adapted to reject samples from parameter space that was not included in the design. Rejected combinations of these parameters were resampled from the restricted 2D parameter space without affecting the sampling frequency across the remaining 25-dimensional parameter space. The majority of incomplete simulations in the design had combinations of Entrain_Amp and Mix_Detrain near to the border of this rejected area of parameter space.

Sensitivity Analysis

Sensitivity analysis (Saltelli *et al.*, 2000; Lee *et al.*, 2013) of global annual mean ERF, ACI and ARI was conducted using 270000 member Monte Carlo samples from Bayesian statistical emulators (O'Hagan, 2006). Each emulator was conditioned on output from the 191 perturbed parameter simulations. Emulators provide a statistical representation of model output for all points within the multi-dimensional parameter space and have been widely used to analyse climate model output (Murphy *et al.*, 2007; Sexton & Murphy, 2012; Lee *et al.*, 2013; Carslaw *et al.*, 2013; Harris *et al.*, 2013; Tett *et al.*, 2013; Regayre *et al.*, 2014; Hamilton *et al.*, 2014; Johnson *et al.*, 2015; Regayre *et al.*, 2015). Here each emulator was validated using the simulations created specifically for the purpose. In each case the extra simulations were combined with the original set of simulations to build new emulators with better space-filling properties. It is assumed that the emulators created using a denser parameter space better represent the multi-dimensional response surface. Histograms of the 270000 member 1850-PD aerosol ERF and PD ToA RSR samples of the emulators are presented in Extended Data Fig 1 and 2 respectively.

The emulator makes the dense sampling of the model output across the full parameter uncertainty space possible. Hence, we can then use variance-based sensitivity analysis techniques with the emulator to quantify parameter contributions to uncertainty. The statistic considered most in the discussion of these results is the percentage reduction in output variance that could be expected if the parameter, or group of parameters, were known exactly. Interactions between parameters can also be quantified and this informs the interpretation of results.

Reduced dimensionality analysis

The effect of ignoring the uncertainty in the parameter Rad_Mcica_Sigma, which dominates the variance in PD ToA fluxes is summarised in Extended Data Table 4. Contributions to variance from uncertain parameters can be ignored by fixing the parameter in question to some prescribed value, effectively reducing the dimensionality of the parameter space. Removing the Rad_Mcica_Sigma uncertainty from the sensitivity analysis alters the proportions of variance caused by aerosol and the remaining atmospheric parameters. However atmospheric parameters remain the largest source of ToA radiative flux uncertainty.

The dimensionality of the parameter space was reduced in a similar fashion to obtain the credible range of aerosol ERF values in response to aerosol perturbations alone. In this case all atmospheric parameters were set to their median values during sampling. Reducing the dimensionality of parameter space provides a first-order approximation of the aerosol ERF credible interval. Sampled values from the aerosol parameter combinations and the resulting credible interval depend on the atmospheric parameter values prescribed. The representativeness of the reduced dimensionality credible interval depends on the shape of the multi-dimensional response surface in the collapsed dimensions. Median values were used as they combine to provide the region of greatest expert confidence in atmospheric parameter values.

Sensitivity results for other periods

Contributions to variance in ToA radiative fluxes for 1978 and 1850 are provided in Extended Data Fig 3 and 4 respectively. The results are very similar to those in Fig. 1. Contributions to variance in 1978-2008 aerosol ERF, ACI and ARI are presented in Extended Data Fig. 5. The sources and percentage contributions to variance in 1978-PD are different from those in the 1850-PD period (Fig. 2). Sources of changing global mean low cloud fraction variance over the industrial period are presented in Extended Data

Fig. 6. Natural aerosol emission parameters contribute significantly to variance in changing cloud fraction suggesting that, in this model, the strength of the cloud lifetime response to aerosols is highly uncertain in the PI.

Present-day RSR constraints

The $\pm 0.5\,\mathrm{W\,m^{-2}}$ constraint used to produce Fig. 3 represents the observational uncertainty caused by instrument calibration (Loeb *et al.*, 2009) and the $\pm 0.25\,\mathrm{W\,m^{-2}}$ constraint represents within-CERES observational uncertainty (Loeb *et al.*, 2012), assuming no systematic biases. The observational uncertainty ranges used here are made intentionally narrow by neglecting multiple sources of significant satellite observational uncertainty (Hartmann *et al.*, 2013). We assume the model simulates RSR with no error to avoid inflating the RSR range. In practice using a single observational constraint and disregarding the discrepancy between simulated and real world values can lead to over-constraint of model output (Murphy *et al.*, 2007; Sexton *et al.*, 2012; Stephenson *et al.*, 2012).

Credible intervals of RSR and aerosol ERF using different present-day RSR constraints with $\pm 0.25\,\mathrm{W\,m^{-2}}$ observational uncertainty are provided in Extended Data Table 3. The RSR value from the simulation with all parameter values set to their median was chosen as the center of the first theoretical sample as it represents the region of parameter space with highest expert confidence in individual parameter values. Other samples were chosen such that values were towards the ends of the simulated RSR range. Choosing samples near the ends of the RSR range provides a broader test of the capacity for present-day RSR to constrain aerosol ERF, yet produces much smaller samples than those used in Fig 3. A further constraint was placed on Rad_Mcica_Sigma the parameter causing most of the variance in PD RSR and PI-PD aerosol ERF. This parameter was restricted to within 2% of its original range, centred on the modal Rad_Mcica_Sigma value from the $\pm 0.25\,\mathrm{W\,m^{-2}}$ sample. This significantly reduces the sample size but, as in all other cases, the aerosol ERF is poorly constrained by the very tight present-day RSR constraint.

Bibliography

Bastos, L. S., & O'Hagan, A. 2009. Diagnostics for Gaussian process emulators. *Technometrics*, **51**, 425–438.

Bond, T. C., Doherty, S. J., Fahey, D. W., Forster, P. M., Berntsen, T., DeAngelo, B. J., Flanner, M. G., Ghan, S., Krcher, B., Koch, D., Kinne, S., Kondo, Y., Quinn, P. K., Sarofim, M. C., Schultz, M. G., Schulz, M., Venkataraman, C., Zhang, H., Zhang, S., Bellouin, N., Guttikunda, S. K., Hopke, P. K., Jacobson, M. Z., Kaiser, J. W., Klimont, Z., Lohmann, U., Schwarz, J. P., Shindell, D., Storelvmo, T., Warren, S. G., & Zender, C. S. 2013. Bounding the role of black carbon in the climate system: A scientific assessment. *J. Geo. Res. Atmos.*, **118**, 5380–5552.

Boutle, I. A., Abel, S. J., Hill, P. G., & Morcrette, C. J. 2014. Spatial variability of liquid cloud and rain: observations and microphysical effects. *Quart. J. Roy. Meteor. Soc.*, **140**, 585–594.

Browse, J., Carslaw, K. S., Arnold, S. R., Pringle, K. J., & Boucher, O. 2012. The scavenging processes controlling the seasonal cycle in Arctic sulphate and black carbon aerosol. *Atmos. Chem. Phys.*, **12**, 6775–6798.

Carslaw, K. S., Lee, L. A., Reddington, C. L., Pringle, K. J., Rap, A., Forster, P. M., Mann, G. W., Spracklen, D. V., Woodhouse, M., Regayre, L. A., & Pierce, J. R. 2013. Large contribution of natural aerosols to uncertainty in indirect forcing. *Nat.*, **503**, 67–71.

der Werf, G. R. Van, Randerson, J. T., Giglio, L., Collatz, G. J., Mu, M., Kasibhatla, P. S., Norton, D. C., DeFries, R. S., Jin, Y., & van Leeuwen, T. T. 2010. Global fire emissions and the contribution of deforestation, savanna, forest, agricultural, and peat fires (1997-2009). *Atmos. Chem. Phys.*, **10**, 11707–11735.

Ghan, S. J. 2013. Technical Note: Estimating aerosol effects on cloud radiative forcing. *Atmos. Chem. Phys.*, **13**, 9971–9974.

HadGEM3. 2016. *Met Office climate prediction model: HadGEM3 family.* ***http://www.metoffice.gov.uk/research/modelling–systems/unified–model/climate–models/hadgem****. Accessed: March 2016.*

Hamilton, D. S., Lee, L. A., Pringle, K. J., Reddington, C. L. S., Spracklen, D. V., & Carslaw, K. S. 2014. Occurrence of pristine aerosol on a polluted planet. *Proc. Nat. Ac. Sci.*, **111**, 18466–18471.

Harris, G. R., Sexton, D. M. H., Booth, B. B. B., Collins, M., & Murphy, J. M. 2013. Probabilistic projections of transient climate change. *Clim. Dyn.*

Hartmann, D. L., A. M. G. Klein Tank, Rusticucci, M., Alexander, L. V., Brönnimann, S., Charabi, Y., Dentener, F. J., Dlugokencky, E. J., Easterling, D. R., Kaplan, A., Soden, B. J., Thorne, P. W., Wild, M., & Zhai, P. M. 2013. Observations: Atmosphere and Surface. *In:* Stocker, T. F., Qin, D., Plattner, G. K., Tignor, M., Allen, S. K., Boschung, J., Nauels, A., Xia, Y., Bex, V., & Midgley, P. M. (eds), *Climate Change 2013: The Physical Science Basis. Contribution of Working Group I to the Fifth Assessment Report of the Intergovernmental Panel on Climate Change.* Cambridge, United Kingdom and New York, NY, USA: Cambridge University Press.

Hetzel, J. 2012. *Package 'Trapezoid'.* https://cran.r-project.org/web/packages/trapezoid/trapezoid.pdf.

Jeuken, A., Siegmund, P., Heijboer, L., Feichter, J., & Bengtsson, L. 1996. On the potential of assimilating meteorological analyses in a global climate model for the purpose of model validation. *J. Geo. Res.*, **101**, 16939–16950.

Johnson, J. S., Cui, Z., Lee, L. A., Gosling, J. P., Blyth, A. M., & Carslaw, K. S. 2015. Evaluating uncertainty in convective cloud microphysics using statistical emulation. *J. Adv. Model. Earth Syst.*, **7**, 162–187.

Köhler *et al.* 2006. Water activity and activation diameters from hygroscopicity data - Part II: Application to organic species. *Atmos. Chem. Phys.*, **6**, 795–809.

Kooperman, G. J., Pritchard, M. S., Ghan, S. J., Wang, M., Somerville, R. C. J., & Russell, L. M. 2012. Constraining the influence of natural variability to improve estimates of global aerosol indirect effects in a nudged version of the Community Atmosphere Model 5. *J. Geo. Res.*, **117**, 1–16.

Korhonen, H., Carslaw, K. S., Spracklen, D. V., Mann, G. W., & Woodhouse, M. T. 2008. Influence of oceanic dimethyl sulfide emissions on cloud condensation nuclei concentrations and seasonality over the remote southern hemisphere oceans: A global model study. *J. Geo. Res.*, **113**, 16.

Lamarque, J. F., Bond, T. C., Eyring, V., Granier, C., Heli, A., Kilmont, Z., Lee, D., Liousse, C., Mieville, A., Owen, B., Schultz, M. G., Shindell, D., Smith, S. J., Stehfest, E., Van Aardenne, J., Cooper, O. R., Kainuma, M., Mahowald, N., McConnell, J. R., Naik, V., Riahi, K., & van Vuuren, D. P. 2010. Historical (1850-2000) gridded anthropogenic and biomass burning emissions of reactive gases and aerosols: methodology and application. *Atmos. Chem. Phys.*, **10**, 7017–7039.

Lebsock, M., Morrison, H., & Gettleman, A. 2013. Mircophysical implications of cloud-precipitation covariance derived from satellite remote sensing. *J. Geo. Res. Atmos.*, **118**, 6521–6533.

Lee, L. A., Pringle, K. J., Reddington, C. L., Mann, G. W., Stier, P., Spracklen, D. V., Pierce, J., & Carslaw, K. S. 2013. The magnitude and causes of uncertainty in global model simulations of cloud condensation nuclei. *Atmos. Chem. Phys.*, **13**, 8879–8914.

Loeb, N. G., Wielicki, B. A., Doelling, D. R., Smith, G. L., Keyes, D. F., Kato, S., Manalo-Smith, N., & Wong, T. 2009. Toward optimal closure of the Earth's top-of-atmosphere radiation budget. *J. Climate.*, **22**, 748–766.

Loeb, N. G., Kato, S., Su, W., Wong, T., Rose, F. G., Doelling, D. R., Norris, J. R., & Huang, X. 2012. Advnaces in understanding top-of-atmosphere radiation variability from satellite observations. *Surv. Geophys.*, **33**, 359–385.

Mann, G. W., Carslaw, K. S., Spracklen, D. V., Ridley, D. A., Manktelow, P. T., Chipperfield, M. P., Pickering, S. J., & Johnson, C. E. 2010. Description and evaluation of GLOMAP-mode aerosol microphysics model for the UKCA composition-climate model. *Geosci. Mod. Dev.*, **3**, 519–551.

Mann, G. W., Carslaw, K. S., Ridley, D. A., Merikanto, D. V. Spracklen K. J. Pringle J., Korhonen, H., Schwarz, J. P., Lee, L. A., Manktelow, P. T., Woodhouse, M. T., Schmidt, A., Breider, T. J., Emmerson, K. M., Reddington, C. L., Chipperfield, M. P., & Pickering, S. J. 2012. Intercomparison of modal and sectional aerosol microphysics representations within the same 3-D global chemical transport model. *Atmos. Chem. Phys.*, **12**, 4449–4476.

Murphy, J., Booth, B. B. B., Collins, M., Harris, G. R., Sexton, D. M. H., & Webb, M. J. 2007. A methodology for probabilistic predictions of regional climate change from perturbed physics ensembles. *Philos. Trans. Roy. Soc. London A*, **365**, 1993–2028.

O'Hagan, A. 2006. Bayesian analysis of computer code outputs - A tutorial. *Reliability engineering and system safety*, **91**, 1290–1300.

Petters, M. D., & Kreidenweis, S. M. 2007. A single parameter representation of hygroscopic growth and cloud condensation nucleus activity. *Atmos. Chem. Phys.*, **7**, 1961–1971.

Pringle, K. J., Carslaw, K. S., Fan, T., Mann, G. W., Hill, A., Stier, P., Zhang, K., & Tost, H. 2012. A multi-model assessment of the impact of sea spray geoengineering on cloud droplet number. *Atmos. Chem. Phys.*, **12**, 11647–11663.

Reddington, C. L., Carslaw, K.S., Spracklen, D.V., Frontoso, M.G., Collins, L., Merikanto, J., Minikin, A., Hamburger, T., Coe, H., Kulmala, M., Aalto, P., Flentje, H., Plass-Dulmer, C., Birmili, W., Wiedensolher, A., Wehner, B., Tuch, T., Sonntag, A., O'Dowd, C.D., Jennings, S.G., Dupuy, R., Baltensperger, U., Weingartner, E., Hansson, H.C., Turnved, P., Laj, P., Skellegri, K., Boulton, J., Putaud, J.P., Gruening, C., Swietlicki, E., Roldin, P., Henzing, J.S., Moerman, M., Mihalopoulos, N., Kouvarakis, G., Zdimal, V., Zikova, N., Marinoni, A., Bosasoni, P., & Duchi, R. 2011. Primary versus secondary contributions to particle number concentrations in the european boundary layer. *Atmos. Chem. Phys.*, **11**, 12007–12036.

Regayre, L. A., Pringle, K. J., Booth, B. B. B., Lee, L. A., Mann, G. W., Browse, J., Woodhouse, M. T., Rap, A., Reddington, C. L. S., & Carslaw, K. S. 2014. Uncertainty in the magnitude of aerosol-cloud radiative forcing over recent decades. *Geophys. Res. Lett.*, **41**, 9040–9049.

Regayre, L. A., Pringle, K. J., Lee, L. A., Booth, B. B. B., Rap, A., Browse, J., Mann, G. W., Woodhouse, M. T., Reddington, C. L. S., & Carslaw, K. S. 2015. The climatic importance of uncertainties in regional aerosol-cloud radiative forcings over recent decades. *J. Climate.*, **28**, 6589–6607.

Saltelli, A., Tarantola, S., & Chan, K. P. S. 1999. A quantitative model-independent method for global sensitivity analysis of model output. *Technometrics*, **41**, 39–56.

Saltelli, A., Chan, K., & Scott, E. M. 2000. *Sensitivity Analysis*. Oxford, U.K.: Wiley.

Schmidt, A., Ostro, B., Carslaw, K. S., Wilson, M., Thordarson, T., Mann, G. W., & Simmons, A. J. 2011. Excess mortality in europe following a future laki-style icelandic eruption. *Proc. Nat. Ac. Sci.*, **108**, 15710–15715.

Sexton, D. M. H., & Murphy, J. M. 2012. Multivariate probabilistic projections using imperfect climate models Part II: robustness of methodological choices and consequences for climate sensitivity. *Clim. Dyn.*, **38**, 2543–2558.

Sexton, D. M. H., Murphy, J. M., Collins, M., & Webb, M. J. 2012. Multivariate probabilistic projections using imperfect climate models Part I: outline of methodology. *Clim. Dyn.*, **38**, 2513–2542.

Sexton, David M. H., Karmalkar, A., Murphy, J., Booth, B. B. B., & Regayre, L. A. In prep.. The elicitation of distributions of parameters in HadGEM3 versions GA4 and GA7 for use in perturbed parameter ensembles. *Hadley Centre technical note, Met Office, U.K.*

Spracklen, D. V., Pringle, K. J., Carslaw, K. S., Chipperfield, M. P., & Mann, G. W. 2005a. A global off-line model of size-resolved aerosol microphysics: I. Model development and prediction of aerosol properties. *Atmos. Chem. Phys.*, **5**, 2227–2252.

Spracklen, D. V., Pringle, K. J., Carslaw, K. S., Chipperfield, M. P., & Mann, G. W. 2005b. A global off-line model of size-resolved aerosol microphysics: II. Identification of key uncertainties. *Atmos. Chem. Phys.*, **5**, 3233–3250.

Spracklen, D. V., Carslaw, K. S., Merikanto, J., Mann, G. W., Reddington, C. L., Pickering, S., Ogren, J. A., Andrews, E., Baltensperger, U., Weingartner, E., Boy, M., Kulmala, M., Laakso, L., Lihavainen, H., Kivekas, N., Komppula, M., Mihalopoulos, N., Kouvarakis, G., Jennings, S.G., O'Dowd, C., Birmili, W., Wiedensolher, A., Weller, R., Gras, J., Laj, P., Sellegri, K., Bonn, B., Krejci, R., Laaksonen, A., Hamed, A., Minikin, A., Harrison, R. M., Talbot, R., & Sun, J. 2010. Explaining global surface aerosol number concentrations in terms of primary emissions and particle formation. *Atmos. Chem. Phys.*, **10**, 4775–4793.

Spracklen, D. V., Jimenez, J. L., Carslaw, K. S., Worsnop, D. R., Evans, M. J., Mann, G. W., Zhang, Q., Canagaratna, M. R., Allan, J., Coe, H., McFiggans, G., Rap, A., & Forster, P. 2011a. Aerosol mass spectrometer contraint on the global secondary organic aerosol budget. *Atmos. Chem. Phys.*, **11**, 12109–12136.

Spracklen, D. V., Carslaw, K. S., Pöschl, U., Rap, A., & Forster, P.M. 2011b. Global cloud condensation nuclei influenced by carbonaceous combustion aerosol. *Atmos. Chem. Phys.*, **11**, 9067–9087.

Stephenson, D. B., Collins, M., Rougier, J. C., & Chandler, R. E. 2012. Statistical problems in the probabilistic prediction of climate change. *Environmetrics*, **23**, 364–372.

Taylor, K. E., Stouffer, R. J., & Meehl, G. A. 2012. An Overview of CMIP5 and the Experiment Design. *Bull. amer. Meteor. Soc.*, **93**, 485–498.

Telford, P. J., Braesicke, P., Morgenstern, O., & Pyle, J. A. 2008. Technical Note: Description and assessment of a nudged version of the new dynamics Unified Model. *Atmos. Chem. Phys.*, **8**, 1701–1712.

Tett, S. F. B., Rowlands, D. J., Mineter, M. J., & Cartis, C. 2013. Can top-of-atmosphere radiation measurements constrain climate predictions? part II: Climate sensitivity. *J. Climate.*, **26**, 9367–9383.

van Aalst, M., van den Broeck, M., Bregman, A., Brühl, C., Steil, B., Toon, G., Garcelon, S., Hansford, S., Jones, R., Gardiner, T., Roelofs, G., Lelieveld, J., & Crutzen, P. 2004. Trace gas transport in the 1999/2000 Arctic winter: comparison of nudged GCM runs with observations. *Atmos. Chem. Phys.*, **4**, 81–93.

West, R. E. L., Stier, P., Jones, A., Johnson, C. E., Mann, G. W., Bellouin, N., Partridge, D. G., & Kipling, Z. 2014. The importance of vertical velocity variability for estimates of the indircet aerosol effects. *Atmos. Chem. Phys.*, **14**, 6369–6393.

Zhang, K., Wan, H., Liu, X., Ghan, S. J., Kooperman, G. J., Ma, P. L., Rasch, P. J., Neubauer, D., & Lohmann, U. 2014. Technical Note: On the use of nudging for aerosol-climate model intercomparison studies. *Atmos. Chem. Phys.*, **12**, 8631–8645.

Table 1: Descriptions of the perturbed parameters 1-15 used to create the ensemble and the probability density functions used in the sampling process.

Index	Name	Source	Description	PDF
1	Rad_Mcica_Sigma	Atm	Fractional standard deviation of sub-grid condensate seen by radiation	Trapezoid (0.1,0.4,1.5,2.2,2,2)
2	C_R_Correl	Atm	Cloud and rain sub-grid horizontal spatial correlation	Trapezoid (0.0,0.6,0.9,1.0,1.8,1.1,1.5)
3	Niter_Bs	Atm	Number of microphysics iteration sub-steps	Uniform (5,20)
4	Ent_Fac_Dp	Atm	Entrainment amplitude	Trapezoid (0,0.5,2,4,2,2)
5	Amdet_Fac	Atm	Mixing detrainment rate	Trapezoid (0,0.5,10.0,15.0,2,2)
6	Dbsdtbs_Turb_0	Atm	Cloud erosion rate	Trapezoid (0,1e-04,5e-04,1e-03,2,2)
7	Mparwtr	Atm	Maximum value of function controlling convective parcel maximum condensate	Trapezoid (1e-3,1e-3,1.5e-3,2e-3,2,2)
8	Dec_Thres_Cld	Atm	Threshold for cloudy boundary layer decoupling	Trapezoid (0.01,0.011,0.1,0.8,2,4,4)
9	Fac_Qsat	Atm	Rate of change in convective parcel maximum condensate	Uniform (0.25,1)
10	Ageing	Aer	Ageing of hygrophobic aerosols (no of monolayers of organic material)	Trapezoid (0.3,1,5,10,2,2)
11	Cloud_pH	Aer	pH of cloud droplets	Trapezoid (4.6,5.3,6.3,7,4,2)
12	Carb_BB_Ems	Aer	Carbonaceous biomass burning emissions scale factor	Trapezoid (0.25,0.8,2.2,4,2,2)
13	Carb_BB_Diam	Aer	Carbonaceous biomass burning emission diameter (nm)	Trapezoid (90,160,240,300,2,2)
14	Sea_Spray	Aer	Sea spray aerosol scale factor	Trapezoid (0.125,0.6,3,8,4,3)
15	Anth_SO2	Aer	Anthropogenic SO_2 emission scale factor	Trapezoid (0.6,0.81,1.09,1.5,2,2)

Table 2: Descriptions of the perturbed parameters 16-27 used to create the ensemble and the probability density functions used in the sampling process.

Index	Name	Source	Description	PDF
16	Volc_SO2	Aer	Volcanic SO_2 emission scale factor	Trapezoid (0.71,0.99,1.7,2.38,4,1.1)
17	BVOC_SOA	Aer	Biogenic secondary aerosol formation from volatile organic compounds scale factor	Trapezoid (0.81,1.08,3.5,5.4,3,3)
18	DMS	Aer	Di-methyl-Sulphide surface ocean SO_2 concentration scale factor	Trapezoid (0.5,1.26,1.82,2,2,3)
19	Dry_Dep_Acc	Aer	Accumulation mode dry deposition velocity scale factor	Trapezoid (0.1,0.32,3.16,10,2,2)
20	Dry_Dep_SO2	Aer	SO_2 dry deposition velocity scale factor	Trapezoid (0.2,0.56,1.78,5,2,2)
21	Kappa_OC	Aer	Köhler coefficient of organic carbon	Trapezoid (0.1,0.14,0.25,0.6,4,4)
22	Sig_W	Aer	Updraft vertical velocity standard deviation	Trapezoid (0.1,0.36,0.44,0.7,2,2)
23	Dust	Aer	Dust emission scale factor	Trapezoid (0.5,0.7,1.4,2,2,2)
24	Rain_Frac	Aer	Fraction of cloud cloud covered area in large-scale clouds where scavenging occurs	Trapezoid (0.3,0.31,0.55,0.7,2,3)
25	Cloud_Ice_Thresh	Aer	Threshold of cloud ice fraction above which nucleation scavenging is suppressed	Trapezoid (0.1,0.105,0.35,0.5,2,3)
26	BC_RI	Aer	Imaginary part of black carbon refractive index	Trapezoid (0.2,0.352,0.616,0.8,4,2)
27	OC_RI		Imaginary part of organic carbon refractive index	Trapezoid (0,0,0.05,0.1,2,6)

Table 3: PD RSR constraints and the resulting 95% credible intervals of 1978 and 1850 RSR as well as 1978-PD and 1850-PD aerosol ERF. Median, High and Low columns contain output from the theoretical constraints centred on the ensemble median and selected extreme PD RSR values. The final column contains output from the near-CERES sample with Rad_Mcica_Sigma restricted to within 2% of its original range.

Constraint	Median	High	Low	Near-CERES with restricted Rad_Mcica_Sigma
PD RSR	102.6, 103.1	128.1, 128.6	88.6, 89.1	98.1, 98.5
1978 RSR	102.6, 103.1	128.2, 128.6	88.6, 89.1	98.0, 98.5
1850 RSR	100.3,101.9	125.0, 126.2	86.7, 88.1	95.8, 97.3
1978-PD ERF	-0.07, 0.07	-0.09, 0.05	0.01, 0.09	-0.09, 0.07
1850-PD ERF	-2.27, -1.00	-1.87, -0.72	-2.41, -1.51	-2.19, -0.97
1850-PD ERF credible range	1.27	1.15	0.9	1.22

Table 4: Percentage contributions to variance in ToA radiative fluxes from atmospheric and aerosol parameters with and without consideration of uncertainty in the parameter Rad_Mcica_Sigma.

Output	RSR	Cloudy-sky RSR	Clear-sky RSR	Cloudy-sky OLR
Atmospheric parameters unrestricted	79	82	4	91
Aerosol parameters unrestricted	19	8	88	3
Atmospheric parameters with Rad_Mcica_Sigma uncertainty neglected	50	59	1	80
Aerosol parameters with Rad_Mcica_Sigma uncertainty neglected	44	27	91	7

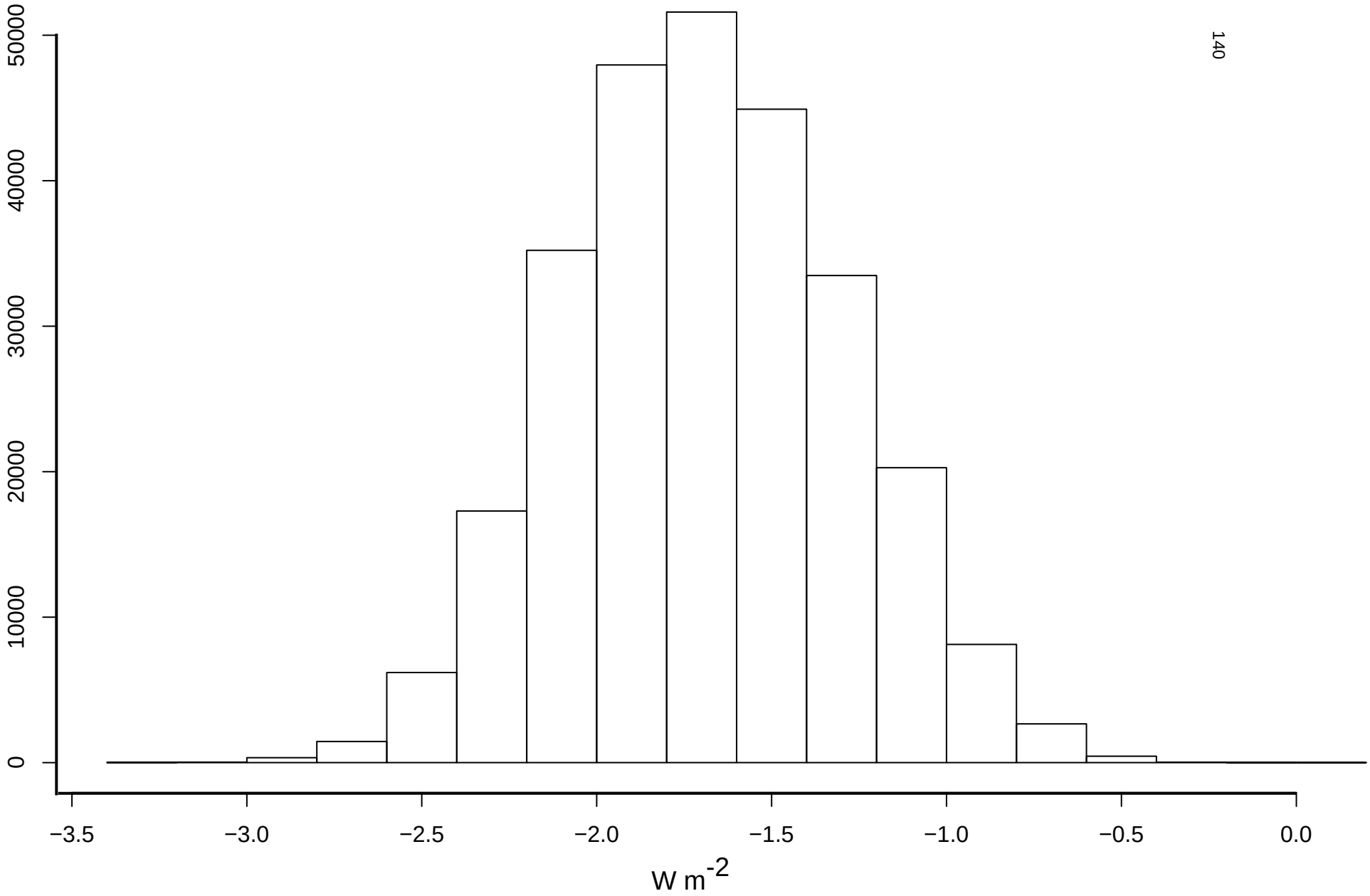

Extended Data Fig. 1. Histogram of the 270000 member Monte Carlo sample of 1850-PD annual global mean aerosol ERF, sampled across the 27-dimensional parameter space.

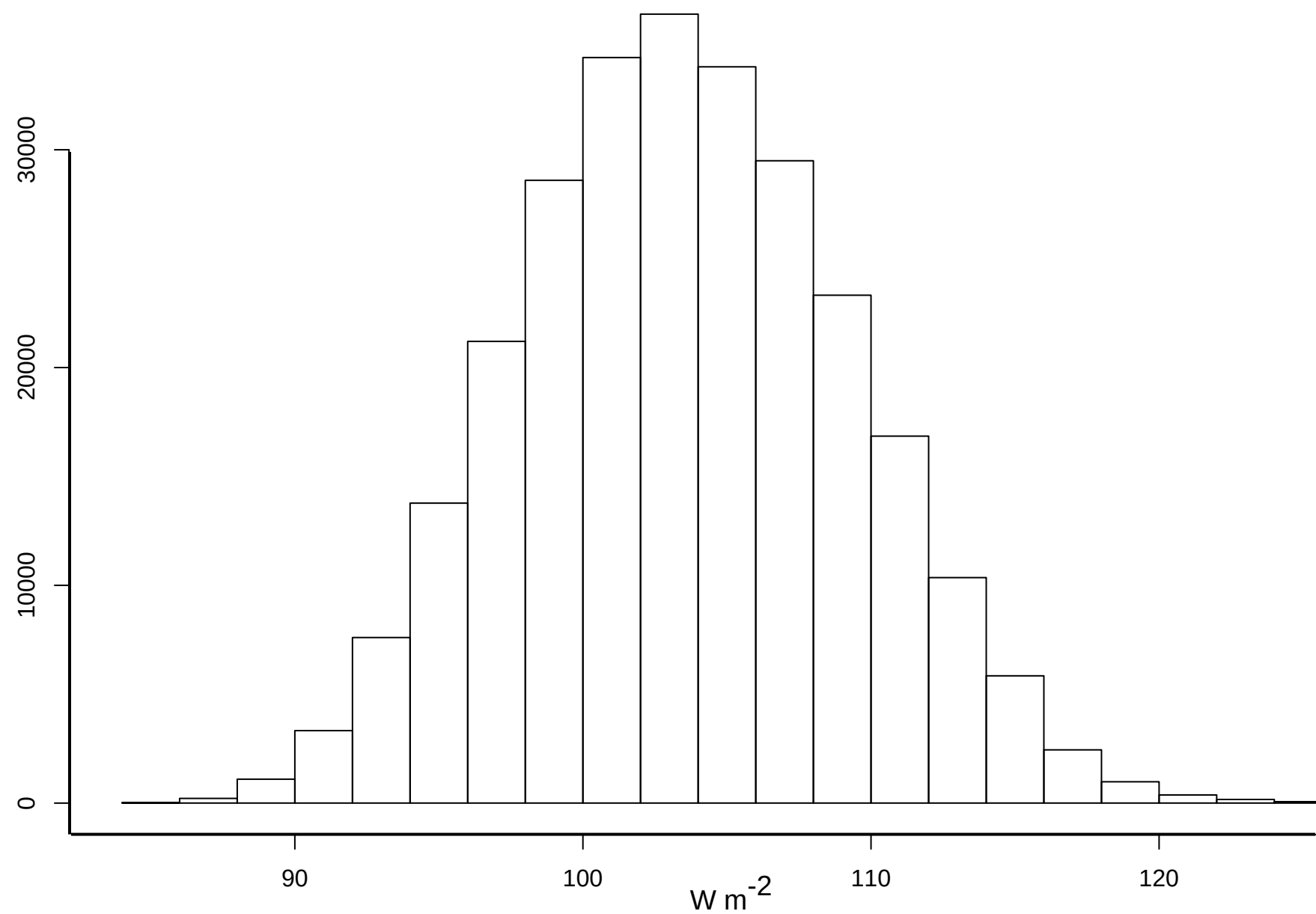

Extended Data Fig. 2. Histogram of the 270000 member Monte Carlo sample of PD annual global mean RSR, sampled across the 27-dimensional parameter space.

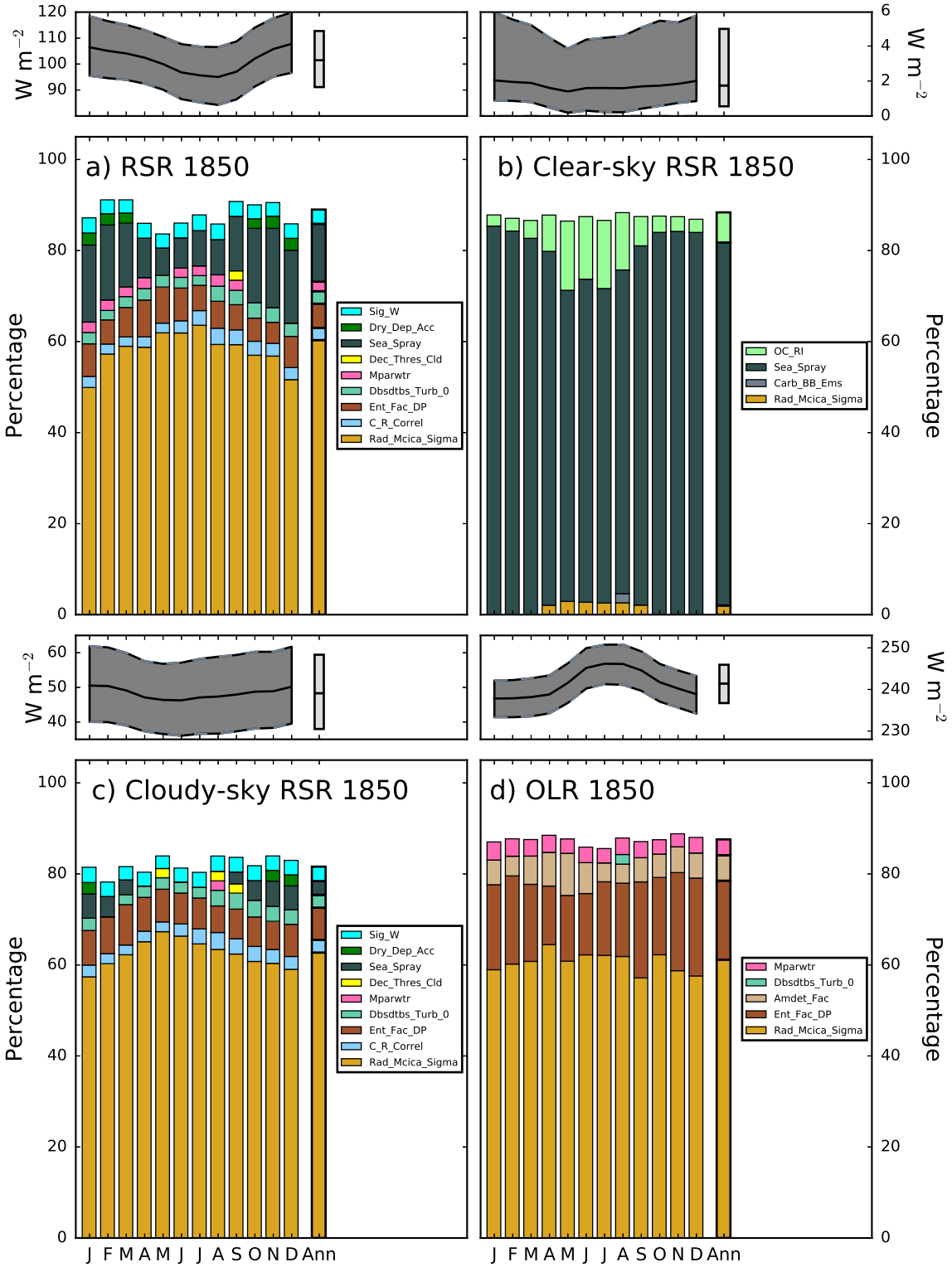

Extended Data Fig. 3. Percentage contributions to variance in PI global, monthly and annual mean ToA a) RSR, b) Clear-sky RSR c) Cloudy-sky RSR and d) OLR. Graphical features are identical to Fig. 1 in the main article.

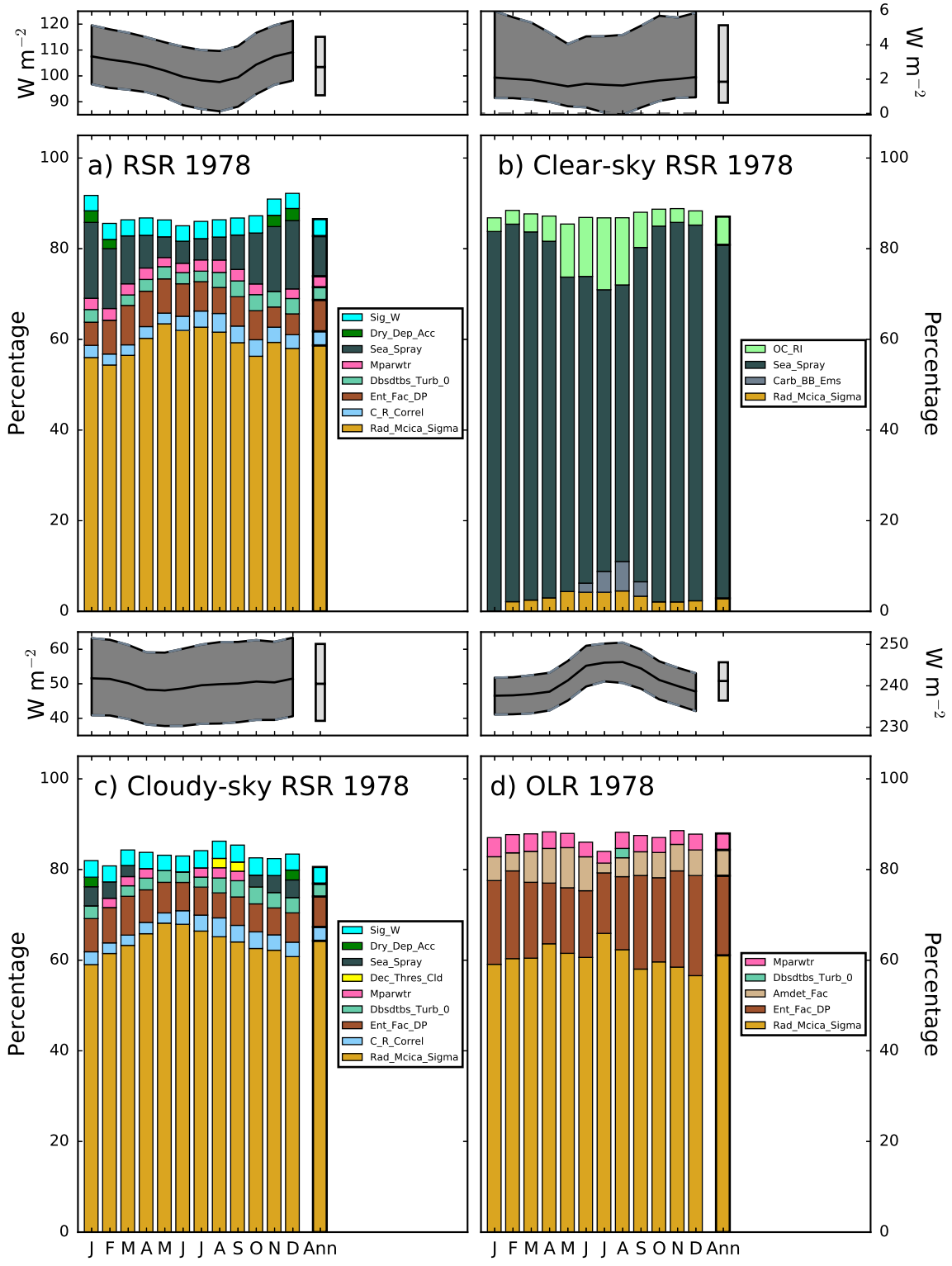

Extended Data Fig. 4. Percentage contributions to variance in 1978 global, monthly and annual mean ToA a) RSR, b) Clear-sky RSR c) Cloudy-sky RSR and d) OLR. Graphical features are identical to Fig. 1 in the main article.

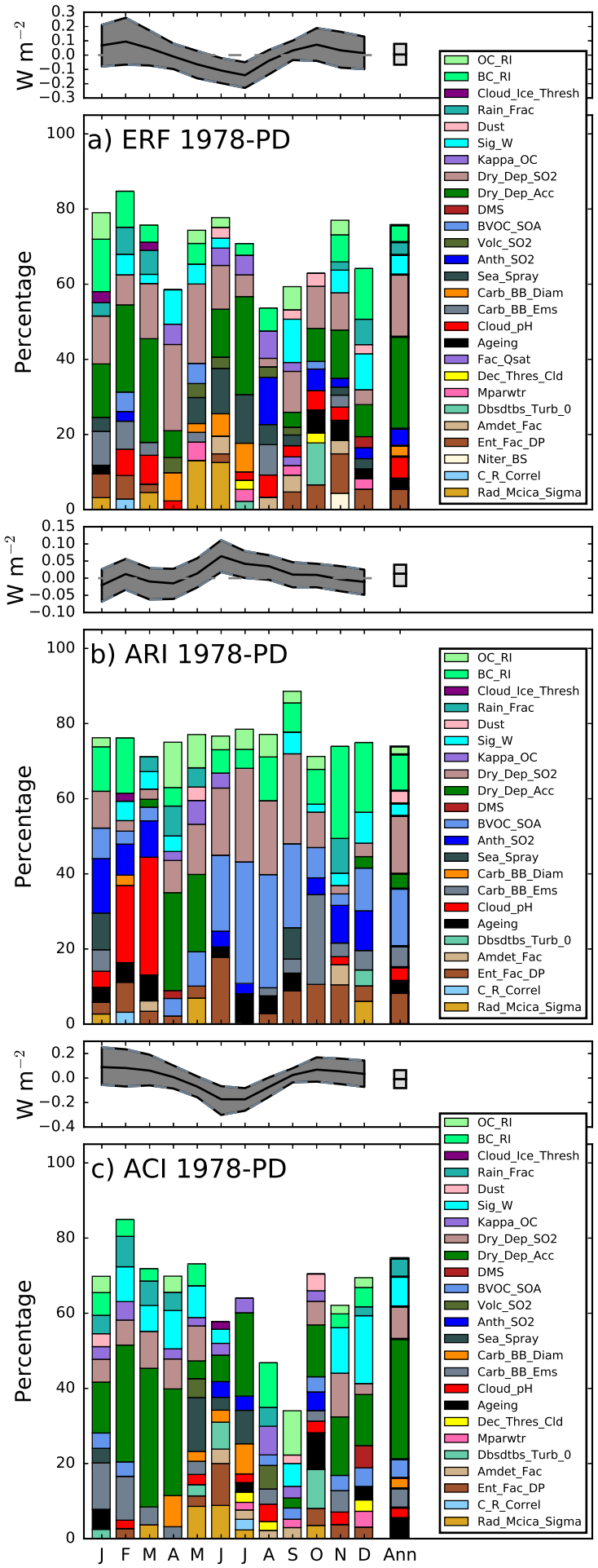

Extended Data Fig. 5. Percentage contributions to variance in 1978-PD a) aerosol ERF, b) ARI and c) ACI. Graphical features are identical to Fig. 1 in the main article.

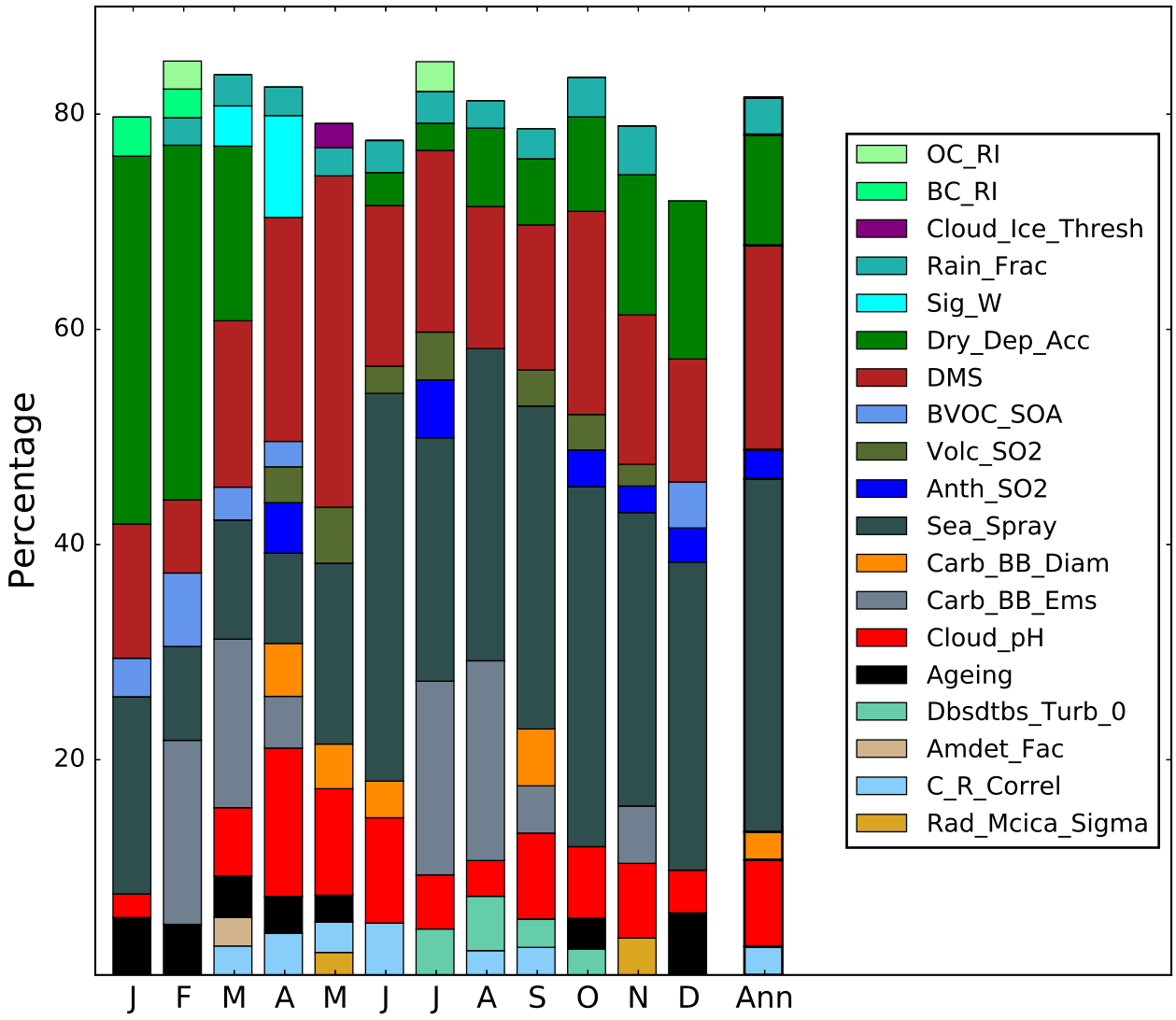

Extended Data Fig. 6. Percentage contributions to variance in 1850-PD low cloud fraction. Graphical features are identical to Fig. 1 in the main article.

Extended Data Fig. 7. Histogram of normalised Rad_Mcica_Sigma values in a) the unconstrained sample and b) the tightest CERES observationally constrained sample.

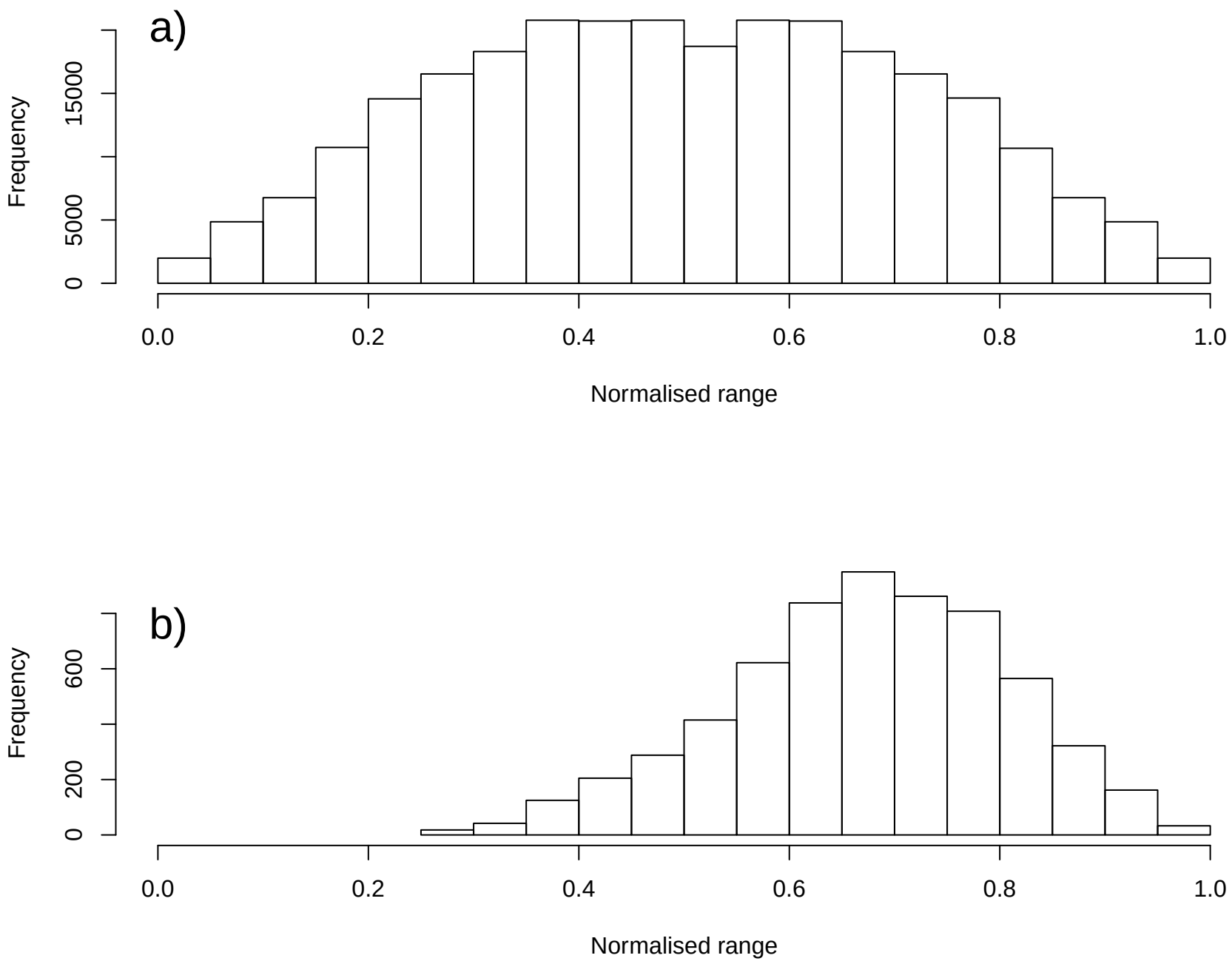

Appendix 4 - The GLOMAP model

The evolution of the The GLObal Model of Aerosol Processes (GLOMAP) (Spracklen *et al.*, 2005; Mann *et al.*, 2010, 2012) is described here in order to indicate the thoroughness with which its capacity to simulate aerosol distributions has been tested, thereby establishing the suitability of GLOMAP for creating single model PPEs (Collins *et al.*, 2010).

The GLOMAP model when used as a component of the TOMCAT chemical transport model (Chipperfield, 2006), as is the case in Chapters 2-4, uses prescribed, off-line meteorology and clouds; typically meteorological fields from the European Centre for Medium-Range Weather Forecasts (ECMWF) ERA-Interim reanalysis and clouds from International Satellite Cloud Climatology Project (ISCCP) D2 data (Rossow & Schiffer, 1999). Anthropogenic, volcanic and dust emissions are prescribed, as are DMS emissions in the ocean. However, sea spray and DMS emission fluxes into the atmosphere are calculated within the model using wind speed dependent parametrisations. GLOMAP can be coupled to the latest versions of HadGEM3, as described in Chapter 5 and Appendix 3 and can be used in a 'nudged' configuration with prescribed meteorological fields or a 'free-running' configuration with meteorological fields calculated internally.

The earliest version of the model (Spracklen *et al.*, 2005) predicted Cloud Condensation Nuclei (CCN) concentrations without distinction between aerosol chemical species. The current model version is capable of distinguishing between sulphate, organic carbon (OC), black carbon (BC), sea spray and dust, and thus allows for distinct aerosol evolution depending on the size and hydrophilic nature of the species (Mann *et al.*, 2012).

The average aerosol size distribution in a GLOMAP model grid box can be used to calculate Cloud Drop Number Concentration (CDNC). Cloud drops are defined to be those aerosols large enough to activate and form cloud droplets, for a given updraught speed at a fixed pressure level, using a mechanistic scheme (Abdul-Razzak & Ghan, 2000; Nenes & Seinfeld, 2003) essential for realistic CDNC simulation (Pringle *et al.*, 2009). Empirical schemes that relate CDNC to aerosol number or mass, but not both, are shown to create systematic regional differences in CDNC. In such simplified schemes an increase in mass typically leads to an increase in CDNC, with no regard for potential growth of individual CCN through condensation or collision and coalescence. Empirical schemes lead to maximum ACI uncertainty in regions of persistent stratocumulus cloud, the Arctic and Southern oceans (Pringle *et al.*, 2009). These regions are inherently sensitive to changes in aerosol due to the small background CDNC, as discussed in Chapter 2. The use of empirical schemes is an important source of uncertainty in RF that is avoided when using GLOMAP. The default fixed updraft speed in the GLOMAP model is 0.15m s^{-1} over all continental regions and 0.3m s^{-1} over marine regions. In Chapter 5 where GLOMAP is coupled to HadGEM3, samples of updraft speeds are used so as to include sub-grid variation in the droplet activation calculations and the standard deviation of the updraft speed probability density function (Sig_W) is perturbed.

A sectional two-moment scheme is used to represent the global aerosol size distribution (Spracklen *et al.*, 2005). The two-moment scheme utilises both aerosol mass and number, making it superior to single-moment schemes used in all but the most recent GCMs as it is produce physically explicable regional variance in CDNC (Bellouin *et al.*, 2012).

The 'modal' version of GLOMAP used in this research is a simplification of the 'bin' version, designed to be computationally efficient and therefore making it suitable for inclusion in GCMs (Mann *et al.*, 2010). The major simplification of the model version used by (Spracklen *et al.*, 2005) is the representation of the aerosol size distribution,

where seven modes are used to represent the aerosol distribution; four soluble modes for nucleation, Aitken, accumulation and coarse aerosols, as well as three insoluble modes spanning Aitken to coarse aerosols. Each mode remains dynamic in the representation of number and mass, yet is restricted to having a log-normal shape. Furthermore process rates for each mode are determined by mode average rather than full mode size range integration. Using modal averages particularly affects particle growth and nucleation scavenging rates potentially simulating excess mass in the free troposphere. However, the 'modal' aerosol representation produces comparable results to the computationally expensive 'bin' version of GLOMAP, so long as the mode widths and inter-modal separation sizes are well tuned (Mann *et al.*, 2012). The widths of the Aitken and Accumulation modes are sources of parametric uncertainty and their roles as sources of aerosol ERF uncertainty are examined in Chapters 2-5.

A comparison of a version of the HadGEM model coupled to GLOMAP, with a version using the simpler mass-based 'CLASSIC' scheme (Bellouin *et al.*, 2012), reveals that GLOMAP, with its capacity to simulate regional changes in CDNC, leads to a doubling of ARI forcing and a global average decrease in simulated ACI forcing by approximately 20%. The ACI forcing is weaker because by simulating particle formation and retaining number and mass in the nucleation mode, GLOMAP produces a larger background CDNC and the relationship between cloud albedo and CDNC is strongly non-linear (Twomey, 1974; Taylor & McHaffie, 1994) as emphasised in Chapter 2.

It has been shown in this Appendix that the GLOMAP model is sophisticated in its treatment of aerosol and performs to a standard acceptable for inclusion in GCMs used to produce climate projections for policy development, establishing GLOMAP and HadGEM3 coupled to GLOMAP as suitable models for use in the sensitivity analyses conducted within this thesis.

Appendix 5 - Identifying a suitable anthropogenic emission inventory

In Chapter 2 emission fluxes were prescribed using the 'AeroCom' emission inventory (Dentener *et al.*, 2006). The 'AeroCom' dataset is only available for the years 1750 and 2000, being designed for a specific set of AeroCom experiments. In order to explore the temporal dependence of the sensitivity analysis results in Chapter 2 an alternative emission inventory was required. Furthermore, the experimental design for Chapter 3 required emission inventories for the years 1850, 1978, 1998 and 2008. Alternative emission inventory configurations are explored here and critiqued according to their ability to maximise comparability with the broader Chapter 2 experimental design.

The three alternatives considered for representing anthropogenic emissions were:

- Option 1: Use the AeroCom emission inventory for the years where it is available and the MACCity emission dataset, a linear interpolation of the ACCMIP dataset (Lamarque *et al.*, 2010), for all remaining years. The year 1998 could potentially be exchanged for the year 2000 in the experimental design.
- Option 2: Use changes in the MACCity emission inventory to scale AeroCom emissions between 1750 and 2000 and extrapolate to 2008, thus only directly using AeroCom emissions.
- Option 3: Rely solely on the MACCity emission dataset for all years, without reference to the AeroCom emission inventory.

Fig. A7.12 shows the aerosol distribution produced by GLOMAP simulations for each emission inventory for the year 2000 and how they compare to North Atlantic marine BL observations (Raes *et al.*, 2000). This region contains persistent stratocumulus clouds

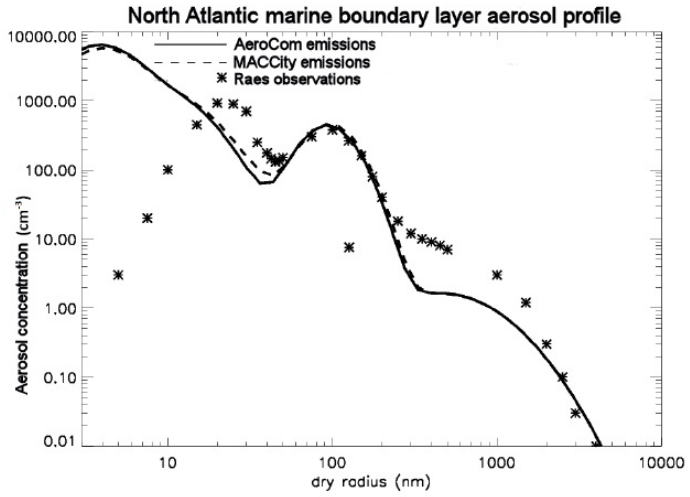

Figure 7.12: Aerosol distributions produced by GLOMAP for the year 2000 using AeroCom (bold) and MACCity (dashed) emissions. Observed North Atlantic marine BL aerosol concentrations at a range of radii are shown using stars for comparison.

and hence is an important region for ACI forcing calculations. The differences in regional aerosol distributions in this region are typical for these two emission inventories. The nucleation and Aitken mode aerosol concentrations differ slightly because the MACCity inventory includes updated shipping sector emissions. The differences between regional aerosol distributions from using the two inventories is far smaller than the difference between model output and the observations.

Because contributions to ACI variance are calculated within each model grid box, the spatial representation of emission fluxes is crucially important. Fig. A7.13 shows the differences in BC and OC emission fluxes between the AeroCom and MACCity emission inventories for the year 2000. The spatial representation of regional emissions clearly differs substantially between inventories. MACCity was developed using predominantly the same inventories as AeroCom (Dentener *et al.*, 2006; Lamarque *et al.*, 2010), yet in most cases, these inventories have been updated to incorporate technological advances and historical observations, thus its spatial representation is more reliable.

Budgets for the two datasets for the year 2000 are summarised in Table A.7.12. Differences in SO_2 emissions are partly caused by the method of categorising emissions into sectors, however the higher emissions in BC, OC and CO result from insights into historical emissions incorporated into the MACCity emission inventory.

The magnitude of emission flux differences in some model grid boxes has the potential to generate artificially large aerosol ERF estimates, making option one unsuitable. The AeroCom inventory is far sparser than MACCity for most emission sectors and has peak regional emissions in different model grid boxes. Differences in the spatial representations of carbonaceous aerosol emissions from the shipping sector have high potential to generate spurious ACI forcing values if differences in CDNC and effective radius between the two inventories were used calculate aerosol forcing.

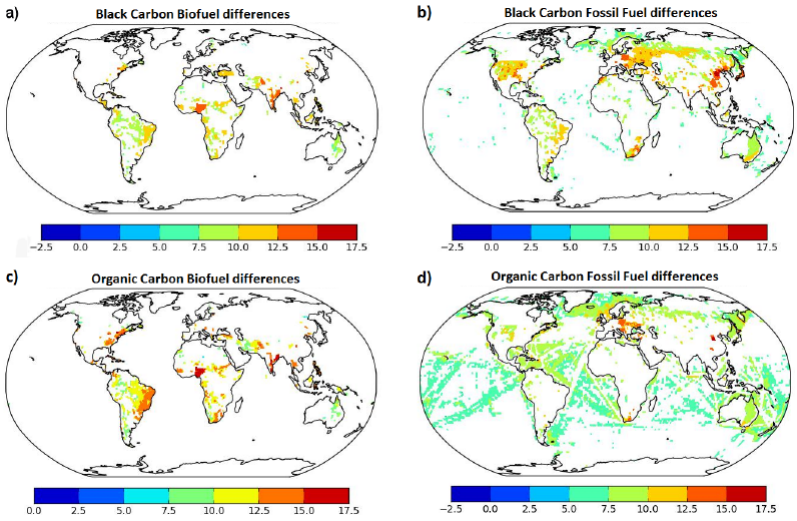

Figure 7.13: Carbonaceous emission flux differences between the MACCity and AeroCom datasets for the year 2000. All fluxes are shown in $\mathrm{kg\,m^{-2}\,s^{-1}}$ on a logarithmic scale. a) and b) contain values for BC and c) and d) contains values for OC. a) and c) are from the biofuel sector. c) and d) are from the fossil fuel sector. In each case the AeroCom values were subtracted from MACCity values within each model grid box.

Emission sector	AeroCom	MACCity	Ratio MACCity/AeroCom
Domestic SO_2	1.21E+10	1.05E+10	0.87
Industry SO_2	5.01E+10	3.54E+10	0.71
Shipping SO_2	9.43E+09	1.44E+10	1.52
Power plant SO_2	6.00E+10	6.68E+10	1.11
Road transport SO_2	2.60E+09	5.99E+09	2.30
Total SO_2	1.36E+11	1.33E+11	0.98
BC biofuel	2.30E+09	2.90E+09	1.26
BC fossil fuel	3.87E+09	3.94E+09	1.02
Total BC	6.17E+09	6.84E+09	1.11
OC biofuel	1.27E+10	1.61E+10	1.27
OC fossil fuel	4.16E+09	8.00E+09	1.92
Total OC	1.69E+10	2.41E+10	1.43
CO	4.86E+16	6.34E+16	1.30

Table 7.12: Year 2000 emission flux totals in $\mathrm{kg\,m^{-2}\,s^{-1}}$ for the AeroCom and MACCity emission inventories and the ratio of inventory totals.

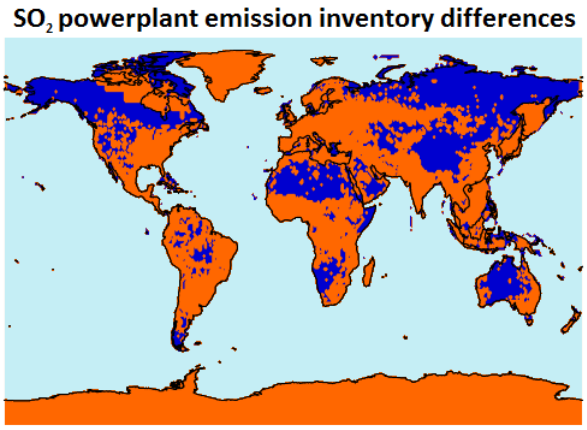

Figure 7.14: Differences in the spatial reprentation of SO_2 emissions from powerplants between the AeroCom and MACCity inventories. Grid boxes shaded dark blue represent locations where the MACCity emission inventory for the year 2000 has SO_2 emissions from the powerplant sector, yet the AeroCom emission inventory does not.

The differences in spatial representation of emission fluxes also limits the practical application of option two. Scaling of AeroCom was attempted using the average MACCity emission flux trend, for each sector, in a halo of 5 grid boxes; the central grid box and the nearest grid box in the latitudinal and longitudinal directions. Scaling in this manner can be used to produce emission datasets for the years 1978, 1998 and 2008 for most sectors, however in a small number of sectors the spatial differences in emission fluxes were too great for the halo of grid boxes to capture. Fig. A7.14 shows the locations where year 2000 emissions of SO_2 from powerplants exist in the MACCity inventory, but not in AeroCom. The lack of spatial consistency between the emission inventories rules out the temporal scaling of emissions via option two.

The AeroCom and MACCity anthropogenic emission inventories are too disparate for the application of either option one or two, thus the MACCity was used independently (Option 3) for alternative reference years in Chapter 2 and all simulations in Chapters 3-5. Choosing to use the MACCity anthropogenic emission inventory constitutes a structural change in the experimental design of Lee *et al.* (2013) and the main part of Chapter 2. Further structural changes that have the potential to improve the relevance of the sensitivity analyses implemented and analysed in Chapters 3 and 4 are considered in the following Appendix.

Appendix 6 - Structural changes to the GLOMAP model

Structural uncertainty in the GLOMAP model is explored in this Appendix by testing two alternative microphysical process parametrisations. The sensitivity analyses of Lee *et al.* (2013) and Chapter 2 revealed inadequacies in the model (Carslaw *et al.*, 2013) prompting the improvement of some process parametrisations. Firstly, the rate of removal of aerosol via wet deposition within low-level stratocumulus clouds is tested . This is a new parametrisation designed to improve aerosol concentration representations in regions of persistent stratocumulus cloud (Browse *et al.*, 2012) important for ACI forcing. Secondly, the particle formation parametrisation within the continental boundary layer is altered so that it is enhanced in the presence of organic material

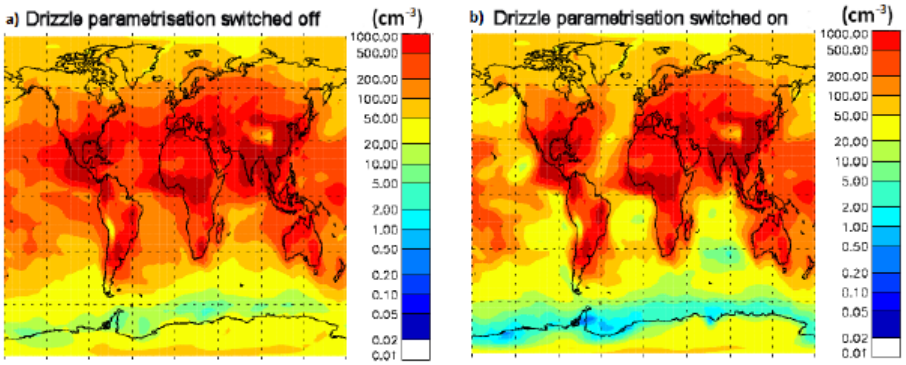

Figure 7.15: Accumulation mode aerosol concentrations (cm^{-3}) for January where a) no drizzle parametrisation is implemented and b) the drizzle parametrisation is implemented.

(Metzger *et al.*, 2010). This change brings the model in line with theoretical developments regarding particle formation.

Each structural change is implemented in isolation and after a 3 month spin-up period, using year 2008 anthropogenic emissions and meteorology. The resulting monthly average aerosol concentrations for January are compared to those from a control simulation where the default scheme is used. These tests therefore provide a first order assessment of the influence of each scheme on aerosol concentrations within GLOMAP. These two structural changes are examined here in the context of including them and their associated parameter perturbations in the experimental design of the PPEs created for Chapters 3-5.

Drizzle in low level stratocumulus clouds

The drizzle parametrisation for low-level stratocumulus clouds (Browse *et al.*, 2012) is implemented here, with the parameter set to its median value as elicited by experts for Chapters 3 and 4. Fig. A7.15 shows Accumulation mode aerosol concentrations before and after implementing the drizzle parametrisation. Fig A7.16 shows the proportion of Accumulation mode aerosol from the control case remaining when the drizzle parametrisation is implemented. Low-level stratocumulus cloud fields occur predominantly off the Western coast of continents, in regions known to be important for ACI forcing. It is in the regions of persistent Stratocumulus cloud and the Summer pole that the drizzle parametrisation has the greatest influence as intended.

Structural uncertainty represented by including the drizzle parametrisation is large enough to warrant including the parametrisation in the version of the model used to generate the PPE used in Chapters 3 and 4 and to perturb parameters related to the drizzle parametrisation. However, in regions where the drizzle parametrisation significantly reduces aerosol concentrations, particle formation occurs more prolifically, as shown in Fig. A7.17. GLOMAP marine boundary layer aerosol concentrations are known to be positively biased (Spracklen *et al.*, 2010) and applying the drizzle scheme in isolation exacerbates the bias. This issue is addressed in the following section.

Particle formation in the boundary layer with organics

In Lee *et al.* (2013) and Chapter 2 the nucleation of aerosol particles from precursor gas

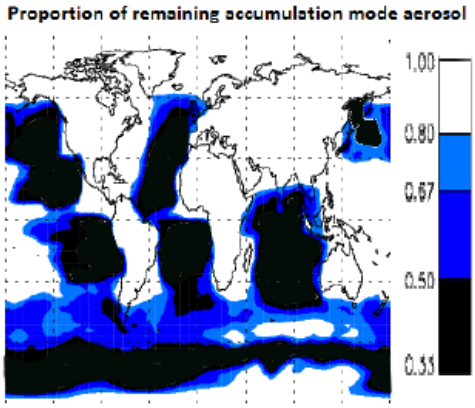

Figure 7.16: The proportion of January average Accumulation mode aerosol from the control simulation remaining when the drizzle parametrisation is implemented.

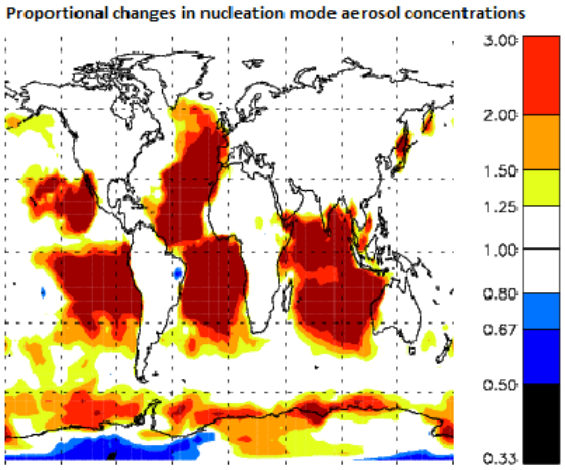

Figure 7.17: The proportional change in average January nucleation mode aerosol concentrations when the drizzle scheme is implemented.

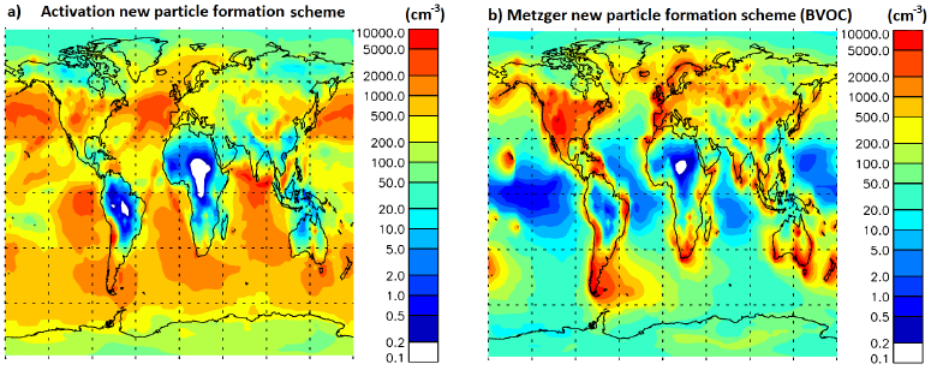

Figure 7.18: Average January nucleation mode aerosol concentrations (cm^{-3}) where a) the default 'Activation' particle formation scheme is used and b) the 'Metzger' particle formation scheme is implemented.

species is parametrised using the 'Activation' scheme (Kulmala *et al.*, 2004, 2006) which generates new particles in the boundary layer in proportion to available sulphuric acid. Introducing this scheme alleviated a low model bias in continental boundary layer aerosol concentrations (Spracklen *et al.*, 2010), yet introduced a positive nucleation mode aerosol bias in the Northern Hemisphere marine boundary layer evident in Fig. A7.12.

Lab-based experiments reveal that the rate of particle formation and the hygroscopicity of newly formed particles are higher than can be explained by formation from SO_2 alone (Metzger *et al.*, 2010). In theory the presence of organic material helps to stabilise the H_2SO_4 clusters which explains observed particle formation rates and hygroscopicities. This theory is supported by the direct measurements of the hygroscopicity of newly formed particles in the presence of biogenic volatile organic compounds (BVOC) (Keskinen *et al.*, 2013), using the CERN CLOUD chamber (Kirkby, 2013).

An implementation of the 'Metzger' particle formation scheme, where particles nucleate in proportion to available H_2SO_4 and organic mass derived from BVOC, reduces the spurious nucleation mode aerosol concentrations produced by other particle formation schemes (Metzger *et al.*, 2010) and also generates an improved representation of the seasonal cycle in CCN concentrations as compared to observations in regions of high BVOC flux (Scott *et al.*, 2013). Fig. A7.18 shows the desired effect of implementing the Metzger scheme on nucleation mode aerosol concentrations is replicated with the GLOMAP model.

BVOCs are believed to be the predominant source of organic matter in the atmosphere (Andreae & Rosenfeld, 2008), however including a representation of anthropogenic volatile organic compounds (AVOC) in the GLOMAP model, in concentrations proportional to anthropogenic CO emissions, the simulated OC mass concentrations better match observations over North America, Europe and Asia (Spracklen *et al.*, 2011). The same observed OC mass concentrations for North America (Bahadur *et al.*, 2009) are compared, in Fig. A7.19, to simulated concentrations where the Metzger scheme is active and either BVOCs are the sole source of OC or where both OC sources are used. The AVOC contribution clearly improves the agreement between simulated and observed OC mass in this region.

Although representing AVOC emissions within the model enhances OC mass

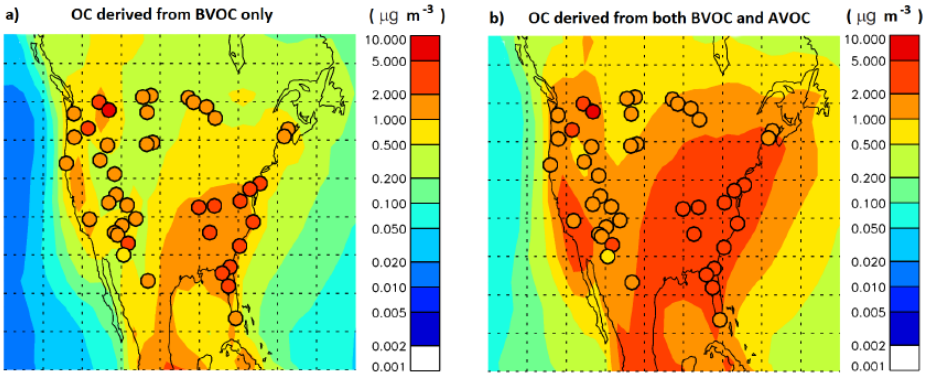

Figure 7.19: Average January OC mass concentrations, in $\mu g\,m^{-3}$, over North America for a) the Metzger particle formation scheme where BVOC contribute to aerosol nucleation and b) the Metzger scheme where both BVOC and AVOC contribute to particle formation. Observations are represented by colored circles. Simulated concentrations are represented by the underlying background shading.

concentration comparisons to observations, it has the detrimental effect of generating excessive nucleation mode aerosol concentrations in the marine boundary layer, as shown in Fig. A7.20, similar to the 'Activation' scheme. Nucleation mode aerosol concentrations in the marine boundary layer are far higher when AVOC contribute to the particle formation process. This is a result of the relatively long lifetimes of anthropogenic compared to biogenic volatile organic compounds, which allows AVOCs to be advected substantial distances before particle formation occurs.

In order to restrict excessive new particle formation over marine regions, the 'Metzger' scheme is limited to acting in the continental boundary layer only for the ensemble created for Chapters 3 and 4. Nucleation and Aitken mode concentrations showing the effect of this restriction are presented in Fig. A7.21. Continental nucleation mode concentrations are very similar in the two nucleation configurations although marine concentrations are greatly reduced. Nucleated aerosol can be advected over marine regions as can be seen for example off the South African coast in Fig. A7.21c. The aerosol distribution over the North Atlantic with the spatially restricted particle formation scheme compare favourably with observations (Dingenen *et al.*, 1995), as shown in Fig. A7.22.

Because the spatially restricted version of the Metzger particle formation parametrisation produces a significant improvement in model-observation comparisons it was implemented in the model configuration used to create the PPE for Chapters 3 and 4. The spatial restriction was not applied when creating the PPE for Chapter 5 because that model configuration had no available representation of AVOCs.

Appendix 7 - Parameter screening tests

In this Appendix the effects of parameter perturbations are tested in isolation using OAT tests. Each series of tests serves as a screening mechanism to inform the inclusion of parameters in the PPEs. Furthermore, analysis of OAT tests provides insight into the process-based, physical responses of aerosol distributions and TOA fluxes to extreme parameter perturbations. The screening tests provide an opportunity to assess the effect of each parameter on model output without needing to account for interactions between

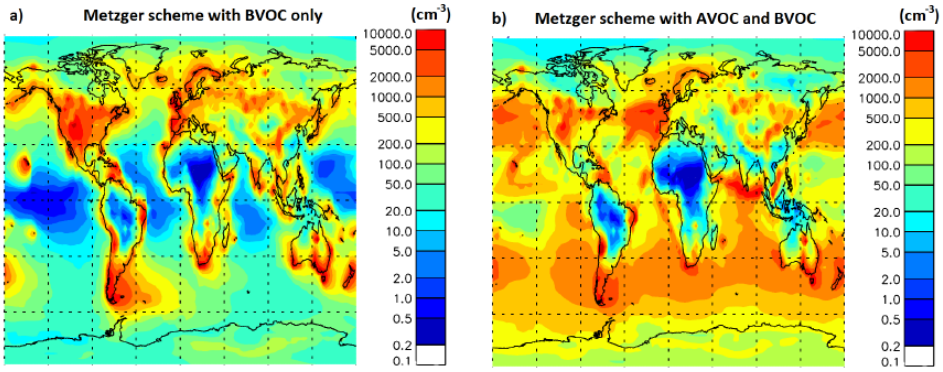

Figure 7.20: Average annual nucleation mode aerosol concentrations (cm^{-3}) at the surface for a) the Metzger particle formation scheme where BVOC contribute to aerosol nucleation and b) the Metzger scheme where both BVOC and AVOC contribute to particle formation.

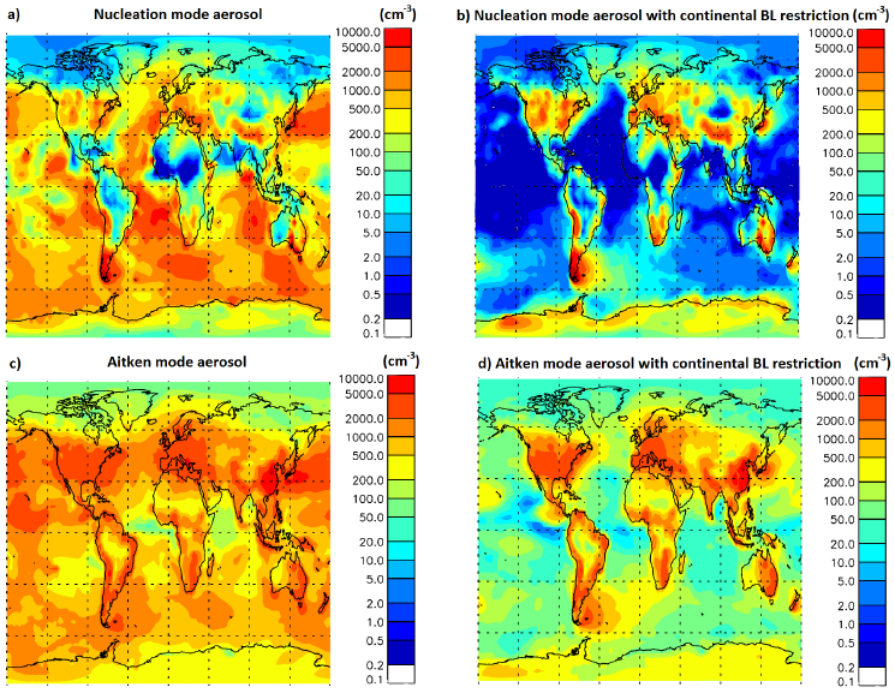

Figure 7.21: Average January boundary layer aerosol concentrations (cm^{-3}) for a) and b) the nucleation mode, c) and d) the Aitken mode. Metzger particle formation ocurrs throughout the atmosphere in a) and c), but is restricted to the continental boundary layer in b) and d).

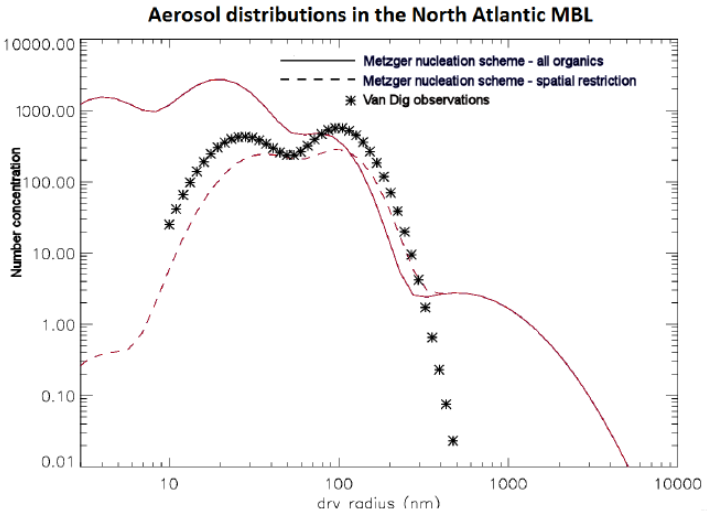

Figure 7.22: Aerosol distributions for January 2008 where Metzger particle formation ocurrs throughout the atmosphere (bold) and is restricted to the continental boundary layer (dashed). Observed North Atlantic aerosol concentrations at a range of radii are shown using stars for comparison.

parameter perturbations.

GLOMAP screening tests

GLOMAP simulations with each of the 31 aerosol parameters used to create the PPE of Chapters 3 and 4 are individually perturbed to the upper and lower limits of their ranges to provide a first order assessment of the influence of uncertain aerosol parameters on aerosol concentrations. One month simulations (after two months of spin-up from an arbitrary simulation) were created for each test, using anthropogenic emissions for the years 1978 and 2008. A further pair of simulations was created with all parameters set to their median values. Restricting the simulations to a single analysis month significantly reduces the computational cost of performing screening tests, but also introduces a risk that parameters which contribute to variance seasonally may have their influence on model output overlooked. The seasonality of parametric influence on aerosols as identified by (Lee *et al.*, 2013) was therefore considered in the interpretation of these results.

In Fig. A7.23 the proportional changes to the median simulated monthly mean surface CCN concentration, from the sixty-two OAT tests for each emission year, are provided for a) the global mean, b) the model grid box containing Cape Grim, c) the Southern Ocean regional mean and d) the North Atlantic main hurricane development regional mean, as characterised by Booth *et al.* (2012). These regions were chosen because of the presence of observational data or for their perceived climatological importance. Table A.7.13 matches the index in Fig. A7.23 with the parameter names. In the median simulations the 2008 global mean CCN concentration is 1.33% larger than the 1978 average. Those parameters which generate the largest changes in globally averaged CCN concentrations in one year but not the other have the greatest potential to affect ACI forcing over the 1978-2008 period. Conversely, since forcing is calculated using the ratio of CDNCs, parameters that systematically influence CCN concentrations in both periods

Table 7.13: Parameter names and the index used for Fig. A7.23.

Index	Parameter key	Index	Parameter key	Index	Parameter key
1	BL_Nuc	11	FF_Ems	21	Volc_SO2
2	FT_Nuc	12	BB_Ems	22	BVOC_SOA
3	Ageing	13	BF_Ems	23	AVOC_SOA
4	Acc_Width	14	FF_Diam	24	DMS
5	Ait_Width	15	BB_Diam	25	Nuc_Scav_Diam
6	Nuc_Ait_Sep	16	BF_Diam	26	T_Ice
7	Ait_Acc_Sep	17	Prim_SO4_Frac	27	Drizz_Rate
8	Act_Diam	18	Prim_SO4_Diam	28	Dry_Dep_Ait
9	Cloud_pH_Clean	19	Sea_Spray	29	Dry_Dep_Acc
10	Cloud_pH_Poll	20	Anth_SO2	30	Dry_Dep_SO2
				31	Dust

will likely have limited influence on globally averaged forcing uncertainty as described in Chapter 5.

Dry_Dep_Acc produces by far the strongest response in globally averaged CCN concentration, in agreement with Lee *et al.* (2013), although here it can be seen that the response to this parameter is largely at its upper extreme. During the elicitation exercise probability density functions were elicited for each parameter and the distribution for Dry_Dep_Acc has a long upper tail, indicating that the upper extreme is highly unlikely and will be sampled infrequently in the sensitivity analysis. The likelihood of extreme parameter values is easily overlooked in OAT tests, where the model response at the extreme edges of the multi-dimensional parameter space are being examined, rather than the output variance across the multi-dimensional response surface. As such the screening tests are not sufficient for quantifying parametric uncertainty.

The parameters which stand out regionally in the version of the model used by Lee *et al.* (2013) also generate substantial changes in CCN concentrations in these screening tests, despite the structural changes described in Appendices 5 and 6. In the Southern Ocean, for example, the three parameters making the greatest contributions to CCN concentration variance in Lee *et al.* (2013); Act_Diam, Ait_Width and Dry_Dep_Acc, generate some of the largest OAT proportional changes.

The proportional changes to global mean CCN concentrations resulting from OAT perturbations are generally consistent between years. In a few cases such as Dry_Dep_SO_2, AVOC_SOA and Anth_SO_2 the proportional CCN responses vary between years especially at the lower extremes. This is the result of spatial changes in the anthropogenic emissions and suggests that these parameters may contribute substantially to ACI forcing variance over the 1978-2008 period. There are relatively large changes in CCN concentration proportional responses to some parameters in the model grid box containing Cape Grim. The parameters in question are anthropogenic in nature; Prim_SO_4_Frac and Prim_SO_4_Diam. CCN concentrations are affected by these parameters because anthropogenic emissions are entering a relatively clean atmosphere at Cape Grim. Although SO_4 parameters have little influence globally, they have significant influence on local aerosol concentrations. The highly localised influence of the SO_4 parameters are highlighted in Fig. A7.24, which shows the ratio of Aitken aerosol mode concentrations for the perturbed and median simulations for January 2008. Not only do the parameters have highly localised effects, their effects also cancel. Perturbing Prim_SO_4_Frac to its upper extreme and Prim_SO_4_Diam to its lower extreme produce

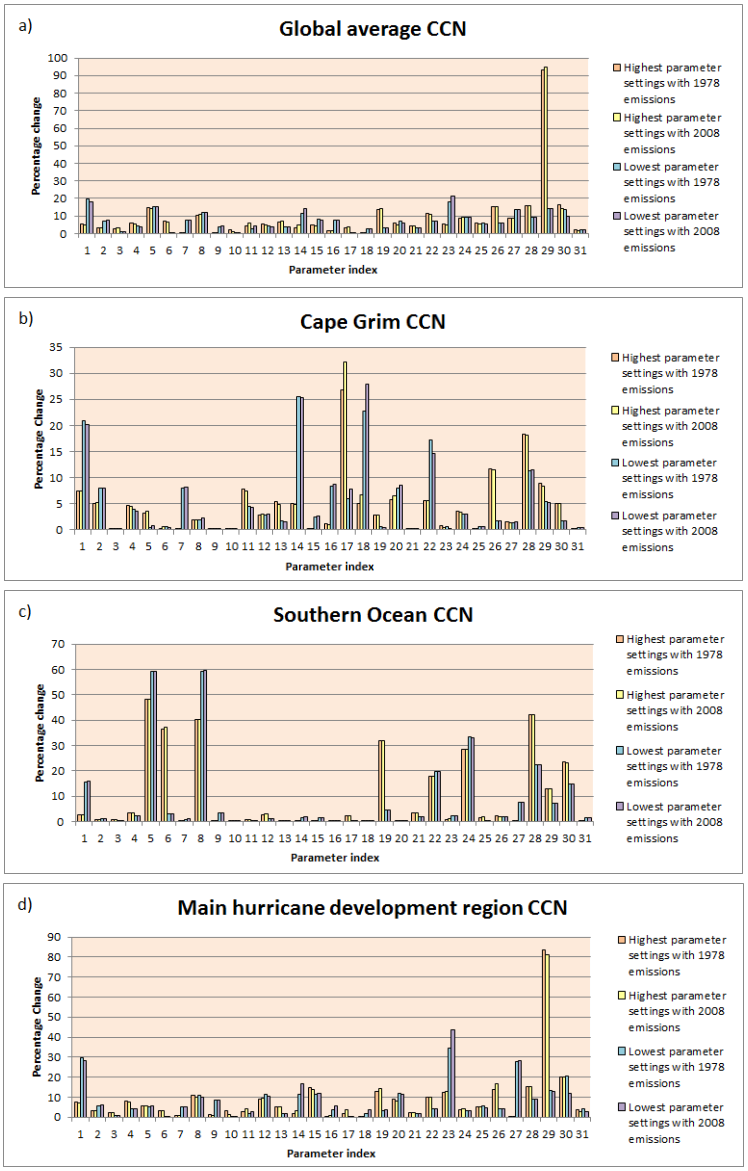

Figure 7.23: Percentage changes to globally averaged January CCN concentrations (cm^{-3}) resulting from perturbations to individual parameters for a) Global average, b) the model grid box containing Cape Grim, c) The southern ocean average and d) the MHDR average. The simulations with all parameters set to their median values, for 1978 and 2008, serve as the baseline CCN concentrations. All parameters have been perturbed to the upper and lower extremes of the ranges used in Chapters 3 and 4. A legend is provided here in Table A.7.13.

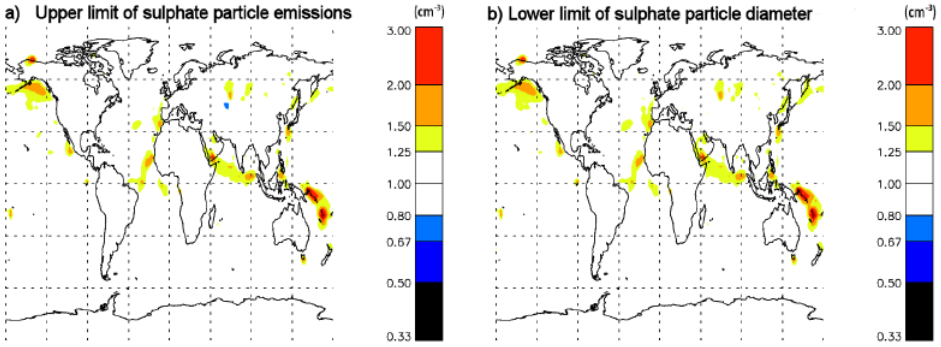

Figure 7.24: Percentage changes to median January 2008 Aitken mode aerosol concentrations (cm^{-3}) for a) parameter 17, the fraction of SO_2 emitted as sulphate particles, perturbed to its upper limit and b) parameter 18, the diameter of those particles, perturbed to its lower limit.

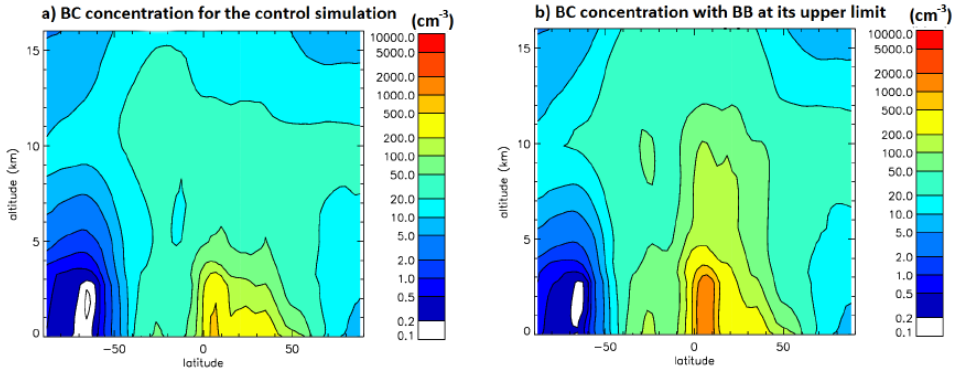

Figure 7.25: Latitudinal means of January 2008 BC concentrations (cm^{-3}), throughout the atmosphere for a) the median simulation and b) the simulation where the BB_Ems is perturbed to its lowest limit.

very similar Aitken mode aerosol responses, hence their relative importance is best determined using a sensitivity analysis where parameters are perturbed simultaneously.

Aerosol ERF in the main hurricane development region is likely to be influenced by uncertainty in BB_Ems and BB_Diam, given the differences in magnitude of CCN concentration changes in Fig. A7.23d. These carbonaceous aerosol parameters have a strong influence on CCN concentrations in equatorial regions where they are produced in the Southern Hemisphere Summer being analysed. However, this effect may be limited to a single season and may not be replicated in periods of high carbonaceous aerosol emissions in other regions. The equatorial carbonaceous aerosols analysed in the OAT test are lofted in the tropics and advected poleward into the Northern Hemisphere, as can be seen by the comparison of BC concentrations in Fig. A7.25.

Of the parameters introduced in Chapter 3 as structural advances to those used in Lee *et al.* (2013) and Chapter 2, the 'Metzger' particle formation rate, BL_Nuc, has the largest influence on CCN concentrations, exerting influence in most regions. Dry_Dep_SO_2 makes a substantial contribution to CCN concentrations in some regions,

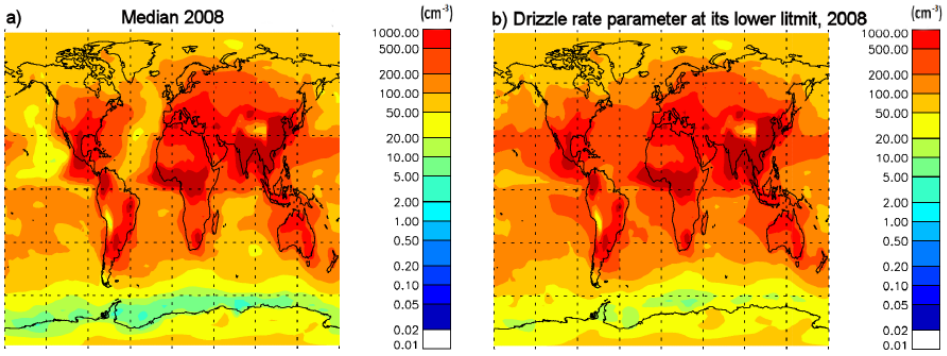

Figure 7.26: Average January 2008 accumulation mode concentrations (cm^{-3}) from a) the median run and b) the run where parameter 27, Drizz_Rate, is perturbed to its lowest limit.

although this parameter has a skewed distribution making the likelihood of sampling at the upper extreme very low. The effect of T_Ice and Drizz_Rate OAT perturbations on global mean CCN concentrations are relatively small, although Drizz_Rate influences CCN concentrations in climatically important regions of persistent stratocumulus cloud, as seen in Fig. A7.26.

The influence of a number of OAT perturbations on CCN concentrations increases with altitude for a number of parameters. In the case of Volc_SO_2, the emission flux varies with altitude, so the influence of the OAT perturbations on surface CCN concentrations in limited. Similarly FT_Nuc is designed to act at cold temperatures, hence perturbations to this parameter have a larger influence on CCN at high altitudes.

The OAT test results in this section confirm that the GLOMAP model and parameter perturbations are performing as expected. The analysis of parametric behaviour emphasises the importance of separating spatial and temporal parametric contributions to aerosol ERF variance. The OAT tests were performed for January 1978 and 2008, whereas the sensitivity analyses in this thesis are performed using monthly and annual means from full year simulations. Although the screening tests are informative parameters are perturbed to extreme values only, which are the most unlikely values for the parameters to take. A variance-based sensitivity analysis accounts for the probability density functions assigned to each uncertain parameter and thus provides a much fuller examination of the parametric influences on aerosol distributions and ACI forcing.

HadGEM screening tests

The version of the HadGEM3 model coupled to GLOMAP in Chapter 5 has never before been subject to multiple extreme parameter perturbations, as are required to produce an emulator, multi-dimensional response surface and subsequent variance-based sensitivity analysis. The OAT screening tests conducted here informed the inclusion of parameters in the Chapter 5 PPE; designed to include a broad range of aerosol and atmospheric parameters, many of which had not been previously perturbed to their extreme values in this model configuration.

As in the GLOMAP parameter screening tests the HadGEM3 tests required several months of spin-up before producing data to be analysed. In order to reduce computational costs each parameter was perturbed to its maximum value only and data

produced for a single month using year 2008 anthropogenic emissions. Output from individual perturbations was compared to output from the median simulation, where all parameters were set to their median values. Global plots of column total aerosol concentrations for all species and size modes were produced, along with vertical profiles of global distributions and the proportional changes from the median simulation. Ratios of TOA fluxes, precipitation, cloud fraction and atmospheric humidity were also plotted globally and analysed.

A small number of atmospheric parameters elicited by Sexton *et al.* (In prep.) for inclusion in a perturbed parameter framework, produced responses in the aerosol and atmospheric states indiscernible from that generated by internal variability in the 'nudged' configuration used in Chapter 5 (described in Appendix 3). This subset of parameters was consequentially removed from the HadGEM3 PPE design. The removal of these parameters does not imply they are not important components of the model because the role of parametrisations in producing plausible model output is unrelated to its contribution to output variance, where that contribution is small (Carslaw *et al.*, 2013). The size of the HadGEM3 PPE was limited by available computing resources, hence the removal of least important parameters at the screening stage allowed for the inclusion of parameters which produce important regional, not global responses. Furthermore, the density of simulations across the multi-dimensional parameter space was increased as a result of the reduction in parameter numbers, improving the resulting emulator performance.

Appendix 8 - Analysis of extreme ensemble members

Parameter combinations that result in the ten smallest and ten largest global annual mean 1850-PD aerosol ERF values in the PPE used in Chapter 5 are analysed here in greater detail. These 20 ensemble members make up just over 10% of the simulations used to create and validate the model emulator. The 1850-PD aerosol ERF, ACI and ARI values for each simulation are presented in Table A.7.14.

The ensemble design requires in remote corners of multi-dimensional parameter space so that statistical interpolation between design points is possible. The parameter combinations resulting in extreme model output are likely to be the product of multiple extreme parameter combinations and as such are not intended to be representative of the default model response. Aerosol ERF values range from -3.41 to -2.74 $\mathrm{W\,m^{-2}}$ for the smallest ERF ensemble subset, all of which were ruled out by the present-day observed RSR constraint applied in Chapter 5. For the largest aerosol ERF ensemble subset, values range from -0.93 to -0.42 $\mathrm{W\,m^{-2}}$. All values are at the edge or outside of the 95% credible range of the 270000 member sample of the emulator used to perform sensitivity analysis in Chapter 5. The parameter perturbations included in the extreme aerosol ERF simulations are within the expert elicited limits of each individual parameter, but the likelihood of sampling these combinations from an emulator, using the combined parameter probability density functions, is small.

Parameter values for each of the extreme aerosol ERF simulations are presented in Fig. A7.27. In each figure there are 27 horizontal lines, one for each parameter, containing 10 points coloured individually for the 10 ensemble members in each case. The points are the cumulative probabilities for each PPE member, calculated as the probability of sampling a value equal to or less than the actual value from the appropriate probability density function for each parameter. Examining Fig. A7.27 line by line reveals which parameters have a tendency to be high or low in each subset of the ensemble. A summary of the tendencies is provided for low aerosol ERF values in Table A.7.15 and for high values in Table A.7.16.

Parameter index	aerosol ERF	ACI forcing	ARI forcing
Smallest aerosol ERF			
136	-3.407	-3.246	-0.161
129	-3.251	-3.114	-0.137
101	-3.163	-3.327	0.164
118	-3.036	-3.123	0.087
187	-2.980	-2.911	-0.068
191	-2.848	-2.726	-0.121
121	-2.821	-3.041	0.220
75	-2.770	-2.824	0.054
88	-2.747	-2.771	0.024
63	-2.735	-2.724	-0.012
Largest aerosol ERF			
102	-0.416	-0.523	0.107
81	-0.511	-0.434	-0.077
105	-0.723	-0.635	-0.088
43	-0.775	-0.838	0.063
30	-0.786	-0.910	0.124
47	-0.860	-0.933	0.073
183	-0.864	-0.812	-0.052
148	-0.894	-1.104	0.210
126	-0.927	-0.978	0.051
90	-0.930	-0.783	-0.147

Table 7.14: The ten smallest and ten largest 1850-PD aerosol ERF values from the Chapter 5 PPE, with associated ACI and ARI forcing values.

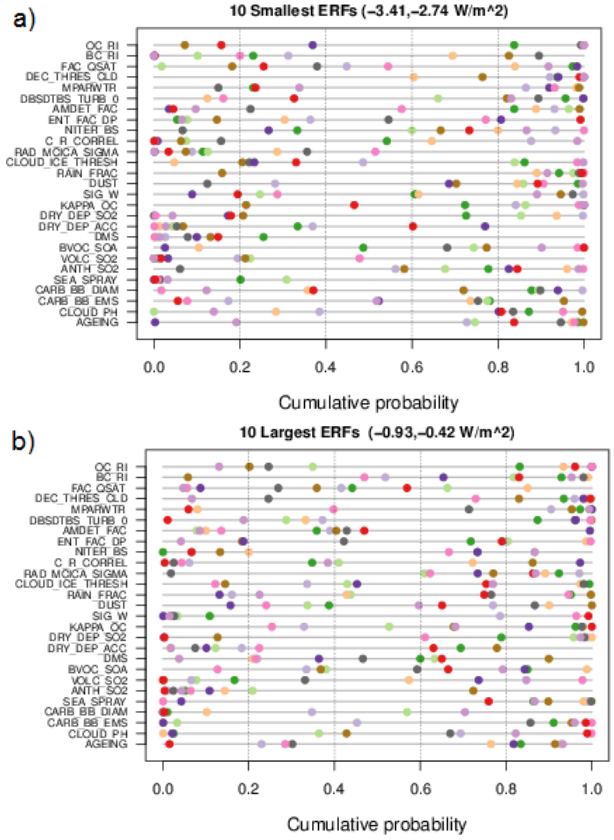

Figure 7.27: Parameter values for each parameter in the ensemble members producing the a) ten smallest and b) ten largest aerosol ERF values.

Combined high anthropogenic emissions with low natural emissions produces the strongest negative forcing in agreement with the discussion in Chapter 2 about the importance of PI natural aerosol emission uncertainty for ACI forcing. Interpretation of the effects of other parameters is informed by the OAT screening tests described in Appendix 7 and further analysis of output from individual ensemble members. Low values of Rad_Mcica_Sigma in most of these simulations causes clouds to be represented more homogeneously, producing stronger radiative effects. Rad_Mcica_Sigma is an important source of uncertainty in both TOA RSR and aerosol ERF, as shown in Chapter 5. Large Rain_Frac values cause cloud to form in a larger fraction of model grid boxes, hence a greater fraction of cloud drops and moisture are removed from the atmosphere within a model timestep. Therefore high Rain_Frac values further amplify the high anthropogenic emission, low natural aerosol forced response. High Dec_Thres_Cld values cause greater mixing in the atmospheric boundary layer, increasing the stratocumulus cloud fraction and thus the magnitude of aerosol ERF.

There are exceptions to the general pattern. Ensemble member 121 (grey dots in Fig. A.7.27) has very low anthropogenic emissions and a relatively high Rad_Mcica_Sigma value, hence this simulation is an exception to the general pattern detected in other low aerosol ERF ensemble members. The relatively low Dry_Dep_SO2 value mitigates the

Parameter	Tendency	Evidence
Dec_Thres_Cld	Large	All values larger than 0.6
Rad_Mcica_Sigma	Small	All values lower than 0.6
Rain_Frac	Large	9/10 values larger than 0.8
DMS	Small	All values lower than 0.4
Volc_SO2	Small	All values lower than 0.6
Anth_SO2	Large	9/10 values larger than 0.4
Sea_Spray	Small	All values lower than 0.4

Table 7.15: The parametric tendencies within ensemble members producing the ten smallest 1850-PD aerosol ERF values from the Chapter 5 PPE. The direction of the parametric tendency towards large or small values in the sample is provided along with evidence of for classifying the parametric tendencies.

Parameter	Tendency	Evidence
BC_RI	Large	9/10 values larger than 0.4
Amdet_Fac	Small	9/10 values lower than 0.6
Rad_Mcica_Sigma	Large	9/10 values larger than 0.6
Anth_SO2	Small	9/10 values lower than 0.4
Sea_Spray	Large	8/10 values larger than 0.6

Table 7.16: The parametric tendencies within ensemble members producing the ten largest 1850-PD aerosol ERF values from the Chapter 5 PPE. The format is identical to Table A.7.15.

impact of the small Anth_SO2 value on aerosol ERF. A low Mparwtr value partially explains why the high Rad_Mcica_Sigma value is unimportant for aerosol ERF calculation in this case. By increasing precipitation efficiency and making the atmosphere drier the low Mparwtr effectively removes cloud from the atmosphere, reducing the impact of Rad_Mcica_Sigma in the radiation calculation. Large BC_RI values act to increase ARI and decrease ACI forcing, with competing influences on aerosol ERF. Ensemble member 121 has the largest ARI forcing value (0.22 $\mathrm{W\,m^{-2}}$) of the small aerosol ERF ensemble subset.

Another interesting exception to the general small aerosol ERF pattern is simulation 118 (shaded brown in Fig. A7.27a)) which has the lowest Rain_Frac value and a moderate Anth_SO2 value. Aerosol ERF in this simulation is likely determined by several parameters near the end of their individual ranges (OC_RI, Mparwtr, Amdet_Fac, Carb_BB_Ems, Cloud_pH and Ageing) which may be influencing aerosol ERF in combination.

At the other end of the simulated aerosol ERF scale the sample of ten largest values generally have inverse parameter combinations (Table A.7.16) to those in the small aerosol ERF sample; low anthropogenic and high natural aerosol emissions and high Rad_Mcica_Sigma. Furthermore, generally small Amdet_Fac values increase precipitation and reduce atmospheric humidity, significantly altering aerosol size distributions near source regions. High values of BC_RI increase the efficiency with which carbonaceous aerosols are scavenged, removing a significant component of anthropogenic aerosol forcing from the present-day atmosphere.

Simulation 102 (grey dots in Fig. 7.27b)) has a very low Rad_Mcica_Sigma value which contrasts with the general pattern. However this simulation also has numerous parameters (BC_RI, Dbsdtbs_Turb_0, c_r_correl, Cloud_Ice_Thresh, Sig_W, Kappa_OC, Dry_Dep_SO2, Anth_SO2, Sea_Spray and Carb_BB_Diam) with values near the limit of their ranges. This simulation shows that although a high Rad_Mcicia_Sigma value can increase aerosol ERF, it is not essential for producing exceptionally high values.

There are 2 simulations, 126 and 90, that produce very similar aerosol ERF values, -0.927 and -0.930 $\mathrm{W\,m^{-2}}$ respectively, but have distinct regional ARI and ACI forced responses. Simulation 126 is shaded pink in Fig. A7.27b) and simulation 90 is shaded brown. Both simulations have low BC_RI values, with very high Carb_BB_Ems and low Carb_BB_Diam values. However, ARI forcing is strongly positive over China and the Pacific in simulation 126, but not 90. Ent_Fac_Dp and Sig_W are relatively low in simulation 90 and high in simulation 126.

The fact that there are several distinct combinations of parameter values that cause extremely small global annual mean aerosol ERF provides further support for the claim made in Chapter 5 that tuning of GCMs should be done cautiously because of model equifinality.

References - Appendices

Abdul-Razzak, H., & Ghan, S. J. 2000. A parameterisation of aerosol activation: 2. Multiple aerosol types. *J. Geo. Res.*, **105**, 6837–6844.

Andreae, M. O., & Rosenfeld, D. 2008. Aerosol-cloud-precipitation interactions. part 1. the nature and sources of cloud-active aerosols. *Ear. Sci. Rev.*, **89**, 13–41.

Bahadur, R., Habib, G., & Russell, L. M. 2009. Climatology of PM2.5 organic carbon concentrations from a review of ground based atmospheric measurements by evolved gas analysis. *Atmos. Env.*, **43**, 1591–1602.

Bellouin, N., Mann, G. W., Woodhouse, M. T., Johnson, C., Carslaw, K. S., & Dalvi, M. 2012. Impact of the modal aerosol scheme GLOMAP-mode on aerosol forcing in the Hadley Centre Global Environmental Model. *Atmos. Chem. Phys.*, **12**, 21437–21479.

Booth, B. B. B., Dunstone, N. J., Halloran, P. R., Andrews, T., & Bellouin, N. 2012. Aerosols implicated as a prime driver of twentieth-century North Atlantic climate variability. *Nat.*, **484**, 228–232.

Browse, J., Carslaw, K. S., Arnold, S. R., Pringle, K. J., & Boucher, O. 2012. The scavenging processes controlling the seasonal cycle in Arctic sulphate and black carbon aerosol. *Atmos. Chem. Phys.*, **12**, 6775–6798.

Carslaw, K. S., Lee, L. A., Reddington, C. L., Mann, G. W., & Pringle, K. J. 2013. The magnitude of uncertainty in global aerosol. *Farr. Disc.*, **165**, 495–512.

Chipperfield, M. P. 2006. New version of the TOMCAT/SLIMCAT off-line chemistry transport model. *Quart. J. Roy. Meteor. Soc.*, **132**, 1179–1203.

Collins, M., Booth, B. B. B., Bhaskaran, B., Harris, G. R., Murphy, J. M., Sexton, D. M. H., & Webb, M. J. 2010. Climate model errors, feedbacks and forcings: a comparison of perturbed physics and multi-model ensembles. *Clim. Dyn.*, **36**, 1737–1766.

Dentener, F., Kinne, S., Bond, T., Boucher, O., Cofala, J., Generoso, S., Ginoux, P., Gong, S., Hoelzemann, J. J., Ito, A., Marelli, L., Penner, J. E., -P.Putaud, J., Textor, C., Schulz, M., van der Werf, G. R., & Wilson, J. 2006. Emission of primary aerosol and precursor gases in the years 2000 and 1750 prescribed data-sets for AeroCom. *Atmos. Chem. Phys.*, **6**, 4321–4344.

Dingenen, R. Van, Raes, F., & Jensen, N. R. 1995. Evidence for anthropogenic impact on number concentration and sulfate content of cloud-processed aerosol-particles over the north-Atlantic. *J. Geo. Res. Atmos.*, **100**, 21057–21067.

Keskinen, H., Virtanen, A., Jontsensaari, J., Tsagkogeorgas, G., Duplissy, J., Schobesberger, S., Gysel, M., F.Riccobono, Slowik, J. G., Bianchi, F., Yli-Juuti, T., Lehtipalo, K., Breitenlechner, L. Rondo M., Kupc, A., Almeida, J., Amorim, A., Dunne, E. M., Downard, A. J., Ehrhart, S., Franchin, A., Kajos, M. K., Kirkby, J., Kürten, A., Neiminen, T., Makhmutov, V., Mathot, S., Meittinen, P., Onnela, A., Petäjä, T., Praplan, A., Santos, F. D., Schallhart, S., Sipilä, M., Stozhkov, Y., Tomé, A., Vaattovaara, P., Wimmer, D., Prevot, A., Dommen, J., Donahue, N. M., Flagan, R. C., Weingertner, E., Viisanen, Y., Riipinen, I., Hansel, A., Curtius, J., Kulmala, M., Worsnop, D. R., Baltensperger, U., Wex, H., Stratmann, F., & Laaksonen, A. 2013. Evolution of particle composition in CLOUD nucleation experiments. *Atmos. Chem. Phys.*, **13**, 5587–5600.

Kirkby, J. 2013. *Atmospheric Nucleation and Growth in the CLOUD Experiment at CERN*. 1527 edn. AIP Conference Proceedings.

Kulmala, M., .Kerminen, V. -M, Anttila, T., Laaksonen, A., & O'Dowd, C. D. 2004. Organic aerosol formation via sulphate cluster activation. *Geophys. Res. Lett. Atmos.*, **109**, D04205.

Kulmala, M., Lehtinen, K. E. J., & Laaksonen, A. 2006. Cluster activation theory as an explaination of the linear dependence between formation rate of 3nm particles and sulphuric acid concentration. *Atmos. Chem. Phys.*, **6**, 787–793.

Lamarque, J. F., Bond, T. C., Eyring, V., Granier, C., Heli, A., Kilmont, Z., Lee, D., Liousse, C., Mieville, A., Owen, B., Schultz, M. G., Shindell, D., Smith, S. J., Stehfest, E., Van Aardenne, J., Cooper, O. R., Kainuma, M., Mahowald, N., McConnell, J. R., Naik, V., Riahi, K., & van Vuuren, D. P. 2010. Historical (1850-2000) gridded anthropogenic and biomass burning emissions of reactive gases and aerosols: methodology and application. *Atmos. Chem. Phys.*, **10**, 7017–7039.

Lee, L. A., Pringle, K. J., Reddington, C. L., Mann, G. W., Stier, P., Spracklen, D. V., Pierce, J., & Carslaw, K. S. 2013. The magnitude and causes of uncertainty in global model simulations of cloud condensation nuclei. *Atmos. Chem. Phys.*, **13**, 8879–8914.

Mann, G. W., Carslaw, K. S., Spracklen, D. V., Ridley, D. A., Manktelow, P. T., Chipperfield, M. P., Pickering, S. J., & Johnson, C. E. 2010. Description and evaluation of GLOMAP-mode aerosol microphysics model for the UKCA composition-climate model. *Geosci. Mod. Dev.*, **3**, 519–551.

Mann, G. W., Carslaw, K. S., Ridley, D. A., Merikanto, D. V. Spracklen K. J. Pringle J., Korhonen, H., Schwarz, J. P., Lee, L. A., Manktelow, P. T., Woodhouse, M. T., Schmidt, A., Breider, T. J., Emmerson, K. M., Reddington, C. L., Chipperfield, M. P., & Pickering, S. J. 2012. Intercomparison of modal and sectional aerosol microphysics representations within the same 3-D global chemical transport model. *Atmos. Chem. Phys.*, **12**, 4449–4476.

Metzger, A., Verheggen, B., Dommen, J., Duplissy, J., Prevot, A. S. H., Weingartner, E., Riipinen, I., Kulmala, M., Spracklen, D. V., Carslaw, K. S., & Baltensperger, U. 2010. Evidence for the role of organics in aerosol particle formation under atmospheric conditions. *Proc. Nat. Ac. Sci.*, **107**, 6646–6651.

Nenes, A., & Seinfeld, J. H. 2003. Parameterization of cloud droplet formation in global climate models. *J. Geo. Res.*, **108**.

Pringle, K. J., Carslaw, K. S., Spracklen, D. V., Mann, G. M., & Chipperfield, M. P. 2009. The relationship between aerosol and cloud drop number concentrations in a global aerosol microphysics model. *Atmos. Chem. Phys.*, **9**, 4131–4144.

Raes, F., Bates, T., McGovern, F., & Liedekerke, M. Van. 2000. The 2nd Aerosol Characterization Experiment (ACE-2): general overview and main results. *Tell. Ser. B-Chem. and Phy. Meteor.*, **52**, 111–125.

Rossow, W. B., & Schiffer, R. A. 1999. Advances in understanding clouds from ISCCP. *B. Am. Meteorol. Soc.*, **80**, 2261–2288.

Scott, C. E., Rap, A., Spracklen, D. V., Forster, P. M., Carslaw, K. S., Mann, G. W., Pringle, K. J., Kivekās, N., Kulmala, M., Lihavainen, H., & Tunved, P. 2013. The direct and indirect radiative effect of biogenic secondary orgainc aerosol. *Atmos. Chem. Phys.*, **13**, 16961–17019.

Sexton, David M. H., Karmalkar, A., Murphy, J., Booth, B. B. B., & Regayre, L. A. In prep.. The elicitation of distributions of parameters in HadGEM3 versions GA4 and GA7 for use in perturbed parameter ensembles. *Hadley Centre technical note, Met Office, U.K.*

Spracklen, D. V., Pringle, K. J., Carslaw, K. S., Chipperfield, M. P., & Mann, G. W. 2005. A global off-line model of size-resolved aerosol microphysics: I. Model development and prediction of aerosol properties. *Atmos. Chem. Phys.*, **5**, 2227–2252.

Spracklen, D. V., Carslaw, K. S., Merikanto, J., Mann, G. W., Reddington, C. L., Pickering, S., Ogren, J. A., Andrews, E., Baltensperger, U., Weingartner, E., Boy, M., Kulmala, M., Laakso, L., Lihavainen, H., Kivekas, N., Komppula, M., Mihalopoulos, N., Kouvarakis, G., Jennings, S.G., O'Dowd, C., Birmili, W., Wiedensolher, A., Weller, R., Gras, J., Laj, P., Sellegri, K., Bonn, B., Krejci, R., Laaksonen, A., Hamed, A., Minikin, A., Harrison, R. M., Talbot, R., & Sun, J. 2010. Explaining global surface aerosol number concentrations in terms of primary emissions and particle formation. *Atmos. Chem. Phys.*, **10**, 4775–4793.

Spracklen, D. V., Jimenez, J. L., Carslaw, K. S., Worsnop, D. R., Evans, M. J., Mann, G. W., Zhang, Q., Canagaratna, M. R., Allan, J., Coe, H., McFiggans, G., Rap, A., & Forster, P. 2011. Aerosol mass spectrometer contraint on the global secondary organic aerosol budget. *Atmos. Chem. Phys.*, **11**, 12109–12136.

Taylor, J. P., & McHaffie, A. 1994. Measurements of cloud susceptibility. *J. Atmos. Sci.*, **51**, 1298–1306.

Twomey, S. 1974. Pollution and the planetary albedo. *Atmos. Env.*, **8**, 1251–1256.